Scanning Tunneling Microscopy and Atomic Force Microscopy Measurements on Correlated Systems

Dissertation zur Erlangung des akademischen Grades eines
Doktors der Naturwissenschaften (Dr. rer. nat.)

vorgelegt von
Matthias Münks

an der

Universität
Konstanz

Mathematisch-Naturwissenschaftliche Sektion
Fachbereich Physik

Tag der mündlichen Prüfung: 17.10.2017
1. Referent: Prof. Dr. Klaus Kern
2. Referent: Prof. Dr. Fabian Pauly

Zusammenfassung

Die magnetischen Signaturen einzelner Atome auf Oberflächen oder eingebettet in molekularen Strukturen hängen größtenteils von der unmittelbaren Umgebung ab. Zu Beginn dieser Arbeit präsentieren wir Messungen einzelner Co Atome auf einer h-BN/Rh(111) Oberfläche mit einem kombinierten Rastertunnel- und Rasterkraftmikroskop. Wir zeigen wie diese Co Atome CoH_x Komplexe bilden, die je nach Ihrem Wasserstoffgehalt (Co, CoH, $\mathrm{CoH_2}$) verschiedene Spinsignale zeigen ($S = 3/2, S = 1, S = 1/2$). Die h-BN Entkopplungslage besitzt eine periodische Welligkeit von 100 pm senkrecht zur Rh(111) Oberfläche, wodurch nicht nur die magnetische Anisotropie der CoH_x Komplexe beeinflusst wird sondern auch deren Kopplungsstärke zu dem Rh Substrat. Diese Welligkeit führt zu einem sehr weichen Substrat welches aktiv mit der Spitze verformt werden kann während man parallel die involvierten kurzreichweitigen Kräfte und Tunnelströme misst.

Eine einzigartige Eigenschaft der Rastersondenmikroskopie ist die präzise Kontrolle über beide Elektroden, der Probe und Spitze, welche die einzelnen Atome oder Moleküle im Tunnelkontakt untersuchen. Im weiteren Verlauf zeigen wir, wie eine Pt Spitze mit einzelnen Co oder H Atomen funktionalisiert werden kann. Mit einer Co-funktionalisierten Spitze können wir kontrolliert an ein CoH_x Komplex auf der h-BN/Rh(111) Oberfläche ankoppeln. Wir sehen Hinweise auf Spin-Spin Korrelationen zwischen dem stark hybridisierten Co Atom auf der Pt Spitze und dem Elektronenbad in der Pt Spitze wenn diese stark an ein schwach hybridisiertes CoH_x auf der Probe angekoppelt wird. Die Tunnelspektroskopie zeigt eine Asymmetrie die normalerweise nur für spin-polarisierten Elektronentransport in Magnetfeldern auftritt. Wir zeigen, dass diese Asymmetrie hier ohne Magnetfelder auftritt, durch die Kopplungsstärke kontrolliert werden kann und der Ursprung der Spin-Spin Korrelationen in der funktionalisierten Spitze liegt. Wenn die Pt Spitze mit einem H Atom funktionalisiert und in die unmittelbare Nähe eines CoH Komplexes gebracht wird, können wir das H Atom reversibel an den CoH Komplex binden sowie entfernen und so den Spinzustand kontrollieren. Die Tunnelspektroskopie zeigt den Übergang des CoH $S = 1$ Komplexes mit magnetischer Anisotropie zu einem $\mathrm{CoH_2}$ $S = 1/2$ Komplex mit einer Kondo Resonanz während zur gleichen Zeit die Kraftmessungen einen Übergang zu einem energetisch günstigeren Potential zeigen. Stumpfe Spitzen scheinen aktiv die Adsorbierungslandschaft der CoH Komplexe auf der h-BN Schicht zu modifizieren.

Unsere Experimente erlauben eine atomar präzise Kontrolle über molekulare magnetische Strukturen. Wir zeigen, dass Schlüsselparameter wie die magnetische Anisotropie der CoH_x Komplexe sowie deren Kondo-Interaktion oder Spin-Spin Korrelationen mit einer Metallelektrode gemessen und kontrolliert werden können.

Abstract

The magnetic signatures of single atoms on surfaces or embedded in different molecular configurations vastly depend on their adjacent environment. Placing transition metal Co atoms on a h-BN/Rh(111) substrate allows us to probe their magnetic signatures with scanning tunneling microscopy and spectroscopy as well as atomic force measurements. We show how hydrogen adsorption creates cobalt hydride complexes, Co, CoH and CoH_2, for which the hydrogen actively controls the observed spin state, $S = 3/2$, $S = 1$, $S = 1/2$. A new approach is the h-BN decoupling layer that mediates the cobalt hydrides' coupling to the Rh(111) metal due to its intrinsic spatial corrugation. This corrugation not only adjusts the magnetic anisotropy energies of the adsorbed complexes but also beds them on an ultrasoft substrate that can actively be manipulated with tip interactions while monitoring the involved forces.

A unique feature of scanning probe experiments is the precise control over both metal electrodes, tip and sample, that address the atoms or molecules in the tunnel junction. We show how Pt tips are functionalized with single Co or H atoms. In the case of a Co-functionalized Pt tip, we can controllably couple it to a CoH_x system on the h-BN/Rh(111) surface. Signatures of correlations between the strongly hybridized spin on the tip and its electron bath are seen when it is coupled to the weakly hybridized cobalt hydride on the sample surface. Tunneling spectroscopy uncovers an asymmetry reminiscent of spin-polarized transport in magnetic fields. We show that, even at zero field, this asymmetry is exclusively controlled by the coupling strength and related to spin-spin correlations in the functionalized tip. Furthermore, we can actively control the chemical composition of the CoH_x systems. When the Pt tip is functionalized with a single hydrogen atom and brought in proximity to a CoH system, we can reversibly attach and remove the additional hydrogen atom in order to control the spin state of a CoH system and change a CoH $S = 1$ signature with magnetic anisotropy to a CoH_2 $S = 1/2$ Kondo resonance. Blunt tip apexes seem to actively change the adsorption environments of the CoH_x complexes when brought into close proximity to the h-BN substrate. All of these modifications are actively monitored in their tunneling current, frequency shift and spectroscopic signals.

The results of our experiments allows an atomically precise control over magnetic molecular junctions. We show how key parameters such as the magnetic anisotropy energies of adsorbed CoH_x systems, their Kondo exchange coupling to the metal electrode as well as hidden spin-spin correlations of these systems with a bare metal electrode can be monitored and actively controlled.

Keywords: Combined STM/AFM, qPlus, Correlated and coupled atomic spins, Surface Magnetism, Magnetic Anisotropy, Kondo.

Publications

Since the beginning of the Ph.D. thesis, three publications have been published and two more are in the process of being drafted:

- P. Jacobson, T. Herden, **M. Muenks**, G. Laskin, O. Brovko, V. Stepanyuk, M. Ternes, K. Kern. Quantum engineering of spin and anisotropy in magnetic molecular junctions. *Nature Communications* 6, 8536 (2015).
- **M. Muenks**, P. Jacobson, M. Ternes, K. Kern. Correlation-driven transport asymmetries through coupled spins in a tunnel junction.
  Nature Communications 8, 14119 (2017).
- P. Jacobson, **M. Muenks**, G. Laskin, O. Brovko, V. Stepanyuk, Markus Ternes, Klaus Kern. Potential energy driven spin manipulation via a controllable hydrogen ligand.
  Science Advances, (2017)[1].
- **M. Muenks**, P. Jacobson, M. Ternes, K. Kern. Electron transport through correlated Kondo systems in magnetic field. *In preparation*.
- **M. Muenks**, P. Jacobson, M. Ternes, K. Kern. Short-range force and magnetic anisotropy modulation via an ultrasoft substrate. *In preparation*.

---

[1] Manuscript is accepted and will be published in April 2017. M. Muenks and P. Jacobson with equal contribution.

I want to thank

Prof. Dr. Klaus Kern for the possibility to execute research under the best possible circumstances within the academic world. I especially appreciate the experienced freedom to follow my own scientific approach and the encouragement and trust you put into your entire group as well as your ability to extract the important content from a noisy background.

Priv.-Doz. Dr. Markus Ternes for his day to day supervision. Not only your practical knowledge in the lab as a former ham radio enthusiast but also your deep understanding of physics helped and inspired me a lot. I am grateful for your help and the time you took to explain even the trivial details when I asked for it. I truly think you are an outstanding scientist and wish you all the best for your future endeavors!

Dr. Peter Jacobson for being a constant source of inspiration and teaching me an eloquent scientific approach in his function as a mentor and co-author. Thank you for your help in the laboratory and the data analysis as well as the still ongoing discussions about science, politics and life in general.

Prof. Dr. Fabian Pauly for his prompt commitment to being my second referee on this thesis and the discussions about our first results of correlated electron transport. Your expertise as a theoretician in quantum transport will provide a complementary view on this thesis. I wish you all the best for your upcoming research in Okinawa, Japan!

Prof. Dr. Leitenstorfer for his prompt commitment to being on my thesis defense committee. Thank you for providing the knowledge and discussing the femtosecond laser project that is being implemented into the existing machine right now within a Konstanz/Stuttgart research collaboration.

Abhishek Grewal, Yuqi Wang and **Gennadii Laskin** for their past and current commitment to the practical and theoretical tasks during their master and doctoral studies related to our experiments. We really enjoyed ourselves!

Wolfgang Stiepany, **Peter Andler** and **Marko Memmler** for their vast technical expertise and guidance in all matters related to the practical aspects of scanning probe techniques. **Martin Siemers** and **Rafail Chaikevitch** for their professional and uncomplicated support!

Dr. Tobias Herden for handing over a well designed experimental setup and passing on his knowledge. Thank you for a good collaboration in the laboratory!

Dr. Marcel Mausser for a mutual mental and technical support in the precision laboratory, especially for the long hours in the FIB facility. I'm glad we made it!

Sabine Birtel for her generous support provided to everybody under any circumstances. Thank you for cushioning the pressure of bureaucracy!

my fellow **Ph.D. representatives** of 2014: **Dr. Matthias Hepting, Dr. Marcel Mausser, Ekin Simsek, Umut Sanli** and **Ingrid Weinrauch** for great teamwork and the accomplishment of a dozen of soft skill seminars, company meetings and a tremendous Ph.D trip all over Europe!

Dr. Rico Gutzler for his joint training exercises and his stoic acceptance of my ridiculous bets against him.

the daily scientific and worldly but entertaining discussions with my fellow precision lab colleagues: **Shai Mangel, Abhishek Grewal, Yuqi Wang, Tomasz Michnowicz, Anna Roslawska, Jacob Senkpiel, Dr. Sabine Abb, Marcel Pristl, Dr. Benedikt Friess, Andreas Gauss, Patrick Herlinger, Dr. Christian Ast** and **Dr. Lihui Zhou** as well as the hidden people from the main building: **Dr. Stephan Rauschenbach, Diana Hoetger, Andreas Topp, Patrick Alexa, Dr. Kristina Vaklinova** and **Dr. Bastian Kern**.

my German speaking colleagues **Sebastian Koslowski** and **Lukas Schlipf**. I always look forward to spending time with you, inside and outside the scientific world!

the past companions who are now pursuing a successful career elsewhere: **Dr. Christopher Kley, Dr. Berthold Jaeck, Dr. Ivan Pentegov, Dr. Claudius Morchutt, Dr. Christian Dette, Dr. Verena Schendel, Dr. Christoph Grosse, Dr. Soeren Krotzky** and **Dr. Pablo Merino**.

all scientists and staff members of the **University of Konstanz**, especially the **SFB 767**, and the **Max-Planck Institute for Solid State Research** who have provided exciting research projects complementary to our approach to the nanoworld and for their uncomplicated help and exchanges.

last but not least a great scientist who put logical reasoning above all and gave me the reason to start and stay in the field of physics:

> *"For a successful technology, reality must take precedence over public relations, for Nature cannot be fooled."* **(Richard P. Feynman)**.

Contents

CHAPTER 1

INTRODUCTION

This introduction will provide a general overview of the scientific questions and ideas, regarding single magnetic atoms and molecules, that were pursued during the thesis. A brief history of the first as well as the currently employed decoupling mechanisms is given to put the current research efforts into perspective.

1.1 A single atom?

The interest in magnetic impurities in the form of a single atom with unpaired electrons is intrinsically schizophrenic: On the one hand, a single atom is desired that exhibits true quantum character completely unperturbed from its environment, but on the other hand, just by trying to observe the atom, we must perturb it. First, we have to fix the atom's position in space. Second, we need to communicate with it, e.g. by striking it with photons, electrons or other particles and infer the atom's true nature from the interaction results.

Thus, we can ask the question: Is there such a thing as a single atom? The closest we can get to a free atom is probably to trap it in the gentle potential landscape of an optical lattice creating a so called *artificial crystal of light*, and even then, the atom is subject to strong electromagnetic field amplitudes [1]. Free standing electromagnetic waves that form the potential landscape in which one, two or more atoms[1] can be confined in their relative positions to each other, have allowed researchers to build entire band structures and model different phases by tuning the potential well depths such as the Mott insulator phase in which the atoms cannot tunnel to their neighboring atoms. It is a promising technique to experience the true character of free and almost unperturbed quantum objects in a well controlled environment and was awarded with the Nobel prize in physics 1997.

Unfortunately, our daily world is not only made out of light. It is a harsh material scientist's environment in which atoms constantly crash into each other and a single atom, neutral or not, is normally drowning in a sea of particles that interact with all known mechanisms dragging it back into the classical realm. Whether in more common materials such as bulk metals and semiconductors or even small molecules and in confined dimensions: A single atom is always interacting with its entire environment. Therefore, we need to find a realistic approach based on existing materials and engineer them in a beneficial way. When we think about magnetic impurities we start with an electron that carries a charge and a spin and, if it is unpaired, is the building block for magnetism in most d and f materials. An electron likes to occupy space around the positively charged nucleus of an atom which, due to quantum mechanical boundary conditions, is quantized at discrete energy levels. This atomic configuration already strongly modifies the properties of such an electron. For example, f shell electrons are closer to the nucleus and therefore strongly bound to it, while outer shell electrons and especially unpaired electrons in the outer shell of an atom are much more weakly bound to the nucleus and are easily perturbed by the immediate surrounding of the atom. This simple picture allows us to develop a first intuition for the fate of unpaired electrons that bear a spin when they are brought together with other atoms or particles.

---

[1] Although ionized atoms are probably easier to navigate with electromagnetic fields, even neutral atoms can be confined thanks to the Stark shift.

Current research is focusing on two major questions how to utilize a single magnetic impurity. The first one is to use it as a classical bit in terms of permanently storing information, i.e. by polarizing the spin in one direction or the other and how to increase the energy difference between these two states, thereby enabling it for permanent storage applications. The realistic value for a stable bit is given by the superparamagnetic limit, which is still far from the current magnetic anisotropies of single surface adatoms (below 60 meV) that still require liquid helium temperatures for state lifetimes of a few nanoseconds up to hours. In this sense, the research rather explores how to write and how to read information to and from a single atom. The second one is to use it as a model qubit with long decoherence times which is also a measure for the interaction with the environment. A qubit requires the quantum mechanical superposition of two states as it is the case for the CoH $S = 1$ systems presented in this thesis for which the transverse magnetic anisotropy mixes the two $m_z = -1, +1$ states. Experimental approaches include quantum dots (also known as artificial atoms) that try to mimic the structure of an atom by confining a delocalized electron in all spatial dimensions and create a particle in a box problem with different energy levels depending on the material, size and shape of the quantum dot [2] [3] [4]. In this thesis, we will explore how the three unpaired electrons in the d shell of single Co atoms will be perturbed when they are deposited on a Rh(111) metal surface protected by a h-BN decoupling layer.

1.2 How to isolate a single magnetic impurity

A majority of experiments employs evaporated single magnetic atoms on clean epitaxial surfaces in ultrahigh vacuum and a variety of different surfaces on which the atom resides. An overview of recent combinations is shown in table 1.1. From this overview, we deduce that magnetic atoms on bare metal surfaces are subject to strong substrate interactions that either completely erase their magnetic signatures when probed with scanning tunneling spectroscopy or x-ray magnetic circular dichroism, or create a Kondo resonance due to a singlet formation with the substrate electron bath. Since then, different decoupling mechanisms have been employed ranging from topological insulators to superconductors that all have a similar goal: To decouple the magnetic atom from the metal electrode from which it is addressed in electron transport.

The first sign of magnetic signatures of single atoms on surfaces was observed in 1997 for Mn and Gd atoms on the surface of a Nb(110) superconductor that showed in-gap Yu-Shiba-Rusinov states (see table 1.1). This discovery was primarily about the influence on the superconductor and not on the magnetic atoms. The next discovery already put the atom in the center of interest: Kondo signatures for Co atoms on Au(111) were reported in 1998 and have led to

Substrate	Evaporated Atoms	Magnetic Signatures
Metals		
NiAl	Mn	None [5]
Rh(111)	Co	Mixed (Kondo + d) [6]
Au(111)	Co	Kondo [7] [8]
Ag(111)	Co	Kondo [8]
Ag(100)	Co	Kondo [8]
Cu(111)	Co, Fe	Kondo [9] [8]
Cu(100)	Co, Fe	Mixed Kondo [9] [8]
Pd(111)	Co	None, paramagon scattering [6], [10]
Pt(111)	Co, Fe, FeH, Er, (Ho)	MAE / Substrate [11] [12] [13], (None [14] [15])
Semiconductors		
InSb(110)	Fe	Weak MAE $<$ 2 meV [16]
Decoupling Layers		
Al_2O_3/NiAl	Mn	Weak Zeeman splitting [5]
Graphene/Ir(111)	Dy, Co	MAE [17], Charge gating
Graphene/SiC	H	Spin polarization [18]
h-BN/Rh(111)	Co, CoH, CoH_2	MAE $<$ 15 meV and Kondo [19]
Cu_2N/Cu(100)	Co, Fe, Ti, Mn, Cu	MAE $<$ 10 meV and Kondo [20], [21], [22]
Bilayer MgO/Ag(100)	Fe	Weak MAE at 14 meV [23]
Bilayer MgO/Ag(100)	Ho	Lifetimes up to hours [24]
MgO/Ag(001)	Co	MAE of 58 meV [25]
NaCl/Cu(100)	Au, Ag, Co	Charge states [26] [27]
Superconductors		
Nb(110)	Mn, Gd	In-gap Yu-Shiba-Rusinov states [28]
$NbSe_2$	Fe	In-gap Yu-Shiba-Rusinov states [29]
20 ML Pb/Si(111)	Mn, Cr	*Bound states* [30]
Topological Insulators		
Bi_2Se_3	Fe, Co	In-plane MAE [31], In-plane [32]
Bi_2Te_3	Fe, Co, Ni	Out-of-plane [33], In-plane [32], Quenced [34]

Table 1.1: Overview of magnetic atoms on different surfaces. The table shows that the magnetism of single atoms on metal surfaces is quenched, non-descriptive or limited to a Kondo resonance. Only the application of different decoupling mechanisms from the metal electrode, especially decoupling layers, leads to strong signals in tunneling spectroscopy and x-ray magnetic circular dichroism. The magnetic signatures are roughly distinguished between Kondo and magnetic anisotropy energies (MAE). The substrates marked in red are utilized in this thesis. Especially Pt(111), similar to Pd(111), is on the verge to being a ferromagnet and shows strong substrate interactions with magnetic impurities (compare [35] [36], [37]).

the investigation of the influence of minor substrate variations, such as the (111) and (100) orientations of Au, Ag, and Cu, on the magnetic atom due to, e.g. a different number of direct neighbors. The strong substrate interactions are primarily due to the direct hybridization of the magnetic atom with the substrate leading to different occupations of the d orbitals. In most cases, this allows the formation of a singlet state due to strong Kondo exchange interactions with the substrate electron bath which is observable as a Kondo resonance in scanning tunneling spectroscopy (see chapter 3.4.2).

The use of decoupling layers intends to preserve the magnetic orbitals and to shield them from strong Kondo exchange interactions with the metal electrode. The first system to successfully probe different spin states of a single atom was discovered in 2004 for Mn adatoms on Al_2O_3/NiAl for which the Al_2O_3 monolayer decouples the Mn atom from the underlying NiAl electrode. On these decoupled atoms it is possible to perform inelastic electron tunneling spectroscopy also known as *spin-flip spectroscopy* that excites the spin system from its ground to an excited state.

While the spin, S, of an unperturbed magnetic atom prefers no particular direction in space, it does when it is adsorbed on a surface. An exception are $S = 1/2$ systems that show no Kondo resonance such as the Mn atoms on Al_2O_3/NiAl. For this configuration, only an applied magnetic field is able to separate the two $m_z = -1/2, +1/2$ states in energy to make a transition between them possible to observe due to Kramers theorem. This is different for higher spin systems ($S > 1/2$) such as for Co and Fe atoms on Cu_2N/Cu(100) for which coexisting Kondo resonances and magnetic anisotropies as well as their interplay were observed in 2007. For this system, the crystal field of the surface induces a magnetic anisotropy that orients and permanently aligns the spin in space. These discoveries have led to a general understanding of the fate of magnetic atoms on surfaces. Starting from the strongest effect on the magnetic atom, the following will happen: First, charge transfer may take place that shifts the electron occupancy of the entire atom. Then, Coulomb repulsion between the magnetic atom's orbitals and the substrate atoms' orbitals realign the orbital momentum together with spin orbit coupling that further splits the spin states with $S > 1/2$. Depending on the symmetry of the atom's adsorption site relative to the surface lattice this *crystal field* leads to an energy difference that is described in the framework of group theory with Steven's operators (see chapter 3.2.2). Next, Kondo exchange interactions to the substrate will fine tune these energies, a key finding of this thesis (see chapter 3.5), and allow for the determination of the atom's coupling to its environment. Other effects such as phonon coupling to the substrate can occur but are not dominant for the systems shown in table 1.1.

The largest magnetic anisotropy energy almost possible for Co atoms due to a highly symmetric surface adsorption site was measured just recently for Co atoms on MgO/Ag(001) that showed excitation energies up to 58 meV. Utilizing pump-probe experiments and electron spin resonances, electron paramagnetic resonances can be observed for Fe atoms on bilayer MgO/Ag(100) [38] up to an energy relaxation time of $T_1 \approx 0.1$ ms and a phase-coherence time of $T_2 \approx 210$ ns. The latest achievements in 2017 report the successful writing and reading of single-atom magnets for individual Ho atoms on bilayer MgO/Ag(100) [24] which is the final realization of the single-atom bit. Ho atoms as part of the lanthanide series carry their magnetic moment in the $4f$ shell. This means, compared to $3d$ transition metal elements, it is well protected from the environment but also difficult to address [39] which is why tunnel magnetoresistance and a Fe atom sensor were utilized in this experiment [24].

Another approach to decouple magnetic impurities is based on engineered molecules. Once the core of the molecule that contains the magnetic impurity is generated, structural components can be added to control the electron transport through the molecule and to enhance the bonding to metal electrodes [40] or other structures which makes it a powerful tool for bottom up fabrication. A major advantage of an interdisciplinary research group that include physics, chemistry and biology is the combination of novel molecular arrangements and surface studies with scanning probe techniques. The arrangements shown in figure 1.1. show why our system is unique and provides a bridge between different research areas. Not only can we couple two magnetic atoms that are differently adsorbed on their metal electrodes, i.e. one atom is directly hybridized on a metal while the other one is protected by a decoupling layer. Additionally, the decoupled atom is a hybrid configuration between a well defined molecular ligand and an epitaxial metal surface. Chapter three will outline how the small molecular unit H-Co-N shows $S = 1$ signatures that are different for a plethora of environmental geometries since this molecular unit is subject to an ultrasoft h-BN decoupling layer that is mediating the coupling to the metal electrode via its varying spatial corrugation.

Furthermore, we show in chapter six how one single hydrogen atom that is placed on the Pt tip apex can be reversibly attached to and removed from the same molecular unit, effectively controlling the formation of Co-N, H-Co-N and H_2-Co-N. Employing not only the scanning tunneling capabilities of our microscope but also the tracking of atomic forces in the pN range, we can simultaneously measure the involved forces and tunneling currents while monitoring the spectroscopic signatures. This unique combination of tracking all involved signals clearly shows how the hydrogen atom induces a change from a magnetic anisotropy signature to a Kondo resonance.

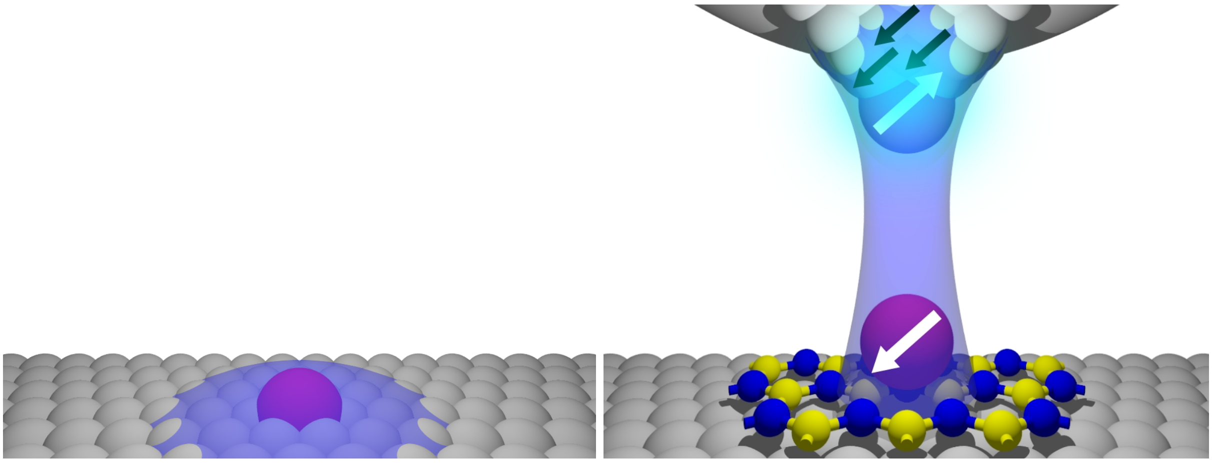

Figure 1.1: Magnetic atoms on surfaces. The drawings illustrate the substrate interactions of adsorbed magnetic impurities and how they are utilized. Left: A magnetic atom that is directly evaporated on a metal surface is subject to strong interactions with the substrate, mainly electron scattering leading to a suppression of any spin signatures in scanning tunneling spectroscopy, or at best, forming a singlet state and thus exhibiting a Kondo resonance (compare table 1.1). Right: A decoupling mechanism such as an insulating monolayer or molecular ligands can protect the atom's magnetic orbitals while still allowing electrons to pass through (bottom). Also sketched is a functionalized STM tip that harbors a magnetic atom on its apex (top). For Co on a Pt tip the strong substrate interaction (see the special case of Pt(111) in table 1.1) is schematically shown as an antiferromagnetic correlation with the substrate electrons. This configuration, which allows a precise control of the two magnetic orbitals' exchange coupling is the focus of chapter six in which surprising transport characteristics through this coupled spin system are presented.

CHAPTER 2

EXPERIMENTAL SETUP

This chapter introduces a combined scanning tunneling and atomic force microscope that is operating in ultrahigh vacuum at 10^{-11} mbar, low temperatures of around 1 K and magnetic fields up to 14 T. The focus will be on the characterization and performance of different tuning fork designs that were implemented and tested throughout this thesis.

2.1 Overview

Scanning probe microscopy is a general term for microscopes that image a sample not with optical means but with the interaction of a scanning probe, the tip, with a sample. More specifically, our setup will employ an atomically sharp metal tip attached to the prong of a tuning fork. When the tip apex is brought in tunnel contact with another metal sample surface, at tip-sample distances around several hundreds of pm, we can controllably move the tip in all spatial directions by piezoelectric actuators at a pm resolution scale and monitor the tunneling current at an applied bias voltage between tip and sample. Furthermore, the tuning fork allows us to monitor the short-range and long-range forces between tip and sample. A detailed description of these techniques is given in this and the next two chapters.

The experimental setup provides a combined scanning tunneling and atomic force microscope (STM/AFM) that is entirely incorporated in an *in-situ* ultrahigh vacuum (UHV) system to prepare samples and transfer them into a home-built head (see figure 2.1).

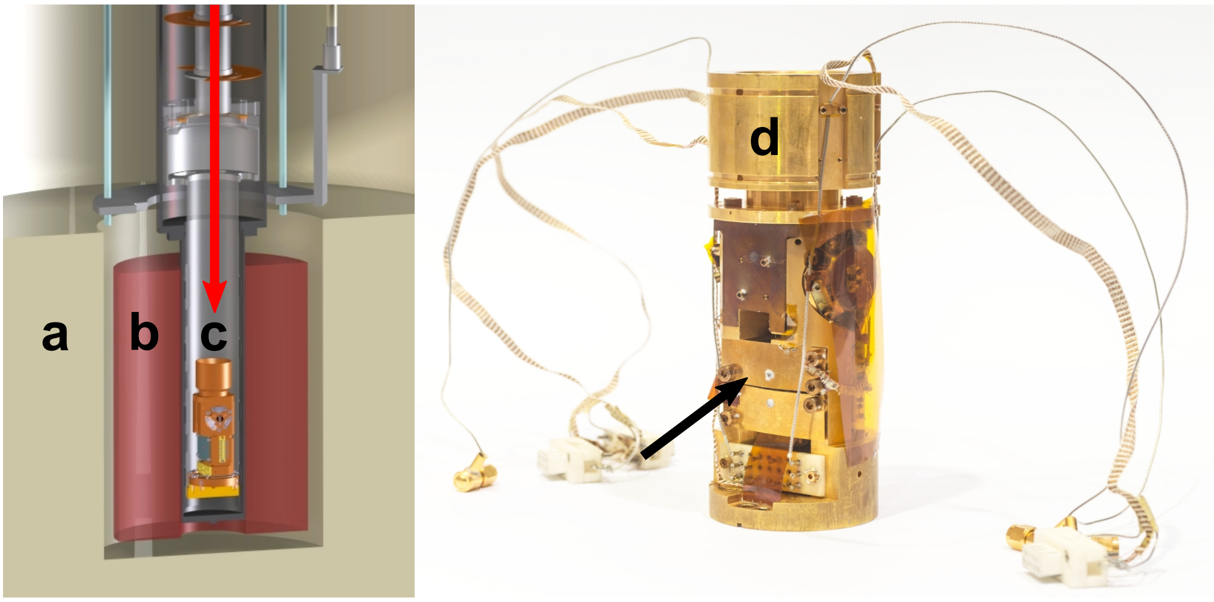

Figure 2.1: Combined STM/AFM head. The head (d) is located inside the UHV volume (c) that connects to the sample preparation chamber from which samples can be transfered into the head (path displayed by a red arrow) with a vertical manipulator. The superconducting magnet (b) surrounds the head and is completely immersed in the liquid helium volume of the cryostat ((a) shows part of the bulk insulation). The enlarged image of the head shows the cable connections of the piezo voltages, tunneling current, bias voltage, and tuning fork signal. The black arrow points to the z-piezo (hidden behind the springs) that is moving the STM/AFM tip as outlined in figure 2.2. Thanks to Dr. Tobias Herden for providing the image.

This head resides inside a He cryostat with a Joule-Thompson cycle that allows temperatures down to 1.1 K. It is further surrounded by a superconducting magnet creating magnetic fields up to 14 T normal to the sample surface. The system was upgraded with an enhanced material selection and an AFM in 2011. Technical details, used materials and performance of the current head version can be found in the Ph.D. thesis of Dr. Tobias Herden [41]. The experimental setup was moved to a newly built precision laboratory of the Max-Planck institute in 2013 that is seismically, acoustically, and electromagnetically shielded from the environment. Together with the new tuning fork design shown in subsection 2.3.3 and several decoupling iterations from electrical and mechanical noise sources it offers an outstanding stability for scanning probe applications.

2.2 A combined Scanning Tunneling and Atomic Force Microscope

The AFM function can be readily implemented within existing STM designs by mounting the STM tip to the prong of a tuning fork. Additionally, two contacts for the produced tuning fork signal (here labeled as "+" and "-") need to be incorporated. The excitation of the tuning fork oscillation is simply realized by adding a sinusoidal excitation voltage directly onto the scan piezo's z-electrode. An important feature of the current design is the carrier unit sketched in figure 2.2. It allows a transfer of different pre-assembled tuning fork sensors onto the fixed scan piezo inside the head, thus reducing their maintenance time.

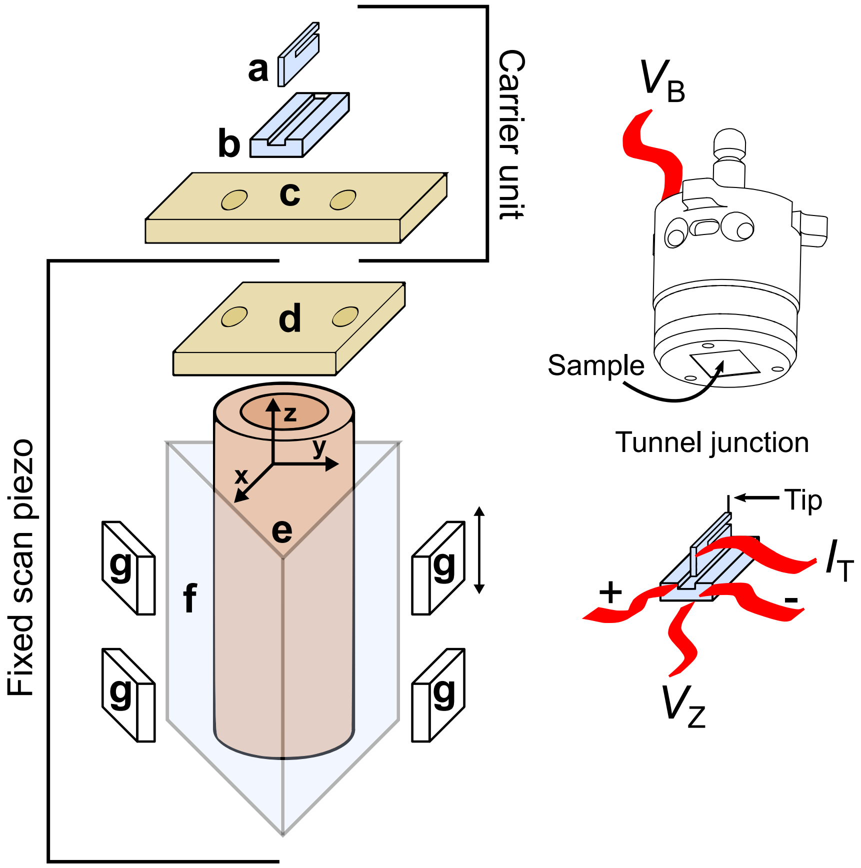

Figure 2.2: Scan piezo with carrier unit and its relevant contacts. The scan piezo (**e**) is held by a sapphire triangle (**f**) which is moved by six coarse approach piezos (**g**). A base plate (**d**) is permanently glued on top of the scan piezo. The tuning fork (**a**), its sapphire holder (**b**), and base plate (**c**) form an exchangeable carrier unit that can be screwed onto (**d**). The main contacts for the STM and AFM operation are: The bias voltage, V_B, applied to the sample, and the tunneling current, I_T. The scan piezo voltage in z direction, V_z, and the two tuning fork signal contacts, $+$ and $-$. Not shown are the two additional electrodes V_x and V_y of the scan piezo and their respective grounds. The sample holder for the sketched SiC sample is shown in subsection 2.4.

The scan piezo shown in figure 2.2 can be moved in x, y and z direction by applying a voltage across the piezo material. Together with the coarse approach piezos that move the entire scan piezo relative to the sample surface (see figure 2.2) we can approach the sample surface until a set tunneling current, I_T, is reached under an applied bias voltage, V_B, to the sample when the atomically sharp metallic tip is brought in close proximity (below 1 nm) to the metallic sample surface. The origin of the tunneling current and its exponential dependency on the tip-sample distance, z, and the sample's and tip's density of states is explained in chapter 3.3. With this configuration we can perform scanning tunneling topography and spectroscopy. For the topography we distinguish between two modes: Constant current and constant height. In constant current STM the tunneling current is kept at a constant setpoint value by an integrated feedback loop that regulates the z-elongation of the scan piezo. Constant height measurements require an alignment of the sample surface plane parallel to the plane of motion of the STM tip as no feedback loop regulates the scan piezo's z-elongation and only the tunneling current is recorded. The elastic and inelastic contributions in spectroscopic measurements and the employment of a lock-in amplifier are outlined in chapter 3.3.

After the discovery and implementation of STM [42] [43] [44], the AFM was developed shortly after [45] and evolved into a powerful tool capable of measuring insulating samples, interatomic forces [46] depending on the tip profile [47], and was used to manipulate single atoms [48]. In these AFM setups, an atomically sharp tip, similar to a STM tip, was attached to the end of a tuning fork cantilever that was brought in close proximity to the sample surface.

A simple representation of the oscillation of a tuning fork cantilever is an effective mass, m, that is hanging from a spring with spring constant, k_0, (stiffness of the tuning fork) attached to a movable support. For this setup, the resonant frequency, f_0, is

$$f_0 = \frac{\omega_0}{2\pi} = \frac{1}{2\pi}\sqrt{\frac{k_0}{m}}. \tag{2.1}$$

If a force acts on the tip of the tuning fork cantilever, due to tip-sample interactions, a shift in frequency can be observed:

$$f = \frac{1}{2\pi}\sqrt{\frac{k_0 + \langle k_z \rangle}{m}} \tag{2.2}$$

with $\langle k_z \rangle$ as the time average over one cycle of the tip oscillation of the vertical force gradient $k_z = \partial F_z / \partial z$ for $|k_z| \ll k_0$ with k_z as the stiffness of the tip-sample interaction [49] [50]. A Taylor expansion of equation 2.2. up to first order yields the relation between the observable frequency shift, $\Delta f = f - f_0$, and k_z: $k_z \approx \frac{2k_0}{f_0}\Delta f$ for small changes of k_z during an oscillation cycle. A more accurate integration that explicitly takes the tuning fork oscillation into account allows to relate force and frequency shift [49] [50]:

$$\Delta f(z') = \frac{f_0}{2k}\frac{2}{\pi A^2}\int_0^{2A} dz \frac{z - A}{\sqrt{2Az - z^2}} F_z(z' + z) \tag{2.3}$$

where z' accounts for the time-averaged tip distance which is closest to the sample at $z = z'$ and farthest away at $z = z' + 2A$ with A as the oscillation amplitude of the tuning fork cantilever. An analytical expression for extracting the force, F_z, from the frequency shift, Δf, was given by Sader and Jarvis and is shown in chapter 4.2 together with an overview of the most common forces in AFM experiments.

Therefore, a force between tip and sample will lead to an observable shift of the oscillation's eigenfrequency that can be deconvoluted back to the force. Usually, an attractive force will cause a shift of the eigenfrequency to lower frequencies while a repulsive force will shift to higher frequencies. To excite the tuning fork we add a sinusoidal excitation voltage at its resonance frequency, $V(t) = V_0\cos(2\pi f_0 \cdot t)$, to the scan-piezo in z-direction. The response oscillation of the tuning fork creates surface charges on the $+$ and $-$ electrodes that are amplified to a voltage signal (see next subsection). To measure the frequency shift of the tuning fork oscillation we use frequency modulation for which the amplitude of the resonator's oscillation is kept constant by a phase-locked loop that compares the frequency of the original AC excitation voltage, $V(t) = V_0\cos(2\pi f_0 \cdot t)$, to the resonator's response frequency, $V(t) = V_0\cos(2\pi f_0 \cdot t + \Delta\phi)$. The feedback loop keeps track of the frequency change to adjust the excitation frequency to a new resonance frequency that is shifted by Δf. A representative amplitude and phase response of one of the qPlus tuning forks is shown in figure 2.6 where the zero phase shift at the eigenfrequency of the tuning fork corresponds to the peak of the amplitude response.

The first AFM experiments that achieved atomic resolution with silicon cantilevers, required large oscillation amplitudes in the order of several nm [51]. This was due to the used silicon cantilevers that were not stiff enough with a spring constant of only a few N/m. The ingenious idea of Franz Giessibl to transform the quartz crystal resonator commonly used in quartz watches into a force sensor with stiffnesses above 1000 N/m, led to oscillation amplitudes that can nowadays be as small as a few pm and have surpassed the spatial resolution of an STM [52]. While these new setups even allow to probe the electron clouds of an atom, the identification of different atoms [53] and molecular bonds with a functionalized tip [54], a reliable chemical identification for all elements is one of the future challenges. While the basic principles have been established the current focus lies on the design of the tuning fork and the tip apex. The following section will present changes to the qPlus design employed for this thesis.

2.3 Tuning fork designs and circuit implementation

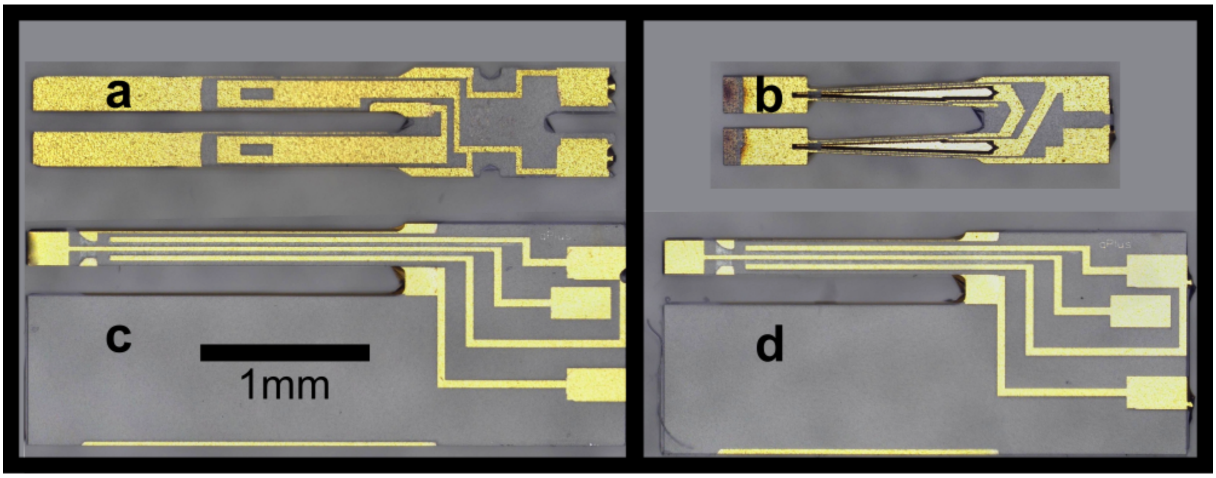

Figure 2.3: Comparison of different tuning forks under an optical microscope. **a)** The E158 model that is used in quartz watches. This model was mainly used for our old and intermediate designs. **c)** The qPlus model from the Giessibl group that was specifically designed for scanning probe applications with a separate electrode for the tunneling current. While **a** and **c** have an eigenfrequency of 32768 Hz, the shorter versions in **b** and **d** have an eigenfrequency of around 50 kHz.

Quartz tuning forks are widely used in the electronic industry for frequency selection or quartz watches where they provide stable oscillations over a wide temperature range and are cheap in production. They have been optimized in dimension to provide the best frequency stability vs. production cost and power consumption. The standard settled for a quartz (SiO_2) crystal only a few mm in length in the shape of an actual tuning fork as shown in figure 2.3a. When the quartz crystal is bent in a specific direction it creates a surface charge that is collected by gold electrodes. For applications in quartz watches, the eigenfrequency of such a tuning fork is precisely tuned to $2^{15}\text{Hz} = 32768\,\text{Hz}$. But why this odd frequency? The base of two is important since one oscillation per second can be precisely derived from 32768 Hz by simply dividing it 15 times by two. This division is done by an integrated circuit that delivers one second voltage pulses driving the hand of a quartz watch. The amount of power the integrated circuit uses was one of the main reasons why 32768 Hz became so popular to drive the oscillation. At this frequency, the power consumption of the integrated circuit is negligible and can live off a small button battery for years while the tuning forks are still easy to manufacture and handle. If the tuning fork would be larger in dimension leading to lower frequencies, the occupied space would be too large and the frequencies would shift into the audible spectrum range. The smaller the tuning fork the more power the integrated circuit consumes. These are mainly the reasons why today we're dealing with this frequency in scanning probe applications as the following large scale production made these oscillators as cheap as a few cents. The E158 model for example can be purchased as a wafer or already prepackaged in vacuum tubes that can be directly soldered into a circuit. In terms of performance enhancement one could also consider faster oscillators. The *Kolibri* sensor from *Specs* operates at 1 MHz and, according to their advertisement, offers a better signal to noise ratio as well as small oscillation amplitudes below 20 pm.

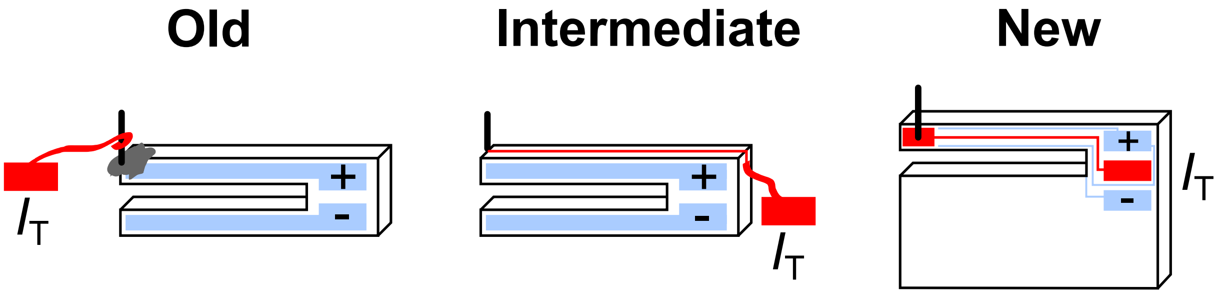

Figure 2.4: Overview of the three different tuning fork designs that were tested during this thesis. While the blue shaded regions sketch the tuning fork electrodes that register the surface charge created by the piezo material, the red path sketches the electrical contact (I_T) to the STM tip that is glued to the end of the tuning fork prong. The old design had no designated contact pad for the tunneling current, therefore the STM tip was first glued onto the tuning fork prong with insulating glue and was then contacted with a thin gold wire. The intermediate design had the electrode directly evaporated onto the top part of the tuning fork prong and provided a straight connection to the STM tip with no moving parts. The new design relies on tuning forks specifically made for the scanning probe community and provides easy to use electrodes for all three contacts.

Not only the tunneling current, I_T, must be amplified, also the produced tuning fork current, "+" and "-", requires amplification when the oscillation amplitude is set to only several pm at cryogenic temperatures. The amplification circuit is sketched in figure 2.5. The preamplifier is placed roughly 30 cm away from the tuning fork and is located outside the UHV chamber in the He exchange gas volume where it still needs to be heated to ensure proper working conditions for the operational amplifiers. Therefore, a 1 kΩ resistor is glued directly on top of each amplifier to ensure a sufficient temperature. The power through the resistor is calibrated against the current drawn by the amplifier in proper working conditions. Instead of one AD823 chip with two built in operational amplifiers that we commonly use for external testing of new tuning forks, the current circuit employs two OPA657 low noise operational amplifiers from *Texas Instruments*. Its transimpedance gain of 10^8 V/A is set by two 100 MΩ resistors while 100 nF and 10 μF capacitors ensure a smooth power voltage with respect to the common ground.

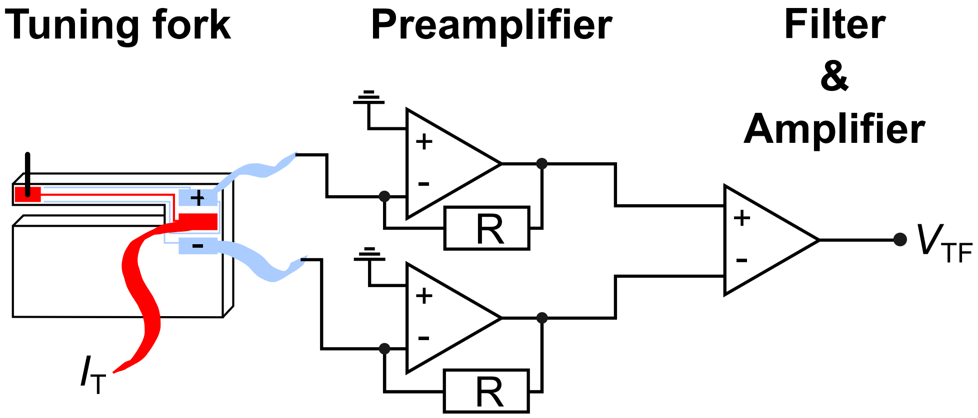

Figure 2.5: Amplification of the tuning fork signal. The mechanically driven tuning fork (held at 1 K) produces a current signal that travels roughly 30 cm to the first preamplification stage (heated to around 80 K) where both signals from the tuning fork are amplified with separate transimpedence amplifiers with a gain of 10^8 V/A. This is followed by an external second amplification stage with an adjustable gain of $10^2 - 10^4$ that additionally employs a bandpass filter, set around the oscillation frequency.

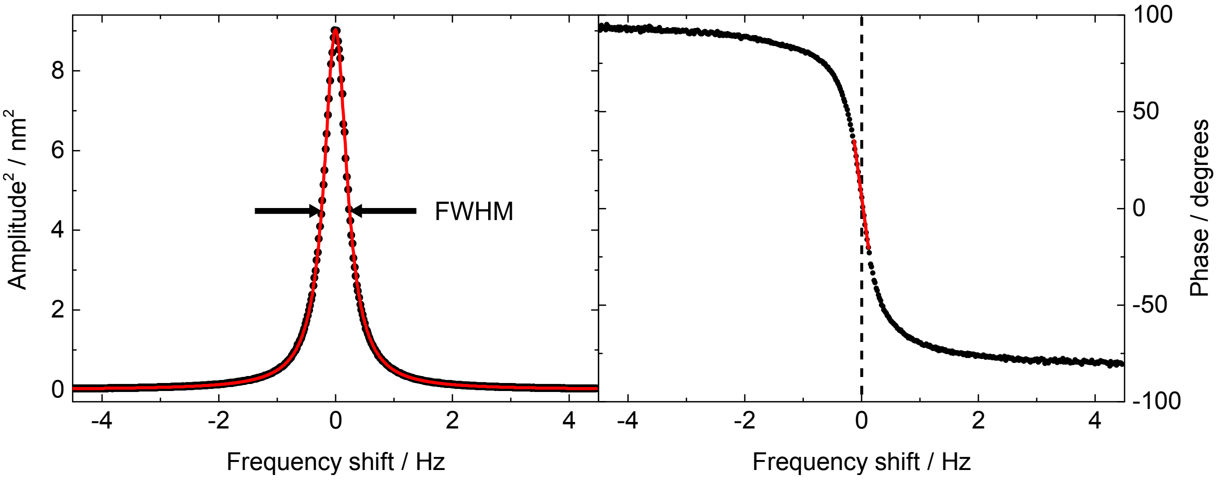

Figure 2.6: Q-factor determination of a new design tuning fork at 1.1 K and 0 T, 200 nm away from the sample surface. Left: The amplitude squared is proportional to the power spectrum (black dots) of the oscillator. A lorentzian fit (red curve) determines a FWHM parameter $w = 0.4787 \pm 0.0005$ Hz from which the q-factor can be determined if the eigenfrequency, f_0, is known. For this dataset: $Q = \frac{f_0}{w} = \frac{29077\text{Hz}}{0.4787\text{Hz}} = 60741$. Right: Similarly a linear fit (red line) to the slope of the phase shift (black dots) in radians yields a similar result depending on the frequency range where a linear approximation is still valid: $Q = \frac{f_0}{2}\frac{d\Phi}{df} \approx 60000$.

The first check of a new tuning fork consists of a resonance curve. For this a sinusoidal voltage signal is applied to the z-piezo that mechanically drives the tuning fork oscillation. Ramping the frequency of this voltage oscillation around the expected eigenfrequency (Normally around 30 kHz for our new designs) readily gives the amplitude response and the phase shift of the amplified tuning fork oscillation frequency compared to the applied excitation voltage frequency. From these curves the q-factor is derived (see figure 2.6) that allows a first estimation of the tuning fork performance.

The q-factor, Q, describes the number of oscillations the tuning fork undergoes after an excitation pulse before it is damped to 1/e of its peak amplitude. Although a high q-factor is desired for a high resolution of the phase-locked loop, a high q-factor is not always beneficial. If the tuning fork is subject to an outside "kick" it might oscillate for a long time before the oscillation dies down. One example where this frequently happens is the coarse approach. If the entire piezo with its tuning fork carrier is suddenly moved by the rough coarse approach piezos (see figure 2.2g), the tuning fork starts to oscillate with an amplitude of around 5-10 nm. For a common q-factor of 60000 and an eigenfrequency of 30 kHz this means, that it takes over two seconds (Q / f_0) to reach 1/e ($\approx$ 37%) of this amplitude. The tip should not approach the sample surface while it is oscillating at a nm scale. Therefore, after each coarse approach step, we wait three seconds before we let the z-piezo extend to its full range to check for tunneling contact. As this approach takes a long time to reach the sample, we implement a sophisticated capacitance measurement between tip and sample that brings the tip quite close to the sample surface (around 1 μm to 10 μm) despite having no optical access.

Each new sensor must be calibrated as the exact oscillation amplitude is not known for an applied excitation voltage and can only be estimated from the height change of the z-piezo when the tuning fork oscillation and the tunneling setpoint feedback loop are both actived. The oscillating tuning fork strongly affects the tunneling current when the tip is in tunneling contact with the sample. If the tunneling current feedback loop is activated it keeps a constant current signal and moves the z-piezo accordingly. The sinusoidal oscillation that is added to the z-piezo is mixed with the exponential dependence of the tunneling current in z, thus at the lower half of one oscillation cycle the current will increase more than at the higher half and the feedback loop will move the tip further away from the surface to maintain a constant current signal. A modified Bessel function of the first kind describes this behavior as argued in [50]:

$$\langle I(z') \rangle = I_0 \frac{1}{2\pi} \int_{-\pi}^{\pi} \exp(2\kappa(z' + A(1 + \sin(t))))dt = I(z' + A) I_0(2\kappa A) \tag{2.4}$$

where as mentioned in the previous subsection, z' denotes the time-average of the tip-sample distance. We also know that the tunneling current is exponentially dependent on the distance and therefore use

$$I(z' + A) = I(z')\exp(-2\kappa\Delta z). \tag{2.5}$$

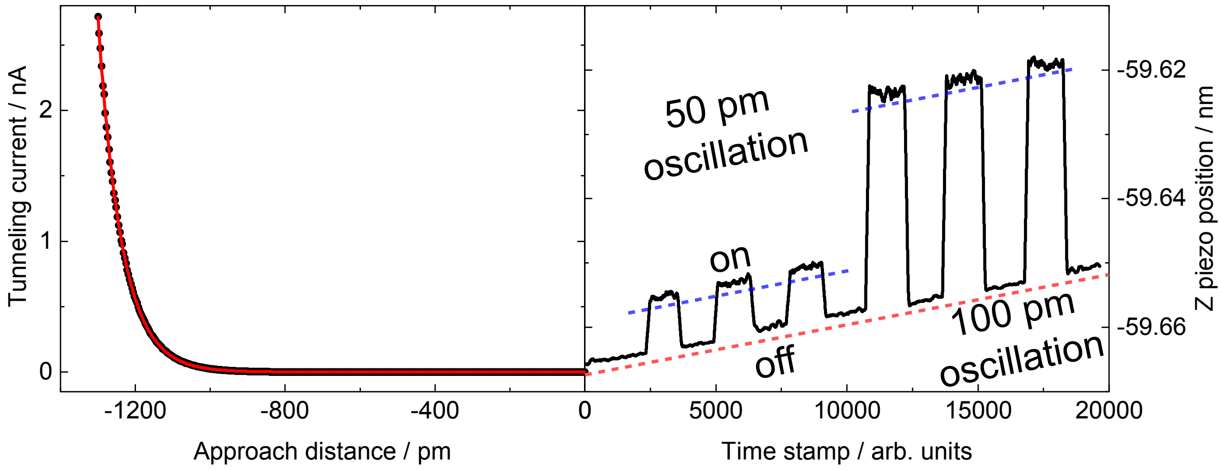

Figure 2.7: New design tuning fork calibration at 1.1 K and 0 T. A stable tip apex usable for topography and spectroscopy is stabilized over a h-BN/Rh(111) sample surface at 20 pA tunneling current setpoint and -100 mV bias voltage. From there the feedback loop is turned off for I(z) spectroscopy. An exponential fit (red curve) yields the exponent $\kappa = 7.91 \cdot 10^{-9} \frac{1}{\mathrm{m}}$ in $I_T(z) = \exp(2\kappa z)$. To check the influence of the tuning fork oscillation the feedback loop was turned back on. The tuning fork was turned on and off three times for two different oscillation amplitudes (50 pm and 100 pm) with its old estimated calibration of 490 pm/V. Linear fits in these two regimes yield a height difference of $\Delta_{50\,\mathrm{pm}} = 9.1\mathrm{pm}$ and $\Delta_{100\,\mathrm{pm}} = 34.1\mathrm{pm}$. The linear slope in the dataset is due to small thermal drift of the z-piezo.

in

$$\langle I(z') \rangle = I(z' + A) I_0(2\kappa A) \tag{2.6}$$

$$\langle I(z') \rangle = I(z') \exp(-2\kappa \Delta z) \cdot I_0(2\kappa A). \tag{2.7}$$

If we assume that the average current is equal to the tunneling current ($\langle I(z') \rangle = I(z')$) as it is controlled by the feedback loop, we arrive at the final expression that allows us to calibrate the oscillation amplitude:

$$\exp(2\kappa \Delta z) = I_0(2\kappa A) \tag{2.8}$$

where we know $\kappa = 7.91 \cdot 10^{-9} \frac{1}{\mathrm{m}}$ from the exponential fit to the tunneling current with $I_T(z) = \exp(2\kappa z)$ and $\Delta z = \Delta_{100\,\mathrm{pm}}$ = 34.1 pm from figure 2.7. A numerical solution to equation 2.8 yields a real oscillation amplitude $A = 97.7$ instead of the set 100 pm. The new calibration yields: $490\mathrm{pm/V} \cdot \frac{97.7\mathrm{pm}}{100\mathrm{pm}} = 478.5\mathrm{pm/V}$.

2.3.1 Old design

If we use the common industrial based tuning fork E158, we still need to provide an electrode for the tunneling current as this model was never intended to carry a STM tip. The standard way to provide this contact at the beginning of this thesis was the direct connection of the tip to a gold wire as it is shown in figure 2.8. This design, however, induced serious strain that could damp the tuning fork's oscillation and was prone to fail as the gold wire was attached to moving parts and could rupture. Another problem was caused by the extensive use of glue for creating this device. First the tip has to be glued onto the tuning fork prong with insulating glue to isolate it from the tuning fork gold pads that are directly underneath. The gold wire is then attached to the tip with conducting glue. These different steps induce large amounts of glue to the entire device and an increase in mass which further makes the prong asymmetric and heavier [55]. Even with the most skilled application of glue it remained difficult to obtain tuning fork resonances without side resonances and with a high q-factor.

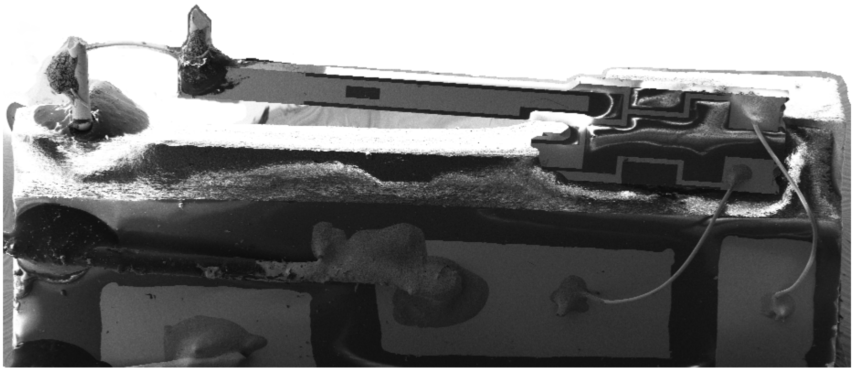

Figure 2.8: SEM image of the old tuning fork design. One prong of the E158 tuning fork is broken off on purpose while the base of the tuning fork is glued to a sapphire carrier. Here, a 75 um Pt tip is glued onto the end of the prong with insulating glue. A gold wire is then wrapped around the tip and fixed with conductive epoxy to make the tunneling current connection. Thanks to Dr. Tobias Herden for providing the image.

2.3.2 Indermediate design

To avoid the problems of the old design such as the insulating glue on the tuning fork prong and the induced strain we bypassed the gold wire connection. It was replaced by a contact path for the STM tip directly on the tuning fork prong. For this we asked the company *Nauga Needles* to evaporate a gold layer on top of a E158 tuning fork prong to directly make an electrical connection without any moving parts and to mount one of their tips to the end of the prong. An overview image of one of the five final probes is shown in figure 2.9.

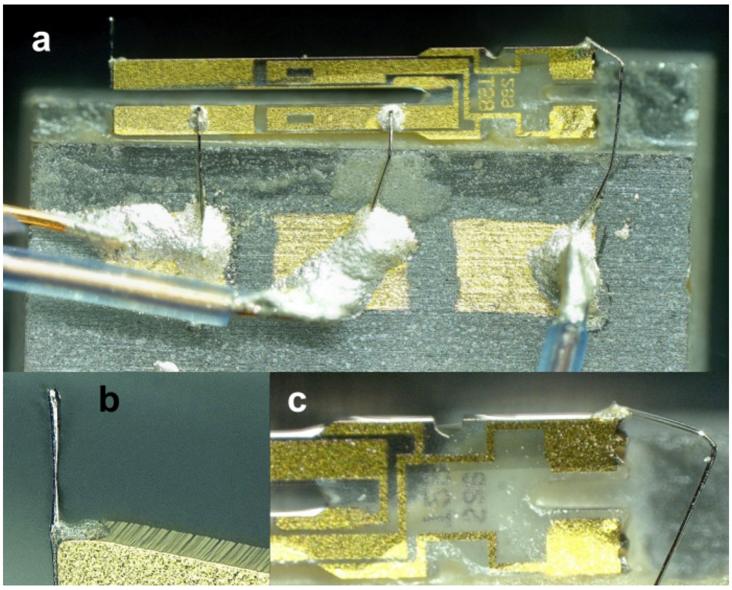

Figure 2.9: Image of the intermediate design. (**a**) Three gold contact pads are clearly visible in the lower half of the image: The two on the left are the tuning fork connections, the one on the right is the tunneling current contact. The sharp STM tip is barely visible at the left end of the upper tuning fork prong (Zoom in (**b**)). From there an evaporated gold layer makes the connection to the tunneling current electrode at the top right at the base of the tuning fork (Zoom in (**c**)).

Although the symmetric mounting of the STM tip and the small extra mass led to a good resonance curve as shown in figure 2.10, this design introduced another problem: Due to the short distances between the evaporated tunneling current electrode and the other two tuning fork electrodes the crosstalk between all electrodes was almost one order of magnitude higher than the old design and not symmetric for the two tuning fork electrodes with respect to the tunneling current. The capacitance between all three electrodes is shown in figure 2.11 and table 2.1. The capacitance between the two tuning fork electrodes, i.e. "+" and "-", is roughly the same for both designs since the same tuning fork model was used and the capacitance is a good measure of the piezo material between these two electrodes.

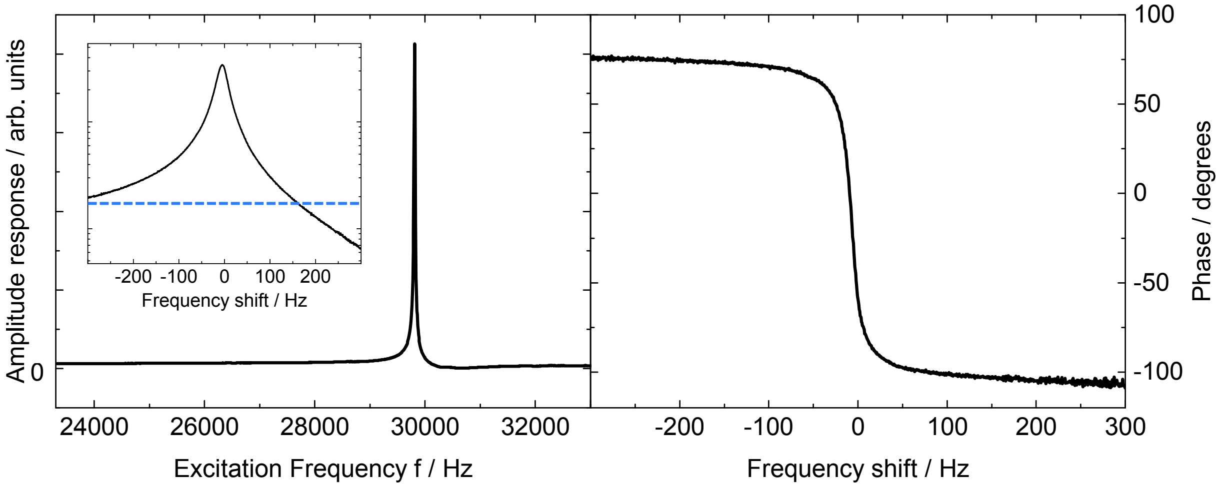

Figure 2.10: Representative resonance curve of one of the intermediate designs at room temperature and in air. The amplitude response is shown on the left. Unlike the old design, no hints of side resonances are visible in the near vicinity of the main resonance peak at around 30 kHz. The asymmetric tails of the resonance are more visible in the inset with a logarithmic scale. A fit to the phase shift yields a q-factor of 1900.

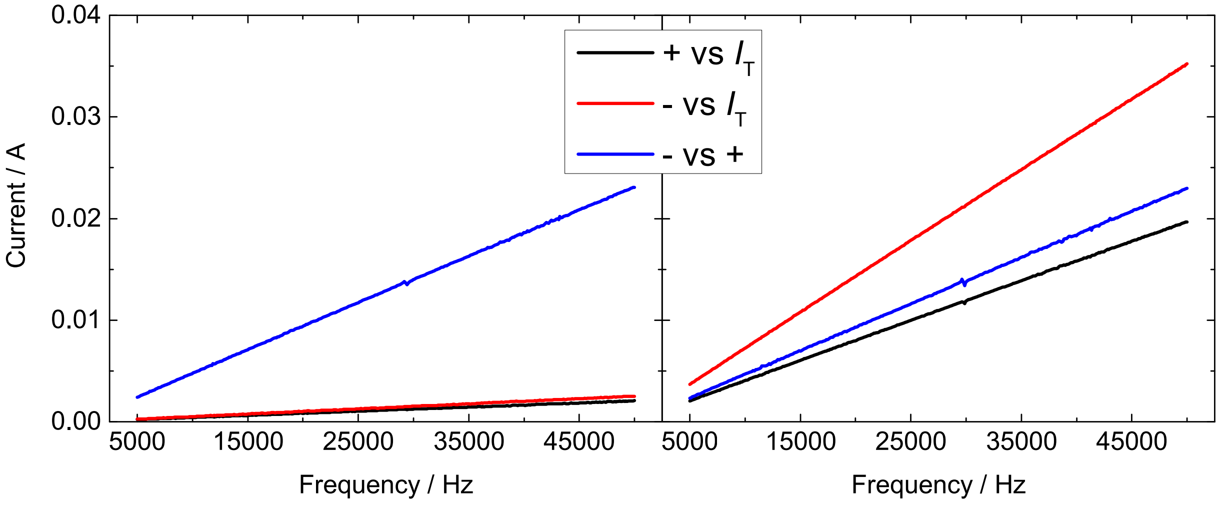

Figure 2.11: Current response to a frequency modulated 100 mV voltage signal between the electrodes on two different tuning fork designs. The current was amplified by 10^4. Left: Capacitance measurement of an old design (green highlighted numbers in table 2.1). Right: Capacitance measurement of an intermediate design (red highlighted numbers in table 2.1). While the blue curves for the tuning fork electrodes yield a similar slope for both designs, the coupling to the tunneling electrode is significantly higher and asymmetric for the intermediate design.

Electrodes	Old design		Intermediate design	
$+$ vs. I_T	29 pF	6.7 pF	37 pF	65 pF
$-$ vs. I_T	28 pF	8.2 pF	72 pF	117 pF
$-$ vs. $+$	90 pF	76 pF	71 pF	74 pF

Table 2.1: Capacitances of two old and two intermediate designs. The numbers highlighted in green and red indicate the best and worst case for both designs. Not only are the capacitances between the tunneling current and the tuning fork electrodes of the intermediate designs much higher but they were also asymmetric by a factor of two and therefore not balanced.

To measure the capacitance between the three different electrodes, the tuning fork was mounted outside on a test stage and the electrodes connected to a frequency generator and a current amplifier. To measure the capacitance between two electrodes, one was supplied with a sinusoidal voltage signal, U = 100 mV, swept from f = 5 kHz to 50 kHz, while the other one was connected to a current amplifier with a gain of 10^4. Examples of the current response functions, $I(f)$, are shown in figure 2.11. From these linear curves, the capacitance, C_p, can be approximated by their slopes as $I(f) = U \cdot 2\pi \cdot C_p \cdot f$.

2.3.3 New design

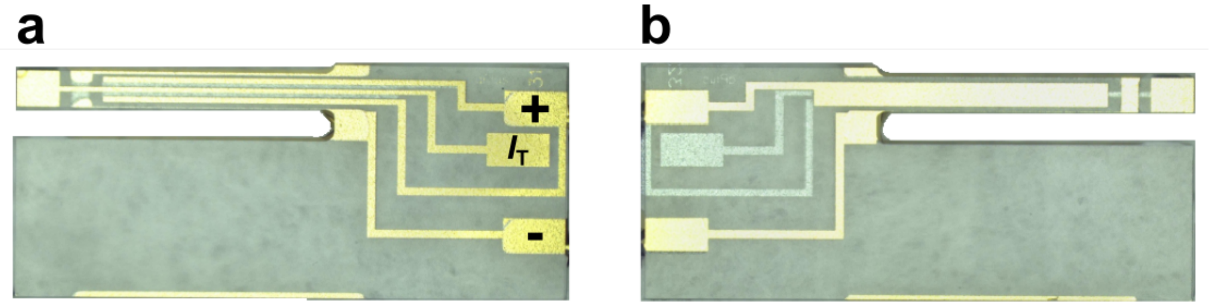

Figure 2.12: Optical microscope image of both sides of the new qPlus design. (a) The front side shows all electrodes: The electrode, I_T, that is directly connected to the pad at the front of the prong where the STM tip will be glued to, and the "+" and "-"electrodes of the tuning fork to collect the surface charges when the tuning fork prong is bent. (b) The back side only has the two tuning fork electrodes. The generous base of the tuning fork allows a secure and stable mounting. Thanks to Franz Giessibl for providing the first sets of tuning forks.

The new qPlus design was specifically produced for scanning probe applications and can be purchased from *Omicron*. It offers three electrodes that are well separated and a designated large gold pad at the end of the tuning fork prong provides a large enough area to attach an STM tip with ease. Only a small amount of conducting glue is needed and the tip can be

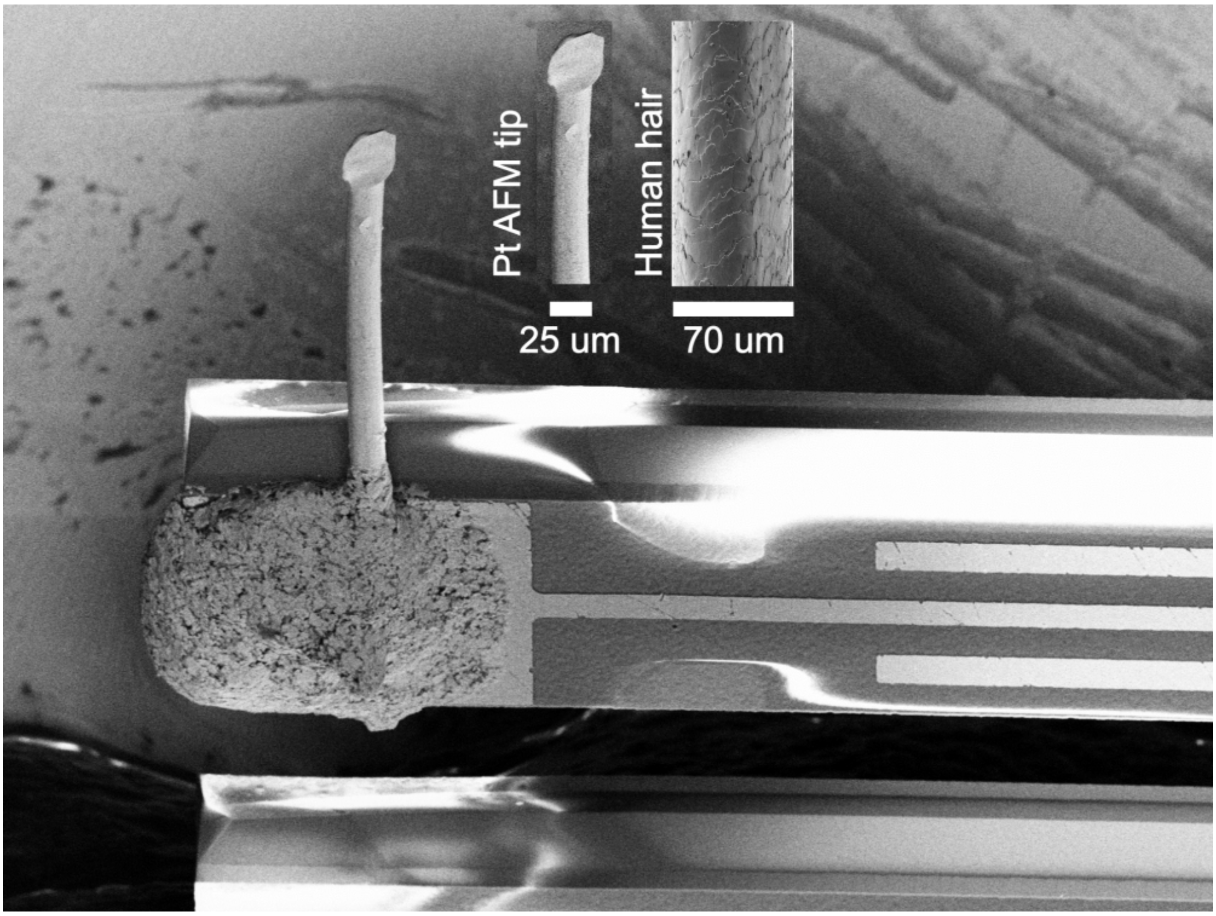

Figure 2.13: SEM image of the tuning fork and a glued Pt tip. For size comparison a human hair is shown next to the Pt tip . Thanks to the *CSIRO* for providing the latter image.

kept reasonably small. Here we used a Pt wire (99,95 % purity) with a diameter of 25 μm. The length of the tip is kept around 0.5 mm and the estimated tip weight[1] is therefore around 5.3 μg. Together with the mass of the glue we stay below 10 μg of additional mass. A tip mounting device was specifically constructed to ensure a clean and quick glue procedure. Since our system does not allow an in-situ tip exchange we are eager to keep the same tip for most of the experiments. In the beginning of this thesis the tuning forks with their mounted tip would commonly fail after a few weeks or months. We found that the tip became semiconducting (i.e. insulating below a certain threshold bias voltage ($|V_B| < 10$ meV) for low temperatures around 1 K), sometimes insulating, or lost its electrical connection entirely. We believe that the glue connection between the Pt tip and its Au pad was mainly responsible and prone to fail.

First, the entire tuning fork itself must be glued to the carrier on top of the piezo with electrically insulating but thermally conductive glue. Then, the STM tip is glued to the gold pad on the tuning fork prong with electrically and thermally conductive glue. The old designs also

---

[1] Pt has a density of 21.45 g/cm^3 near room temperature and the used tip has a calculated volume of roughly $V = \pi r^2 l = 2.45 \cdot 10^{-7}$cm^3.

Connection	Materials	Method
Tuning fork on holder	SiO_2 on Al_2O_3	Epoxy (Torr Seal or H77)
Holder on piezo carrier unit	Al_2O_3 on Cu	Epoxy (Torr Seal or H77)
STM tip on tuning fork prong	Pt on Au	Epoxy (E4110, EJ2189-LV or H20E)
Wires to tuning fork electrodes	Au on Au	Bonding
Wires to outside cabling	Au on Ag	Epoxy (EJ2189-LV)

Table 2.2: Necessary connections of different materials inside the STM head. Highlighted in red is the connection that failed the most in the past with the old epoxy E4110 resulting in tips that either completely fell off the prong or developed a semiconducting behavior over time likely due to a bad connection. Semiconducting in the sense that the tip spectroscopy at low temperatures, < 5 K, showed an insulating gap for low bias voltages that would only vanish with higher temperatures. Field emission at 200 V and up to 20 μA on a Au sample or a direct crash into the Au sample to clean the tip did not restore its original conductive properties.

used glue to connect silver wires to the Au pads of the tuning fork where we now switched to bonding gold wires directly to the gold pads, thus ensuring a much more reliable connection.

All of these connections must withstand temperature cycling ranging from bakeout at around 400 K down to cryogenic temperatures of around 1 K. Sample transfers at room temperature (around 300 K) routinely expose the entire STM head to a rapid heat flow that stays at around 100 K for a few minutes and then slowly cools down to 5 K again. This means constant thermal cycling for every sample exchange that could loosen the glue connections over time. Thus, the connections have to withstand thermal expansion and contraction while also being exposed to mechanical stress and strain due to tip crashes into different samples and occasional field emission treatments. Besides direct Au-Au bonding we commonly employ suitable two component epoxies to electrically connect different materials. Pt (9 ppm/K) and Au (14 ppm/K) expand and shrink less than all of the common UHV epoxies (See table 2.3. CTE index). These different thermal expansion coefficients seem only to have a minor influence on the connection. The hardness of the connections, their residual stress, and ability to inelastically adsorb outside shocks are equally important and are responsible for most failures at low temperatures according to discussions with the epoxy companies. The different materials that need to be connected and the different epoxies under consideration are listed in table 2.2 and 2.3.

In terms of processing we changed from a rapid cure at 100 °C for 1 h to a slow room temperature cure (23 °C for 72 h) that helps to reduce residual stress as it avoids a rapid glass transition at higher temperatures. Also a thorough cleaning procedure of the contacts prior to applying the epoxy was carried out for every contact area (Ultrasonic cleaning in acetone, methanol, isopropyl alcohol, distilled water and dry nitrogen gas blowing).

In order to choose the right epoxy we compared the storage modulus and the shore D factor of

Epoxy	**CTE** (<, >RT)	**Storage modulus** / psi (**Shore D**)	**Thixotropic index**	**Thermal conductivity** / W/mK
H20E	31, 158	808700 (75)	4.6	2.5
E4110	48, 150	518756 (60)	2.1	1.4
EJ2189	53, 107	275557 (60)	5.2	1.4
EJ2189-LV	52, 89	213672 (41)	3.3	2.5
H77	33, 130	950693 (90)	1.4	0.66
TorrSeal	No data	(75 - 80)	"Thick"	No data

Table 2.3: Material properties of different epoxies used in our lab. The coefficient of thermal expansion (CTE) measures the expansion below and above room temperature in parts per million (ppm) per degree Kelvin. The elastic properties are described by the **storage modulus** that basically measures the ability of the epoxy to elastically adsorb an outside shock. The **Shore D** factor is another measure for hardness. The **thixotropic index** described the viscosity, i.e. the higher its value the thicker the epoxy.

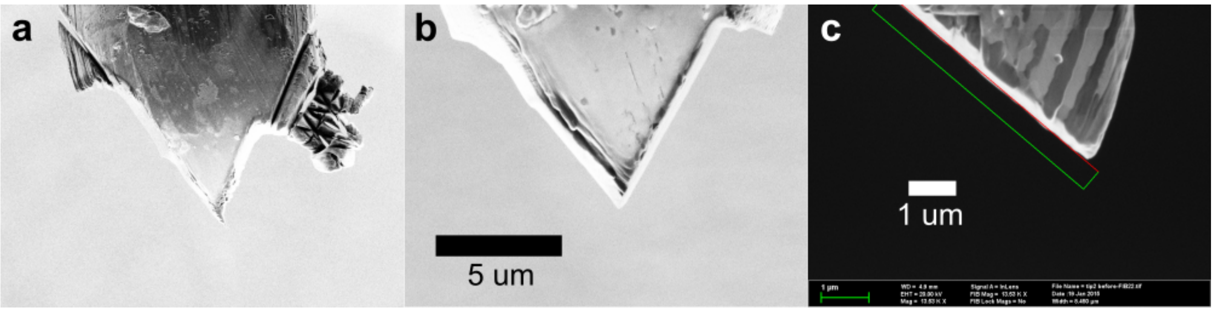

Figure 2.14: SEM images of the FIB cut Pt tip apex. (a) Overview that shows the 25 um Pt wire diameter at the top part of the image. (b) Zooming into the apex shows the resulting pyramidal structure. (c) Rotated side view and final cuts to ensure a smooth tip apex.

different UHV epoxies for low temperature applications (Table 2.3) that determine the inelastic properties and hardness of the connection. We settled for EJ2189-LV as it has the lowest storage modulus and lowest hardness. The common EJ2189 has a high viscosity (thixotropic index) that makes it tough to process. Since the employment of the new gluing procedure and the new epoxy EJ2189-LV, the same STM tip has now been used for over two years in our system.

The final step in preparing the tuning fork is the tip apex shape. Figure 2.13 shows the precut Pt wire that has a wide and undefined apex. A more symmetric tip shape over a few 100 nm is desired to decrease the influence of long range contributions in force measurements. Therefore, we reshape the tip apex with a focused ion beam (FIB) to a pyramid-like shape as shown in figure 2.14.

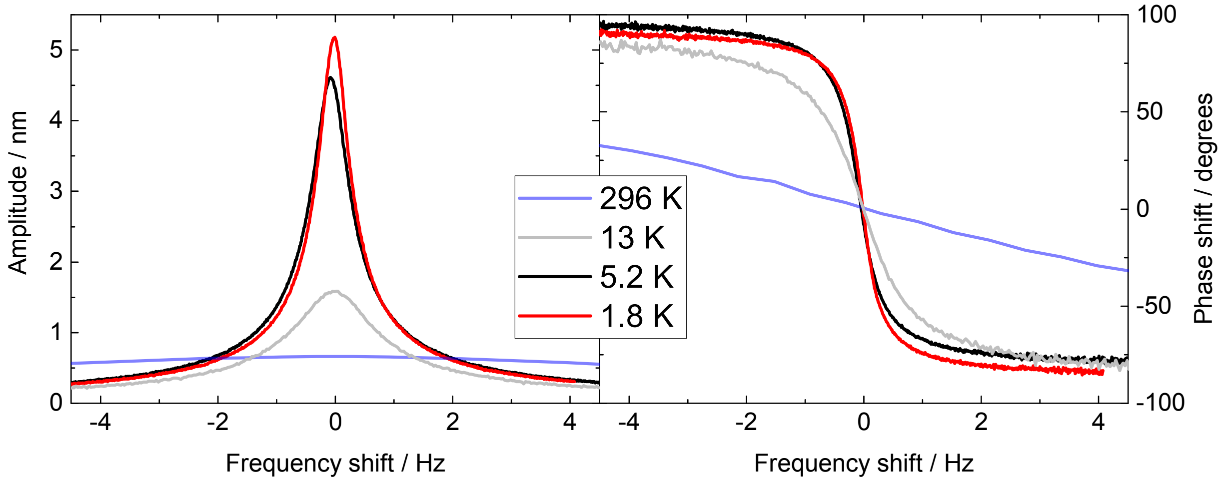

Figure 2.15: Tuning fork resonance evolution with temperature. The q-factor rapidly improves from roughly 2000 (10000 in UHV) at 296 K to 35000 at 13 K and reaches its final value of 60000 around 1-6 K. This strong temperature dependence could be due to the intrinsic quartz properties of the tuning fork itself, the stiffness of all involved components including the glue or the amplifier circuit. The peaks of all curves are roughly shifted to zero frequency shift compared to the eigenfrequency of the curve at 1.8 K. The eigenfrequency at room temperature, $f_0 = 29132$ Hz, is significantly higher than the eigenfrequency at liquid He temperatures ($f_0 \approx 29077$ Hz) for this tuning fork.

2.3.4 Performance in vacuum, low temperatures and magnetic field

The tuning fork parameters such as the q-factor and the excitation decrease significantly in magnetic field. Part of it could be due to the adhesion layer that is used between the gold pads and the SiO_2 material. Most companies evaporate or sputter a 200 nm thick chromium adhesion layer which is an antiferromagnet. A better option would be a non-magnetic titanium adhesion layer as we are able to use in-house. A 20 nm Ti adhesion layer is already sufficient and even provides a better film quality in terms of adhesion and diffusion through gold. Unfortunately most companies are unable to use Ti since it is not compatible with their wet-etching process. Another reason could be eddy currents within moving metallic parts in the magnetic field or the tuning fork preamplifier that is located near the stray field of the superconducting magnet inside the He exchange gas volume which could lead to a degradation of the transimpedance amplifiers.

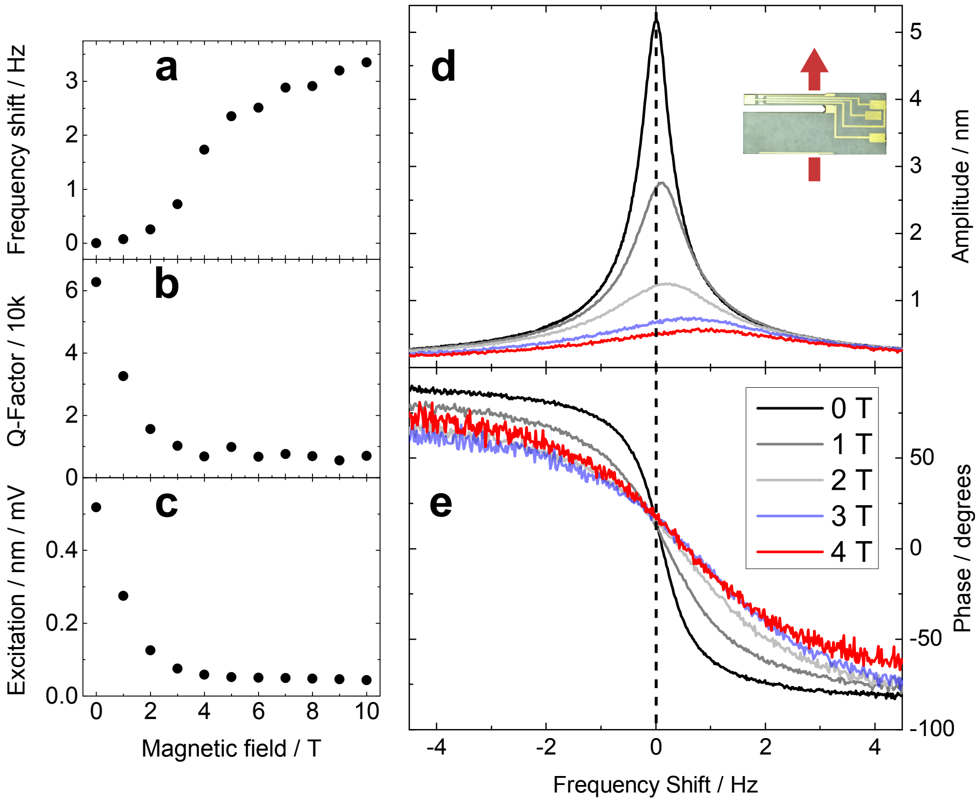

Figure 2.16: Tuning fork in magnetic field. The field was ramped from 0 to 10 T in 1 T increments parallel to the tuning fork oscillation direction (see inset in d). At each field strength, a frequency sweep with $V_{exc} = 10$ mV was performed for which the first five curves are shown in **d** and **e**. From these curves, the derived parameters are shown on the left: The frequency shift (**a**), q-factor (**b**) and the excitation/amplitude ratio for a constant excitation voltage (**c**).

2.4 Sample holder modifications for top-conducting samples

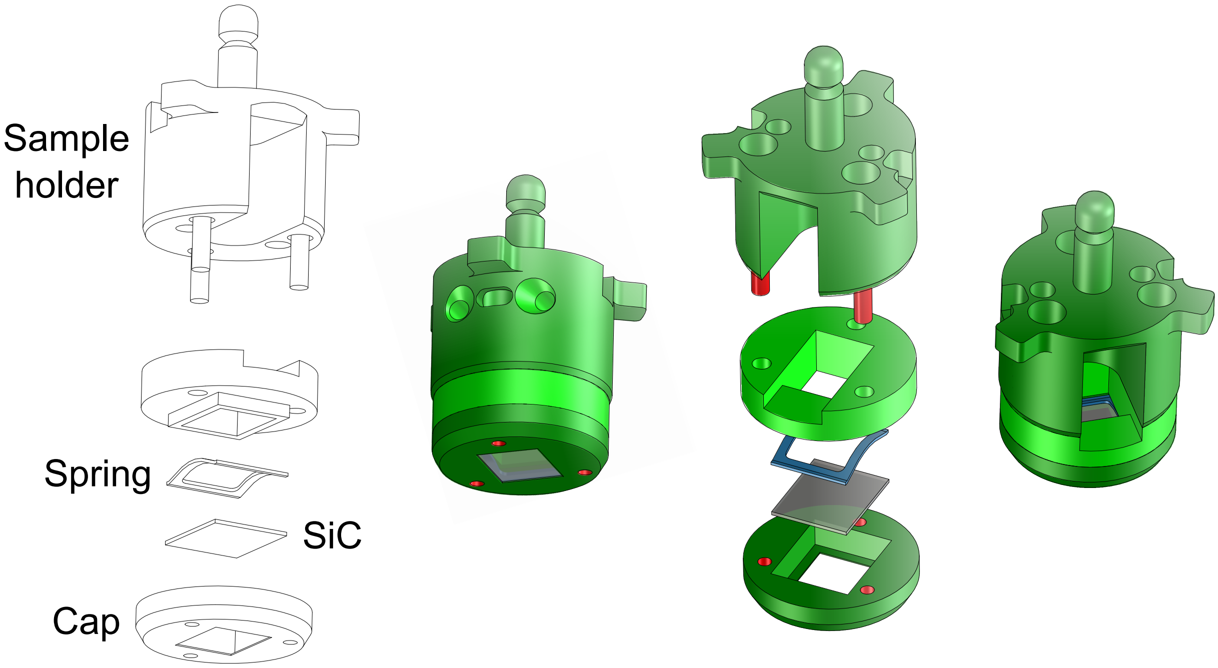

Figure 2.17: CAD overview of modified sample holder. The upper part is the old design, only the bottom part was redesigned to accommodate the new SiC sample holder. The flat SiC sample (roughly 6 mm x 8 mm) is pressed into the cap by a spring that ensures stability over a wide range of temperature cycles. The entire design is made out of Molybdenum.

The old sample holders were designed for bulk metal samples that can be contacted from all sides and pushed against other metal parts. Samples that are only conductive on one side, such as graphene/SiC(000-1), are different as SiC is mainly a fragile and thin insulating silicon wafer that holds only a few graphene layers on one side of its surface (see sample preparation in chapter 7.1). This means that the sample cannot be contacted from the back but has to be electrically contacted at its graphene surface that is facing the tuning fork. To ensure that the tuning fork is not touching the sample holder, even when the sample is rotated, the front part of the cap is as thin as possible (around 100 um). The spring and all other sample holder materials including the M1.4 screws are made out of molybdenum. The spring ensures a rigid sample position that can undergo heating up to 1000 K and cooling down to 1 K.

CHAPTER 3

COBALT HYDRIDES ON A DECOUPLING LAYER

The main results of the following chapter were published in Nature Communications, October 2015[1] [19].

Almost two years of this thesis were dedicated to the sample preparation and characterization of the CoH$_x$/h-BN/Rh(111) samples. Thus, this publication serves as the cornerstone of the next three chapters and the outline of the chapter will closely follow the published data in more depth. It will describe the sample preparation of CoH$_x$/h-BN/Rh(111), justify the magnetic properties of the adsorbed CoH$_x$ systems and introduce the experimental means to probe these magnetic signatures. The main finding, how the coupling to the substrate influences the magnetic anisotropy energies of the cobalt hydride systems, is discussed at the end.

---

[1] P. Jacobson, T. Herden, M. Muenks, G. Laskin, O. Brovko, V. Stepanyuk, M. Ternes, K. Kern, "Quantum engineering of spin and anisotropy in magnetic molecular junctions".

3.1 A recent development: The h-BN/Rh(111) decoupling layer

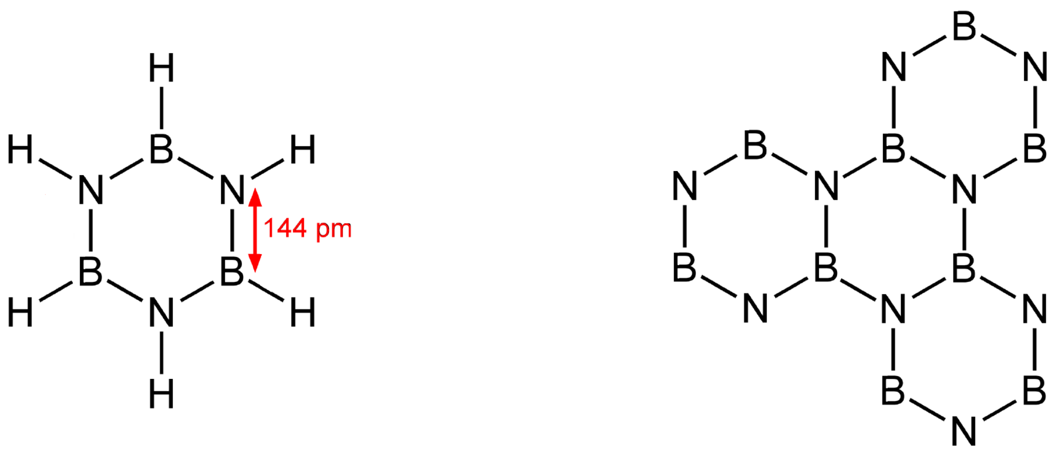

Figure 3.1: h-BN formation. Left: The pristine borazine molecule ($B_3H_6N_3$) as it is introduced into the UHV chamber in its gas phase. A hot Rh(111) surface held at 1100 K acts as a catalyzer and dissociates the hydrogen leaving the BN rings on the surface that self-assemble to a monolayer on top of a transition metal surface (Right).

Employing a single hexagonal boron nitride (h-BN) sheet as a decoupling layer is a relatively new approach. New, compared to the workhorse of the *spins-on-surfaces* community, Cu_2N, that has been around for over a decade and is still in use today (compare table 1.1 in chapter 1). h-BN self-assembles on transition metal surfaces by thermal decomposition of borazine ($B_3H_6N_3$) as schematically sketched in figure 3.1. Successful growth has been reported on: Ni(111), Pd(111), Pt(111), Pd(110), Cu(111), Rh(111) and Ru(001) [56] [57]. The h-BN/Rh(111) [58] approach was used in our setup right after its discovery [59]. Since then Co, Sn or Pb clusters have been grown as well as single molecules deposited with an enhancement of superconducting or magnetic properties thanks to the decoupling effect of the h-BN layer [60] [61].

This work employs a Rh(111) surface which is first cleaned by several sputtering and annealing cycles in a UHV ($< 1 \cdot 10^{-10}$ mbar) preparation chamber. The annealing cycles keep the Rh crystal at a temperature of 1100 K for 20 min before the Rh(111) surface is sputtered with 1.5 kV Ar^+ ions for 30 min. Four cycles are normally enough to refurbish a previously cleaned surface, e.g. to remove an old h-BN layer with sub-adsorbents. During the final annealing cycle the temperature is set to 1080 K and borazine is introduced into the UHV chamber via a leak-valve at a pressure of $1.2 \cdot 10^{-6}$ mbar for two minutes resulting in a self-assembled h-BN monolayer. The h-BN/Rh(111) sample is then quickly transfered into the STM head and cooled down to 5 K. Our STM head design allows the sample to be rotated 180 degrees so that it faces the connected UHV STM chamber and not the STM tip. The STM chamber harbors a homebuilt electron beam Co evaporator from which less than a 0.001 Co monolayer coverage is evaporated onto the h-BN/Rh(111) surface. As the Co evaporator is more than one meter away from the sample surface the Co flux, even for a fraction of a submonolayer, must be quite high. Because of this a large amount of Co has to be evaporated and we believe that residual hydrogen from the Co-rod and W filament bonds to the Co atoms in the gas phase or gets co-deposited, hence the formation of CoH_x complexes. Other research groups that work with Co atoms on decoupling layers such as graphene, have cautiously tried to minimize hydrogen co-deposition during their Co-evaporation. It seems that even careful outgassing and special care taken in material selection do not completely avoid hydrogen contamination.

During the Co deposition the sample temperature roughly rises from 5 K to 20 K and then quickly cools down to 5 K again. It is crucial to stay at such low temperatures to avoid clustering of the deposited Co atoms on the surface. The final result of a successful CoH_x/h-BN/Rh(111) sample preparation is shown in a large scale STM image in figure 3.2 and 3.3. The different lattice constants of the h-BN layer and the Rh(111) surface (13 BN units on 12 Rh atoms) lead to a corrugation that is lifting up the h-BN layer from its metal contact (see figure 3.2b).

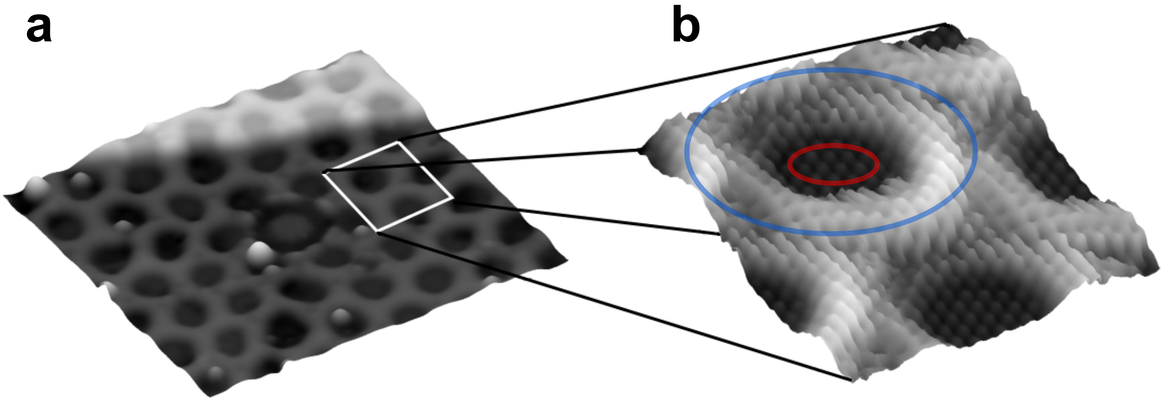

Figure 3.2: Pseudo 3d presentation of h-BN/Rh(111). (a) 15 nm x 20 nm STM constant current image (V_B = -100 mV, I_T = 20 pA) with a distinct step edge and a common defect in the center. Next to the center a white square guides the eye to a 5 nm x 5 nm STM constant current image taken with a functionalized tip (V_B = -15 mV, I_T = 20 pA) in which the BN units and their corrugation are visible. The height difference between the flat pore (red circle) and the rim (blue circle) is around 100 pm. The center of the pore is 3.2 nm away from the next one and defines the unit cell of the repeating h-BN/Rh(111) structure (compare [58]).

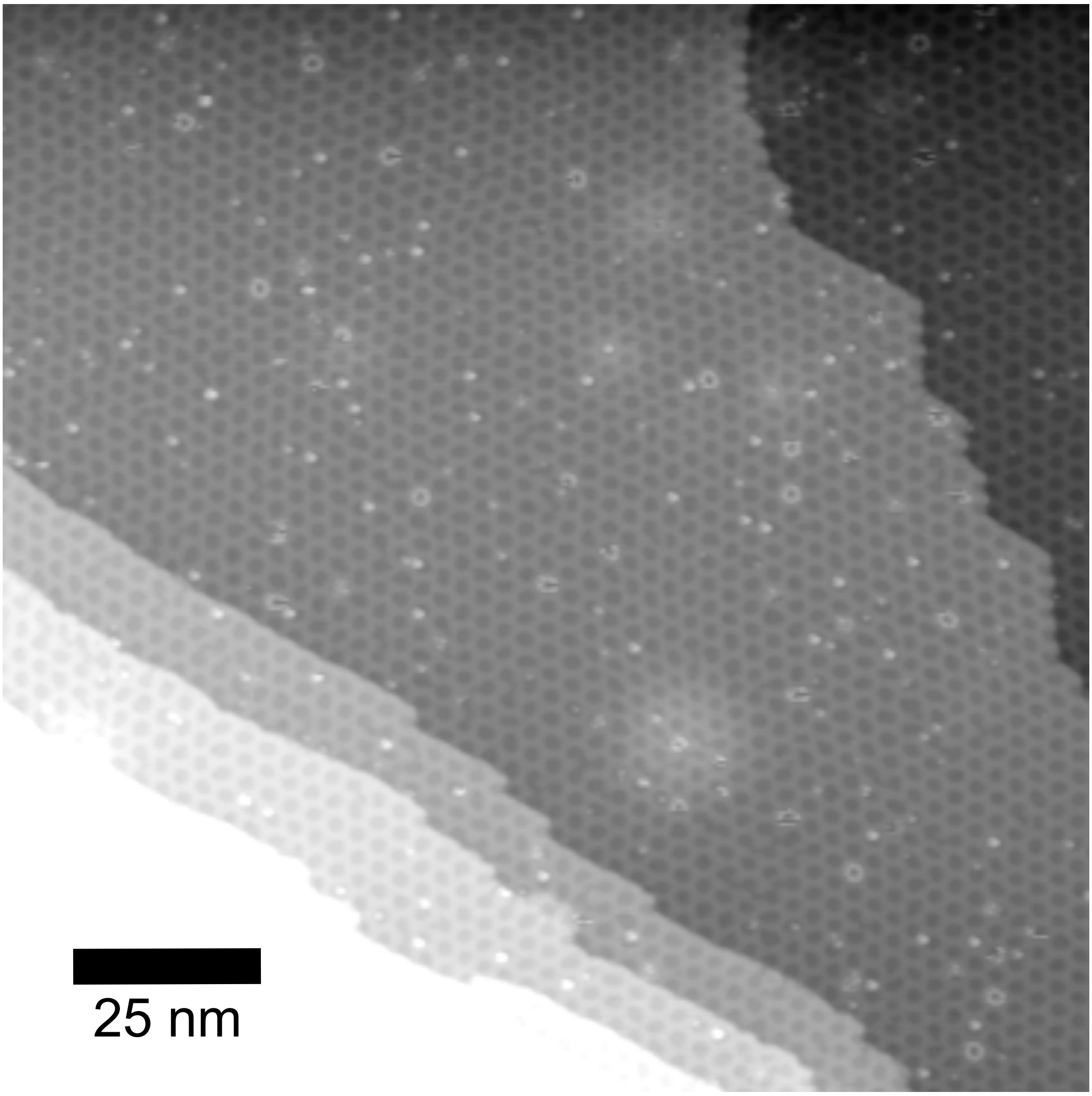

Figure 3.3: Cobalt hydrides on h-BN/Rh(111). Large scale (150 nm x 150 nm) constant current STM image taken at $V_B = -100$ mV and I_T = 20 pA. The dominant step edges correspond to the step edges of the underlying Rh(111) surface and are roughly Δ_z = 190 pm in height. Apart from different CoH$_x$ species, many Co ringstates are present that have been previously observed by another group [62]. The brighter spots on the sample surface might stem from local dopants such as Ar ions buried into the surface during the sputtering procedure (circles with a radius between 2 nm and 10 nm that appear as brighter spots on the sample surface due to a local doping effect).

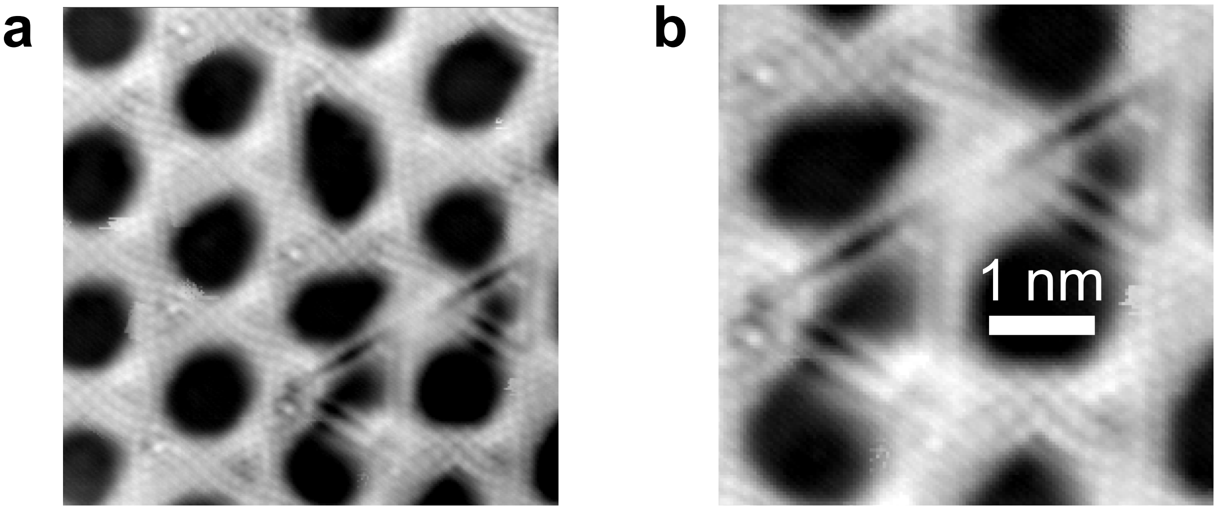

Figure 3.4: Structural defects. Strain, defects and structural changes are a common observation of the h-BN/Rh(111) surface. (a): A 12 nm x 12 nm constant current STM image (I_T = 500 pA, V_B = -15 mV) shows the atomic resolution of the h-BN/Rh(111) surface where distorted h-BN pores, defects on the rim sites and also a new phase, due to carbon contamination that is enlarged in (b), are visible.

Obvious distortions to the CoH$_x$ systems due to nearby defects or strain in the h-BN layer have to be accounted for. The CoH$_x$ systems investigated in chapter 4, 5 and 6 were selected according to certain empirical quality standards: A symmetric and round pore of the h-BN layer indicates less strain contributions compared to distorted pores as shown in figure 3.4.a. Also, CO defects that disguise themselves as protrusions within the pores or other contaminants on the surface were avoided close or nearby CoH$_x$ systems. If contaminants, such as H or H$_2$, are present we can carefully utilize these perturbations as presented in chapter 6. Structural defects as shown in figure 3.4b are most likely due to carbon contamination [Publication in preparation by S. Koslowski]. We were able to avoid these contaminations by initializing the annealing of the Rh(111) crystal at a temperature of 800 K in $2 \cdot 10^{-6}$ mbar oxygen.

A further characterization of the h-BN/Rh(111) surface was carried out together with Dr. Daniel Rosenblatt who summarizes additional data in his Ph.D. thesis [63]. One open question is the role of the workfunction difference across the h-BN. Research groups employing different techniques have come up with values for the workfunction that differ by almost one order of magnitude. We employed Kelvin probe force microscopy (KPFM) with our AFM capabilities to compare the rim and valley region workfunctions of the h-BN/Rh(111) surface and determined a workfunction difference of roughly 80 meV.

3.2 Magnetic signatures

3.2.1 Magnetic moments and theory calculations

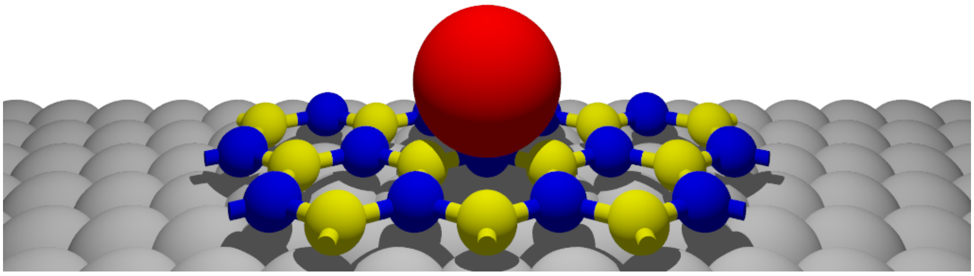

Figure 3.5: Illustration of a Co atom adsorbed on a h-BN/Rh(111) surface. The Co atom (red) sits on a N atom of a flat h-BN monolayer patch (B in yellow and N in blue) that decouples it from the underlying Rh(111) surface (grey).

Hexagonal boron nitride is an indirect bandgap semiconductor [64] with a bandgap of 5.9 eV and decouples the evaporated Co atoms from the underlying Rh(111) metal by hindering the screening of the magnetic properties. Several steps need to be taken into account before we can define and justify the magnetic state of a Co atom on this surface. As already mentioned in the introduction, charge transfer and realignment of the electronic orbitals are the most dominant factors to consider first.

The corrugation of the h-BN sheet does normally not allow to determine the precise adsorption sites of each CoH_x system in STM and AFM experiments. The force measurements in chapter four and the tip functionalization routines in chapter six both show that for short tip-sample distances, required for a determination of the h-BN lattice structure, the CoH_x systems are strongly influenced and subject to change. Thus, apart from our spectroscopic signatures in magnetic field that clearly confirm magnetic systems, we are employing density functional theory (DFT) calculations carried out by Oleg Brovko in the group of Valeri Stepanyuk that are explained in detail in [19]. In summary, they include the on-site Coulomb interaction of the Co d-levels with an LDA+U correction. Four layers of Rh(111) were taken into account together with the BN sheet fully relaxed on the surface. CoH_x species were placed onto this sheet according to the *bridge, top-N, hex* and *top-B* sites near the high symmetry regions v, r_1 and r_2 as shown in figure 3.6 and allowed to relax as described in [19]. Regions outside the high symmetry points (see figure 3.6b) were also considered but would not show significant contributions as the energy maps were "smooth and devoid of local minima". The adsorption energies of each species for each region and their corresponding magnetic moments are displayed in table 3.1.

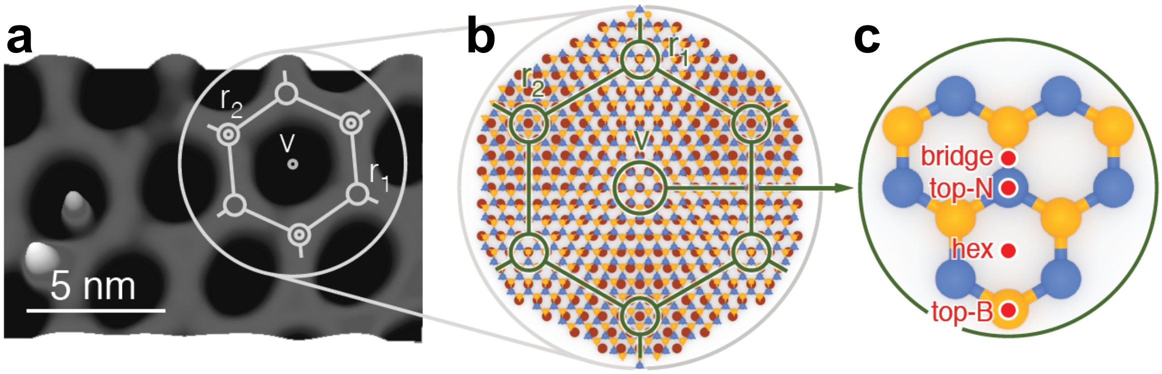

Figure 3.6: Model used for DFT calculations. (a) STM constant current image of h-BN/Rh(111) (V_B = -100 mV, I_T = 20 pA). The circle shows the repeating unit cell that is divided into a valley region (v) and two different rim regions (r_1 and r_2). The atomic structure with B (yellow), N (blue) and Rh (red) atoms of the upper Rh(111) layer is shown in (b). The distinction between the two rim sites is now clear: r_1 has the Rh center atom directly underneath the B atom whereas in r_2 sites this Rh atom is equally far from the B and N atoms.

Species	**Region**	**hex**	**top-B**	**top-N**	**bridge**
Co	v	0	5	23	21
Co	r_2	0	183	427	348
Co	r_1	0	207	351	232
CoH	v	91	739	0	96
CoH	r_2	73	261	0	137
CoH	r_1	0	173	n/c	52
CoH$_2$	v	140	315	0	34
CoH$_2$	r_2	221	510	0	32
CoH$_2$	r_1	57	599	0	24

Species	**Region**	**hex**	**top-B**	**top-N**	**bridge**
Co	v	2.1	2.2	2.2	2.2
Co	r_2	2.1	2.1	2.1	2.2
Co	r_1	2.0	2.1	2.2	2.1
CoH	v	2.0	1.9	2.0	2.0
CoH	r_2	2.1	2.1	2.1	2.1
CoH	r_1	2.1	2.1	n/c	2.1
CoH$_2$	v	1.2	1.6	1.2	1.3
CoH$_2$	r_2	1.3	1.5	1.5	1.6
CoH$_2$	r_1	1.6	1.2	1.5	1.6

Table 3.1: Top: Relative adsorption energies of CoH$_x$ species in meV relative to the lowest adsorption energy value for each row. This shows: The lower the value the more likely the adsorption position with zero (green) being the preferred site. Bottom: Magnetic moments of the same configurations in μ_{B}

From the DFT calculations we can deduce the local adsorption configuration of Co, CoH and CoH_2 species with their respective magnetic moments. Co always resides on the hex site in all regions with a magnetic moment of around 2 μ_B. CoH prefers the top-N site with a possibility of hex site adsorption in r_1 regions even though the numerical calculation did not converge (n/c) in this particular case, and again, a magnetic moment of around 2 μ_B. CoH_2 on the other hand carries a magnetic moment of 1.2 to 1.5 μ_B and prefers the top-N sites for all regions. Figure 3.7a shows the 1.2 eV intrinsic Stoner exchange split d-levels of CoH and CoH_2 (energy difference between the blue peaks in the Co PDOS). From there, the spin asymmetries, i.e. the difference between the majority and minority electron densities, are integrated within spheres around the atoms. From the majority and minority spin projected density of states we can estimate a total spin, $S = 1$ for CoH and $S = 1/2$ for CoH_2.

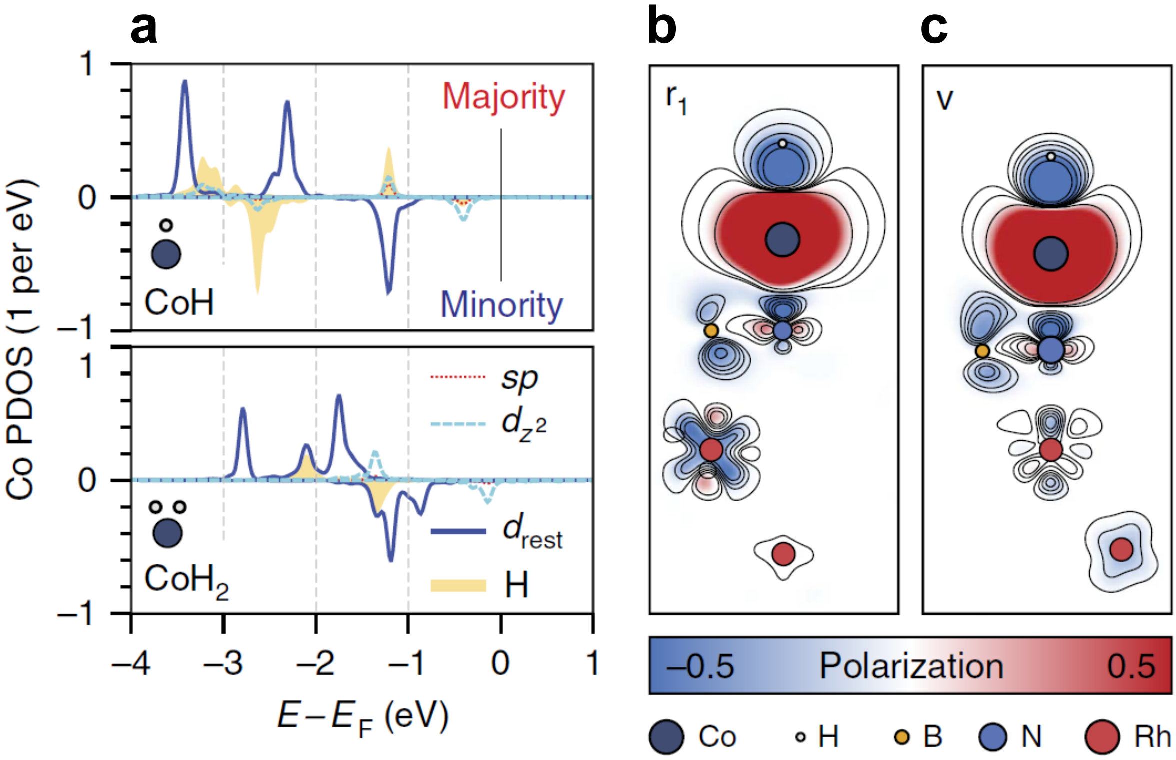

Figure 3.7: Majority and minority spin projected density of states (PDOS). (a) PDOS of the two main species: CoH and CoH_2. (b + c) Spin density distributions for CoH on a top-N site for regions r_1 and v that show the strong z-orientation leading to a strong out-of-plane magnetic anisotropy as further explained in the next subsection.

3.2.2 Magnetic anisotropy energy and its unperturbed Hamiltonian

While the DFT calculations provide the adsorption sites and magnetic moments as well as the total spin, they are less suitable for providing exact magnetic anisotropy energies (MAE) as the *Kohn-Sham* DFT underestimates the orbital moments and their spin-orbit contributions although they are part of the calculations. As the CoH system with total spin, $S = 1$, is the most dominant species and is thoroughly referenced in the next chapters, an introduction to its MAE will follow the $S = 1$ framework.

A spin, S, has $2S + 1$ states that are normally degenerate if the spherical symmetry of the atom is not broken, i.e. the spin eigenstates and their m_z projections prefer no particular direction in their Hilbert space. In the case of CoH with total spin[2] $S = 1$, we consider three spin states with m_z projection: -1, 0 and 1. As the atom's symmetry is strongly broken by the surface, the spin eigenstates are aligned according to the magnetic anisotropies, D and E, that are shown in figure 3.8. Due to the threefold symmetry of the surface (three neighboring B atoms) and a strong alignment in our defined z-direction we expect a strong out of plane contribution, D, to the magnetic anisotropy. A smaller in-plane contribution, E, is expected due to the corrugation of the h-BN, the shift of the underlying Rh atoms and also the tilting of the hydrogen.

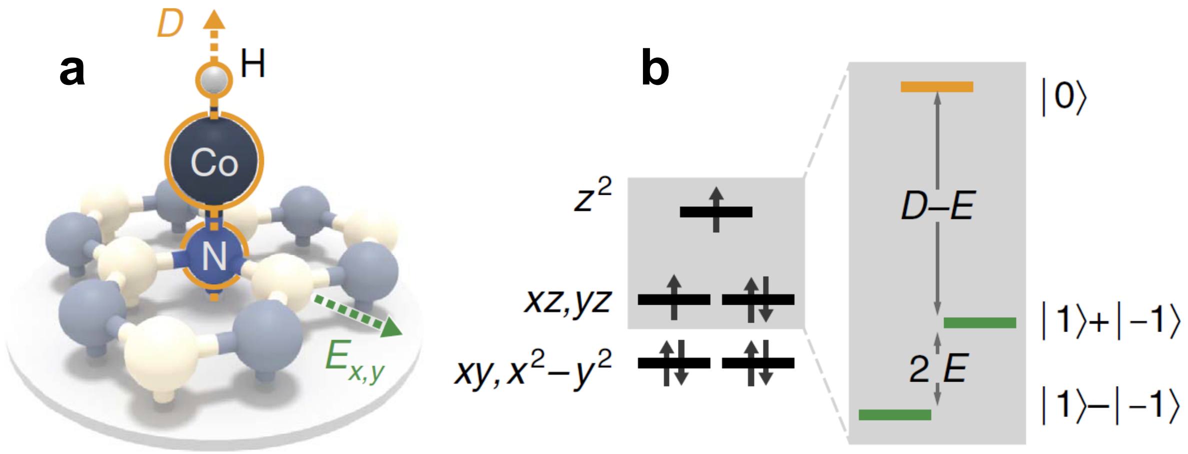

Figure 3.8: Symmetry arguments for magnetic anisotropy. (a) The starting point is a C_{3v} symmetry of the N-Co-H unit directly surrounded by three B atoms that leads to a significant out-of-plane magnetic anisotropy, D. A shift of the underlying Rh atoms, the spatial corrugation and the tilting of the H atom are all minor factors that lead to an in-plane magnetic anisotropy, E. (b) The orbital distributions of the Co $3d^8$ shell are split in energy according to D and E.

---

[2] Note, that for a spin $S = 1$ with a sub-spin structure (e.g. two electrons with $S = 1/2$), four degenerate states should exist. We only consider the total spin $S = 1$ with m_z projections -1, 0 and 1 and neglect the $S = 0$ state as it is further away in energy.

So far we have introduced an overall magnetic moment and a total spin but have neglected the orbital moment, L, as the total angular moment is: $J = L + S$. STM experiments do normally not distinguish between orbital and spin contributions. Complementary x-ray magnetic circular dichroism (XMCD) measurements are needed to get a precise value for the orbital moment for further sum rule calculations. Even then, this topic is still discussed in literature [65] with one problem being the necessary sample averaging of XMCD. For now, it is common practice to describe the magnetic system in a so called *Spin Hamiltonian Approach* that was first used for larger molecular magnets [66]. The orbital angular momentum is discarded and a phenomenological Hamiltonian that describes the overall magnetic behavior is introduced. Therefore, we do not consider the real microscopic origin of the spin anymore: It could be a single electron, several d-shell electrons of a transition metal ion like cobalt or the combined spin and orbital moment of a rare earth ion. In its most general form the Hamiltonian consists of Stevens operators, $\hat{O}_N^k$, that rotate a spin, S, under the most general point group symmetries with the parameters, B_N^k:

$$\mathcal{H}_{CF} = \sum_{\substack{N=2,4,\ldots,2S \\ -N\leq k\leq N}} B_N^k \hat{O}_N^k. \tag{3.1}$$

It is a good approximation to only consider the first terms of the sum, i.e. the quadratic terms, for which the rotation must be symmetric and can further be diagonalized and rotated to write it in familiar x, y, z components. The so produced unperturbed Hamiltonian, $\mathcal{H}_0$, will describe a CoH $S = 1$ system that is subject to a crystal field (CF) inducing MAE:

$$\mathcal{H}_0 = \mathcal{H}_{CF} \tag{3.2}$$

$$\mathcal{H}_0 = DS_z^2 + E(S_x^2 - S_y^2) \tag{3.3}$$

with D (axial) and E (transverse) as the MAE parameters. The spin operators $\boldsymbol{S} = (S_x, S_y, S_z)$ for a $S = 1$ system are derived from the generalized Pauli matrices:

$$S_x = \frac{1}{\sqrt{2}}\begin{pmatrix} 0 & 1 & 0 \\ 1 & 0 & 1 \\ 0 & 1 & 0 \end{pmatrix}, S_y = \frac{i}{\sqrt{2}}\begin{pmatrix} 0 & 1 & 0 \\ -1 & 0 & 1 \\ 0 & -1 & 0 \end{pmatrix}, S_z = \begin{pmatrix} 1 & 0 & 0 \\ 0 & 0 & 0 \\ 0 & 0 & -1 \end{pmatrix}. \tag{3.4}$$

We can solve the eigenvalue equation

$$\mathcal{H}_0 \left|\psi\right\rangle = E \left|\psi\right\rangle \tag{3.5}$$

by diagonalizing the static Hamiltonian $\mathcal{H}_0$. The resulting eigenvectors $\left|\psi\right\rangle$ and eigenvalues ϵ give us the eigenstates and eigenenergies of this system. For $S = 1$, D = -5 meV and E = 1 meV the resulting states are summarized in table 3.2.

The results of this simple diagonalization clearly show that the CoH $S = 1$ system has three

Eigenstate	Eigenenergy / meV	Spin m_z		
		-1	0	1
$\lvert\psi\rangle_1$	0	0.707	0	- 0.707
$\lvert\psi\rangle_2$	2	0.707	0	0.707
$\lvert\psi\rangle_3$	6	0	1	0

Table 3.2: Eigenstates, eigenvalues and their m_z projections for a CoH $S = 1$ system with magnetic anisotropy of D = -5 meV and E = 1 meV.

non-degenerate eigenstates. To determine the occupied states, the thermal occupancy, p_i, is calculated with the respective energy eigenvalues, ϵ_i, in a common Boltzmann distribution:

$$p_i = \frac{e^{\epsilon_i/(k_B T)}}{\sum_{i=1}^{N} e^{\epsilon_i/(k_B T)}} \tag{3.6}$$

where k_B = 0.08617 meV / K and T = 1.5 K. At cryogenic temperatures of around 1.5 K that are commonly achieved in our experiments, this leads to a clear distribution where the groundstate is completely occupied with a probability of $p_1 \geq$ 0.999999. At 77 K (liquid nitrogen), p_1 would only be around 0.5. Applying the usual angular momentum relations to these eigenstates determines the spin S and quantum number m_z:

$$S^2 \lvert S, m_z\rangle = S(S+1)\lvert S, m_z\rangle \quad S_z \lvert S, m_z\rangle = m_z \lvert S, m_z\rangle \tag{3.7}$$

The values in table 3.2 show that the groundstate, $\lvert\psi\rangle_1 = \frac{1}{\sqrt{2}}\lvert -1\rangle - \frac{1}{\sqrt{2}}\lvert +1\rangle$, with energy $\epsilon_1 = 0$, and the first excited state, $\lvert\psi\rangle_2 = \frac{1}{\sqrt{2}}\lvert -1\rangle + \frac{1}{\sqrt{2}}\lvert +1\rangle$, with energy $\epsilon_2 = 2E$, are superpositions of the $\lvert -1\rangle$ and $\lvert +1\rangle$ m_z projections while the second excited state, $\lvert\psi\rangle_3 = \lvert 0\rangle$, with energy $\epsilon_3 = E - D$, is a pure $m_z = 0$ state. Therefore, none of the three states is magnetized, as all contributions average out to $m_z = 0$. This fact will later become important when correlations in these spin systems are introduced.

3.2.3 In magnetic field

The originally degenerate spin states were split in energy by the surface induced magnetic anisotropy. They can be further split by an external magnetic field, $\boldsymbol{B}$, which we limit to B_z since the experimental setup can only apply a field up to 14 T in z-direction (out-of-plane). The effect of the applied magnetic field is added to the Hamiltonian, $\mathcal{H}_0$, as a Zeeman term, $\mathcal{H}_Z$:

$$\mathcal{H}_0 = \mathcal{H}_{CF} + \mathcal{H}_Z \tag{3.8}$$

$$\mathcal{H}_0 = DS_z^2 + E(S_x^2 - S_y^2) + g\mu_B B_z S_z \tag{3.9}$$

where $g \approx 2$ is the gyromagnetic factor[3] and μ_B = 0.0578 meV / T the Bohr magneton. Again, the result of diagonalizing $\mathcal{H}_0$ (see table 3.3) shows a clear shift of the eigenenergies compared to the case for $B_z = 0$ T in table 3.2.

Not so obvious, but more importantly, the m_z projections are now polarized and the groundstate, $|\psi\rangle_1$, as well as the first excited state, $|\psi\rangle_2$, are not equal superpositions anymore but clearly polarized in m_z with a probability of $\langle\psi|\psi\rangle_1 = 0.9372^2 \approx 0.88$ for the groundstate to be polarized in $m_z = -1$, while for the first excited state, the same polarization in $m_z = -1$ only has a probability of $\langle\psi|\psi\rangle_2 = -0.3488^2 \approx 0.12$ but the same high probability of 0.88 for a $m_z = +1$ polarization.

Thus, a transition that excites the groundstate to the first excited state must now, with a high probability, undergo a change in angular momentum of $\Delta m_z = 2$ to switch from $m_z = -1$ to $m_z = +1$. Since the total angular momentum is conserved during the tunneling process and the electron can only flip with $\Delta m_z = \pm 1$, we have to impose this selection rule and this particular transition will be reduced in magnetic field. The effect on the resulting experimental spectrum will be further clarified in figure 3.13.

Eigenstate	Eigenenergy / meV	Spin m_z		
		-1	0	1
$|\psi\rangle_1$	0	0.9372	0	-0.3488
$|\psi\rangle_2$	3.1	0.3488	0	0.9372
$|\psi\rangle_3$	6.5	0	1	0

Table 3.3: Eigenstates and eigenvalues with their m_z projections for a CoH $S = 1$ system with magnetic anisotropy of D = -5 meV and E = 1 meV and a magnetic field B_z = 10 T.

---

[3] The value for $g \approx 2$ does change for different spin systems and must be determined by experiments since it is a consequence of the giant spin approximation and is not expected to be the same as for a free electron.

3.3 Inelastic electron tunneling spectroscopy

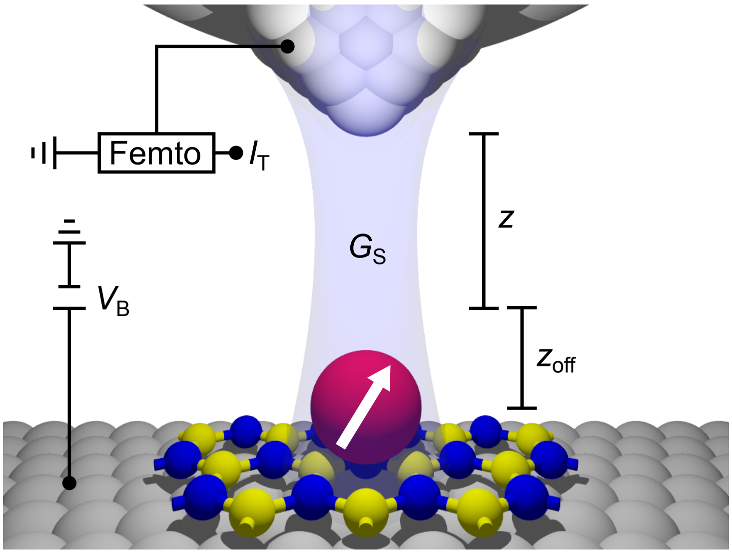

Figure 3.9: Scanning Tunneling Spectroscopy. The scan piezo moves the Pt tip (top) in proximity to the Co atom from figure 3.5 within a fraction of one nm in z-direction . Hot electrons are injected into the spin system by applying a bias voltage, V_B, to the sample. The resulting tunneling current, I_T, is defined by the overall tunneling conductance setpoint G_s = $V_\mathrm{B}/I_\mathrm{T}$. These electrons can now tunnel through the $S = 1$ system and cause excitations from its groundstate to its excited states. Hence, this method is called inelastic electron tunneling spectroscopy. The offset distance, z_off, accounts for the error of the real distance between tip and sample which would require, for example, an $I(z)$ approach curve until point contact is established to determine its exact value.

3.3.1 Elastic tunneling

The tunnel effect between two electrodes (tip and sample) that are only a few hundreds of pm apart from each other (distance z) is the working principle of an STM. When a constant bias voltage, V_B, is applied to the tunnel junction, the Fermi levels of the tip and sample electrodes are not aligned anymore and a tunneling current, I_T, is observed. I_T is an exponential function of the distance z as in first approximation it is proportional to the probability function overlap of an electron in one of the electrodes with the emtpy states in the other electrode when subject to an applied bias voltage: $I_\mathrm{T} \propto |\Psi(z)|^2 = |\Psi(0)|^2 \exp(-2\kappa z)$ with $\kappa = \sqrt{\frac{m_0}{\hbar^2}(\Phi_t + \Phi_s - eV_\mathrm{B})}$ in which Φ_t and Φ_s are the workfunctions of tip and sample and eV_B is the energy of the tunneling electrons. This exponential behaviour makes the STM extremely sensitive to local variations. Figure 3.9 shows the basic experimental situation in which the bias voltage,V_B , is applied to the sample and the resulting tunneling current, I_T, is amplified by a sub femtoampere transimpedance amplifier[4] with an usual gain of 10^9 V/A. A feedback loop controls the z distance

---

[4] DDPCA-300 from the company *Femto* with a variable gain from 10^4 to 10^{13} V/A.

accordingly to increase or decrease the observed tunneling current keeping it at a preset value. In this context we speak of a setpoint current I_S at a constant bias voltage V_B and hence can also define a setpoint conductance $G_\mathrm{S} = V_\mathrm{B}/I_\mathrm{S}$. Together with the local density of states (DOS) of tip and sample and the Fermi-Dirac distribution $f(\epsilon) = 1/(1+\exp(\epsilon/k_\mathrm{B}T))$ a common expression for the tunneling current from tip to sample ($t \rightarrow s$) is:

$$I_{t\rightarrow s} = \frac{4\pi e}{\hbar}\int_{-\infty}^{\infty} \underbrace{\rho_s(\epsilon)}_{\text{DOS sample}} \overbrace{\rho_t(\epsilon - eV_\mathrm{B})}^{\text{DOS tip}} \underbrace{(f_t(\epsilon - eV_\mathrm{B}) - f_s(\epsilon))}_{\text{Available states}} \underbrace{|M(\epsilon - eV_\mathrm{B}, \epsilon)|^2}_{|\Psi(z)|^2} d\epsilon. \tag{3.10}$$

The contribution $I_{s\rightarrow t}$ is added to obtain the overall tunneling current I_T. The exact determination of the matrix element $|M|^2$ has been the subject of many publications over the last decades [43] [67] [68] [69] and will be discussed in detail in the next sections where we consider inelastic excitations. An approximation that only considers the spatial arrangements between tip and sample in an s-wave approximation of the tunneling orbital and only allows for elastic tunneling processes, yields the expression

$$I_\mathrm{T} = c\rho_t \int_0^{eV_\mathrm{B}} \rho_s(\epsilon)d\epsilon \tag{3.11}$$

where the constant prefactor, c, is defined in [70] . From equation 3.11 we immediately see that in this approximation the tunneling current is directly proportional to the sample DOS. By deactivating the STM feedback loop, i.e. keeping the tip height, z, constant over an area of interest, and ramping the bias voltage, V_B, between two preset values we can therefore, in this range, probe the sample DOS in scanning tunneling spectroscopy (STS) experiments. Starting from equation 3.10 and the assumption that all matrix elements $|M|^2$ stay constant we can write:

$$I_\mathrm{T} \propto \int_{-\infty}^{\infty} \rho_s(\epsilon)\rho_t(\epsilon - eV_\mathrm{B})(f_t(\epsilon - eV_\mathrm{B}) - f_s(\epsilon))d\epsilon. \tag{3.12}$$

The first derivate of this expression, $\frac{\partial I_\mathrm{T}}{\partial V}$, can be simplified [70] by assuming a constant DOS of the tip and $T \rightarrow 0$ and yields:

$$\left.\frac{\partial I_\mathrm{T}}{\partial V}\right|_{V_\mathrm{B}} \propto \rho_t\rho_s(eV_\mathrm{B}). \tag{3.13}$$

This means that the derivative of the tunneling current, i.e. its slope, is proportional to the density of states at the current voltage value and allows for a precise evaluation. A simulation of this principle is shown in figure 3.10a, where the tunneling current versus the applied bias voltage is plotted in the elastic regime (constant slope) up to V_B = 8 meV. In practice, the STM tip is moved over the region of interest (e.g. the center of a spherical CoH system) at a setpoint conductance that yields a high enough signal to noise ratio. The STM feedback loop is then turned off and the bias voltage is slowly ramped between two set voltages (here: $V_\mathrm{B} \in [-15, +15]$ meV).

3.3.2 Inelastic tunneling

In the fictitious case displayed in figure 3.10, the elastic processes are described by the linear increase of the tunneling current with a bias voltage up to an energy V_B = 8 meV at which point the tunneling electron can loose its energy $\Delta\epsilon$ = 8 meV to the system and excite it. An example of such an excitation would be the excitation of a spin system [71] [72] [5] or the onset of vibrations or quantized rotations of a molecule [73]. At this voltage, the inelastic pathway provides another tunneling path and adds to the overall tunneling current thus increasing its slope (see figure 3.10a). The number of datapoints is important as they can also lead to artificial broadening effects as seen for the 30 simulated datapoints used in figure 3.10 where each datapoint corresponds to 1 meV.

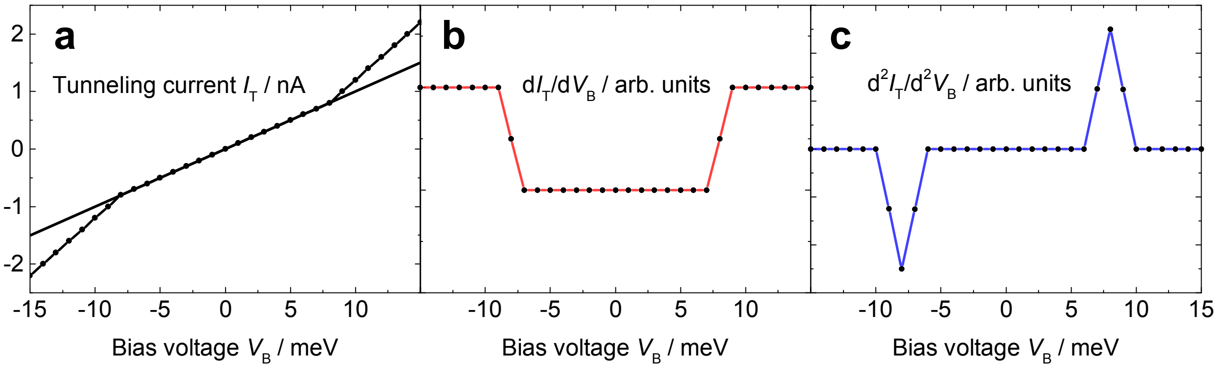

Figure 3.10: IETS signal simulation in the tunneling current (a) and its two derivatives (b and c) with respect to the bias voltage. The onset of inelastic excitations occurs at 8 meV and adds to the elastic contribution of the tunneling current. In the first derivative this corresponds to a step and in the second derivative to a peak. Here the broadening of the steps and peaks is due to the number of datapoints (one datapoints = 1 meV) that is too small.

A real data example is shown in figure 3.11 where we use 400 datapoints for a total voltage interval of 30 meV with each point corresponding to 0.075 meV. The noise in the tunneling current due to low frequency contributions does not allow for a smooth dI/dV signal if a simple numerical derivative is applied to the tunneling current data. The lock-in signal was simultaneously recorded and shows a much higher signal to noise ratio than the numerical derivative of the tunneling current. Thus, we are employing a lock-in detection to enhance the signal. A small sinusoidal voltage with an amplitude, V_m, and a frequency, f, of around 600-800 Hz is added to the bias voltage, i.e.: $eV_\mathrm{B} + eV_m \sin(2\pi f t)$. The amplitude of this voltage is equal to the energy resolution that should be as small as possible compared to the thermal and electronic broadening within the tunneling circuit. The sinusoidal voltage of the lock-in results

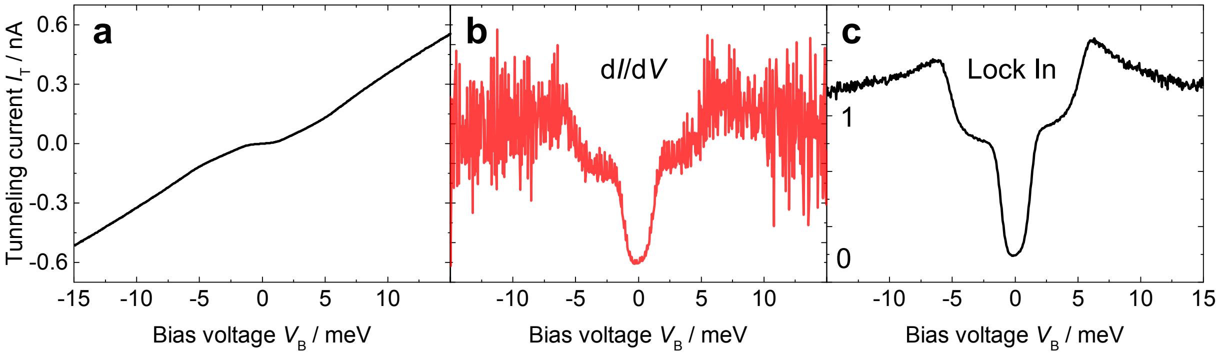

Figure 3.11: IETS signals with different signal to noise ratios for a CoH $S = 1$ dataset with two inelastic excitations at around 1 meV and 5 meV. The direct numerical derivative of the tunneling current (a) leads to a noisy spectrum as seen in (b). The lock-in signal (c) that directly measures the slope of the tunneling current signal provides a much better signal to noise ratio and is shown in comparison to the same dataset.

in an oscillation of the tunneling current with the same frequency. The resulting amplitude, however, is proportional to the slope, $I_\mathrm{T}/V_\mathrm{B}$, as can be seen from the first Taylor expansion term when the upper limit of the integral (eV_B) is replaced by $(eV_\mathrm{B} + eV_m \sin(2\pi f t))$ in equation 3.11.

The modulation voltage of the lock-in signal is usually phase shifted so that the the signal and its noise contribution can be distinguished from each other by taking the lock-in signal as a reference signal. Therefore the lock-in signal is a direct measurement of the first derivative of the tunneling current with an improved signal to noise ratio. However, also the modulation of the lock-in introduces an artificial broadening of the energy resolution [70] in which a δ-function peak in the DOS is broadened to a half-sphere with a width of $2eV_m$. Also the finite temperature introduces a thermal broadening of such a δ-function peak in the tunneling current to a Gaussian peak with a FWHM of $3.2k_\mathrm{B}T$ in the lock-in signal. In terms of inelastic excitations the thermal broadening of both the sample and the tip states alone results in a FWHM of $5.4k_\mathrm{B}T$ (0.52 meV for T = 1.1 K[5]) of the peaks in the derivative of the lock-in signal. The peaks in figure 3.12b and c have a FWHM of around 0.8 meV to 1 meV and thus additional effects such as the already mentioned lock-in broadening or the real temperature at the tunnel junction, which is usually hard to measure except with a superconducting sample, must be responsible for this additional broadening of around 0.4 meV.

Another effect that could have an impact on the broadening is the actual lifetime of the excited states of the spin system. For magnetic atoms on surfaces the measured lifetimes are usually in the order of ps to ns, e.g. [74]. According to the Heisenberg uncertainty principle,

---

[5] After an upgrade to our pumping line we are consistently at 1.1 K. The datasets presented in the next subsections of this chapter were taken at T = 1.4 K.

an energy uncertainty of up to 2 meV ($\Delta E \Delta t \geq \frac{\hbar}{2}$) is possible for 0.1 ps and could therefore lead to quite a dominant contribution to the overall broadening of the inelastic peaks. In our simulations all these broadening effects are included in an effective temperature, T_{eff}, that is usually around 2 K instead of the measured temperature of 1.1 to 1.4 K in experiments.

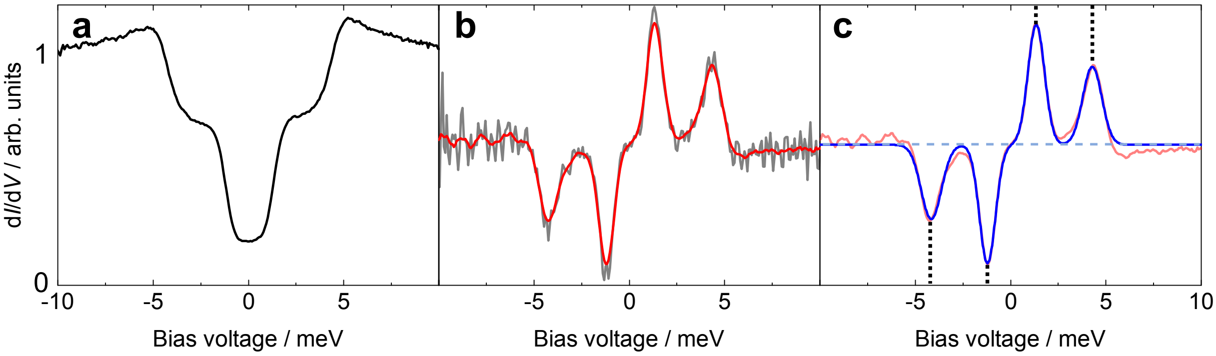

Figure 3.12: Example of the energy step determination of a typical CoH $S = 1$ dataset and the step broadening in experiment (267 points for a total bias voltage range of 20 meV). The noisy grey curve in (b) is the raw point by point derivative of the lock-in signal in (a). This derivative is smoothed by a Savitzky-Golay method (red curve) in 1st polynomial order taking ten neighboring datapoints into account. (c) Four Gaussian fits (blue curve) to the smoothed curve determine the energy positions of the inelastic excitations and their errorbar. From left to right: -4.16 meV (FWHM = 1.06); -1.22 (FWHM = 0.84); +1.35 (FWHM = 0.87); +4.29 (FWHM = 1). As the excitations are symmetric in energy a voltage offset is accounted for by taking the average out of both, the negative and the positive values. In this case the first excited state has an energy of $\epsilon_2 = 1.29$ meV and the second excited state an energy of $\epsilon_3 = 4.23$ meV. From these values and the energy equations defined in the previous subsections we can deduce the magnetic anisotropy parameters: $D = -3.58$ meV and $E = 0.65$ meV.

3.3.3 Probing with a perturbation

The previous subsections introduced the eigenstates of the CoH spin system that are a few meV apart in energy and the experimental method to probe the inelastic transitions between these eigenstates. They were derived from the diagonalization of the unperturbed Hamiltonian, $\mathcal{H}_0$.

In order to calculate the impact on the tunneling current we have to quantify the matrix elements, $|M|^2$, that were introduced in equation 3.10. In inelastic transport experiments tunneling electrons above a certain threshold energy, set by the applied bias voltage, can excite the probed spin system to an excited state. During this tunneling process the total energy and angular momentum are conserved and can be described in the framework of a scattering event between the $S = 1/2$ tunneling electron $\boldsymbol{\sigma}$ and the $S = 1$ system $\boldsymbol{S}$. To describe such a scattering event of the tunneling electron $\boldsymbol{\sigma}$ with the localized spin $\boldsymbol{S}$ we use the *Kondo exchange* Hamiltonian, $\mathcal{H}_1$:

$$\mathcal{H}_1 \propto \frac{1}{2}\boldsymbol{\sigma} \cdot \boldsymbol{S} \tag{3.14}$$

with the Pauli matrices $\boldsymbol{\sigma} = (\sigma_x, \sigma_y, \sigma_z)^T$:

$$\sigma_x = \begin{pmatrix} 0 & 1 \\ 1 & 0 \end{pmatrix}, \sigma_y = \begin{pmatrix} 0 & -i \\ i & 0 \end{pmatrix}, \sigma_z = \begin{pmatrix} 1 & 0 \\ 0 & -1 \end{pmatrix} \tag{3.15}$$

and the eigenstates of the tunneling electron in their m_z projection:

$$\text{Spin Up} = |\phi\rangle_1 = |\uparrow\rangle = \begin{pmatrix} 1 \\ 0 \end{pmatrix} \qquad \text{and} \qquad \text{Spin Down} = |\phi\rangle_2 = |\downarrow\rangle = \begin{pmatrix} 0 \\ 1 \end{pmatrix}. \tag{3.16}$$

Since injecting these electrons is a significant perturbation we need to treat $\mathcal{H}_1$ as a perturbation to the unperturbed Hamiltonian $\mathcal{H}_0$ in equation 3.3. Fermi's golden rule gives us the constant transition rate, W_{fi}, of a quantum system to transition from its initial energy eigenstate $|\Psi\rangle_i$ into a final state $|\Psi\rangle_f$ when subject to a perturbation. This transition rate will be proportional to the observed spectroscopic signal $dI_\mathrm{T}/dV_\mathrm{B}$. The core of this perturbation are the matrix elements, $M_{fi} = \langle\Psi|_f \mathcal{H}_1 |\Psi\rangle_i$, of each transition times the density of final states $\rho(E_f) = \delta(E_f - E_i)$ for a tunneling process in which the energy is conserved:

$$W_{fi} = \frac{2\pi}{\hbar} |\langle\Psi|_f \mathcal{H}_1 |\Psi\rangle_i|^2 \delta(E_f - E_i). \tag{3.17}$$

To solve this equation we employ the Kondo exchange Hamiltonian $\mathcal{H}_1$ and the eigenstates $|\psi\rangle$ and $S = 1$ operators $\boldsymbol{S}$ from $\mathcal{H}_0$. Furthermore, we need to consider the states of the tunneling electrons $|\phi\rangle$ and their operators $\boldsymbol{\sigma} = (\sigma_x, \sigma_y, \sigma_z)^T$ from equations 3.15 and 3.16:

$$|M_{fiea}|^2 \propto |\left\langle \psi_f, \phi_e \right| \boldsymbol{\sigma} \cdot \boldsymbol{S} \left| \psi_i, \phi_a \right\rangle|^2 \tag{3.18}$$

$$M_{fiea} \propto \left\langle \psi_f, \phi_e \right| \boldsymbol{\sigma} \cdot \boldsymbol{S} \left| \psi_i, \phi_a \right\rangle . \tag{3.19}$$

For the total transition intensity we are taking all possible transitions, $\left|\phi\right\rangle_a \rightarrow \left|\phi\right\rangle_e$, of the tunneling electron into account that could cause the $\boldsymbol{S}$ transition from $\left|\psi\right\rangle_i$ to $\left|\psi\right\rangle_f$. In the m_z projection, four scenarios during the scattering event are possible for the tunneling electron:

$$|\uparrow\rangle \rightarrow |\downarrow\rangle \qquad |\uparrow\rangle \rightarrow |\uparrow\rangle \qquad |\downarrow\rangle \rightarrow |\downarrow\rangle \qquad |\downarrow\rangle \rightarrow |\uparrow\rangle . \tag{3.20}$$

Together with the three initial and final eigenstates of the CoH $S = 1$ system we are summing over all possible combinations and get the total transition probability, $|M_{fi}|^2$, for each transition:

$$|M_{fi}|^2 = \sum_{e=1}^{2} \left(\sum_{a=1}^{2} |\left\langle \psi_f, \phi_e \right| \sigma \cdot S \left| \psi_i, \phi_a \right\rangle|^2 \right). \tag{3.21}$$

Since the statistical probability of being in a $|\uparrow\rangle$ or $|\downarrow\rangle$ state are equal for the electrons in the sample and the tip we can assign a probability of $p_a = p_e = 1/4$ to each scattering event:

$$|M_{fi}|^2 \propto \sum_{a,e=1}^{2} p_e p_a \underbrace{\left(|\left\langle \psi_f, \phi_e \right| (\sigma_x S_x + \sigma_y S_y + \sigma_z S_z) \left| \psi_i, \phi_a \right\rangle|^2 \right)}_{\substack{= |\langle \psi_f | S_x | \psi_i \rangle \langle \phi_e | \sigma_x | \phi_a \rangle|^2 \\ + |\langle \psi_f | S_y | \psi_i \rangle \langle \phi_e | \sigma_y | \phi_a \rangle|^2 \\ + |\langle \psi_f | S_z | \psi_i \rangle \langle \phi_e | \sigma_z | \phi_a \rangle|^2}} \tag{3.22}$$

in which $\boldsymbol{S}$ and $\boldsymbol{\sigma}$ act on different subsystems and can be separated for a better guide to the eye. With this we can calculate all possible transitions M_{fi}. In inelastic electron tunneling spectroscopy the electron needs at least the energy of the final state $\left|\psi\right\rangle_f$ to cause an excitation. Since the applied bias voltage V_B determines the electron's energy we are now able to plot the resulting conductance versus the applied bias voltage V_B between tip and sample when we sum over all possible matrix elements with their statistical probability of being in the $S = 1$ initial and final state, p_f and p_i, defined in the earlier subsection, and integrate over the energies:

$$\frac{\mathrm{d}I}{\mathrm{d}V} \propto \int_0^{eV} \sum_{i,f=1}^{3} (1 - p_f) p_i |M_{fi}|^2 \delta(E_f - E_i + \epsilon) d\epsilon. \tag{3.23}$$

Note that an integrated delta Function ($\delta(E_f - E_i)$) yields the step function as seen in the differential conductance. To model the expected spectra we employ simulations done in a Scilab algorithm (see appendix A). These simulations are presented in figure 3.13 for the introduced CoH $S = 1$ system with magnetic anisotropy in zero magnetic field and in 10 T. In this graphi-

M_{fiea}	$\lvert\psi\rangle_1$		$\lvert\psi\rangle_2$		$\lvert\psi\rangle_3$	
$\lvert\psi\rangle_1$	$\boldsymbol{M_{1111}}$	$\boldsymbol{M_{1112}}$	M_{1211}	M_{1212}	M_{1311}	M_{1312}
	$\boldsymbol{M_{1121}}$	$\boldsymbol{M_{1122}}$	M_{1221}	M_{1222}	M_{1321}	M_{1322}
$\lvert\psi\rangle_2$	$\boldsymbol{M_{2111}}$	$\boldsymbol{M_{2112}}$	M_{2211}	M_{2212}	M_{2311}	M_{2312}
	$\boldsymbol{M_{2121}}$	$\boldsymbol{M_{2122}}$	M_{2221}	M_{2222}	M_{2321}	M_{2322}
$\lvert\psi\rangle_3$	$\boldsymbol{M_{3111}}$	$\boldsymbol{M_{3112}}$	M_{3211}	M_{3212}	M_{3311}	M_{3312}
	$\boldsymbol{M_{3121}}$	$\boldsymbol{M_{3122}}$	M_{3221}	M_{3222}	M_{3321}	M_{3322}

Table 3.4: Transition matrix elements. The matrix elements, M_{fiea}, that govern the transition between the three inital, $|\psi\rangle_i$, and final, $|\psi\rangle_f$, eigenstates of the CoH $S = 1$ system plus the submatrices that include the tunneling electron scattering from states, $|\phi\rangle_a$ to $|\phi\rangle_e$. The total number of matrix elements, $36 = 3 \cdot 3 \cdot 2 \cdot 2$, is equal to the total number of sum elements in equation 3.21 and 3.23 and proportional to the total differential conductance at a given bias voltage. At low temperatures of around 1 K and without any pumping effects, only the left third of the matrix (bold M_{f1ea} elements) will contribute to the total transition rate as only the groundstate $|\psi\rangle_1$ is thermally occupied as the initial state.

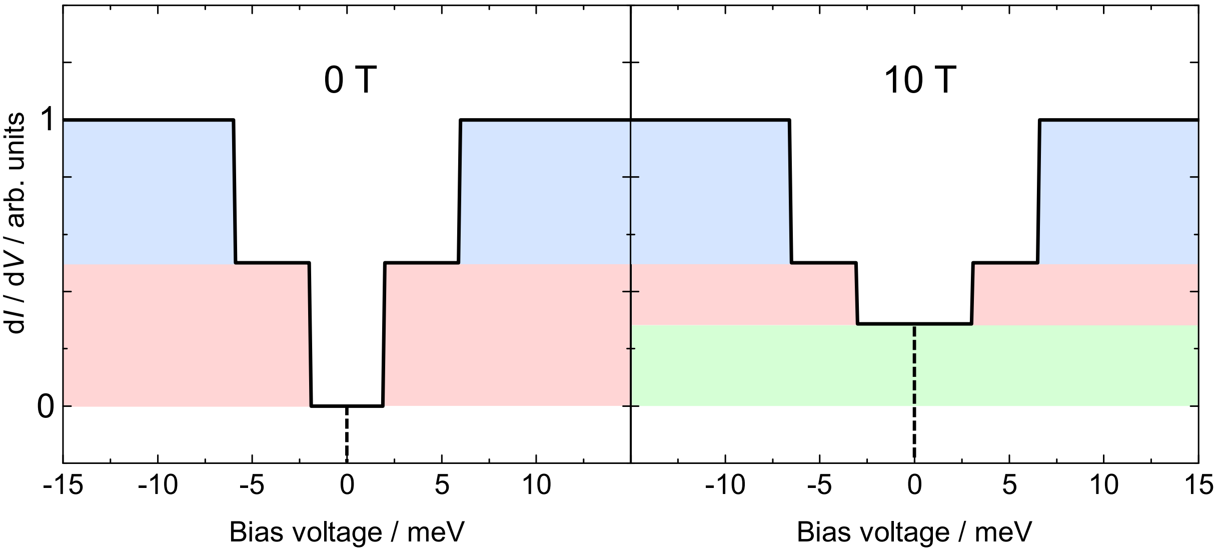

Figure 3.13: Left: Simulated differential conductance for a CoH $S = 1$ system with magnetic anisotropy of D = -5 meV and E = 1 meV at 0 K. Right: Same system with an applied magnetic field B_z = 10 T. The eigenvalues and eigenstates were already calculated in the earlier subsections when the magnetic anisotropy energy was introduced. These graphs were simulated according to the total sum of the matrix elements in table 3.4. Up to the first transition at around 2 meV, the tunneling electron can only scatter the groundstate of the $S = 1$ system (green elements). When the tunneling has enough energy to excite the first eigenstate of the $S = 1$ system, additional matrix elements that govern this transition are added to the total differential conductance (green + red elements). The same for the second excitation at around 6 meV at which the sum includes all possible matrix elements (green + red + blue). From this simulation we can observe the Zeeman shift of the eigenenergies but also and more importantly, the decrease of first excitation transition intensity (red elements) and an onset of the ground state scattering (green elements).

cal representation we can see how energy conservation comes into play. Each time the electron has enough energy to cause an inelastic excitation a stepwise increase in the conductance is visible and the introduced sum in equation 3.23 is only considered for the matrix elements with a high enough energy (see the color coded matrix elements in table 3.4). Furthermore, the magnetic field data shows how angular momentum conservation is important since the intensity of the first excitation is getting weaker, whereas the second one seems to be unaffected compared to the zero field data. This can be explained when the eigenstates in table 3.3 are taken into account. The magnetic field polarizes the ground state in a $m_z = -1$ and the first excited state into a $m_z = 1$ state. Thus, the mentioned selection rules now impose a change of $\Delta m_z = 2$ to cause an excitation. A single electron can only give $\Delta m_z = 0, -1$ or +1 and therefore this transition becomes less likely the more the spin is polarized by the magnetic field. This evolution with magnetic field is crucial to determine the spin of the spin system and the reason why be believe the CoH systems are indeed a $S = 1$ system.

Finally, the influence of the Fermi-Dirac distribution of states in tip and sample leads to a thermal broadening. The influence on the differential conductance step widths is modeled by a step function:

$$\Theta(x) = \frac{1 + (x-1)\mathrm{exp}(x)}{\mathrm{exp}(x)^2} \tag{3.24}$$

in which $x = (eV - E_{if})$ is the applied bias voltage at the energy positions of the steps. The influence of the temperature is shown in figure 3.14. The experimental temperature of around 1.1 K only leads to a marginal broadening and will be neglected in the upcoming 2nd order simulations to focus on the influence of the matrix elements.

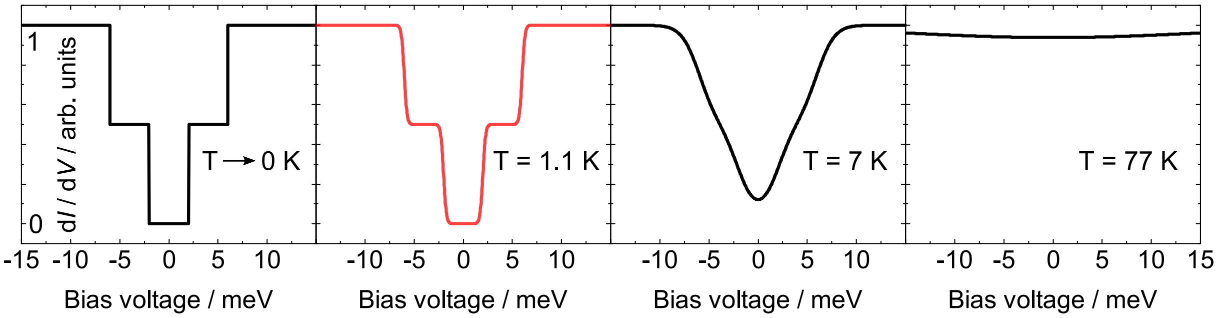

Figure 3.14: Influence of the temperature broadening on the calculated differential conductance. The magnetic signatures are only visible at temperatures < 5 K. At 7 K the steps are almost indistinguishable and completely smeared out at liquid nitrogen temperatures of around 77 K. The temperature in most experiments was around 1.1 K (red curve). Additional broadening of the steps in the real data might be due to a slightly different temperature in the tunnel junction or the short lifetime of the eigenstates.

3.4 Magnetic signatures of CoH_x

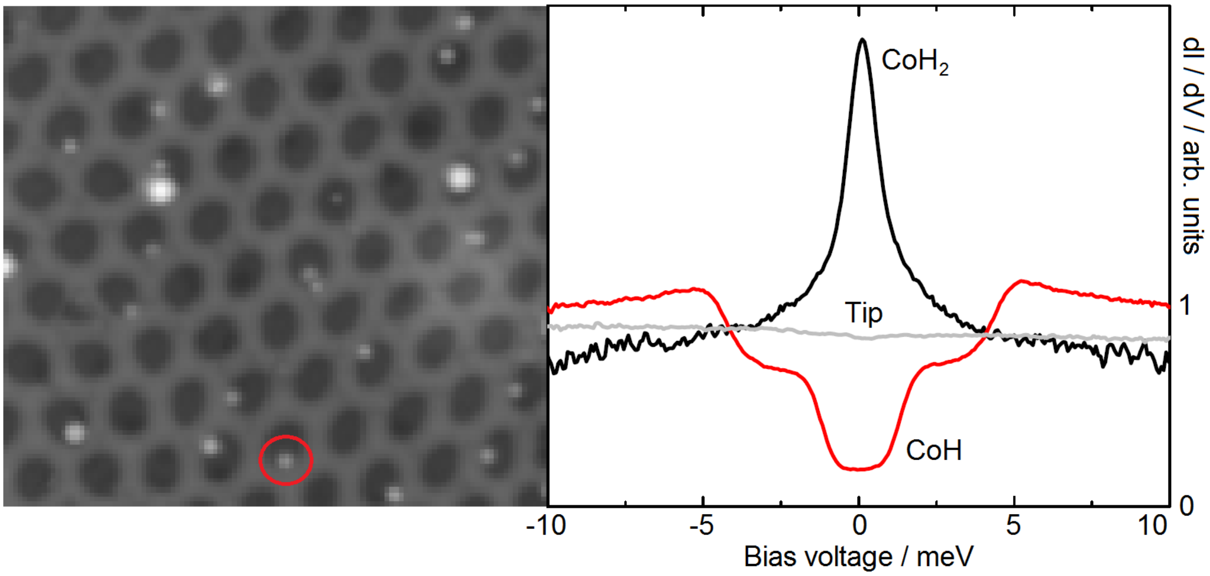

Figure 3.15: Main spectroscopic signatures of CoH_x systems at 1.1 K. A representative 25 nm x 25 nm STM constant current image of CoH_x systems on h-BN/Rh(111). The larger appearing atoms (almost 1 nm diameter) show no spectroscopic features within ± 100 meV. A smaller fraction (around 20 % of the smaller appearing atoms (red circle) typically show a $S = 1$ signature (red curve) while an even smaller fraction exhibits a $S = 1/2$ Kondo peak (black curve). The grey curve shows the background spectrum of a bare Pt tip on the h-BN/Rh(111) surface. All spectra were taken at an initial setpoint of I_T = 500 pA and V_B = -15 mV.

The CoH_x systems were probed with IETS according to the method introduced in subsection 3.3. The spectroscopy of a bare Pt tip on h-BN/Rh(111) together with the two most dominant spectra of CoH and CoH_2 are shown in figure 3.15. The STM overview image in the same figure shows a typical distribution of CoH_x systems. A difference in the topography of CoH and CoH_2 systems was not found as the adsorption site drastically changes the apparent height of the systems in each individual case.

The magnetic character of the two dominant systems is confirmed by measurements in magnetic field in which for a CoH_2 $S = 1/2$ system the Kondo resonance will split with a linearly increasing gap until the resonances cannot be sustained anymore due to a large energy gap between both states. For the CoH $S = 1$ system, the energies also shift according to the strength of the magnetic anisotropy parameters and the scattering intensities between the different eigenstates will change drastically due to the onset of selection rules in magnetic field.

3.4.1 CoH

The magnetic anisotropy originally splits the CoH $S = 1$ states to the energy levels shown in the simulated evolution in figure 3.16. It also shows, how an applied magnetic field, B_z, up to 14 T further shifts these states in energy employing the Zeeman Hamiltonian in equation 3.8 and diagonalizations in 0.1 T steps. Experimental datasets shown in figure 3.17 confirm this evolution of the system with magnetic field. The Zeeman shift in energy is clearly visible but also the decrease of the first excitation intensity as well as an increase in the ground state scattering intensity is present. Thus, this evolution of the spectra confirms the magnetic $S = 1$ character for the CoH systems.

While the majority of CoH systems are out-of-plane species with $D > 3E$ with the spin's easy axis in the z-direction, also in-plane CoH species are observed for which $D < 3E$ with an easy plane in the xy-plane.

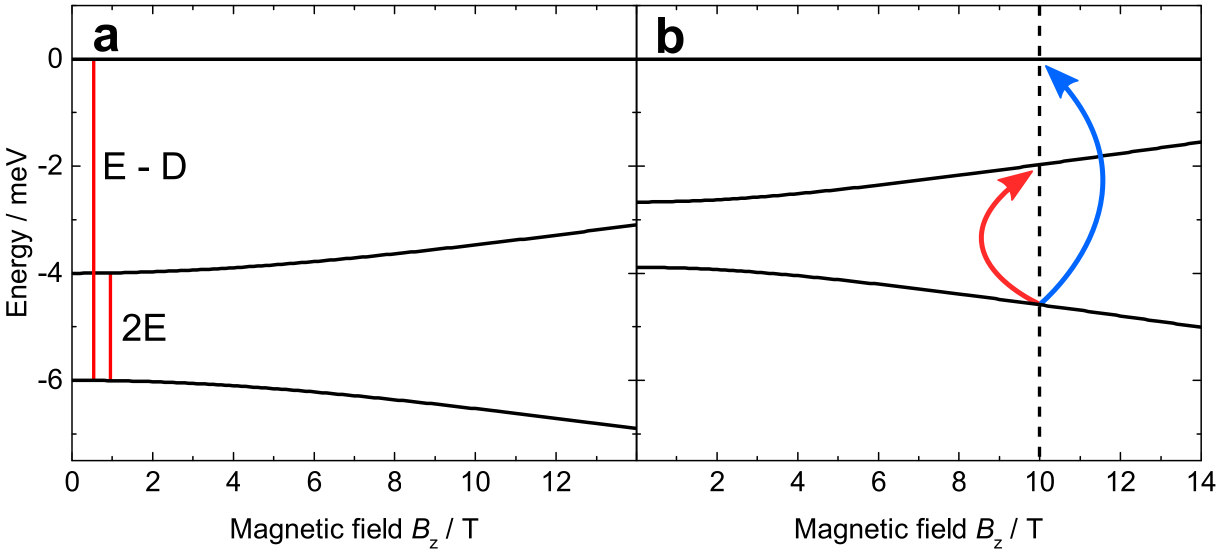

Figure 3.16: Energy evolution of the eigenstates of two different CoH $S = 1$ systems in magnetic field, B_z, from 0 T to 14 T. (a) The standard case with MAE: $D = -5$ meV and $E = 1$ meV that define the starting energies of the three eigenstates. Note that the energies here do not include an offset energy and that the groundstate is at -6 meV and not 0 meV. (b) For the experimental datasets in figure 3.17, the MAE parameters $D = -3.28$ meV and $E = 0.61$ meV are used. At B_z = 10 T, the excitations from the groundstate to the first excited state (red arrow) and from the groundstate to the second excited state (blue arrow) are highlighted. The energy gap that separates these states increased for both excitations in field and fits the simulation as shown in figure 3.17.

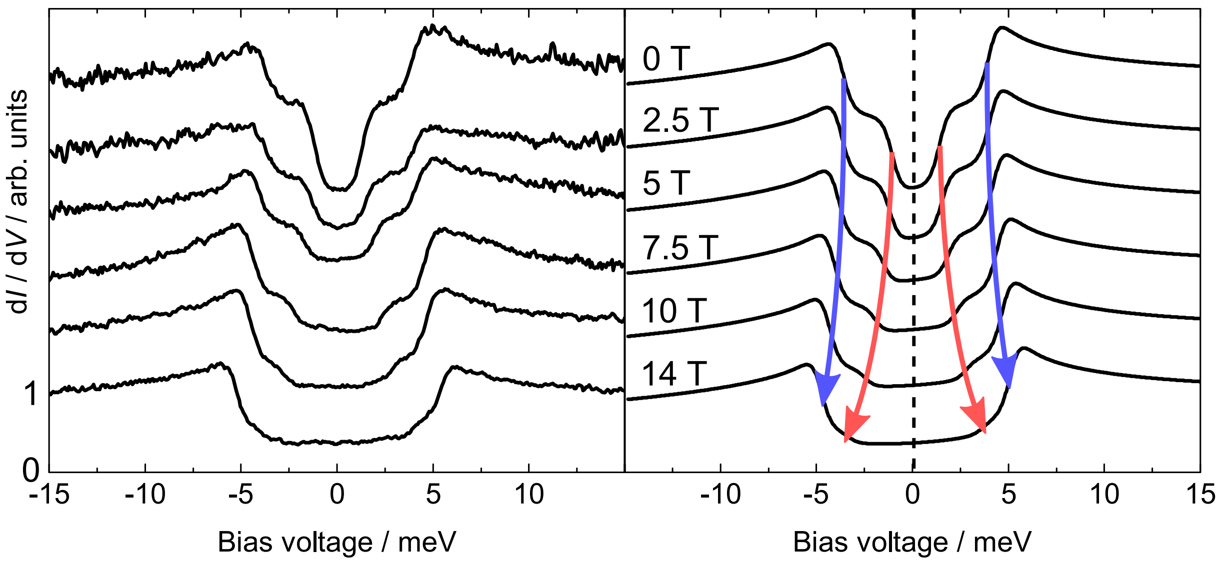

Figure 3.17: Experimental datasets and their simulations of a CoH $S = 1$ system in magnetic field. Left: Six spectra taken over the same CoH $S = 1$ system at 0T, 2.5 T, 5 T, 7.5 T, 10 T and 14 T. A second order fit to the 0 T spectrum determines the MAE parameters: $D = -3.28$ meV and $E = 0.61$ meV. Right: Second order simulations executed with the Scilab program from Dr. Markus Ternes at the same field strengths and with the same MAE parameters closely follow the experimental evolution of the spectrum. The arrows highlight the energy shifts of the two excitations similar to figure 3.16b where the excitation from the groundstate to the first excited state (red arrow) and the excitation from the groundstate to the second excited state are shown.

3.4.2 CoH$_2$ and the layman's view of a Kondo resonance

As the eigenstates and the resulting spectroscopic signatures of the CoH $S = 1$ systems have been introduced at length, this subsection will briefly introduce the Kondo signature of the CoH$_2$ $S = 1/2$ systems. The main ingredients for a Kondo resonance are: A degenerate groundstate of a spin system and a process that scatters between these states. This process is normally provided by the tunneling electrons that are injected into the spin system as it is the case for STS. Not only these electrons can scatter of the degenerate groundstate but also the substrate electrons that constantly scatter with the spin system regardless of an applied bias voltage.

The Kondo effect is widely known for bulk systems. A metal such as a solid Au block exhibits a high resistance at low temperatures if it contains a small percentage of magnetic impurities (e.g. Fe or Co) due to a large number of scattering events that hinder the overall transmission rate of a conduction electron [75]. This is true for transport experiments through a metal but how is this different for a tunnel junction? The conductance of an electron through a tunnel junction depends on the number of possibilities that lead to a transition. This means that if a localized magnetic impurity provides additional scattering events for a tunneling electron it will increase the tunnel probability and hence lead to a Kondo resonance that is a peak in the differential conductance.

A perturbation approach based on the Anderson-Appelbaum model [76] reproduces this behavior when the interferences between the different order contributions (see the next subsection) are taken into account. Summing over all transition intensities and integrating over the energy bandwith, ω_0, of the substrate electrons with the spin system leads to the observable differential conductance in STM experiments:

$$\frac{\mathrm{d}I}{\mathrm{d}V} \propto \rho_s(\epsilon_F) \int_{-\omega_0}^{\omega_0} \frac{g(\epsilon)}{\epsilon} \quad d\epsilon \tag{3.25}$$

in which the integration of ($1/\epsilon$) leads to the logarithmic lineshape of the Kondo resonance. However, this approach is only valid as long as the second order terms are small compared to other orders. When the second order term becomes as large as the first order term, the perturbation approach breaks down and other methods such as renormalization groups need to be employed. The characteristic energy at which this happens is defined by the Kondo temperature [77] that is approximated to

$$T_\mathrm{K} = \frac{\Gamma}{k_\mathrm{B}} \tag{3.26}$$

where Γ is the FWHM of the Kondo resonance at T = 0 K. Magnetic atoms on metal surfaces normally do not exhibit a symmetric Kondo resonance but an interference pattern that could be falsely interpreted as a dip. This is due to interference between two tunneling pathways, i.e. the Kondo scattering between tip and magnetic impurity and the direct tip-metal cross section. As in the case of the tuning fork and a harmonic oscillator, two resonances can lead to very different interferences depending on their relative contributions. In practice, these Kondo resonances are fitted to a Frota lineshape [78] that includes the interference between the Lorentzian and the constant part of the Kondo resonance and is in our case a good enough approximation. The $\mathrm{CoH_2}$ $S = 1/2$ systems are not subject to magnetic anisotropy and a twofold degenerate groundstate exists that can lead to a Kondo resonance. An applied magnetic field splits these states according to figure 3.18 and will lead to the destruction of the Kondo resonance as can be seen in the experimental datasets in figure 3.19.

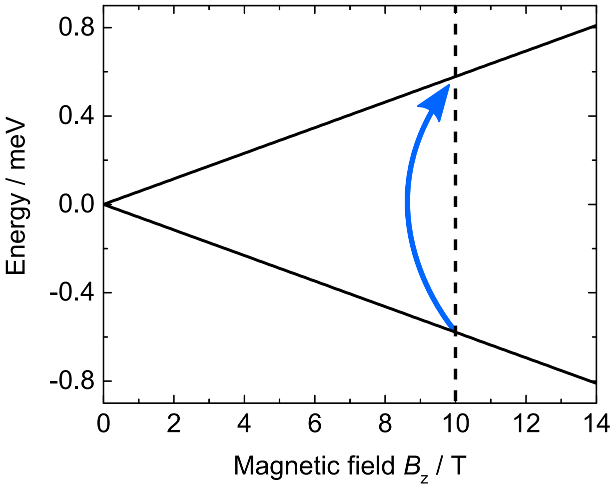

Figure 3.18: Energy evolution of the CoH$_2$ $S = 1/2$ system eigenstates in magnetic field. The originally degenerate states at 0 T are linearly split up to an energy gap of roughly $\Delta\epsilon \approx 1$ meV at 10 T that clearly leads to a groundstate and excited state permitting inelastic excitations (blue arrow) visible as steps in the differential conductance.

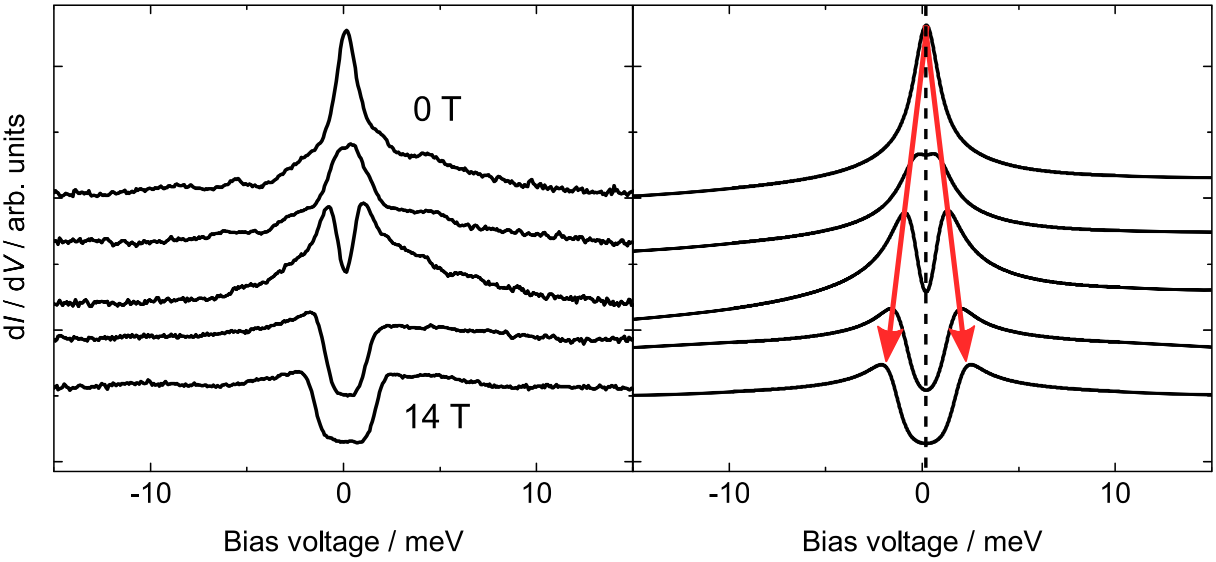

Figure 3.19: Experimental datasets and evolution of a CoH$_2$ $S = 1/2$ system in magnetic field. Left: The experimental spectra of the Kondo resonance at 0 T, 2.5 T, 5 T, 10 T and 14 / (from top to bottom). Right: The red arrows show the linear evolution of the split Kondo resonance. Even though the energy positions of the simulated Kondo resonance peaks fit the experimental spectra quite well, the strength of the individual Kondo resonances is overestimated in the simulations as the tunneling electrons are the cause of the Kondo resonance in the simulation. Since the tunneling elctrons will always have enough energy to bridge the energy gap due to their applied bias voltage energy, their relative scattering will not die down unlike the contributions from the substrate electrons.

3.5 Measuring the interaction with the environment: The Kondo coupling

Considering the experimental results, two important questions arise when we compare the acquired CoH $S = 1$ spectra to the transition rates given by first order perturbations: Where do the intensity peaks at the outer excitation steps originate from and why are the magnetic anisotropy energies different for every system? The Kondo resonance for the CoH$_2$ $S = 1/2$ introduced the second order contributions to the total transition rate and indeed, the peaks of the CoH $S = 1$ are related to the exact same perturbation.

The fits to the datasets in the CoH subsection were performed with a perturbation model that also includes second order contributions. The user-friendly Scilab code together with a fit routine that implements both orders with additional parameters such as possible Coulomb interaction was developed by Dr. Markus Ternes. While the familiar first order contributions only take direct transitions between real states into account:

$$W'_{fi} = \frac{2\pi}{\hbar} | \langle\psi|_f \mathcal{H}_1 |\psi\rangle_i |^2 \, \delta(\epsilon_f - \epsilon_i) \tag{3.27}$$

we can also expand to second order contributions that are mediated by an intermediate state, $|\psi\rangle_m$:

$$W''_{fi} = \frac{2\pi}{\hbar} \lambda \left| \sum_m \frac{\langle\psi|_f \mathcal{H}_1 |\psi\rangle_m \langle\psi|_m \mathcal{H}_1 |\psi\rangle_i}{\epsilon_i - \epsilon_m} \right|^2 \delta(\epsilon_f - \epsilon_i) \tag{3.28}$$

where $\lambda \propto J\rho_0$ is later defined as the interaction strength of the spin system with the substrate. Since in equation 3.28 two probabilities are multiplied, the resulting transition rate will be much smaller compared to the first order one. However, also virtual intermediate states lead to a possible transition from a real initial to a real final state of the spin system. Now, as the tunnel junction is strongly located in all dimensions we specifically consider the interferences between the first and second order terms for the overall transition probabilities, thus leading to additional third order terms when the fourth order terms are neglected:

$$W_{fi} \propto \left(|M_{fi}|^2 + \rho_0 J \sum_m \left(\frac{M_{mi} M_{fm} M_{if}}{\epsilon_i - \epsilon_m} \right) \right) \delta(\epsilon_f - \epsilon_i) \tag{3.29}$$

where the matrix elements M include the eigenstates of the $S = 1$ system and the tunneling electrons. Not only the overall transition rate is enhanced but also the energies of the eigenstates are renormalized and can be approximated in terms of the MAE parameters, D and E, as:

$$D(J\rho_s) \approx D_0(1 - \alpha(J\rho_0)^2) \qquad E(J\rho_s) \approx E_0(1 - \beta(J\rho_0)^2) \tag{3.30}$$

where α and β depend on the energy bandwidth, ω_0, of the Kondo exchange interactions and are derived from the integration over all possible final state energies as shown in [19]. We estimate ω_0 between 0.4 eV and 1.2 eV.

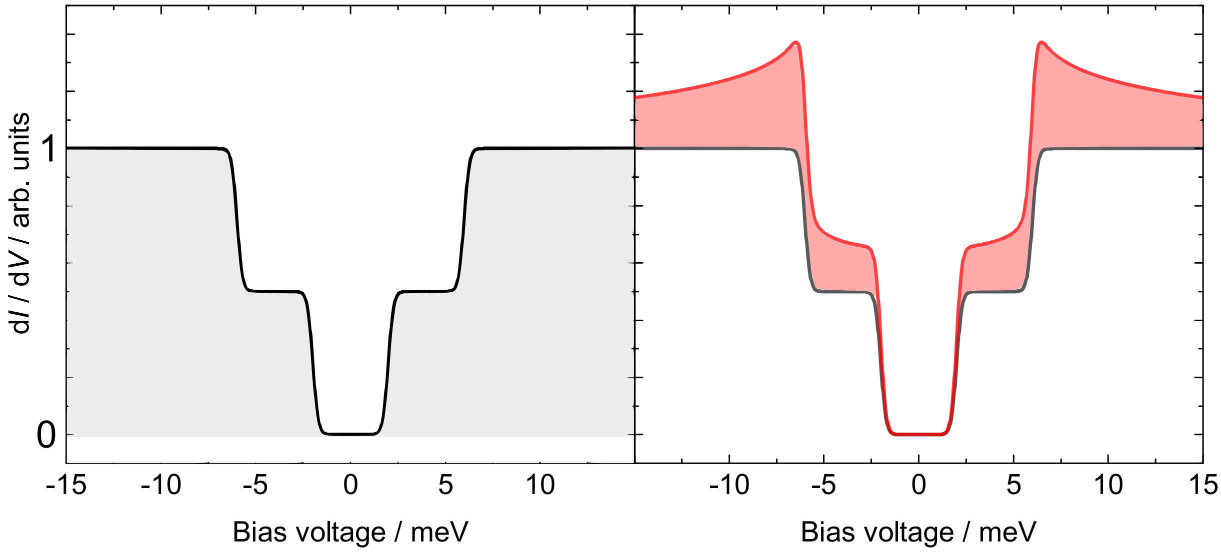

Figure 3.20: Third order contributions for a CoH $S = 1$ system with $D = -5$ meV and $E = 1$ meV at 1.1 K. Left: Contribution to the differential conductance (grey shaded area) only using second order terms. Right: The matrix elements of the third order calculation (red shaded area) with $J\rho_0 = -0.1$ add up to the second order matrix elements and lead to the characteristic peaks at the second excitation step around -6 meV and +6 meV. Note that the energy positions of the two steps have slightly shifted to smaller energies.

With the magnetic anisotropy being responsible for the eigenstate energies of the spin system, the third order contributions due to the Kondo exchange with the substrate electrons can fine-tune these energies. An analogy with an harmonic oscillator helps to clarify the energy renormalization [79]. When a free harmonic oscillator with mass, m, and spring constant k, is displaced from its equilibrium position, it will oscillate with its well known eigenfrequency, $f_0 \propto \sqrt{(k/m)}$. If this motion is subject to friction such as oscillating in air, the eigenfrequency shifts to lower energies and the amplitude gets damped. A microscopic picture that takes every air molecule and its interaction with other molecules as well as the rough oscillator's surface area into account would be far too complicated to compute. Thus, this damping is described with a general dissipative bath that leads to an energy renormalization. In quantum mechanical systems, these energy corrections can be quantified by a broadening and a shift in energy of the system's eigenstates. In our case, the CoH $S = 1$ eigenstates that are subject to an interaction with the electron bath of the substrate will experience this broadening and energy shift as shown in figures 3.20, 3.21 and 3.22.

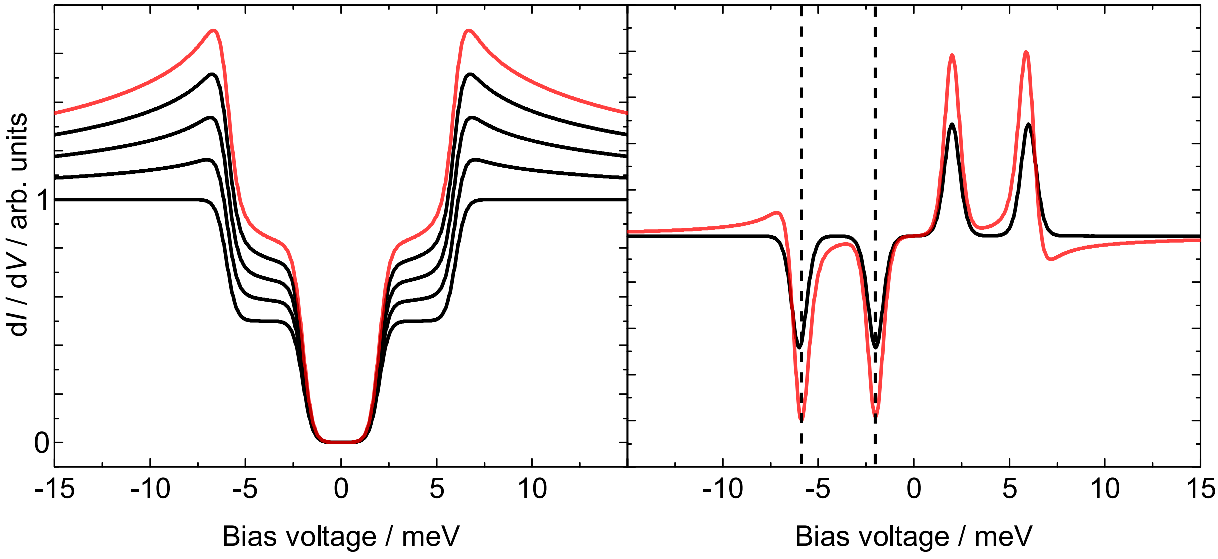

Figure 3.21: Simulation of increasing the Kondo coupling from $J\rho_s$ = 0 (lower black curve) to a realistic value of $J\rho_s$ = -0.2 for a CoH $S = 1$ system with $D = -5$ meV and $E = 1$ meV at 2 K. Not only the overall differential conductance increases together with the Kondo coupling strength but also the step positions shift in energy. A derivative of the curves highlights the energy shifts: The original system's outer energy step position was at -6 meV according to table 3.2 for the example spin system. A Kondo exchange coupling of $J\rho_0$ = -0.2 has shifted this energy position to -5.81 meV. The outer step is shifted to lower energies (in this case by around 3%).

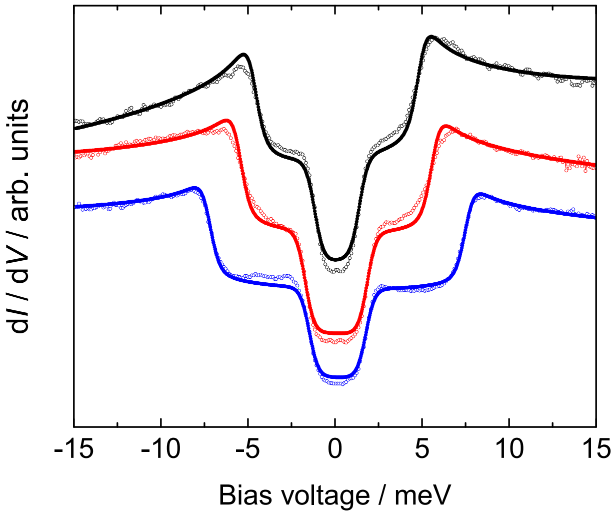

Figure 3.22: Three experimental spectra and their third order fits. The higher the coupling to the substrate the smaller the magnetic anisotropy energies: From low coupling of $J\rho_s$ = -0.11 and D = -6.58 meV (blue curve), to an intermediate coupling of $J\rho_s$ = -0.15 and D = -4.66 meV (red curve) to a strong coupling $J\rho_s$ = -0.27 and D = -4.13 meV (black curve).

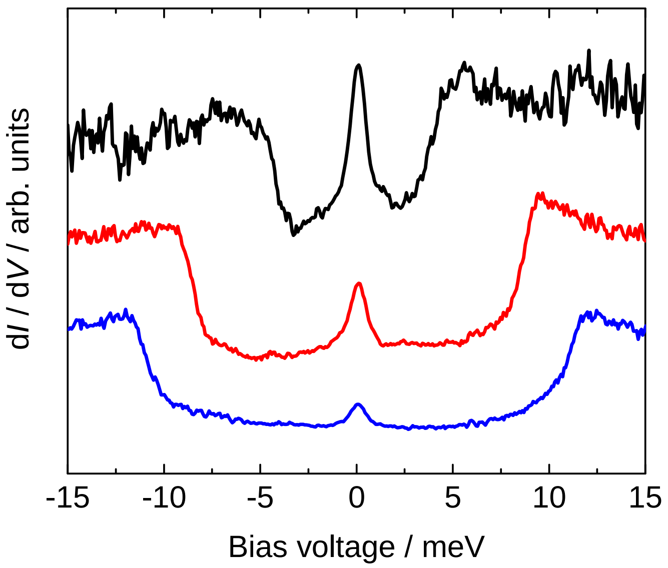

Figure 3.23: Co atoms on h-BN/Rh(111) at 1.3 K with $S = 3/2$ signatures. Similarly to the results of Oberg *et al.* presented in figure 3.24, the intensity of the Kondo resonance is correlated with the energy position of the step excitations. The blue spectrum shows rather large excitation energies around $|V_B|$ = 10 meV and a low intensity Kondo resonance, whereas the black spectrum shows small excitation energies around $|V_B|$ = 4 meV and a high intensity Kondo resonance. Spectra are offset for better visualization.

3.6 Discussion

This chapter has shown the magnetic signatures of CoH_x systems on h-BN/Rh(111) and determined their coupling strength to the Rh substrate that is fine-tuning the magnetic anisotropy parameters. While the magnetic origins are evident due to measurements in magnetic field, the reasons that could lead to different spin systems are experimentally not well defined. We rely on DFT support to determine the adsorption positions of the CoH_x systems and the number of hydrogen atoms attached to a Co atom that change the overall magnetic moment. This makes it difficult to determine the exact reason for the broad distribution of different values for the magnetic anisotropy of the CoH systems and their Kondo coupling strength to the substrate. The shift between the h-BN lattice and the underlying Rh(111) lattice as well as local strain or defects such as CO could be responsible for these broad changes. The simplest solution would be to correlate the distance of the CoH complex to the Rh(111) surface with its Kondo exchange strength but the experimental datasets show that there is no significant correlation (compare the two CoH systems displayed in figure 4.9 and 4.10 of the next chapter which yield the opposite trend for their magnetic anisotropy energies). As seen in our experiments the CoH atoms do not prefer the high symmetry points of the h-BN layer used for the DFT calculations but rather the regions in between, i.e. the ring boundary of the pores. This could be the reason for a plethora of different out-of and in-plane species as well as different crystal field parameters. Even for well defined systems such as Co atoms on a flat Cu_2N/Cu(001) surface [80] or on G/Ir(111) [81], it remains difficult to pin down the exact cause for the change in magnetic anisotropy and the Kondo coupling to the substrate. Figure 3.24 shows these datasets that are similar to our observations of Co atoms on h-BN/Rh(111) shown in figure 3.23. In their experiments, the distance of the Co atom to the edge of the decoupling island seems to correlate with the intensity of the Kondo resonance and hence the Kondo coupling to the Cu(001) substrate.

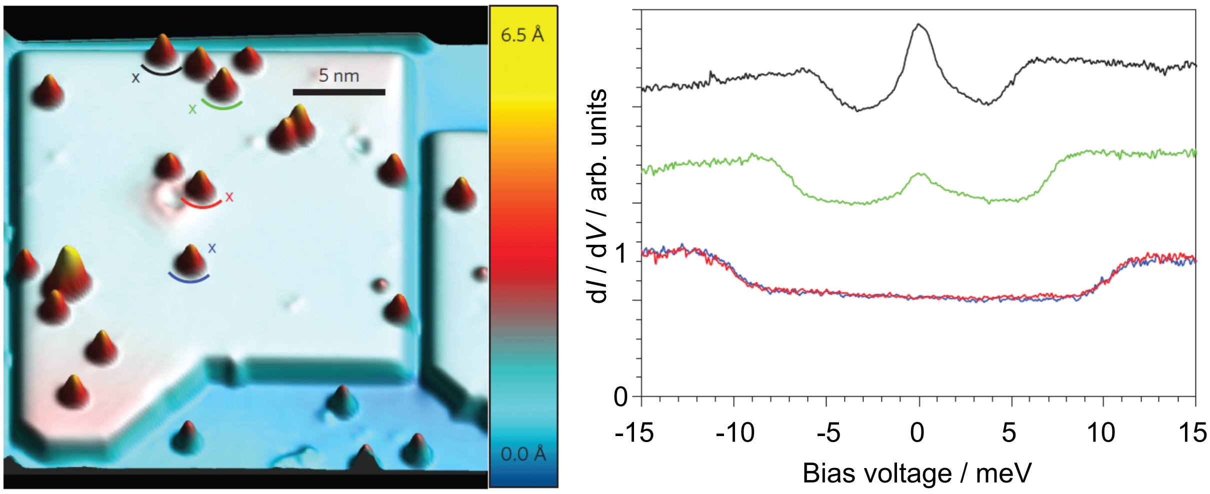

Figure 3.24: Topography (V_B = 100 meV and I_T = 100 pA) and spectroscopy of Co $S = 3/2$ atoms on a Cu_2N island on Cu(001) at 2.5 K. The color coded arcs around the Co atoms indicate the spectra on the right that were taken over these atoms. The further the atom is away from the island's edge the more pronounced the Kondo peak and the lower the inelastic spin excitation steps. Images adapted from [80] that presented similar results as in [19]. Adapted by permission from Macmillan Publishers Ltd: Nature Nanotechnology [80], copyright (2013).

CHAPTER 4

FORCE MEASUREMENTS

This chapter will introduce the AFM function of the qPlus-design complementary to its STM capabilities. It will describe how the frequency shift of the tuning fork oscillation can be used to derive topographic information as well as approach and retract curves on the surface and on single atoms and molecules. Background subtraction and a deconvolution of the frequency shift as well as the current signal are necessary to calculate the force and current datasets. We found that the spatial corrugation of the h-BN decoupling layer is strongly influencing the force signals when an adsorbed CoH system is approached or imaged.

4.1 Obtaining the frequency shift and forces

4.1.1 Frequency modulation AFM and force contributions

Frequency modulation atomic force microscopy (FM-AFM) tracks the frequency change of the tuning fork oscillation to derive the forces acting on the tip-sample junction [82]. The forces that lead to a frequency shift of the tuning fork oscillation can be grouped into short-range (< 1 nm) and long-range (> 1 nm) contributions with their relative tip-sample distances schematically shown in figure 4.1a. A short explanation is given in the same order as the range of the forces.

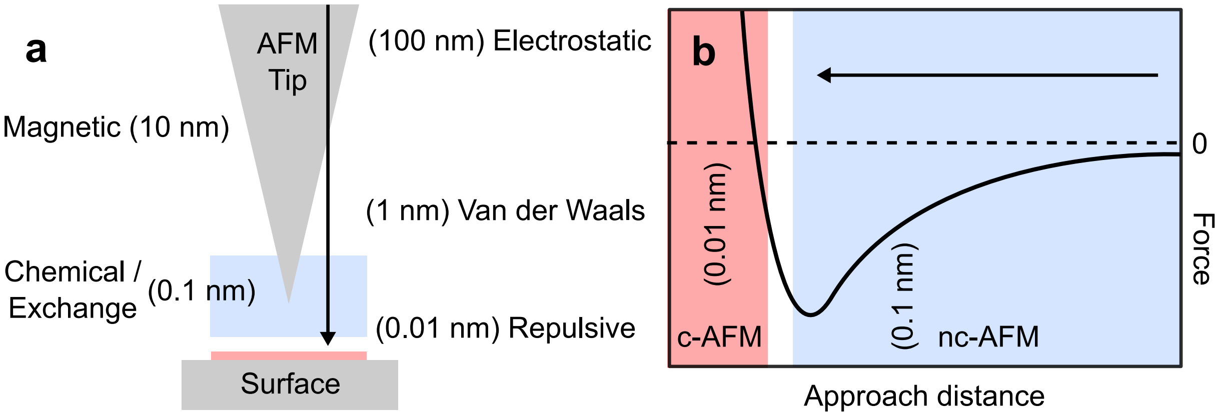

Figure 4.1: Schematic view of long and short range forces acting between tip and sample surface. (a) The red and blue shaded areas highlight the regions of interest for STM experiments at tip-sample distances of several hundreds of pm. The Lennard-Jones potential in (b) shows the typical force landscape in which forces below zero are attractive (non-contact AFM) and above zero are repulsive (contact AFM).

The most common long-range force is the **electrostatic force**, F_{el}, due to the capacitance, C, between tip and sample with an applied bias voltage V_B. It is approximated by taking the derivative with respect to the tip-sample separation distance, z, of the electrical energy ($E = 1/2CU^2$) with $U = V_B - \frac{\Delta\phi}{e}$ [83]:

$$F_{el} = -\frac{\partial}{\partial z}\frac{1}{2}CU^2 = -\frac{1}{2}\frac{dC}{dz}\left(V_B - \frac{\Delta\phi}{e}\right)^2 \tag{4.1}$$

where $\Delta\phi$ is the local contact potential difference between tip and sample and C depends on the geometry of tip and sample. This dependence of the force, i.e. frequency shift in AFM experiments, on the applied bias voltage allows the determination of local contact potential differences in Kelvin Probe Force Microscopy [84] [85].

The **magnetic force**, F_{mag}, between a magnetic sample and tip is used for magnetic force microscopy [86] and can be described with $\boldsymbol{m}$ as the magnetic moment of the tip and $\boldsymbol{H}$ as the stray magnetic field of the sample:

$$F_{mag} = \mu_0 \cdot \boldsymbol{m}(\nabla \boldsymbol{H}), \tag{4.2}$$

where μ_0 is the magnetic constant.

Van der Waals forces can be divided into different contributions [87]: dipole-induced exchange with a non-polarized object (Debye), exchange between permanent dipoles (Keesom) and exchange induced by charge-fluctuations (London) which is normally referred to when van-der-Waals interactions are mentioned. The geometry of the relative electrodes strongly determines the force characteristics, for example the van der Waals force between two single atoms scales with $1/z^7$ while the force between two surfaces scales with $1/z^3$ [87].

Chemical forces can lead to chemical bonds at sufficiently short ranges. They include covalent, metallic or ionic bonds and also van-der-Waals contributions [88].

Pauli repulsion forces stem from the Pauli exclusion principle which forbids for two identical fermions to occupy the same space, i.e. the same quantum state, at the same time. It is phenomenologically approximated with a range of $1/z^{12}$ as part of the Lennard-Jones potential shown in figure 4.1b.

The typical tip-sample distances, z, in STM are of the order of several hundreds of pm for which mainly repulsive (Pauli exclusion principle, $z < 0.01$ nm) and chemical or exchange ($z \approx 0.1$ nm) up to van der Waals forces ($z > 1$ nm) are of interest. A frequency sweep that determines the center frequency, f_0, of the tuning fork as shown in chapter two is performed at sufficiently large tip-sample distances (> 100 nm) to define a reasonable zero frequency for the frequency shift Δf. When the tip is now brought into the tunneling regime, the STM feedback loop is turned off and a $\Delta f(z)$ curve can be taken by slowly moving the tip towards the sample by several hundreds of pm and bringing it back to the original tunneling setpoint position. The shape of such a $\Delta f(z)$ curve normally follows a curve similar to the one sketched in figure 4.1b. To ensure a fast and reliable tracking of the frequency shift change during the tip approach and retract curves, an AFM feedback loop is employed that keeps track of the amplitude and the phase change. The amplitude oscillation is kept constant while the phase shift ensures a reliable tracking of the frequency shift by directly comparing the phase of the excitation voltage frequency output to the phase of the amplified tuning fork oscillation frequency input.

4.1.2 Deconvolution

The frequency shift and ultimately the force largely depend on the contributions from the tip. Depending on the composition and shape of the tip apex (up to several tenths of nm) the long-range force contributions can vary for each tip. Therefore, we take two different sets of $\Delta f(z)$ approach curves: One over the system of interest, in this chapter for example a CoH system, and one over the bare h-BN/Rh(111) surface at the same height. The two curves are then subtracted from each other to minimize the influence of the long range forces which can be assumed to be equal in both measurements. An example is shown in figure 4.2 and 4.3 where a CoH system was approached with a bare Pt tip. For the approach curves, the tip is stabilized over the center of the atom at a setpoint conductance of V_B = -15 mV and I_T = 20 pA. The STM feedback loop is then turned off and the tip is slowly ($\approx$ 20 pm / s) moved towards the sample by roughly 300 pm after which it is retracted by over 1 nm. The tip is then moved to an empty valley region over the h-BN/Rh(111) while the STM feedback loop is still turned off and the same approach and retract curve is taken. To check if the tip contributions are fully taken into account these two frequency shift curves should match at large relative distances so that the difference becomes zero. The example in figure 4.3 shows that this is already the case near the starting position of around 300 pm.

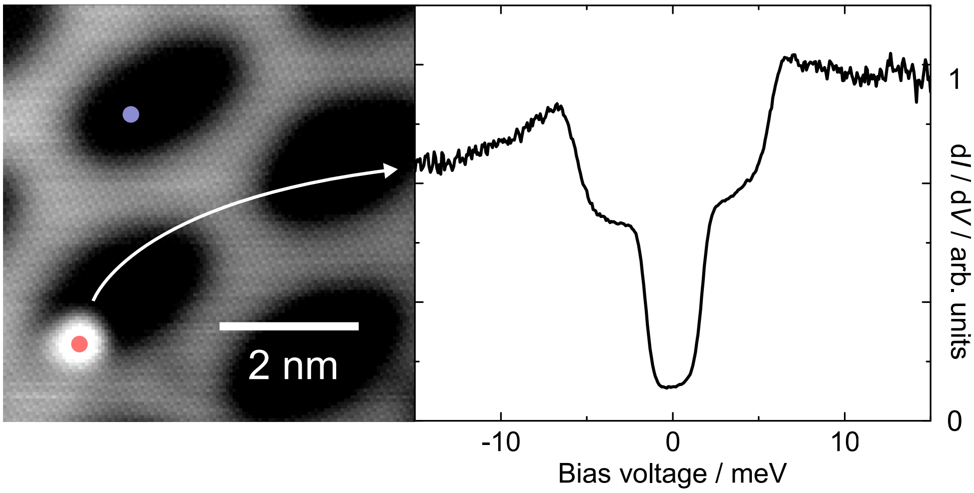

Figure 4.2: Example of a CoH $S = 1$ system adsorbed on h-BN/Rh(111) at 1.1 K. The STM constant current image (V_B = -15 mV and I_T = 20 pA) shows the position of the CoH complex at which the differential conductance spectrum (red dot) shown on the right and the approach and retract curves (red and blue dots) shown in the next figure were taken.

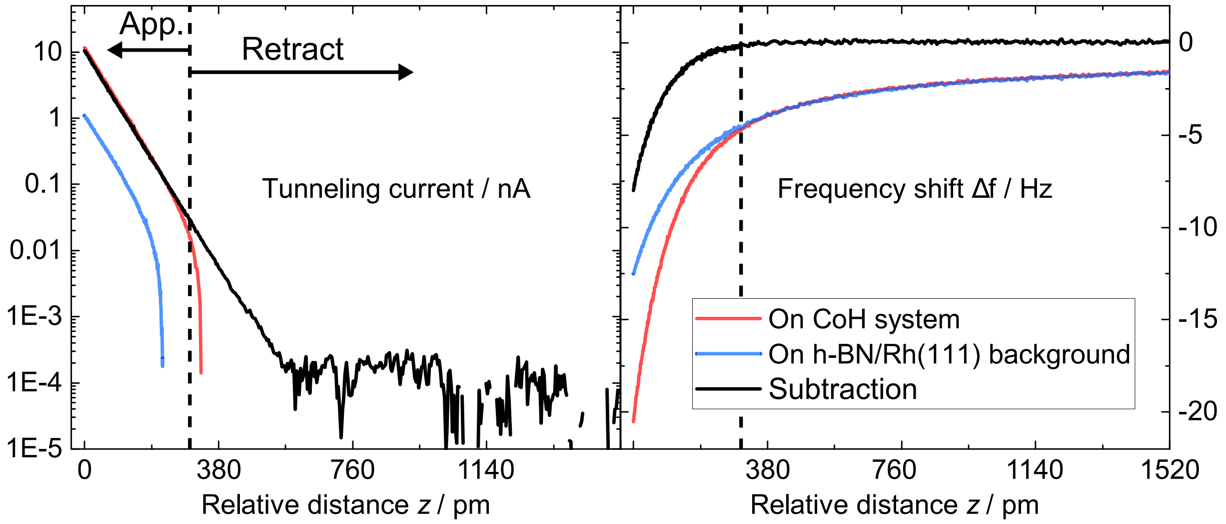

Figure 4.3: Approach and Retract curves over the CoH system shown in figure 4.2. The STM tip is stabilized at a conductance setpoint of -15 mV and 20 pA over the center of the CoH system (red dot). The STM feedback loop is then turned off, the gain of the Femto amplifier changed to 10^8 V/A and spectroscopy is performed by approaching the CoH atom by 300 pm and then retracting by over 1000 pm. To account only for the short range forces the blue curve is subtracted form the red curve and should result in a short range curve that approaches zero within a few 100 pm as it is the case here.

The subtracted frequency shift and tunneling current approach curves need to be further processed to yield the force and tunneling current without the convolution of the tuning fork oscillation. The force is not directly proportional to the observed frequency shift but rather to the average force gradient for which the tuning fork oscillation is the dominant perturbation especially for larger amplitudes. To calculate the force, a deconvolution method was developed by Sader and Jarvis [89] in a closed analytical form:

$$F(z) = \frac{2k}{f_0} \int_z^{\infty} \left[\left(1 + \frac{\sqrt{A}}{8\sqrt{\pi(t-z)}} \right) \Delta f(t) - \frac{A^{3/2}}{\sqrt{2(t-z)}} \frac{\mathrm{d}\Delta f(t)}{\mathrm{d}t} \right] \mathrm{d}t \qquad (4.3)$$

where k is the stiffness (1800 N/m), f_0 the center frequency (29077 Hz) and A the oscillation amplitude (50 pm - 150 pm) of the tuning fork. The frequency shift, Δf, is given in discrete data points (1 point for each pm) making it suitable for the application of the trapezoidal rule for the integration and the derivation is replaced by its difference quotient. This approach together with a comparison of the Sader-Jarvis method with the matrix method is shown in [90]. For the datasets used in this thesis we employ a Scilab script that is shown in appendix B. A similar deconvolution can be performed for the tunneling current. We compare the tunneling current approach with and without tuning fork oscillation in chapter six.

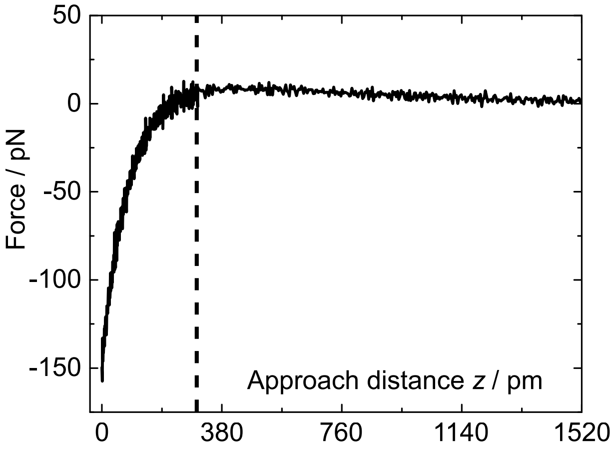

Figure 4.4: Deconvoluted force. Acquired from the subtracted frequency shift in figure 4.3 according to equation 4.3 and implemented in the Scilab algorithm shown in appendix B.

4.2 Force-distance curves on CoH systems

Approach and retract curves taken over CoH_x systems on h-BN/Rh(111) are subject to the lateral and vertical stiffness of the h-BN decoupling layer. Previous work [91] has shown that the large corrugation of the h-BN monolayer yields stiffnesses of around 1 N/m. To get a first understanding of CoH systems on this ultrasoft decoupling layer, we can use the AFM not only for approach and retract curves but also for constant height topography in which the frequency shift value is averaged for every image pixel as shown in figure 4.5.

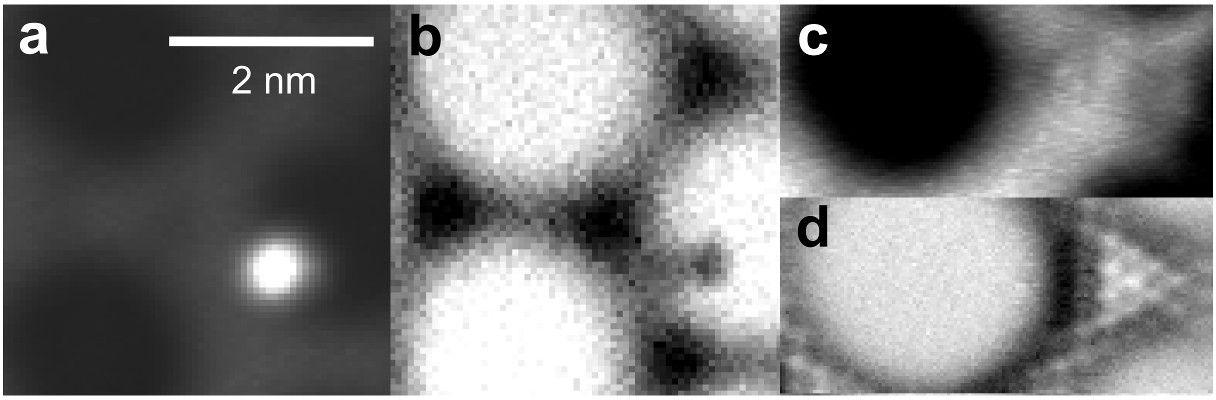

Figure 4.5: Simultaneous constant height STM and AFM topographies. The tip was stabilized at the top left corner near the rim region of the h-BN layer at setpoint parameters: I_T = 20 pA and V_B = -15 mV before the I_T feedback loop was disabled. (a) Raw tunneling current signal (From 145 pA (white) to 5 pA (black)) (b) Raw frequency shift signal (Ranging from -2.8 Hz (white) to -6 Hz (black).I_T (c) and Δf (d) signals after approaching by 100 pm to uncover the h-BN hexagons (from 400 pA (white) to 100 pA (black) and -4 Hz (white) to -13 Hz (black).

The constant height AFM images in figure 4.6 show that CoH$_x$ systems scanned at different tip sample distances allow to visualize the underlying h-BN lattice structure when reaching the Pauli repulsion regime. Unfortunately, moving the tip closer than 250 pm in z leads to strong tip interactions and dislocation of the CoH$_x$ systems as shown in figure 4.7. The influence of the adsorption site of a CoH system on h-BN/Rh(111) is shown for three representative $I(z)$ and $\Delta f(z)$ approach curves in figures 4.7 to 4.10 for three different CoH systems. The valley or rim regions of the corrugated h-BN layer lead to different force signatures likely due to the stiffness of the h-BN.

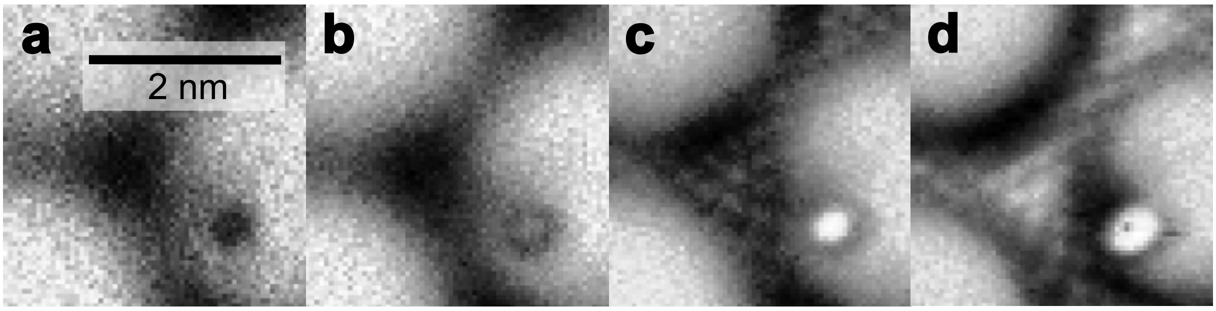

Figure 4.6: AFM constant height topography of the CoH system in figure 4.5 for different tip-sample distances. (a) The setpoint parameters (I_T = 20 pA and V_B = -15 mV) in the top left corner near the valley region define the starting distance. For each image in (b), (c), and (d) the tip is moved closer by 50 pm amounting to a total distance of 200 pm. The frequency shift range is color coded from black to white: ((a): -6 Hz to -2.1 Hz, (b): -8.9 Hz to -2.7 Hz, (c): -11.4 Hz to -2.1 Hz, (d): -13.9 Hz to -2.7 Hz).

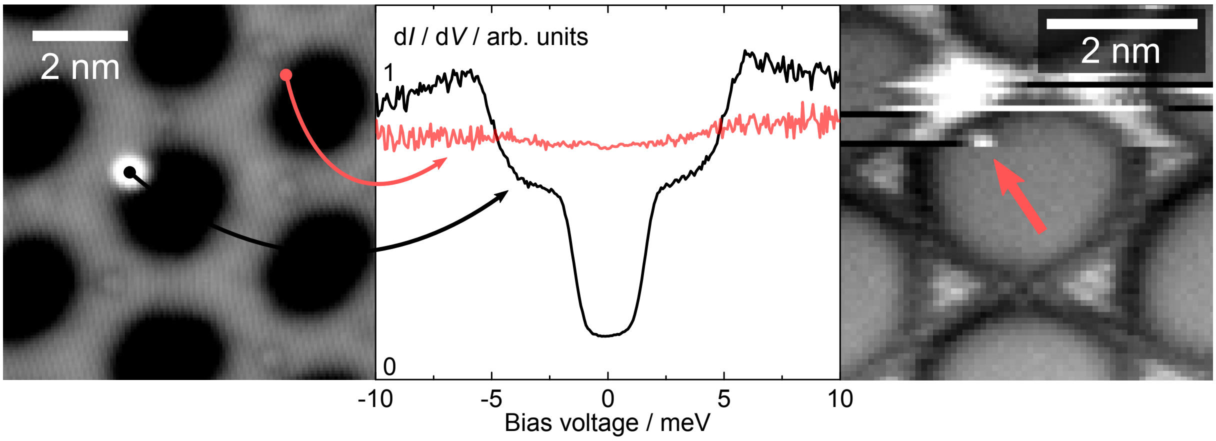

Figure 4.7: CoH adsorbed near the rim region of the h-BN layer. Left: Constant current STM image (I_T = 20 pA and V_B = -15 mV). Middle: The spectra taken over the CoH system (black) and a similar h-BN background (red) show a non-functionalized tip. Right: Constant height AFM topography (+ 250 pm in z) that led to the dislocation of the CoH system (red arrow).

The excitation voltage, V_{ex}, is added to the z-piezo to excite the tuning fork to an oscillation amplitude of 50 pm. Dissipative processes will require more energy for the same oscillation strength, therefore it is crucial to keep track of the excitation voltage during all approach and retract curves. A simple calculation yields the power dissipation per oscillation cycle of the tuning fork. The energy stored in the mechanical motion of the tuning fork is $E = \frac{1}{2}k_0A^2$, where k_0 is the spring constant and A the oscillation amplitude of the tuning fork. The intrinsic energy loss per oscillation cycle is $D = 2\pi E/Q = (\pi k_0 A^2)/Q$ with Q as the quality factor of the tuning fork. For our tuning fork parameters the dissipation per cycle normally lies between 5 meV and 40 meV depending on the q-factor of the resonator.

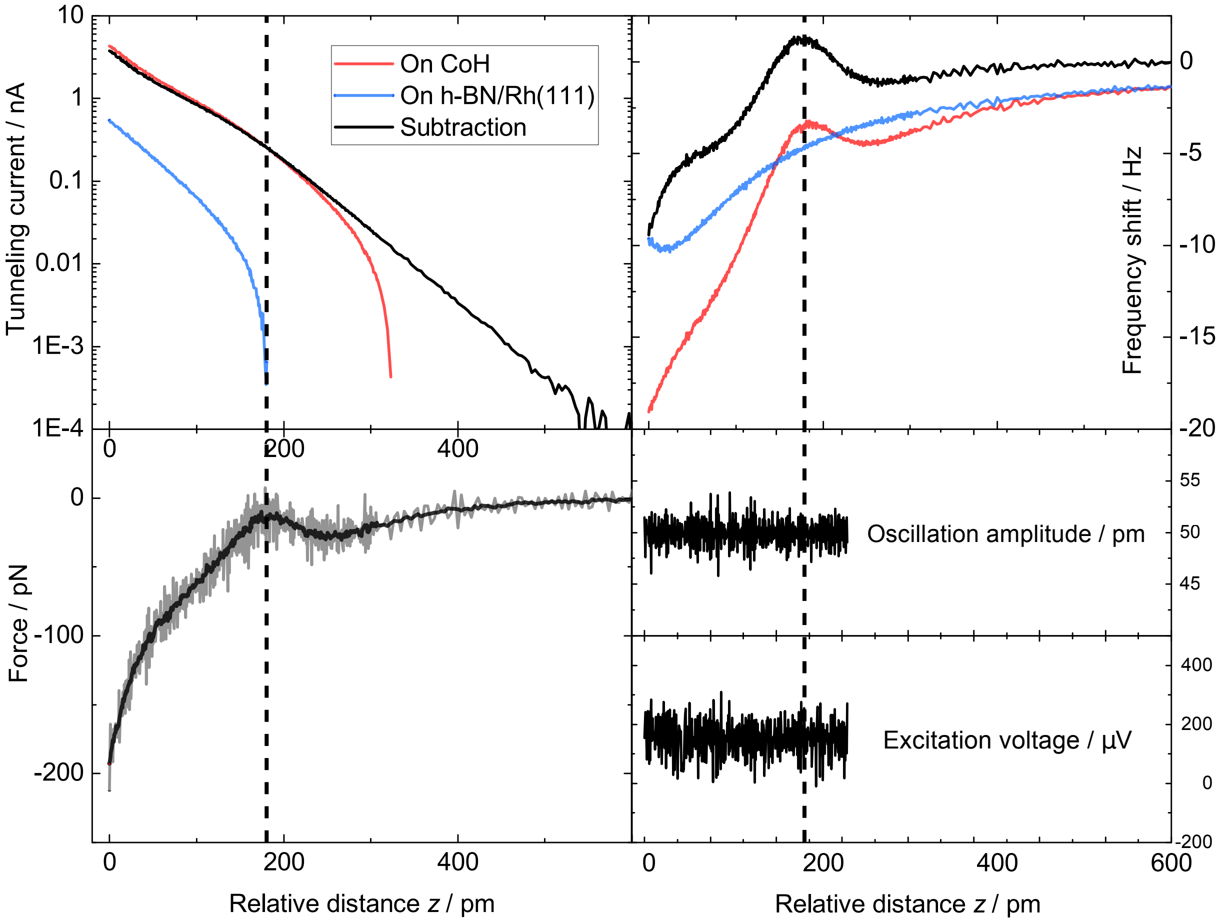

Figure 4.8: Combined STM and AFM measurements on a CoH system adsorbed near the rim region of h-BN (same system as in figure 4.7). The tunneling current and the frequency shift both show strong variations at short tip-sample distances. While the less attractive part already starts before 200 pm the tunneling current deviates from its exponential shape only after the turning point around 180 pm at which the attractive part dominates the signals once again. The oscillation amplitude and the excitation voltage stay constant during the entire distance range.

Upon approach of a CoH system on the soft rim region of the h-BN layer, the $I(z)$ and $\Delta f(z)$ curves in figure 4.9 over the CoH system (red) show strong variations from the h-BN background (blue) taken at the same height. Similar to the dataset in figure 4.8, the force curve shows a less attractive part relatively early around 200 pm and an attractive part around 130 pm before it transitions into a strong repulsive signal around 70 pm. Interestingly, the excitation voltage stays constant until the onset of the strong repulsive part around 70 pm. This could be a hint for dissipative processes due to the strong interaction with the CoH system on the ultrasoft rim site. Contrary to the dataset in figure 4.9, the approach curves of a CoH system on the flat valley region of the h-BN layer shows the expected unperturbed curves. Upon approach, the $I(z)$ and $\Delta f(z)$ curves in figure 4.10 over the CoH system (red) and the h-BN background (blue) are almost featureless and show a constant exponential increase of the current and the expected decrease in the frequency shift and force.

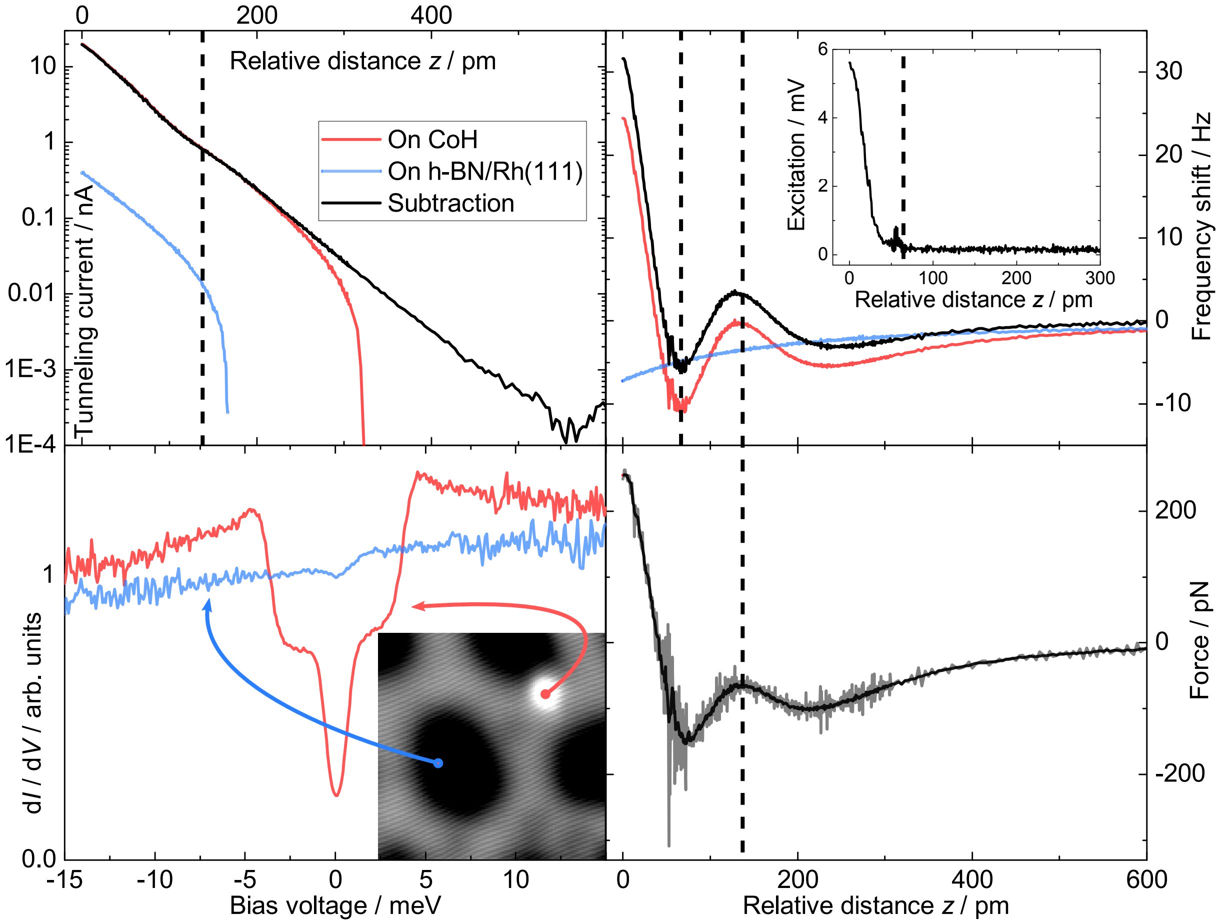

Figure 4.9: Combined STM and AFM measurements on a CoH system on the rim region of h-BN. The constant current STM topography inset (taken at V_B = -15 mV and I_T = 20 pA) shows the CoH system located at the rim region of the h-BN layer, a region that is subject to strong tip interactions as shown in figure 4.6. The dI/dV spectra over the CoH system (red curve) and the h-BN (blue curve) show a non-functionalized tip.

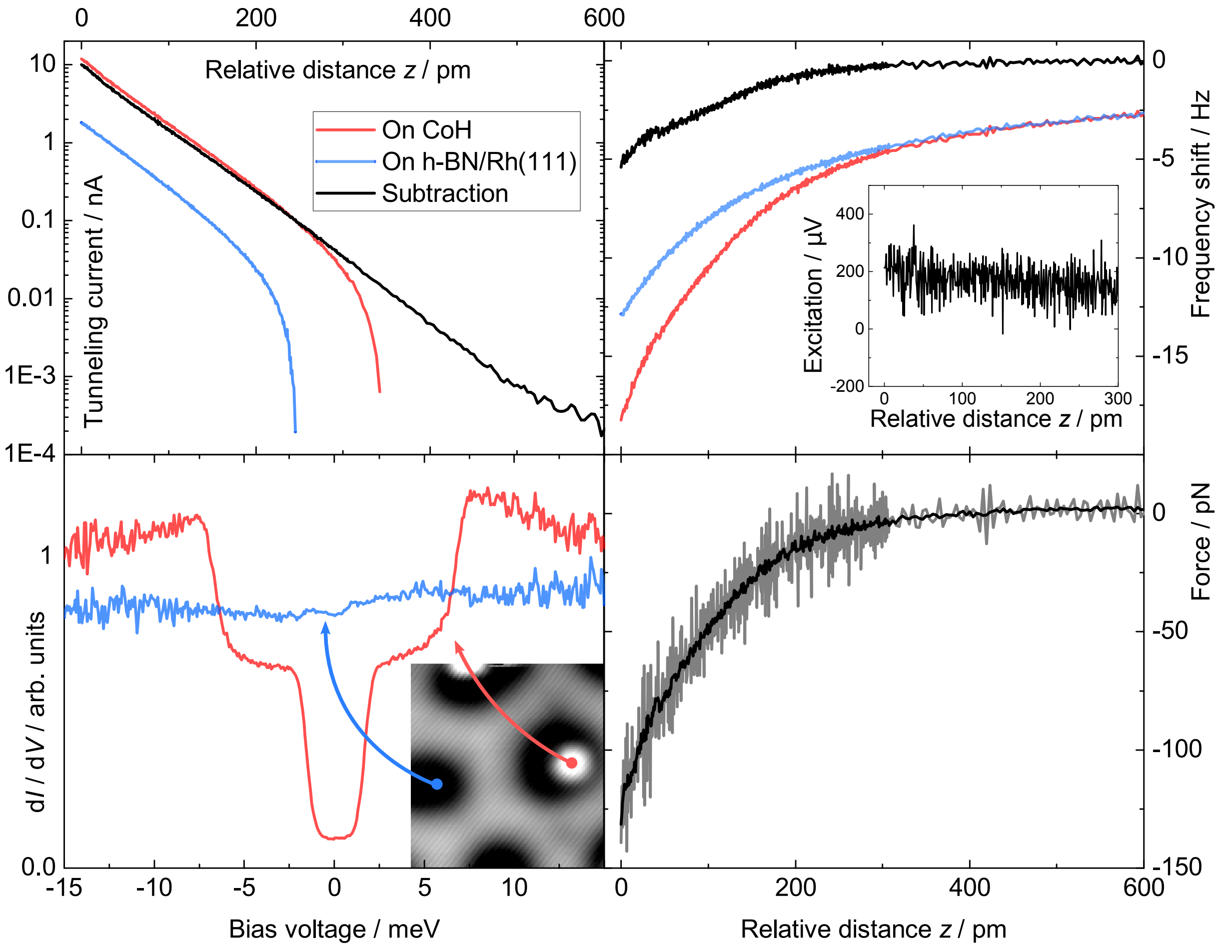

Figure 4.10: Combined STM and AFM measurements on a CoH system near the valley region of h-BN. The constant current STM topography inset (taken at V_B = -15 mV and I_T = 20 pA) shows the CoH system located close to the valley region of the h-BN layer. This region remains flat compared to the rim regions of the corrugated h-BN layer. The dI/dV spectra over the CoH system (red curve) and the h-BN (blue curve) show a non-functionalized tip.

4.3 Discussion

This chapter has shown the AFM capabilities of the combined qPlus design. The general understanding of the origin of the frequency shift will be vital for the data presented in chapter 6 in which changes of the CoH$_x$ spin signatures are accompanied by distinct force signals over the systems. While the ultrasoft h-BN/Rh(111) surface is a wonderful playground to investigate magnetic atoms and other adsorbents, it is difficult to compare datasets to each other as the tip apex, the underlying strain of the h-BN and other effects strongly influence the force approach curves as seen in the previous subsection. Comparing the constant height AFM images to the constant current STM images shows that the rim region which is pushed towards the Rh(111) surface by the tip approach is not as wide as it seems. This could explain why the CoH system shown in figure 4.2 and 4.3 has no repulsive parts or deviations in the force although it seems to be located on the rim region in the STM topography. Comparing the CoH systems in figure 4.9 and 4.10 confirms the assumption that the closer the CoH system is adsorbed to the rim region the stronger the influence on the observed force signals. Although the setpoint conductance was kept at -15 mV and 20 pA over the center of the CoH$_x$ systems to start the approach and retract curves before the feedback loop was turned off, the force curves for different CoH systems were not matching each other. The reason for this variation could be the dI/dV at -15 mV that is largely determined by the spin system's inelastic excitation intensities. The higher the density of states at this setpoint voltage the further the tip is away from the sample and thus the force curve would need to include an offset in the distance. A better approach for future measurements would be to define the tip-sample distance in a more reliable way, for example by performing an $I(z)$ and $\Delta f(z)$ approach and retract curve over the same region on a h-BN valley or h-BN rim until point contact of the tip apex with the h-BN surface is observed. However, this approach probably also depends largely on the strain of the underlying h-BN/Rh(111) and could easily be different for different tip apexes that change throughout different experiments.

Another observation was the ringstate of Co atoms on h-BN/Rh(111) that is believed to originate from the weakening of the h-BN to Rh(111) substrate bond for 60 BN unit cells due to a bistable Co adsorption complex [62]. AFM topography could help to quantify the tip sample interactions and the origin of the ringstate. We found that most of the ringstates are too fragile for close AFM experiments and dislocate to a stable adsorption position of the Co atom on the h-BN layer while the underlying h-BN layer seems to be unperturbed.

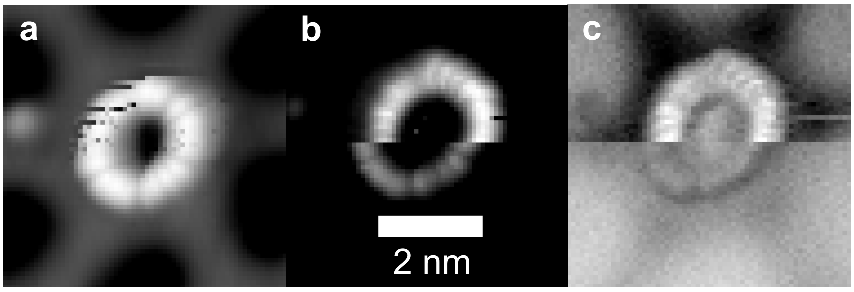

Figure 4.11: STM and AFM topography of a Co atom's ringstate on h-BN/Rh(111). (a) Constant current STM image taken at V_B = -200 mV and I_T = 20 pA. (b) and (c): Constant height STM and AFM topography. Setpoint parameters V_B = -200 mV and I_T = 20 pA at the bottom left starting point define the height of the scan. Frequency shift range from -4 Hz (white) to -12.8 Hz (black). Scan speed was set to 1 nm / s, yet the tip or the Co atom changed during the scan leading to a stronger signal in the tunneling current and frequency shift.

CHAPTER 5

CORRELATION DRIVEN TRANSPORT ASYMMETRIES IN TUNNEL JUNCTIONS

The main results of the following chapter were published in Nature Communications, January 2017[1] [92].

Magnetic atoms have been assembled on surface lattices to produce coupled spin systems from two atoms up to larger clusters. These arrangements were limited to the underlying lattice structure and allowed the determination of exchange coupling values between magnetic atoms by performing scanning tunneling spectroscopy over each individual atom. However, this approach is fundamentally different from two atoms that are coupled in a tunnel junction where the exchange coupling is steadily controlled by their separation distance and electron transport is probed *through* this coupled spin system. This chapter will show how spin-spin correlations arise at strong coupling strengths and how this can lead to an observable asymmetry in the differential conductance that was previously only known from spin-polarized electron transport in magnetic fields.

---

[1] M. Muenks, P. Jacobson, M. Ternes, K. Kern, "Correlation-driven transport asymmetries through coupled spins in a tunnel junction"

5.1 Coupled atoms on surfaces

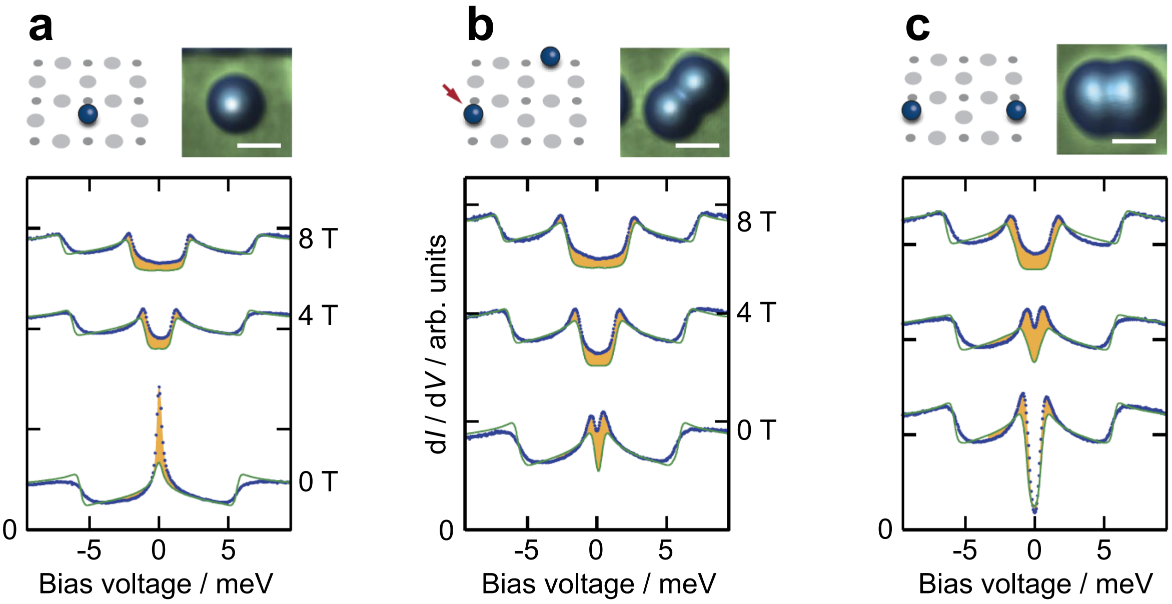

Figure 5.1: Example of coupled Co atoms on $Cu_2N/Cu(001)$ adapted from [93]. (a) A Co $S = 3/2$ atom adsorbed on a Cu_2N island exhibits two inelastic excitation steps and a Kondo resonance around the Fermi energy. The splitting of the Kondo resonance in energy is shown for magnetic fields of 4 T and 8 T applied normal to the sample surface together with a sketch of the underlying Cu_2N lattice and the STM topography (scale bar = 1 nm). (b) + (c) Placing another Co $S = 3/2$ atom next to the original one alters its spectroscopic signatures as if subject to a magnetic field. Depending on the lattice site and therefore Co-Co separation distance, different exchange coupling strengths between the Co atoms are observed.

When two magnetic atoms are brought in proximity to one another (< 1 nm), the magnetic d-orbitals will eventually overlap leading to a direct exchange coupling between them. For magnetic atoms on surfaces for which the eigenstates are already subject to magnetic anisotropy (modeled by $\boldsymbol{S}_1 D \boldsymbol{S}_1$ as shown in chapter 3), this coupling is modeled by an exchange term that is added to the original Hamiltonian, $\mathcal{H}_0$, of the original spin system, S_1, that included the crystal field, $\mathcal{H}_{CF}$ contribution, and Zeeman terms, $\mathcal{H}_Z$. Similar to the magnetic anisotropy energy, this exchange term in its most general form, $\boldsymbol{S}_1 J \boldsymbol{S}_2$, can be reduced to the exchange interaction, H_{SS}, which in its dot-product form guarantees rotation symmetry and has been used to model the exchange interaction of coupled atoms on surfaces (compare [93] from figure 5.1):

$$\mathcal{H}_0 = \mathcal{H}_{CF} + \mathcal{H}_Z + \underbrace{J_{12} \boldsymbol{S_1} \cdot \boldsymbol{S_2}}_{\mathcal{H}_{SS}} \tag{5.1}$$

where, J_{12}, is the exchange coupling strength. A possible antisymmetric part of the exchange interaction (Dzyaloshinskii-Moriya) can be modeled as a vector product between the two spin systems, $\boldsymbol{S_1} \times \boldsymbol{S_2}$, but will not be employed in this thesis as it is less likely to occur, e.g. when the exchange interaction between two spin systems is mediated by conduction electrons as recently observed in [94].

Horizontal atom manipulation to build up coupled systems was first performed on Cu(111) surfaces in which the atom structures mainly created a 2D potential well for the free surface electrons [95] [96]. To model effects of direct exchange coupling of magnetic orbitals, the atoms should be decoupled from the metal substrate. The epitaxial and flat Cu_2N/Cu(110) surface allows a precise horizontal arrangement according to the underlying Cu_2N lattice structure and is suitable to determine the exchange coupling values as shown in figure 5.1 where the dominant splitting of the Kondo resonance in energy can be fitted to the exchange coupling strength with an isotropic Heisenberg model (compare [93] and table 1.1).

The decoupling effect of the h-BN/Rh(111) surface has been shown in chapter 3, but horizontal manipulation of Co atoms is difficult due to the corrugation of the h-BN monolayer. An example where two magnetic systems are in proximity to each other by chance is shown in figure 5.3. Compared to the sharp Kondo resonance in subsection 3.4, the Kondo resonance here seems to be broadened by the possible influence of the $S = 1$ system.

A well characterized exception in which no decoupling layer is needed are magnetic atoms on magnetically susceptible surfaces such as Pt and Pd. For Co atoms on Pt(111) the Ruderman-Kittel-Kasuya-Yosida (RKKY) interaction was mapped in its strength and directionality [37]. This RKKY interaction describes the indirect oscillatory exchange coupling of two magnetic impurities that is mediated by the conduction electrons of the metal substrate and strongly dependents on the Fermi surface of the metal. In this sense Pt is special as it is on the verge of being a ferromagnet and provides a strong orbital moment that is interacting with the magnetic impurity [11] [36] [97] [98].

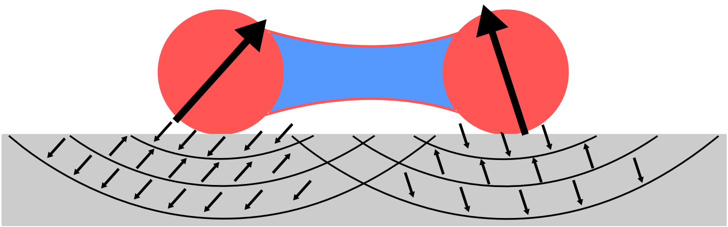

Figure 5.2: Schematics of different coupling mechanisms of magnetic atoms (red spheres) on surfaces: Direct exchange coupling for shorter distances around 0.1 nm or dipolar coupling for larger distances around 1 nm between the magnetic orbitals of the atoms (blue area) or indirect magnetic coupling mediated by the substrate (grey area), here in the form of substrate electrons that oscillate in their spin polarization relative to the magnetic impurities.

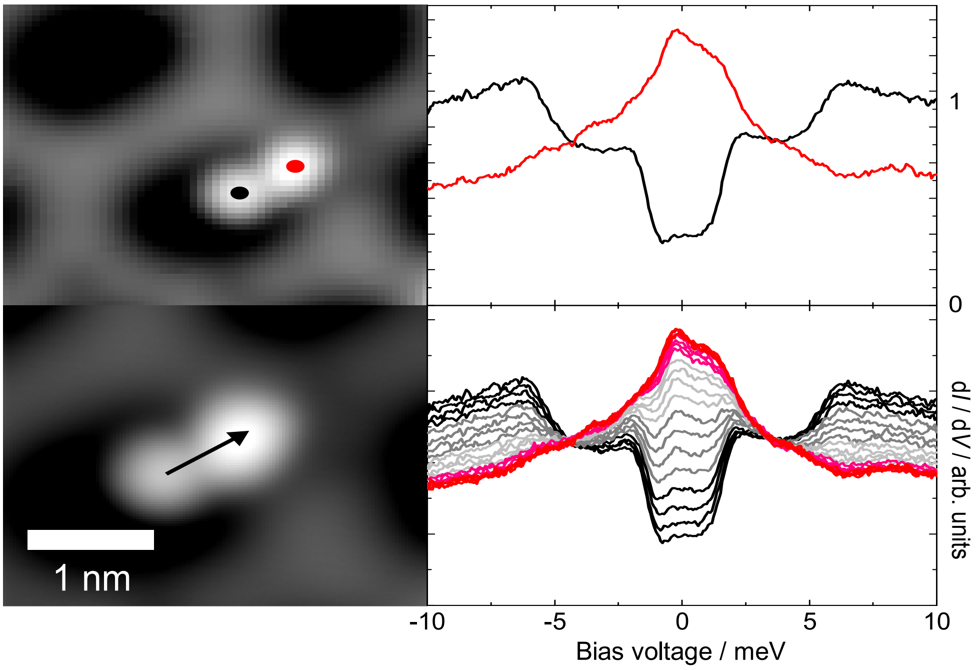

Figure 5.3: STM constant current topography and spectroscopy of a coupled CoH and CoH_2 system on h-BN/Rh(111) at 1.1 K and 0 T. Top: Overview image of the CoH (black dot) and the CoH_2 (red dot) systems and their corresponding spectroscopic signatures (black and red curves corresponding to the colored dots). Bottom: Spectra taken along the black line in 40 pm distance steps show just an overlap of the two magnetic signatures. The broadening of the Kondo that at this temperature normally has a much sharper resonance could be due to the proximity of the CoH system.

5.2 Coupled atoms in an STM junction

While the horizontal manipulation of CoH_x systems on the corrugated h-BN/Rh(111) is hard to achieve due to the softness of the substrate [91] and the abundance of different adsorption sites, we noticed that vertical manipulation, i.e. transferring CoH_x systems onto the Pt tip apex, is readily achieved by gently approaching the system in z-direction until a distinct jump in current, I, and frequency shift, Δf, occurs. An example with full experimental datasets including $I(z)$ and Δf(z) curves during the manipulation event as well as spectroscopy of tip and CoH system before and after the manipulation event is shown in figures 5.4 and 5.5. The spin system on the tip apex, S_2, can now be utilized by coupling it to another CoH_x spin system, S_1, on the h-BN/Rh(111) surface. The coupling strength, J, between these spin systems is proportional to the orbital overlap between the two atoms and thus in STM experiments also proportional to the distance, $\exp(z)$, between tip and sample, that is directly controlled by the tunneling conductance setpoint. Thus, we are now able to control the full range of coupling from $J \to 0$ meV for large distances at the onset of the tunneling current, up to large couplings, $J \approx 2$ meV, for shorter distances before the atom is dislocated by the tip. The surprising experimental results at zero field that resemble a spectral evolution seen for spin polarized tips in magnetic field [99] will be explained by taking spin-spin correlations into account.

5.2.1 Tip functionalization

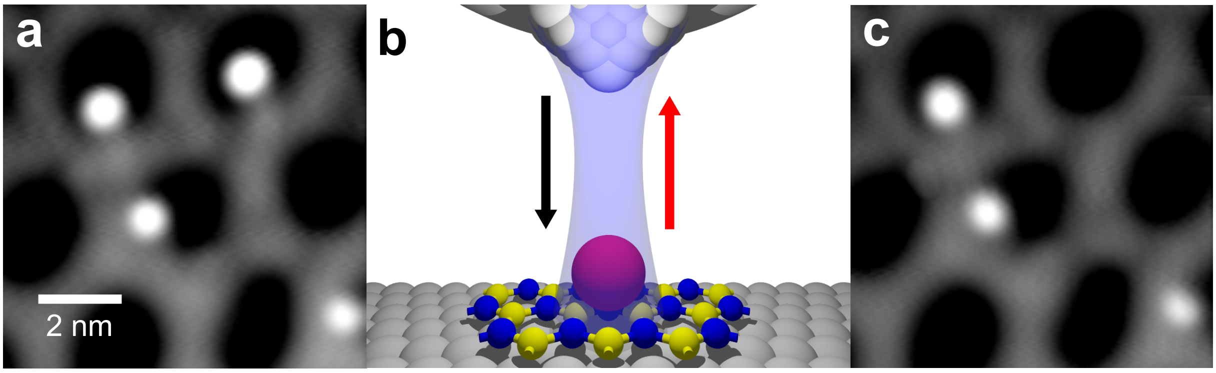

Figure 5.4: Schematics of vertical atom manipulation to create a functionalized tip. (a) and (c) show constant current STM images (I_T = 20 pA, V_B = 100 mV) of CoH_x systems on h-BN/Rh(111) before and after the manipulation procedure illustrated in (b). The tip was stabilized over the upper right CoH system in (a) and moved several hundreds of pm towards the atom in z-direction until a distinct decrease in the tunneling current occurred after which the tip was withdrawn to its original position. Experimental approach (black arrow) and retract (red arrow) $I(z)$ and Δf(z) curves for another dataset are shown in figure 5.5.

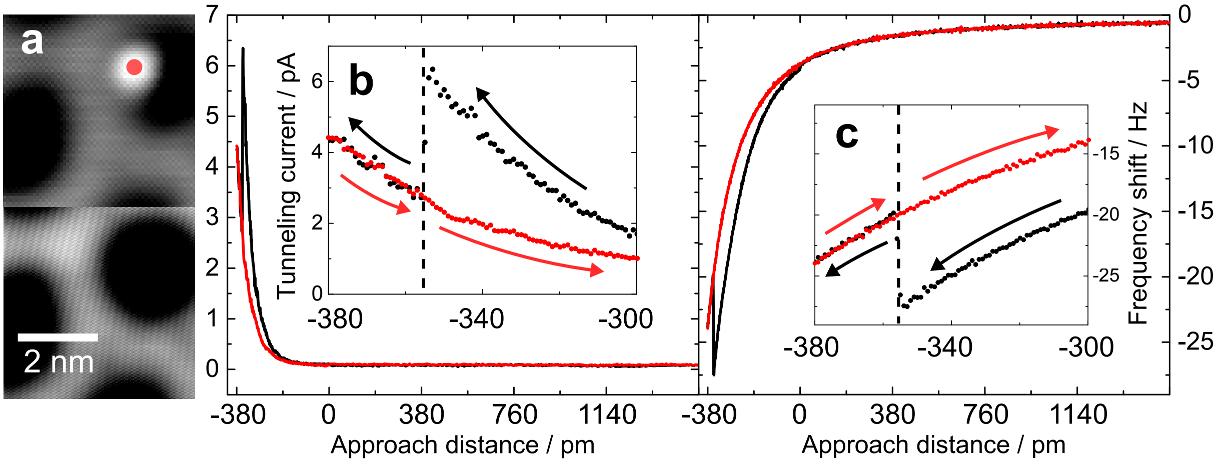

Figure 5.5: Approach and retract curves over a CoH $S = 1$ system during vertical manipulation. (a) Constant current STM topography (V_B = -100 mV, I_T = 20 pA) of the CoH system before (top) and after (bottom) the manipulation event. The tip was stabilized over the CoH system (red dot) at V_B = -15 mV and I_T = 20 pA which defines zero distance in (b) and (c). The STM feedback loop was then turned off and approach (black curves) and retract (red) curves were taken 380 pm towards the atom and 1500 pm away from zero (At V_B = 0 meV with only the LI osc. of 200 μV). The tunneling current and the simultaneously recorded frequency shift clearly show a distinct change at -355 pm at which the current and the frequency shift rapidly decrease and indicate a change in the tunnel junction. Oscillation amplitude during experiment: $A = 50$ pm.

The tip functionalization is performed with vertical atom manipulation as outlined in figure 5.4. The STM tip is stabilized over the center of a CoH $S = 1$ system at setpoint parameters of V_B = -15 mV and I_T = 20 pA and from this distance slowly (10 pm / s) moved towards the spin system and back. Before point contact between the tip apex and the spin system, the CoH system is dislocated from its original position at an approach distance of around -350 pm. This manipulation event leads to a sharp drop in the tunneling current and a decrease in the frequency shift due to the absence of the CoH system as shown in figure 5.5a. "Blunt" tip apexes provide a suitable surface to harbor a Co atom as the last atom of the tip apex and successful Co/Pt tip functionalization results in a sharp topography as consistently seen for the systems in figure 5.9, 5.10 and 5.20. To further check if the Co atom resides at or near the Pt tip apex, we performed STS before and after the manipulation. As seen in figure 5.6 the previously flat spectrum of the bare Pt tip on h-BN/Rh(111) shows a distinct spectral change if the Co atom resides near or at the tip apex. Especially by comparing these results to experiments that investigated Co atoms on Pt(111) [100] [101], we can find striking similarities between the observed dips of Co atoms on fcc and hcp sites on Pt(111) and our Co-functionalized Pt tips (see figure 5.7).

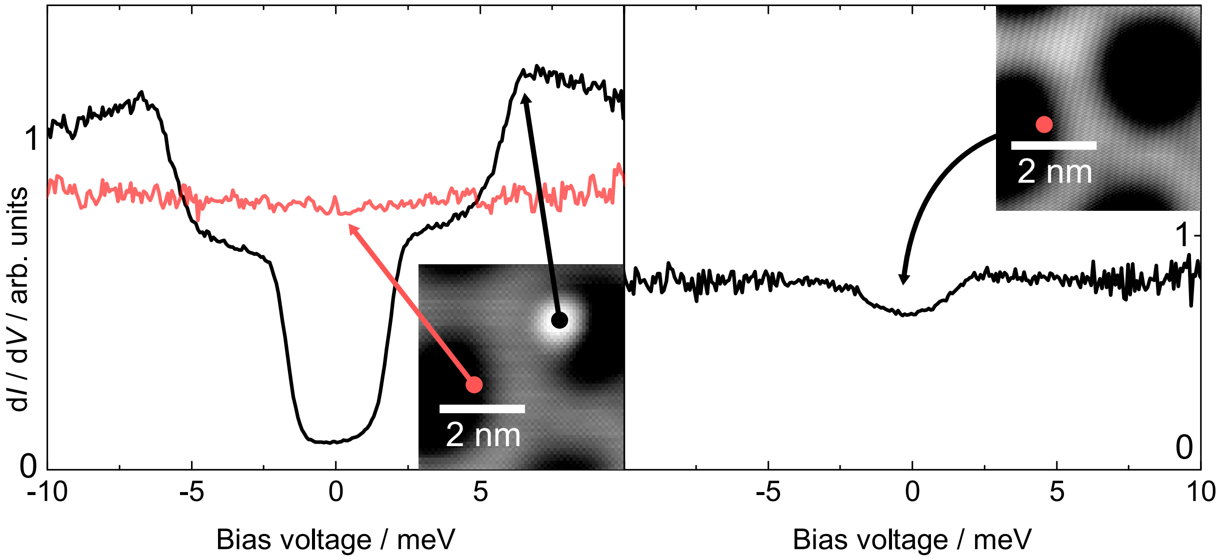

Figure 5.6: Spectroscopy before and after vertical manipulation of the CoH system shown in figure 5.4. Left: $S = 1$ signature of the CoH system (black dot and curve) and the background spectrum of the bare Pt on h-BN/Rh(111) taken at V_B = -15 mV and I_T = 500 pA before disabling the feedback loop. Right: Tip spectroscopy after the manipulation event shows a 2 meV wide dip on h-BN/Rh(111).

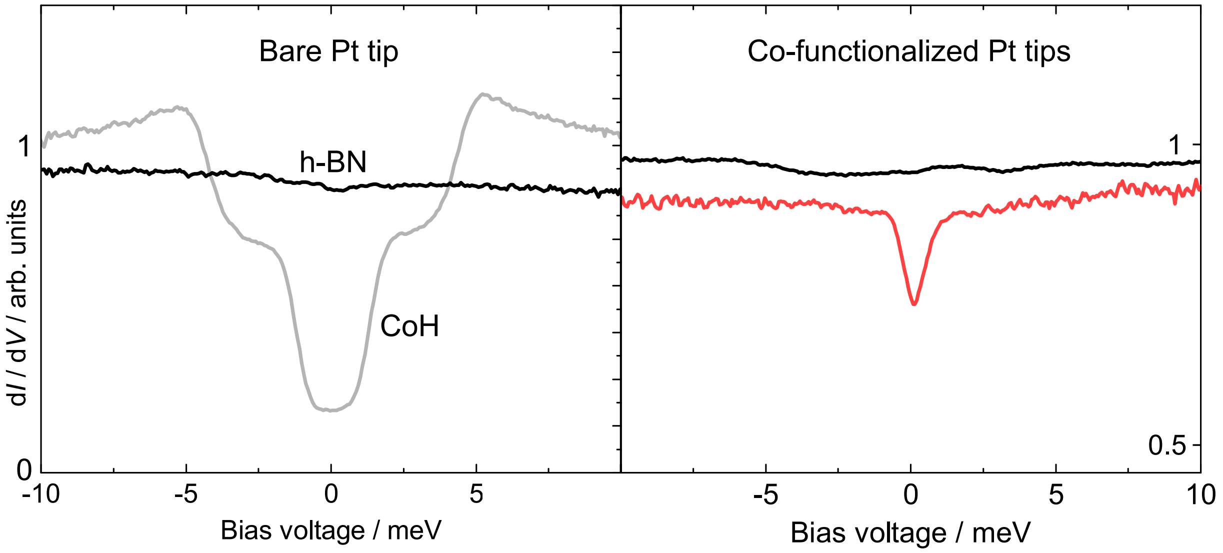

Figure 5.7: Spectroscopy of Co-functionalized tips. Left: For comparison the CoH and tip background spectra on h-BN/Rh(111) are shown. Right: Two typical spectra of Co-functionalized tips on h-BN/Rh(111). The red curve shows a similar 1 meV wide dip of the same intensity that was observed for CoH system on Pt(111) [100]. The black curve shows features that resemble the spectral signatures of Co atoms on Pt(111) ffc and hcp sites [100].

5.2.2 Experimental observations

To approach CoH$_x$ spin systems on the h-BN/Rh(111) surface, the tip is positioned above the center of the system at a setpoint of V_B = -15 mV and I_T = 500 pA. This corresponds to a low conductance setpoint of $|G_\mathrm{S}| = I_\mathrm{T}/V_\mathrm{B} = 33$ nS and, for this tunnel junction, to a large separation distance between tip and sample of roughly 600 pm at which we are still able to obtain a significant signal to noise ratio for spectroscopic measurements. Taking this initial low conductance setpoint as the starting point we obtain an unperturbed spectrum that allows us to characterize the unperturbed spin system and then move the tip closer to the sample by keeping V_B the same and increasing I_T up to 8 nA (533 nS). The main changes to CoH systems approached with bare and different Co-functionalized Pt tips are shown in the next three figures.

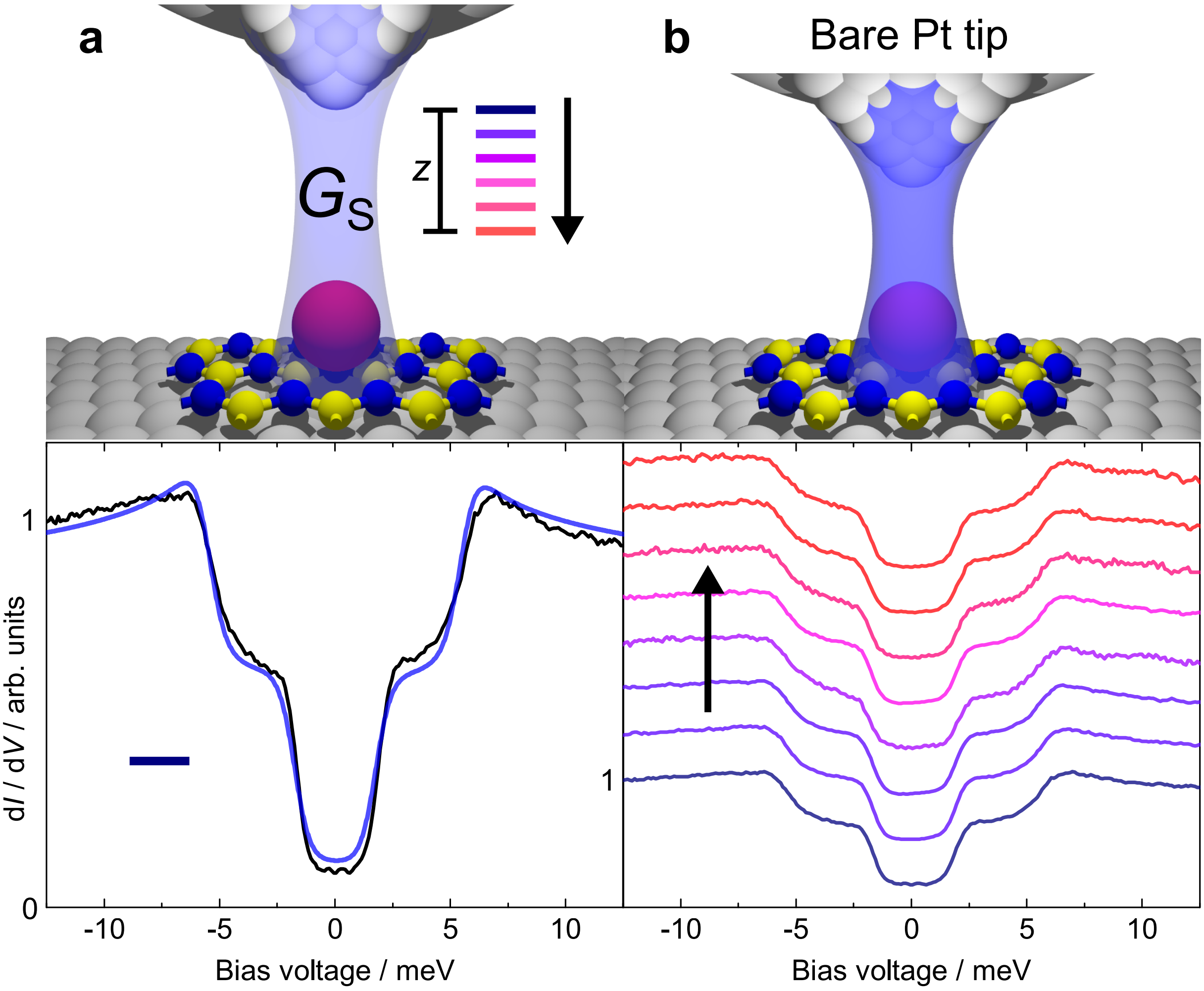

Figure 5.8: Approach of a CoH $S = 1$ system with a bare Pt tip. (a) The CoH $S = 1$ spectrum (black curve) is fitted (blue curve) with the parameters: D = -4.6 meV, E = 0.8 meV and $J\rho_s$ = -0.14 at the lowest conductance setpoint $G_\mathrm{S} = 33$ nS. (b) An approach from 33 nS (blue) to 470 nS (red) shows no significant changes in the spectral shape.

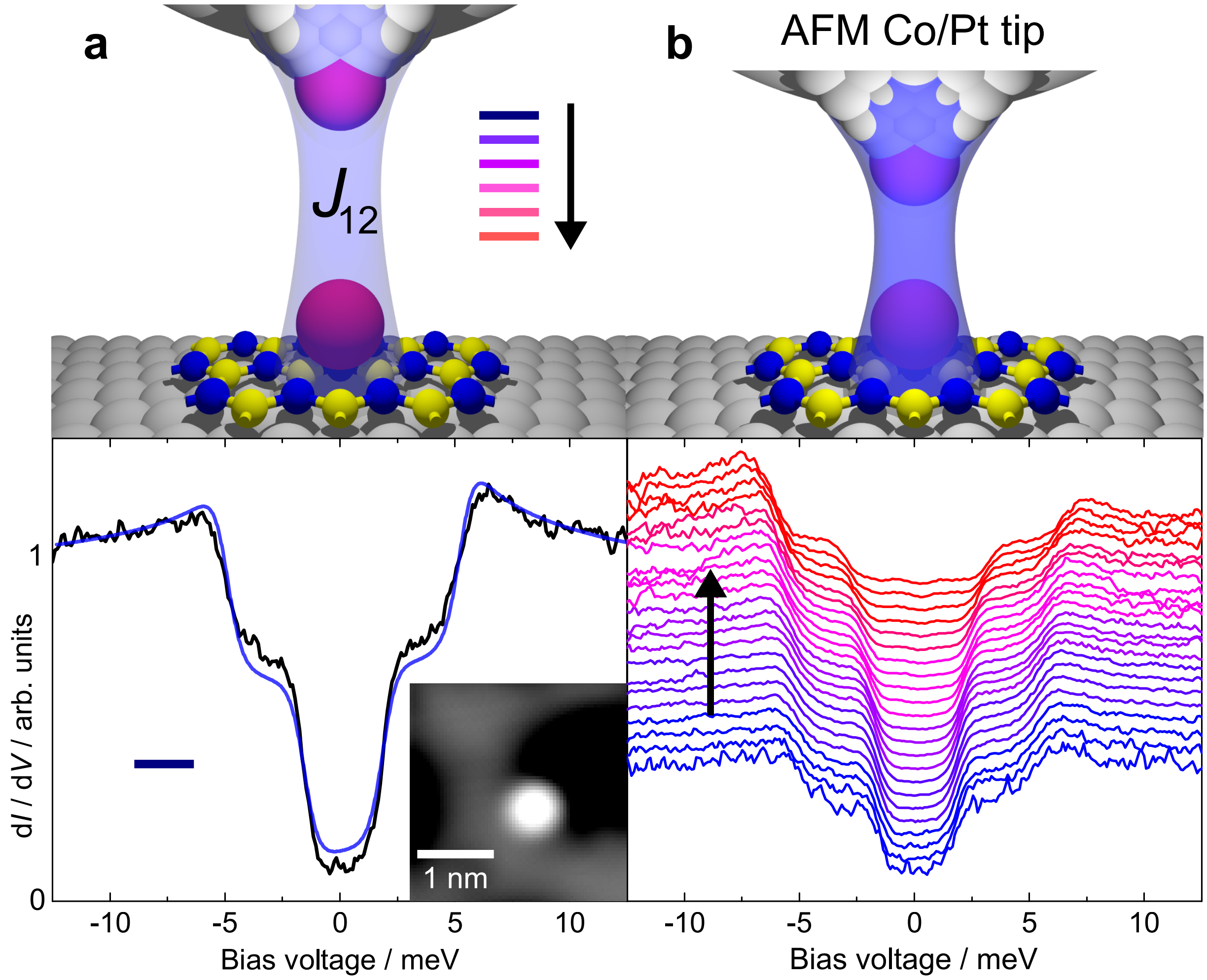

Figure 5.9: Approach of a CoH $S = 1$ system with a Co-functionalized tip. (a) The conductance setpoint, G_S, is now controlling the direct exchange coupling, J_{12}, between the CoH $S = 1$ system on the sample (S_1) and the Co spin system on the tip (S_2). At a low conductance setpoint ($G_\mathrm{S} = 33$ nS) the CoH spectrum is unperturbed (black curve) and can be fitted with the parameters: D = -4.2 meV, E = 0.8 meV and $J\rho_s$ = -0.13 (blue curve). The constant current STM image (V_B = -15 mV and I_T = 20 pA) shows a sharp topography of the CoH system adsorbed at the edge of a rim region (see chapter 3). (b) Approaching this system with the same Co-functionalized tip from a setpoint conductance of G_S = 3.3 nS (blue) to 630 nS (red) shows an evolution of the spectral $S = 1$ signatures. Three changes can be readily seen: The energies of both excitation steps shift to higher energies by over 1 meV, the outer excitation step (around 5 meV) shows an intensity asymmetry in the bias voltage and the inner excitation step (around 1 meV) intensity decreases compared to the outer excitation step intensity. Furthermore, small changes are visible such as a spectroscopic feature appearing around zero bias and a higher peak intensity of the outer excitation steps.

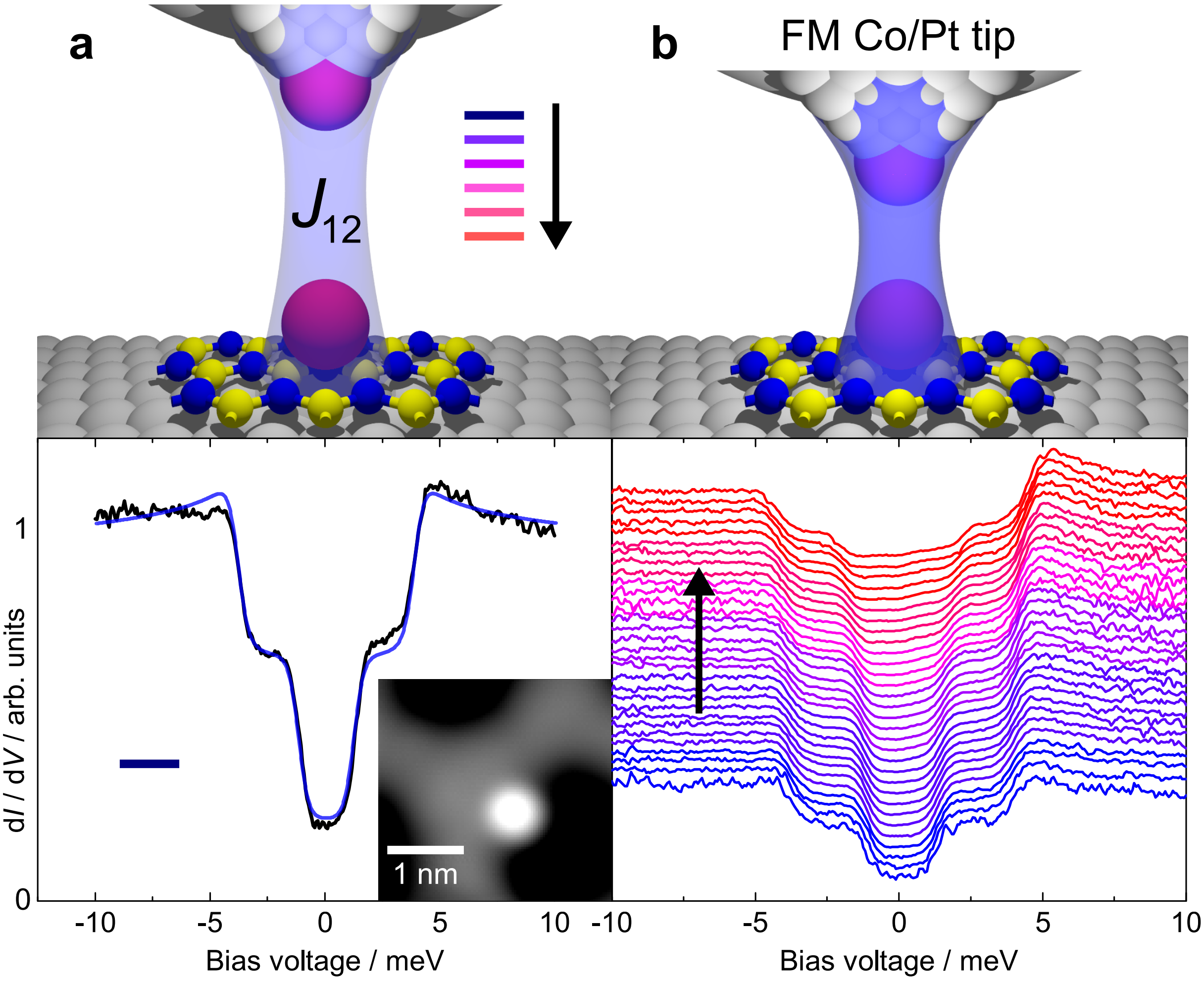

Figure 5.10: Approach of a CoH $S = 1$ system with a different Co-functionalized tip. (a) The conductance setpoint, G_S, controls the direct exchange coupling, J_{12}, between the CoH $S = 1$ system on the sample (S_1) and the Co spin system on the tip (S_2). At the lowest conductance setpoint ($G_\mathrm{S} = 3.3$ nS) the CoH spectrum is unperturbed and can be fitted with the parameters: D = -3.2 meV, E = 0.6 meV and $J\rho_s$ = -0.10. The constant current STM image (V_B = -10 mV and I_T = 10 pA) shows a sharp topography of the CoH system adsorbed at the edge of a rim region. (b) Approaching this system with the same Co-functionalized tip from 3.3 nS to 300 nS shows a significant continuous evolution of the spectral $S = 1$ signatures. As in the previous dataset of figure 5.9 in which a different tip and CoH system were used, three changes can be readily seen: The energies of both excitation steps shift to higher energies by almost 1 meV, the outer excitation step (around 5 meV) shows an intensity asymmetry in the bias voltage and the inner excitation step (around 1 meV) intensity decreases compared to the outer excitation step intensity. Note, that the asymmetry here is opposite to the one shown in figure 5.9.

5.3 Expanding the transport model

Coupling the two spin systems S_1 and S_2 as shown in figure 5.9 and 5.10 fundamentally changes the observed spectra compared to the unperturbed CoH $S = 1$ (S_1) system's spectrum on the sample. Chapter three already introduced the theoretical model for the CoH $S = 1$ system to describe its spectral signatures at zero magnetic field and for higher magnetic fields by introducing the Hamiltonian, $\mathcal{H}_0$. To describe the observed changes in the spectrum for high conductance setpoints, i.e. high direct exchange coupling, J_{12}, we will expand this model. We assume that the Co system on the Pt tip apex (S_2) can be described as a $S = 1/2$ system. In particular, this assumption expands the Hilbert space as the new total spin satisfies the triangular condition, $|S_1 - S_{1/2}| \leq S \leq S_1 + S_{1/2}$, :

$$\frac{1}{2} \leq S \leq \frac{3}{2} \tag{5.2}$$

and can therefore only be $\frac{1}{2}$ or $\frac{3}{2}$. The possible m_z projections yield $(2S_{3/2} + 1) + (2S_{1/2} + 1) = 4 + 2 = 6$ states in total and the resulting Hilbertspace is $(2S_1 + 1)(2S_{1/2} + 1) = 3 \cdot 2 = 6$-dimensional. Following the approach from the previous chapter we can again define a Hamiltonian $\mathcal{H}_0$ that describes the coupled spin system with the already introduced decoupled CoH $S = 1$ system on the sample (S_1). To account for the second spin at the tip (S_2), we introduce an additional exchange coupling term $\mathcal{H}_{SS}$ and an additional Zeeman term $\mathcal{H}_{Z2}$ if a magnetic field is applied:

$$\mathcal{H}_0 = \mathcal{H}_{CF} + \mathcal{H}_{Z1} + \mathcal{H}_{Z2} + \mathcal{H}_{SS} \tag{5.3}$$

$$\mathcal{H}_0 = DS_{1z}^2 + E(S_{1x}^2 - S_{1y}^2) + g\mu_B B_z S_{1z} + g\mu_B B_z S_{2z} + \boldsymbol{J}_{12}\boldsymbol{S}_1 \cdot \boldsymbol{S}_2 \tag{5.4}$$

where $\boldsymbol{J}_{12}$ is the coupling strength and $\boldsymbol{S}_1$ and $\boldsymbol{S}_2$ are the operators of the two spin systems. These operators are expanded by taking the tensor product with the corresponding unity matrix of the other spin system:

$$S_{1x} = S_x \otimes \mathbb{1}^{(2x2)} \qquad S_{1y} = S_y \otimes \mathbb{1}^{(2x2)} \qquad S_{1z} = S_z \otimes \mathbb{1}^{(2x2)} \tag{5.5}$$

$$S_{2x} = \mathbb{1}^{(3x3)} \otimes \sigma_x \qquad S_{2y} = \mathbb{1}^{(3x3)} \otimes \sigma_y \qquad S_{2z} = \mathbb{1}^{(3x3)} \otimes \sigma_z \tag{5.6}$$

which ensures that the resulting higher dimensional operator will only act on the previous spin's subspace whereas the other spin's subspace will be left unchanged due to the identity operation. Since the magnetic anisotropy is only acting on the CoH $S = 1$ system it is justified to only consider this subspace in the extended Hilbert space. For the exchange Hamiltonian, $\mathcal{H}_{SS}$, we consider the full exchange interaction between the spin-1 and spin-1/2 system as a tensor product between both spin operators:

$$\mathcal{H}_{SS} = \boldsymbol{J}_{12}\boldsymbol{S}_1 \cdot \boldsymbol{S}_2 = J_x S_{1x} \otimes S_{2x} + J_y S_{1y} \otimes S_{2y} + J_z S_{1z} \otimes S_{2z}. \tag{5.7}$$

Diagonalizing the Hamiltonian $\mathcal{H}_0$ (equation 5.3) for the coupled spin system yields six eigenstates and eigenenergies instead of the previous three for the single CoH system. The eigenstates with their m_z projections and respective energies are listed for a direct exchange coupling value of $J \to 0$ meV in table 5.1 and $J_x = J_y = J_z = 2$ meV in table 5.2. $J \to 0$ meV corresponds to the case in which the Co-functionalized tip is far away from the sample and indeed, the only difference between the values listed in table 5.1 and the previous CoH case shown in table 4.2 is the two-fold degeneracy due to the additional $S = 1/2$ system on the tip. The situation changes for $J = 2$ meV that describes a smaller tip-sample distance equal to a higher orbital overlap of the two spin systems and therefore a higher coupling. The eigenstates are still two-fold degenerate but the exchange coupling has led to a polarization of the m_z projections that resembles the effect of an applied magnetic field to the CoH system previously shown in table 4.3. By changing the coupling strength J_{12} from -4 meV to 4 meV in 0.1 meV steps and diagonalizing H_0 for every step we can plot the energy evolution of the three two-fold degenerate eigenstates. Figure 5.11 shows the principal energy evolution for a CoH $S = 1$ system with $D = -5$ meV and $E = 1$ meV for Heisenberg ($J_{12} = J_x = J_y = J_z$) and Ising ($J_{12} = J_z$) coupling.

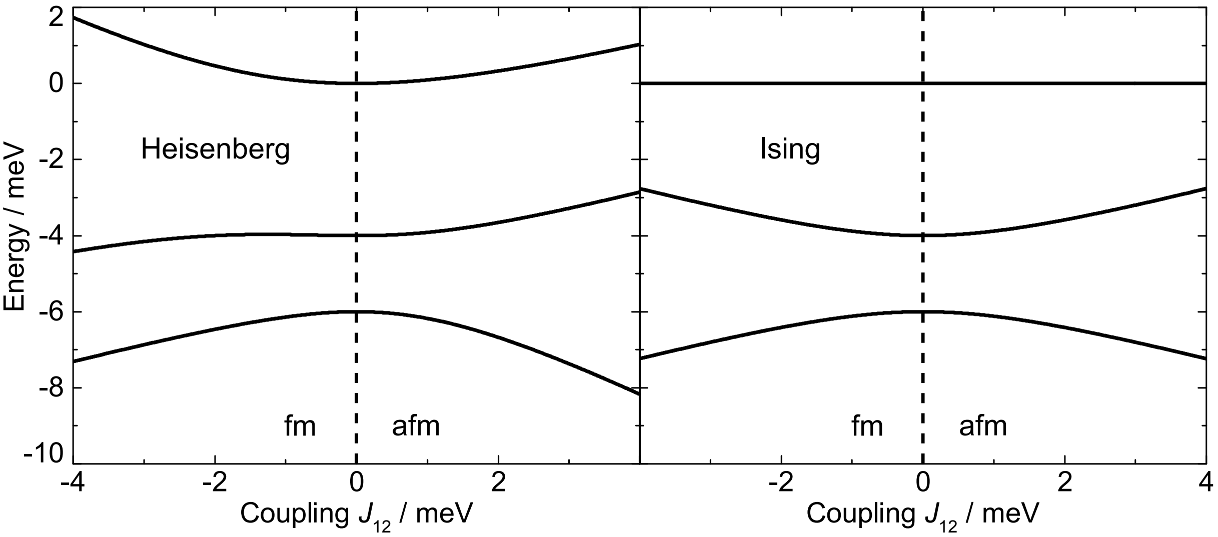

Figure 5.11: Simulation of the three twofold-degenerate eigenstates' energy evolution with coupling strength for a coupled CoH ($S = 1$) and Co/Pt ($S = 1/2$) system. The magnetic anisotropy for the CoH system was set to $D = -5$ meV and $E = 1$ meV. Left: A Heisenberg-like coupling ($J_{12} = J_x = J_y = J_z$) leads to a non-symmetric shift in energies for fm and afm coupling. Right: The Ising-like coupling ($J_{12} = J_z$ and $J_x = J_y = 0$) is symmetric for fm and afm coupling.

$\lvert\psi\rangle_i$	ϵ / meV	Spin $(1 \otimes \frac{1}{2})\ m_z$					
		$\left(-1-\frac{1}{2}\right)$	$\left(-1+\frac{1}{2}\right)$	$\left(0-\frac{1}{2}\right)$	$\left(0+\frac{1}{2}\right)$	$\left(1-\frac{1}{2}\right)$	$\left(1+\frac{1}{2}\right)$
$\lvert\psi\rangle_1$	0	0	-0.707	0	0	0	0.707
$\lvert\psi\rangle_2$	0	0.707	0	0	0	-0.707	0
$\lvert\psi\rangle_3$	2	0	-0.707	0	0	0	-0.707
$\lvert\psi\rangle_4$	2	0.707	0	0	0	0.707	0
$\lvert\psi\rangle_5$	6	0	0	0	1	0	0
$\lvert\psi\rangle_6$	6	0	0	1	0	0	0

Table 5.1: Eigenstates and eigenvalues together with their m_z projection for a coupled CoH ($S = 1$ with D = -5 meV and E = 1 meV) and Co/Pt ($S = 1/2$) system. When $J \to 0$ the previous case as in table 4.2 is established except that all states are twofold-degenerate. The m_z projections displayed in the brackets are (m_z^s and m_z^t) for the sample (-1,0,1) and tip (-1/2, 1/2) spin system.

$\lvert\psi\rangle_i$	ϵ / meV	Spin $(1 \otimes \frac{1}{2})\ m_z$					
		$\left(-1-\frac{1}{2}\right)$	$\left(-1+\frac{1}{2}\right)$	$\left(0-\frac{1}{2}\right)$	$\left(0+\frac{1}{2}\right)$	$\left(1-\frac{1}{2}\right)$	$\left(1+\frac{1}{2}\right)$
$\lvert\psi\rangle_1$	0	0	0.918	-0.194	0	0	-0.343
$\lvert\psi\rangle_2$	0	0.343	0	0	0.194	-0.918	0
$\lvert\psi\rangle_3$	3.02	0	0.324	-0.125	0	0	0.937
$\lvert\psi\rangle_4$	3.02	0.937	0	0	-0.125	0.324	0
$\lvert\psi\rangle_5$	6.99	0.052	0	0	0.972	0.225	0
$\lvert\psi\rangle_6$	6.99	0	0.225	0.972	0	0	0.052

Table 5.2: Eigenstates and eigenvalues together with their m_z projection for a coupled CoH ($S = 1$ with D = -5 meV and E = 1 meV) and Co/Pt ($S = 1/2$) system. A coupling of $J = 2$ meV polarizes the eigenstates to specific m_z projections.

Up to now the exchange coupling describes the energy shifts in the spectra by expanding the Hamiltonian, $\mathcal{H}_0$, but does not yet explain the occurring asymmetry in transition intensities for higher conductance setpoints. For this we take the perturbation Hamiltonian $\mathcal{H}_1$ and the participating tunneling electrons into account. We start with the following assumptions: The CoH $S = 1$ system on the surface does not influence the substrate electrons in the underlying Rh metal because it is decoupled by the h-BN layer. On the other hand, the Co atom that was placed directly on the bare Pt tip is very likely to strongly hybridize with the Pt metal and therefore we expect the state of the Co $S = 1/2$ system to influence the electrons in the Pt tip. To model this influence we take a correlation of the adsorbed Co atom with the local electrons into account. While the electrons in the Rh sample have an equal statistical distribution ($p = 0.5$) of spin up $\lvert\uparrow\rangle$ and spin down $\lvert\downarrow\rangle$ states:

$$0.5\,\lvert\uparrow\rangle\langle\uparrow\rvert + 0.5\,\lvert\downarrow\rangle\langle\downarrow\rvert \tag{5.8}$$

the important electrons close to the Fermi energy in the Pt tip are assumed to have a skewed statistical distribution:

$$\alpha \left|\uparrow\right\rangle \left\langle\uparrow\right| + \beta \left|\downarrow\right\rangle \left\langle\downarrow\right| \tag{5.9}$$

where α and β are the statistical probabilities ($\alpha + \beta = 1$) of the Pt tip bath electrons and are, in our model, determined from the current eigenstate of the coupled spin system. This means for each of the six eigenstates, $\left|\psi\right\rangle_1$ to $\left|\psi\right\rangle_6$, we first determine its m_z^t projection of the spin 1/2 state, $\uparrow_{m_z}$ and $\downarrow_{m_z}$, and then employ the correlation strength, C, to correlate this spin state antiferromagnetically (afm, $C \in [-1, 0]$) or ferromagnetically (fm, $C \in [0, 1]$) with the electron bath in the Pt tip that was originally in an equal distribution of spin up and spin down states. The statistical probabilities of the electron baths are best described as density matrices for the Rh sample ($\hat{p}_\mathrm{S}$) and the Co/Pt tip ($\hat{p}_\mathrm{T}$):

$$\hat{p}_\mathrm{S} = \begin{pmatrix} 0.5 & 0 \\ 0 & 0.5 \end{pmatrix} \quad ; \quad \hat{p}_\mathrm{T} = \begin{pmatrix} 0.5 & 0 \\ 0 & 0.5 \end{pmatrix} + C \sum_{i=x,y,z} \langle S_{2i} \rangle \cdot \sigma_i . \tag{5.10}$$

As an example we take the first state $\left|\psi\right\rangle_1$ of the two degenerate groundstates for a coupling strength $J \to 0$ meV and $J = 2$ meV from table 5.1 and 5.2. For $J \to 0$ meV:

$$\left|\psi\right\rangle_1 = -0.707 \left|-1, \frac{1}{2}\right\rangle + 0.707 \left|1, \frac{1}{2}\right\rangle \tag{5.11}$$

we take the m_z^t projection of the two spins and see that this state is completely in the $\left|\uparrow\right\rangle$ state ($\equiv +\frac{1}{2}$) for $S = 1/2$ and has an equal mixture of $\left|-1\right\rangle$ and $\left|+1\right\rangle$ for $S = 1$ in the m_z^s projection. For the strongly coupled case, i.e. $J = 2$ meV:

$$\left|\psi\right\rangle_1 = 0.918 \left|-1, \frac{1}{2}\right\rangle - 0.194 \left|0, -\frac{1}{2}\right\rangle - 0.343 \left|1, \frac{1}{2}\right\rangle \tag{5.12}$$

the spin $S = 1/2$ state has slightly shifted to $(|0.918|^2 + |-0.343|^2) \left|\uparrow\right\rangle = 0.96 \left|\uparrow\right\rangle$ and $|-0.194|^2 \left|\downarrow\right\rangle = 0.04 \left|\downarrow\right\rangle$ whereas the $S = 1$ state is strongly polarized in the $|0.918|^2 \left|-1\right\rangle = 0.84 \left|-1\right\rangle$ state with contributions from $|-0.194|^2 \left|0\right\rangle = 0.04 \left|0\right\rangle$ and $|-0.343|^2 \left|-1\right\rangle = 0.12 \left|1\right\rangle$. To grasp the importance of this polarization we simplify all eigenstates in table 5.2 to their highest contribution, e.g. for $\left|\psi\right\rangle_1$ in equation 5.14:

$$\left|\psi\right\rangle_1 \approx \left|-1, \frac{1}{2}\right\rangle . \tag{5.13}$$

As the combined system is always in the ground state $\left|\psi\right\rangle_1$ or $\left|\psi\right\rangle_2$ at our measurement temperature of around 1.4 K, we identify the following possible excitations, I_{fi} (red and blue matrix elements in table 5.3):

$$I_{31} \mathrel{\widehat{=}} |\psi\rangle_1 \rightarrow |\psi\rangle_3 \Rightarrow (-1,\uparrow) \rightarrow (+1,\uparrow) \Rightarrow \Delta m_z = +2, 0 \tag{5.14}$$

$$I_{41} \mathrel{\widehat{=}} |\psi\rangle_1 \rightarrow |\psi\rangle_4 \Rightarrow (-1,\uparrow) \rightarrow (-1,\downarrow) \Rightarrow \Delta m_z = 0, -1 \tag{5.15}$$

$$I_{32} \mathrel{\widehat{=}} |\psi\rangle_2 \rightarrow |\psi\rangle_3 \Rightarrow (+1,\downarrow) \rightarrow (+1,\uparrow) \Rightarrow \Delta m_z = 0, +1 \tag{5.16}$$

$$I_{42} \mathrel{\widehat{=}} |\psi\rangle_2 \rightarrow |\psi\rangle_4 \Rightarrow (+1,\downarrow) \rightarrow (-1,\downarrow) \Rightarrow \Delta m_z = -2, 0 \tag{5.17}$$

$$\boldsymbol{I}_{\mathbf{51}} \mathrel{\widehat{=}} |\psi\rangle_1 \rightarrow |\psi\rangle_5 \Rightarrow (-1,\uparrow) \rightarrow (0,\uparrow) \Rightarrow \Delta m_z = +1, 0 \tag{5.18}$$

$$I_{61} \mathrel{\widehat{=}} |\psi\rangle_1 \rightarrow |\psi\rangle_6 \Rightarrow (-1,\uparrow) \rightarrow (0,\downarrow) \Rightarrow \Delta m_z = +1, -1 \tag{5.19}$$

$$I_{52} \mathrel{\widehat{=}} |\psi\rangle_2 \rightarrow |\psi\rangle_5 \Rightarrow (+1,\downarrow) \rightarrow (0,\uparrow) \Rightarrow \Delta m_z = -1, +1 \tag{5.20}$$

$$\boldsymbol{I}_{\mathbf{62}} \mathrel{\widehat{=}} |\psi\rangle_2 \rightarrow |\psi\rangle_6 \Rightarrow (+1,\downarrow) \rightarrow (0,\downarrow) \Rightarrow \Delta m_z = -1, 0 \tag{5.21}$$

where $\Delta m_z = \Delta m_z^s, \Delta m_z^t$ is the necessary change in angular momentum for the spin 1 system on the sample and the spin 1/2 system on the tip. Since each transition must conserve angular momentum and energy we can immediately see that a change of $\Delta m_z = +2, -2$ is highly unlikely if we only consider single electron tunneling processes. Furthermore we only let the CoH $S = 1$ system flip its spin during the tunneling process as the Co/Pt system is correlated with respect to the CoH system. Since we observe the asymmetry mainly in the second excitation we select the $\boldsymbol{I}_{\mathbf{51}}$ and $\boldsymbol{I}_{\mathbf{62}}$ transitions for further investigation shown in figure 5.12c.

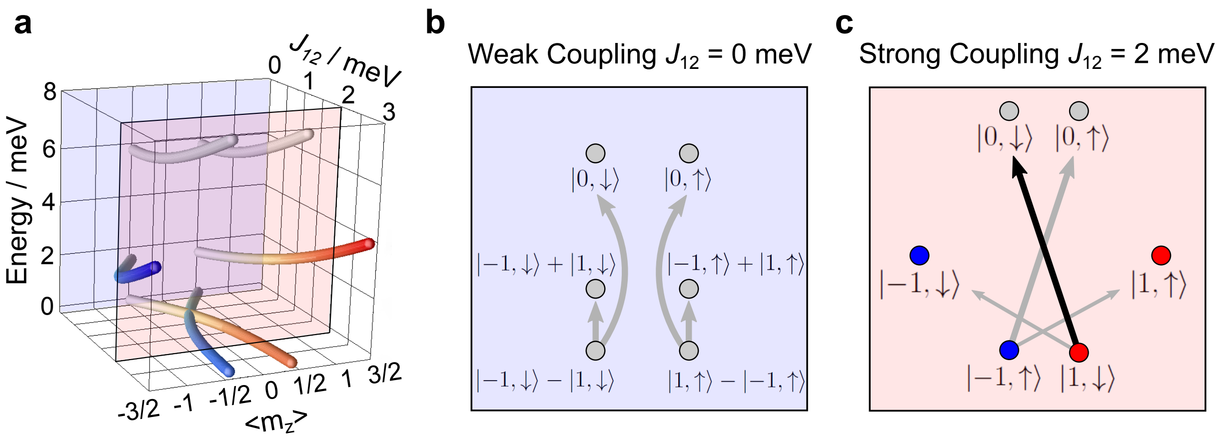

Figure 5.12: State evolution of the coupled spin system. (a) Simulated evolution of the state energies and the total magnetic moment, m_z^t, of the coupled spin system $S_1 = 1$ and $S_2 = 1/2$ with Heisenberg coupling J_{12}. The color shows the projected magnetic moment of the $S_1 = 1$ subsystem where grey: $m_z^1 = 0$, blue: $m_z^1 = -1$ and red: $m_z^1 = -1$. Two cuts at J_{12} = 0 meV and 2 meV are shown in (b) and (c). The grey arrows show the main contributions of the possible transitions from the groundstates to the excited states of the coupled spin system. The bold black arrow highlights an example for the second transition that is referred to in the text.

The highlighted transition in figure 5.12c (bold black arrow):

$$\boldsymbol{I_{62}} \mathrel{\widehat{=}} |\psi\rangle_2 \rightarrow |\psi\rangle_6 \Rightarrow (+1, \downarrow) \rightarrow (0, \downarrow) \Rightarrow \Delta m_z = -1, 0 \tag{5.22}$$

serves as an example to explain the arising asymmetry at high coupling strengths. The $S_1 = 1$ subsystem undergoes a change in angular momentum $\Delta m_z^s = -1$ from $m_z^s = +1$ to $m_z^s = 0$ while the $S_2 = 1/2$ subsystem stays in the $m_z^t = -1/2$ state. This means that the tunneling electron providing the energy for this excitation must also provide a change of $\Delta m_z = +1$ to conserve the total angular momentum. This can only happen if in the same m_z projection the tunneling electron scatters from $|\downarrow\rangle$ to $|\uparrow\rangle$ ($\downarrow \rightarrow \uparrow \Rightarrow \Delta m_z = 1$).

Let us now return to the density matrices that we have introduced to describe the different electron baths in tip and sample. It does make a difference whether the electron is tunneling from the sample to tip (ST) or from tip to sample (TS) as it will start and end in different density of states that prefer certain scattering events. The voltage polarity determines the tunneling direction: For positive bias voltages ($V_\mathrm{B} \in [0, +15]$ meV) the electron traverses from tip to sample. For negative bias voltages ($V_\mathrm{B} \in [0, -15]$ meV) the electron traverses from sample to tip. As the sample harbors the unperturbed electron bath with $\hat{p}_\mathrm{S}$ and the tip a skewed population with $\hat{p}_\mathrm{T}$, the situation is different for each direction. For an afm correlation (C < 0) the tip's electron density is polarized in the $|\uparrow\rangle$ state as the S_2 system is in the $|\downarrow\rangle$ state for both the groundstate and the excited state, whereas the substrate electrons stay unpolarized. The TS pathway allows that the electron stays in the same state ($\uparrow \rightarrow \uparrow \Rightarrow \Delta m_z = 0$) or scatters into a $\downarrow$ state ($\uparrow \rightarrow \downarrow \Rightarrow \Delta m_z = -1$). Both possibilities do not allow the necessary change of $\Delta m_z = 1$ and are thus prohibited. In the same manner the ST pathway allows ($\uparrow \rightarrow \uparrow \Rightarrow \Delta m_z = 0$) or ($\downarrow \rightarrow \uparrow \Rightarrow \Delta m_z = 1$) which meets the requirement and the excitation is enhanced. Thus, the correlation between the spin on the Pt tip and its electron bath can be determined by direct exchange coupling to a second spin system in a tunnel junction.

Simulations up to second order sum over all possible transitions of the matrix elements shown in table 5.3. To simulate the resulting spectrum of the coupled spin system all matrix elements are evaluated with their density matrices for the electron baths in tip and sample according to equations 5.10 for the initial and final states depending on the bias voltage polarity as shown in figure 5.13 in the filled (ST) and lined (TS) color coded regions. Therefore two sets of matrix elements are calculated: M_{fiea}^{ST} for the ST transitions and M_{fiea}^{TS} for the TS transitions. The Scilab[2] code used for the simulations is displayed in the appendix of this thesis. The higher order approach and additional details are provided in [102].

---

[2] Programmed and tested with Scilab version 5.5.2.

M_{fiea}	$\|\psi\rangle_1$		$\|\psi\rangle_2$		$\|\psi\rangle_3 - \|\psi\rangle_6$ not considered
$\|\psi\rangle_1$	M_{1111}	M_{1112}	M_{1211}	M_{1212}	$T << E_{3-6}$
	M_{1121}	M_{1122}	M_{1221}	M_{1222}	
$\|\psi\rangle_2$	M_{2111}	M_{2112}	M_{2211}	M_{2212}	
	M_{2121}	M_{2122}	M_{2221}	M_{2222}	
$\|\psi\rangle_3$	M_{3111}	M_{3112}	M_{3211}	M_{3212}	
	M_{3121}	M_{3122}	M_{3221}	M_{3222}	
$\|\psi\rangle_4$	M_{4111}	M_{4112}	M_{4211}	M_{4212}	
	M_{4121}	M_{4122}	M_{4221}	M_{4222}	
$\|\psi\rangle_5$	M_{5111}	M_{5112}	M_{5211}	M_{5212}	
	M_{5121}	M_{5122}	M_{5221}	M_{5222}	
$\|\psi\rangle_6$	M_{6111}	M_{6112}	M_{6211}	M_{6212}	
	M_{6121}	M_{6122}	M_{6221}	M_{6222}	

Table 5.3: Matrix transition elements for a coupled $S_1 = 1$ and $S_2 = 1/2$ system. All three states are twofold-degenerate and therefore six transitions need to be taken into account: Transitions from the groundstate to the groundstate (green), from the groundstate to the first excited state (red) and from the groundstate to the second excited state (blue) are summed up according to the bias voltage ($|V_B| > E_f - E_i$) as shown in figure 5.13 in which the colors refer to the used matrix elements M^{ST}_{fiea} and M^{TS}_{fiea}.

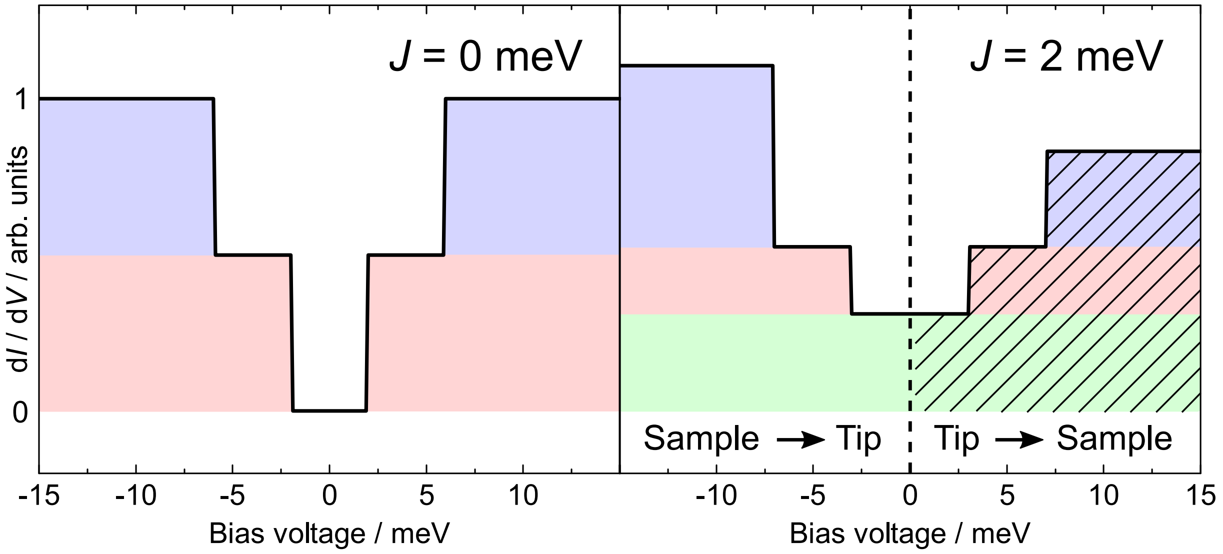

Figure 5.13: Simulated spectra for a coupled spin system ($C = -0.5$, $D = -5$ meV and E = 1 meV). The color coded regions show the used matrix elements from table 5.3 to account for the observed transition intensities. Depending on the bias voltage, the tunneling direction controls the possible scattering events of the tunneling electrons (filled vs. lined regions).

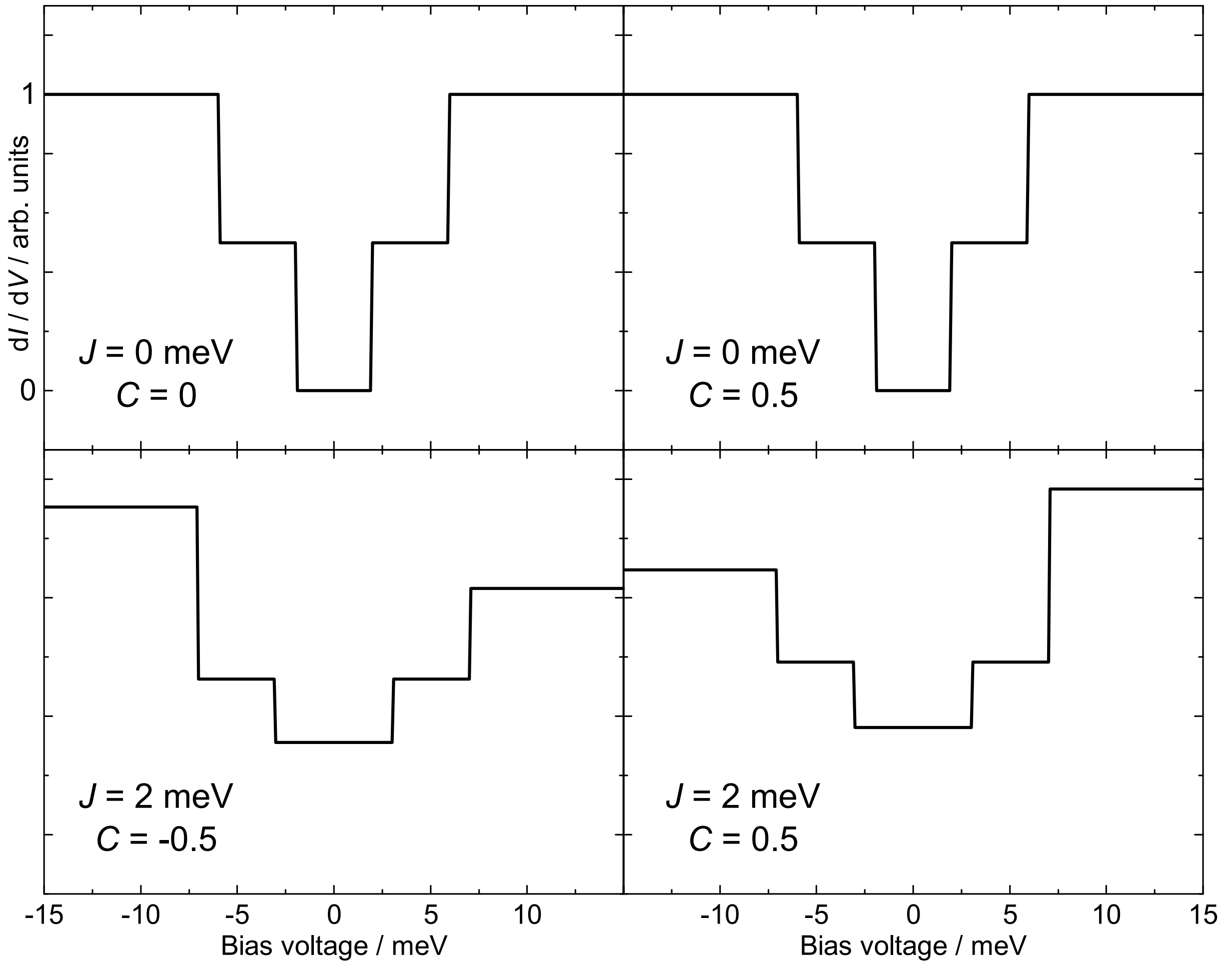

Figure 5.14: Scilab simulations with added coupling, $J_{12} = J_x = J_y = J_z$, between the CoH $S_1 = 1$ and Co/Pt $S_2 = 1/2$ systems as well as the correlation, C, between the Co/Pt $S_2 = 1/2$ system and the bath electrons in the Pt metal tip. The magnetic anisotropy of the CoH system is: D = -5 meV and E = 1 meV. From the simulations we can see that the correlation has no observable effect on the spectrum if the coupling is negligible. Only at sufficiently high coupling strengths the effect of the correlation begins to show and leads to the observable asymmetry in the outer excitation step around ± 7.5 meV.

The two extensions, the exchange coupling term with J_{12} and the density matrices based on the correlation, C, in the Co/Pt tip, to the established spin Hamiltonian model have proven to be able to reproduce the observed experimental results. We can now simulate the shifts in energy and the asymmetry in transition intensities. The evolution of the excitation steps in energy allows us to fit J_{12} according to figure 5.11 and to find the proportionality factor between this coupling J_{12} and the setpoint conductance G_{S}. Once the coupling strength matches the energy evolution of the eigenstates we can then proceed to fit the correlation, C, to match the observed asymmetry evolution. The best fits to the energy evolution of the two excitation steps and their asymmetry observed in the experimental datasets in figures 5.8, 5.9 and 5.10 are displayed in figures 5.15, 5.16 and 5.17. To show the validity of the model, third order fits are shown in figure 5.18 that reproduce the spectral evolution of the datasets extremely well. For the observed asymmetry in the differential conductance we define η_i for the inner and η_o for the outer step as follows:

$$\eta = \frac{h_n - h_p}{h_n + h_p} \tag{5.23}$$

where h_n is the intensity of the steps at negative and h_p the intensity of the steps at positive voltages following the convention for spin-polarized spectra obtained in magnetic fields [99].

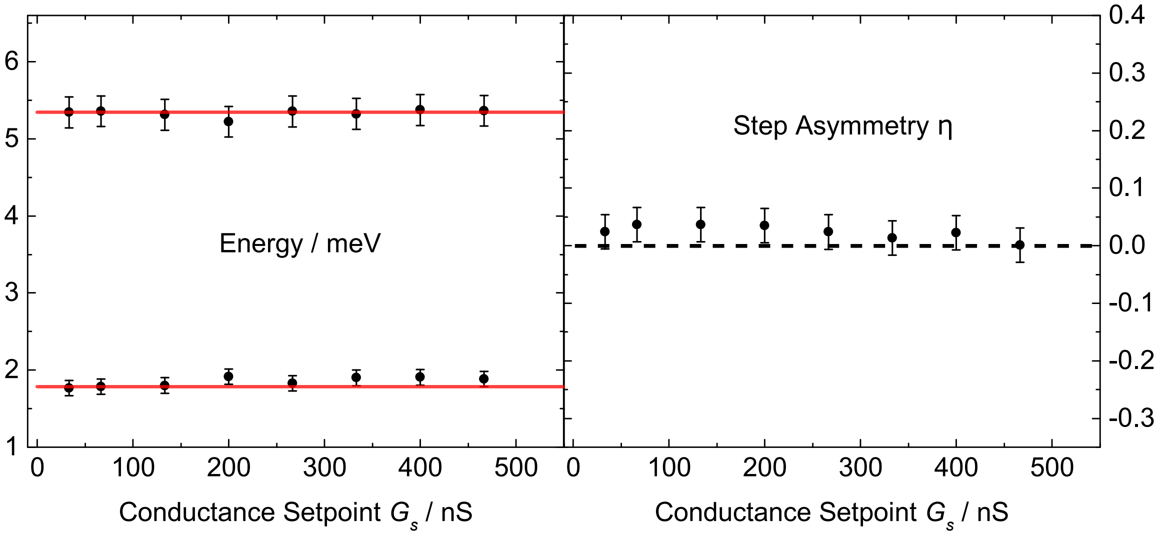

Figure 5.15: Approach of a CoH $S = 1$ system with a bare Pt tip. Energies and asymmetries are derived from the experimental dataset in figure 5.8. Within the errorbars, the energy positions of the two excitation steps at around 1.7 meV and 5.4 meV as well as the asymmetry of the outer excitation step do not deviate from their original values even for high conductance setpoints of almost 500 nS. We therefore conclude that the approach of a CoH system with a bare Pt tip has neither an effect on the system's magnetic anisotropy nor leads it to the occurrence of an asymmetry. The errorbars are half the FWHM of the Gaussian fits to the derivative of the differential conductance.

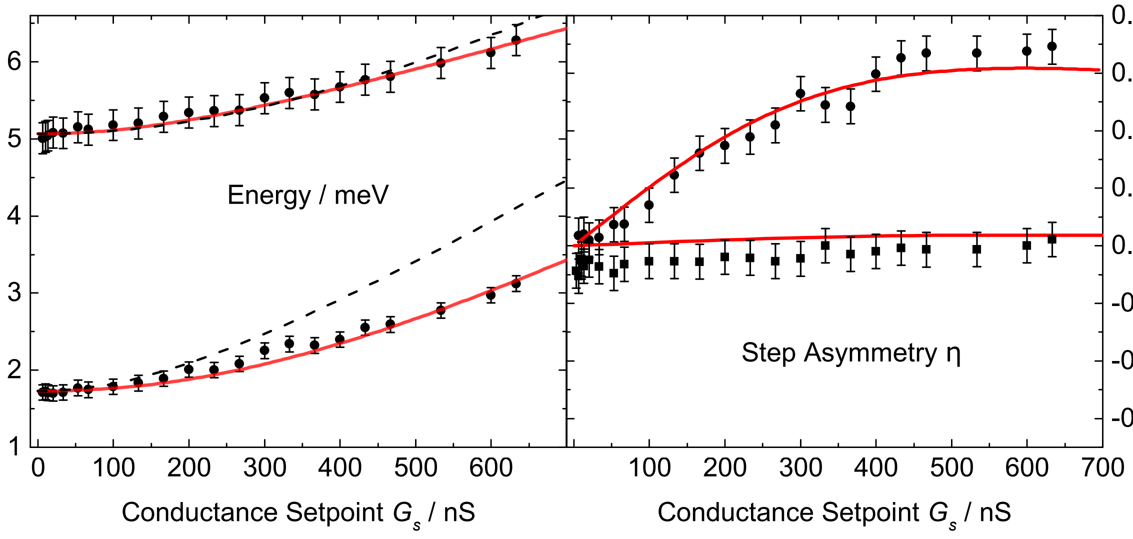

Figure 5.16: Approach of a CoH $S = 1$ system with a Co-functionalized tip for the experimental dataset in figure 5.9. The evolution of both excitation steps to higher energies is modeled with a Heisenberg coupling ($J_{12} = J_x = J_y = J_z$) of $J_{12} = 3.6\mu$eV/ nS x G_S. The asymmetries of the outer and inner (close to zero) excitation steps are modeled best with an antiferromagnetic correlation strength $C = -0.5$. The dashed lines show an Ising fit ($J_{12} = J_z$) to the energy evolution.

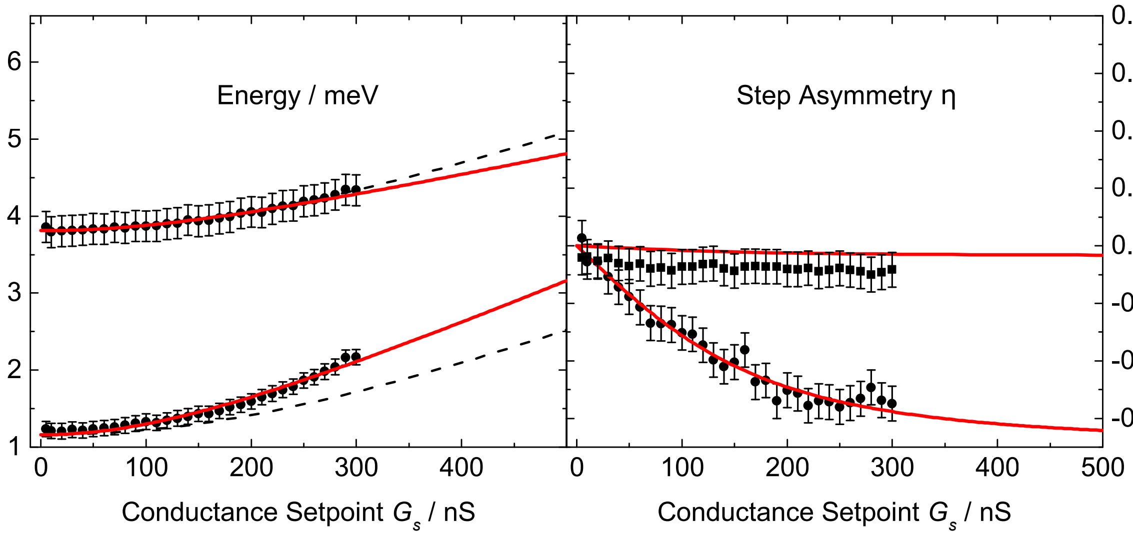

Figure 5.17: Approach of a CoH $S = 1$ system with a Co-functionalized tip for the experimental dataset in figure 5.10. The evolution of both excitation steps to higher energies is modeled with an Ising coupling ($J_{12} = J_z$) of $J_{12} = 5.9\mu$eV/ nS x G_S. The asymmetries of the outer and inner (close to zero) excitation steps are modeled best with a ferromagnetic correlation strength $C = 0.35$. The dashed lines show a Heisenberg fit to the energy evolution.

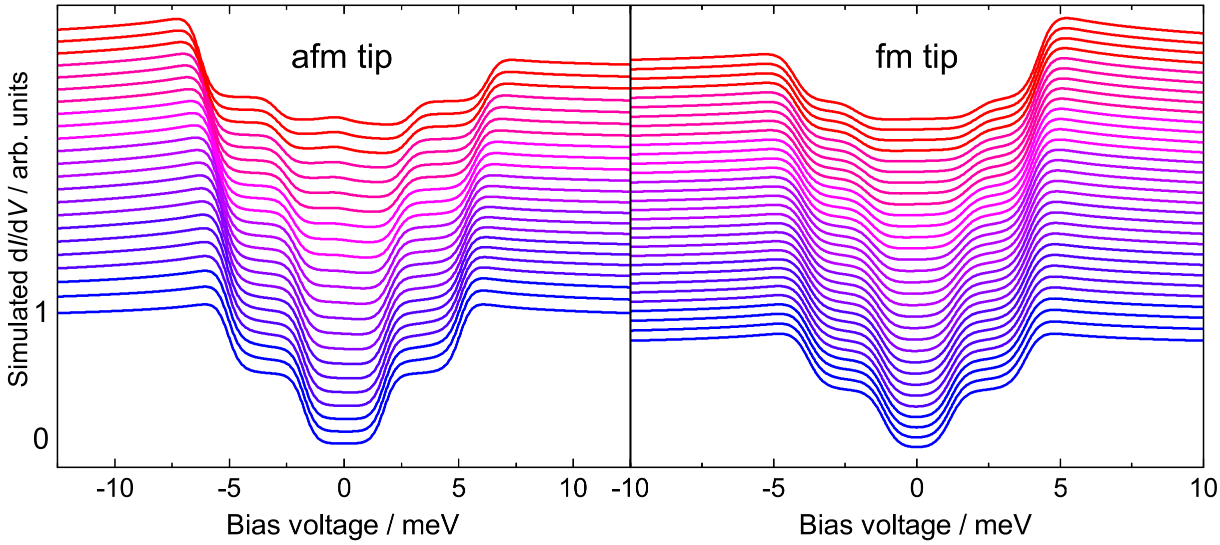

Figure 5.18: Third order simulations for the coupled spin systems in figure 5.9 and 5.10 that were mainly different in their Co/Pt tip correlation that was antiferromagnetic for the dataset in figure 5.9 and ferromagnetic for 5.10. The spectral evolution is extremely well reproduced and even the zero bias feature for the afm tip spectra is occuring in the simulation.

From the fits to the datasets we can deduce that two different Co/Pt tips do exist. One in which the Co atom ($S_2 = 1/2$) is antiferromagnetically correlated with the Pt electron bath and one that shows a ferromagnetic correlation. Yet we can only speculate about the possible reasons that could lead to these two different regimes. Although the CoH $S_1 = 1$ system is well defined and characterized on the h-BN/Rh(111) surface even allowing us to fit the magnetic anisotropy and the Kondo exchange with the Rh metal at low coupling strengths, the Co/Pt tip apex cannot be imaged in the same way. We are therefore dependent on monitoring the vertical-manipulation process and comparing the tip spectroscopy on the h-BN/Rh(111) before and after manipulation. Comparing the spectroscopy with previous experiments on Co atoms on a Pt(111) surface gives similar results but in most cases the spin system is spectroscopically dark as it is strongly hybridized with the Pt metal. Different adsorption sites or neighboring Co atoms on the Pt tip apex could strongly influence the magnetic behavior of the S_2 system and even lead to an afm or fm correlation. Further experiments in an inverted geometry in which the sample harbors a strongly correlated system and the tip apex a decoupled $S_1 = 1$ system with magnetic anisotropy would allow for a complete characterization and could be interesting for further experiments.

5.4 Measurements in magnetic field

At an applied magnetic field of 5 T normal to the sample surface we observe the typical Zeeman shift of a CoH $S = 1$ system as shown in figure 3.17. If we use a Co-functionalized tip we also see signs of spin polarization that lead to an asymmetry in the spectrum. The blue curve in figure 5.19a shows these effects for low coupling strenghts. If we increase the coupling between the CoH system and the Co/Pt tip we can reverse the effect of the magnetic field and obtain a spectrum that resembles the unperturbed case of the CoH system at zero field. The evolution is important as it gives reason to distinguish whether the coupling J_{12} is antiferromagnetic or ferromagnetic. The comparison with simulations show that only an afm coupling reproduces the results in magnetic field.

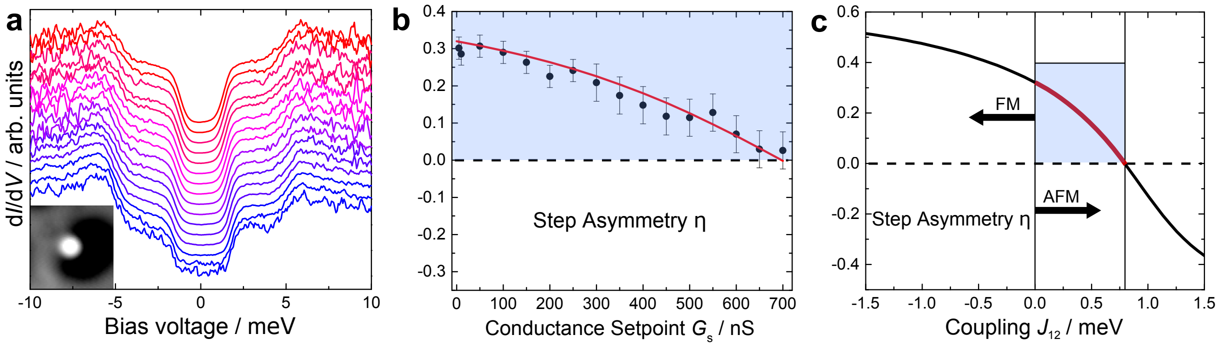

Figure 5.19: Evolution of a CoH complex coupled with a Co/Pt tip in magnetic field B_z = 5 T. (a) The spectrum of the CoH system for low coupling strengths (blue curve at a setpoint conductance of G_S = 20 nS) with $J_{12} = 1.1\mu$eV/nS x G_S, shows the Zeeman shift due to the magnetic field and the spin polarization of the tip. By increasing the coupling strength up to G_S = 700 nS (red curve) the effects of the magnetic field seem to be undone. The energy positions of the excitation steps shift to magnetic anisotropy values of D = 4.05 meV and E = 0.65 meV at 0 T, the intensity of the two excitation steps becomes similar and the asymmetry is brought back to zero. The inset shows an STM constant current image of the CoH system at -10 mV and 10 pA. (b) The Ising-like afm coupling and a ferromagnetic correlation $C = 0.6 \pm 0.05$ yields a good fit to the asymmetry evolution with the conductance setpoint. (c) A simulation that takes both, afm and fm, coupling into account shows that only a considered afm coupling ($J_{12} > 0$) can reproduce the observed evolution of the asymmetry in magnetic field. The blue shaded regions in (b) and (c) label the same range for the asymmetry.

5.5 Lifetime broadening

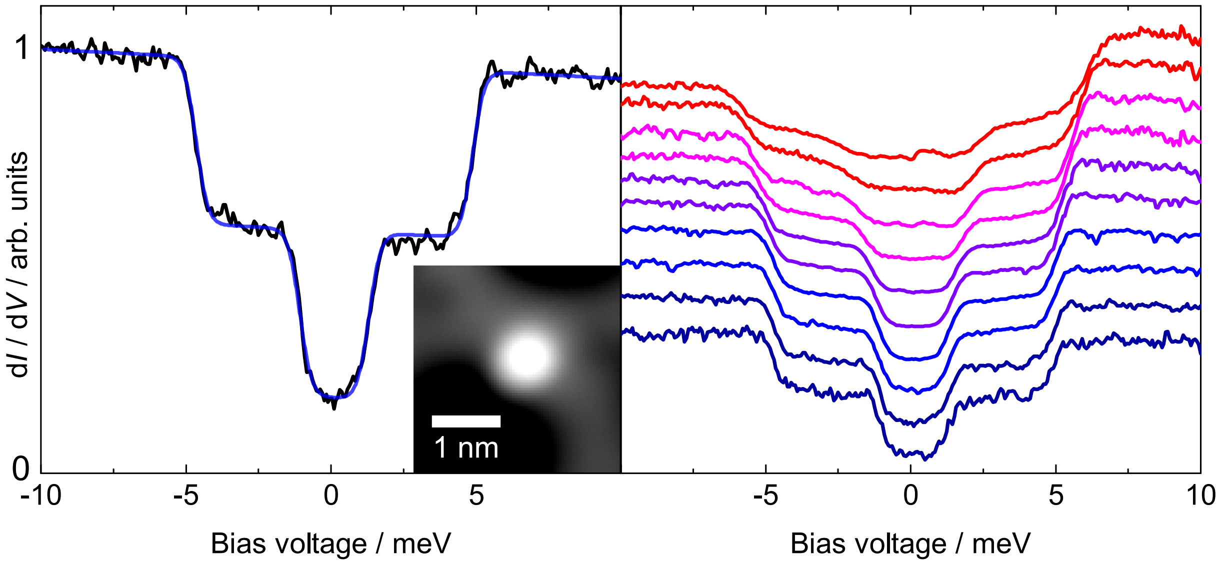

Figure 5.20: Example of a coupled system on the rim region of the h-BN with large lifetime broadening. The fit to the unperturbed CoH system at low conductance setpoints leads to magnetic anisotropy parameters of: $D = -4.2$ meV and $E = 0.6$ meV. The Kondo exchange coupling, $J\rho_s$, of the CoH system with the Rh metal is almost zero, maybe due to the adsorption site on the rim region further away from the Rh metal as compared to the datasets in figures 5.8 to 5.10 in which the CoH systems are closer to the valley regions of the h-BN decoupling layer. Approaching the system with a fm Co/Pt tip leads to a significant broadening especially for the excitations at negative bias.

As discussed in chapter three, the lifetime of the excited states can strongly influence the broadening of the steps in the $\mathrm{d}I/\mathrm{d}V$ spectrum and the derived $\mathrm{d}^2I/\mathrm{d}^2V$ peaks. We know that the temperature and lock-in parameters stay constant during the approach of the CoH systems with Co/Pt tips, which leaves us with the lifetime of the states as one of the possible reasons for the observed broadening of the steps visible in the experimental dataset evolution in figure 5.20 where the red spectrum at high coupling strengths shows a significantly broadened step compared to the blue low coupling spectrum. The derivatives of the differential conductance for these two spectra are shown in figure 5.21. A Gaussian fit to the FWHM yields the values in table 5.4. The broadening of the Gaussian peaks ranges between 0.4 and 0.9 meV which would infer a lifetime decrease from around 0.8 ps to 0.4 ps according the Heisenberg uncertainty principle ($\Delta E \Delta t \geq \hbar/2$). It is not yet understood why the lifetime decreases for higher coupling strengths. A possible reason for the dominance of this effect in the presented dataset could be the low Kondo exchange coupling of the CoH $S = 1$ system to the h-BN/Rh(111) substrate. Normally the Kondo exchange coupling induces scattering events between the adsorbed spin and the conduction electrons that could reset the excited states back to the groundstates. The coupling to another spin system that is strongly hybridized could provide such a scattering source hence leading to shorter lifetimes.

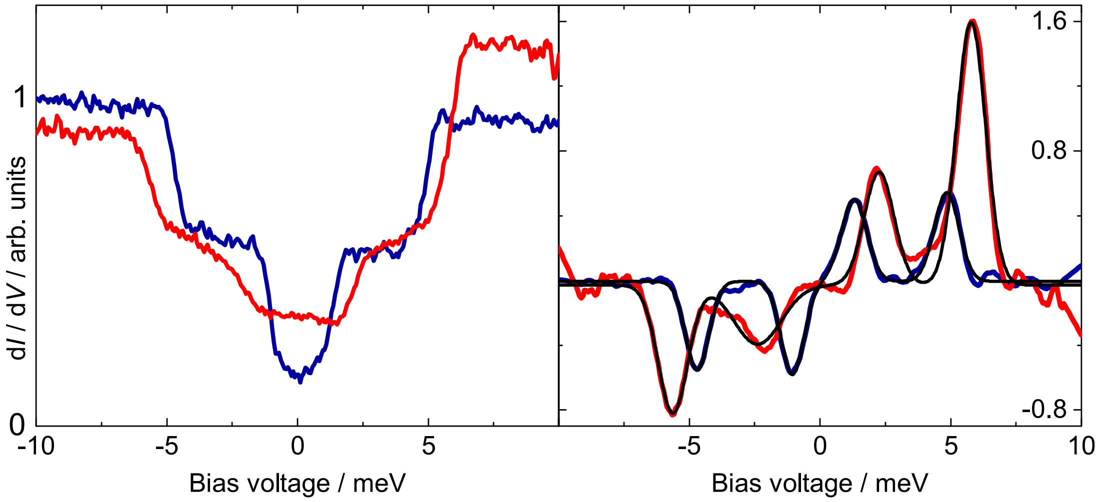

Figure 5.21: Two spectra from the dataset in figure 5.20 in direct comparison (Second spectrum from the bottom and second from the top). The derivative shows that the energies have shifted and the FWHM of the Gaussian-like peaks is significantly increased when the spectrum at high coupling strengths (red curves) is compared to the one for low coupling strengths (blue curves).

	Step position	**Energy / meV**	**FWHM of Gaussian fit**
Low coupling $J_{12} \rightarrow 0$ **meV**	Outer -V_B	-4.69 ± 0.01	1.05 ± 0.02
	Inner -V_B	-1.05 ± 0.01	1.04 ± 0.02
	Inner +V_B	$+1.30 \pm 0.01$	1.15 ± 0.02
	Outer +V_B	$+4.84 \pm 0.01$	1.12 ± 0.02
High coupling $J_{12} \rightarrow 1$ **meV**	Outer -V_B	-5.80 ± 0.03	1.46 ± 0.07
	Inner -V_B	-2.66 ± 0.07	1.96 ± 0.19
	Inner +V_B	$+2.54 \pm 0.03$	1.55 ± 0.09
	Outer +V_B	$+6.01 \pm 0.01$	1.69 ± 0.04

Table 5.4: Derived energies and FWHM values of the two spectra for the lowest and highest coupling strength in figure 5.20. The FWHM increase for high coupling by almost 1 meV is significant, especially for negative voltages at which the transition intensities are damped (red colored cells). The energy difference between the step positions at positive and negative voltages are due to an overall voltage offset that is neutralized if the take the average energy of the step positions at both voltage polarities.

5.6 Coupled and correlated Kondo systems.

As discussed in chapter three, not only CoH systems with $S = 1$ signatures are observed but also CoH_2 systems exist that exhibit a Kondo resonance. This Kondo resonance splits in an applied magnetic field B_z normal to the sample surface with the expected linear Zeeman shift in energy. Similar to the previous subsections, we can couple a Co-functionalized tip to such Kondo systems as sketched in figure 5.22 and shown in figure 5.23. At B_z = 4 T and $J \to 0$ meV for large z distances, the splitting between the $|\uparrow, \uparrow\rangle$ and the $|\downarrow, \downarrow\rangle$ states is roughly 1 meV while the two states at zero energy are not affected and remain degenerate ($|\uparrow, \downarrow\rangle + |\downarrow, \uparrow\rangle$ and $|\uparrow, \downarrow\rangle - |\downarrow, \uparrow\rangle$). When the Co-functionalized tip that is effectively described as a $S = 1/2$ Kondo system is brought in close proximity to the CoH_2 Kondo system on the sample, the exchange coupling leads to a further energy splitting of the four eigenstates of the coupled spin system. While figure 5.22 only sketches the simulated energy evolution, the spectral evolution of the Kondo systems are shown for experimental datasets in figure 5.23. In these datasets, an asymmetry is observed that is explained with the same correlation in the Co-functionalized tip as introduced in the previous subsections. The question about the nature of the transition for intermediate coupling strengths around 0.5 meV remains (compare red shaded ellipse in figure 5.22). The energy resolution in the experimental dataset for a Co/Pt tip in 4 T is too broad to determine the precise energy evolution of the two lowest states around $J \approx 0.5$ meV.

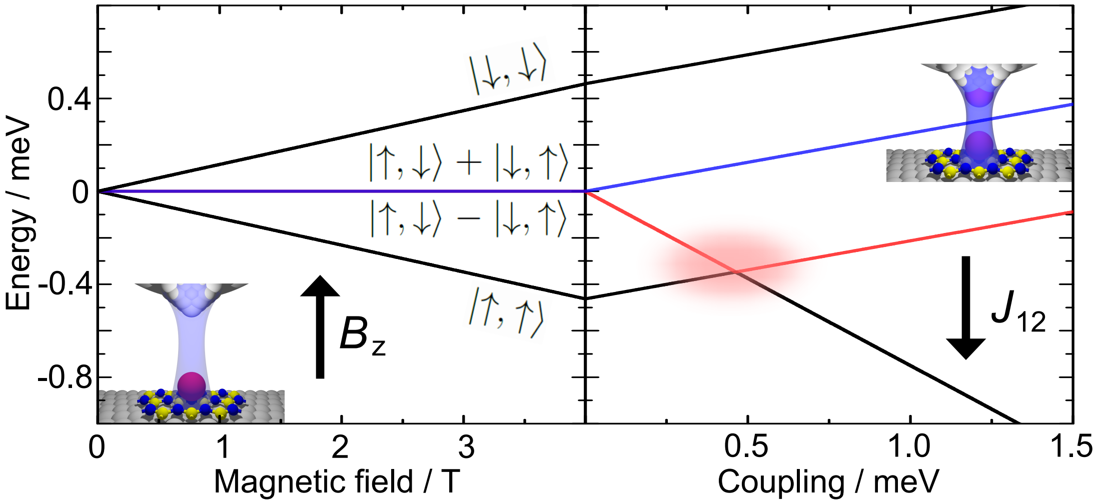

Figure 5.22: Simulated energy evolution of a coupled $S = 1/2$ and $S = 1/2$ system (Singlet, triplet states in ket notation). An applied magnetic field $B_z = 4$ T breaks the degeneracy of the four originally degenerate eigenstates at low coupling strengths $J \to 0$ meV. When the two $S = 1/2$ systems are brought in close proximity to each other by approaching with the Co-functionalized tip, the exchange coupling further splits the eigenstates and leads to a crossing of the two lowest eigenstates (red and black curves).

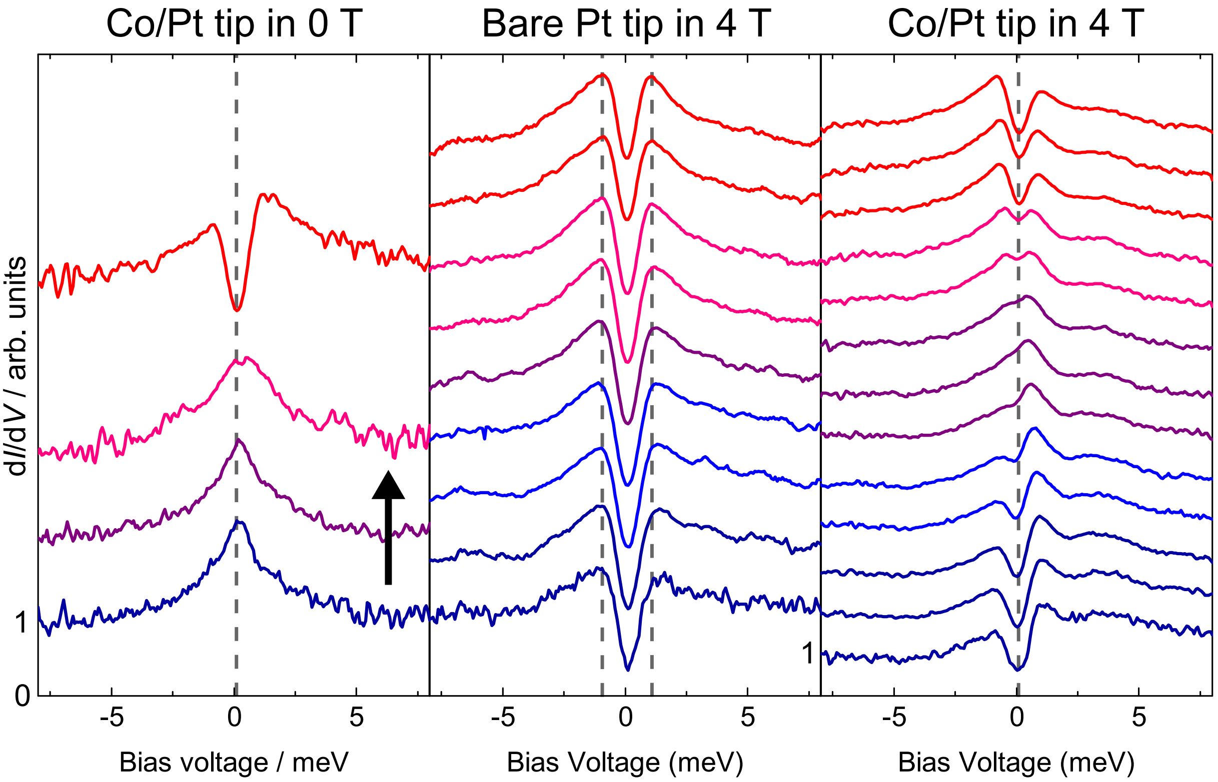

Figure 5.23: Experiments with correlated Kondo systems at 1.3 K. Left: A Co-functionalized tip approaches a CoH_2 system at zero field from $G_S = 1.72 \cdot 10^{-4} G_0$ (blue curve) up to $G_S = 2.58 \cdot 10^{-3} G_0$ (red curve) which leads to an exchange coupling induced splitting of the Kondo resonance and an asymmetry of the peak intensities for different bias voltage polarities. Middle: Approaching a split CoH_2 Kondo resonance at B_z = 4 T with a bare Pt tip from $G_S = 8.60 \cdot 10^{-5} G_0$ to $G_S = 6.02 \cdot 10^{-3} G_0$ does not change the spectral shape. Right: Approaching a split CoH_2 Kondo resonance at B_z = 4 T with a Co-functionalized Pt tip from $G_S = 8.60 \cdot 10^{-5} G_0$ to $G_S = 5.16 \cdot 10^{-3} G_0$ (at -15 mV and 0.1, 0.5, 1, 1.5, 2, 2.5, 3, 3.5, 4, 4.5, 5, 5.5, 6 nA) leads to an energy shift as depicted in figure 5.22 and a change in asymmetry that can be modeled with a change from an fm correlation to afm correlation in the Co/Pt tip.

The original motivation for coupling spin systems on tip and sample was to measure a change of the exchange coupling as a force signal between the two systems. Let's assume that both spin systems, S_1 on the sample and S_2 on the tip, are both aligned along the field direction of an applied magnetic field. Now, when the spin systems are being brought closer to each other there is a distance or coupling strength that favors afm instead of fm coupling. The energy difference between those two coupling regimes should lead to an observable signal in the frequency shift for an $\Delta f(z)$ approach and retract curve. Simulations carried out by Jasper van Veen [103] showed that indeed, this signal is visible as a repulsive force prior to the attractive part of the potential landscape. The approach of the CoH_2 resonance with a Co-functionalized tip shown in figure 5.23 was also executed with an oscillation amplitude of A = 50 pm in a similar conductance regime to that of the state crossing around 0.5 meV. The resulting datasets are shown in figure 5.24. We conclude that the force curve does not show any unusual change compared to the usual datasets shown in chapter four. A subsequent approach sequence for shorter tip sample separations (- 50 pm) led to the dislocation of the CoH_2 Kondo system on the sample. A stronger magnetic field or a lower oscillation amplitude could enhance the signal for future measurements. Also, a more suitable surface on which the magnetic atoms are more stable during approach would allow for force curves at shorter tip sample distances.

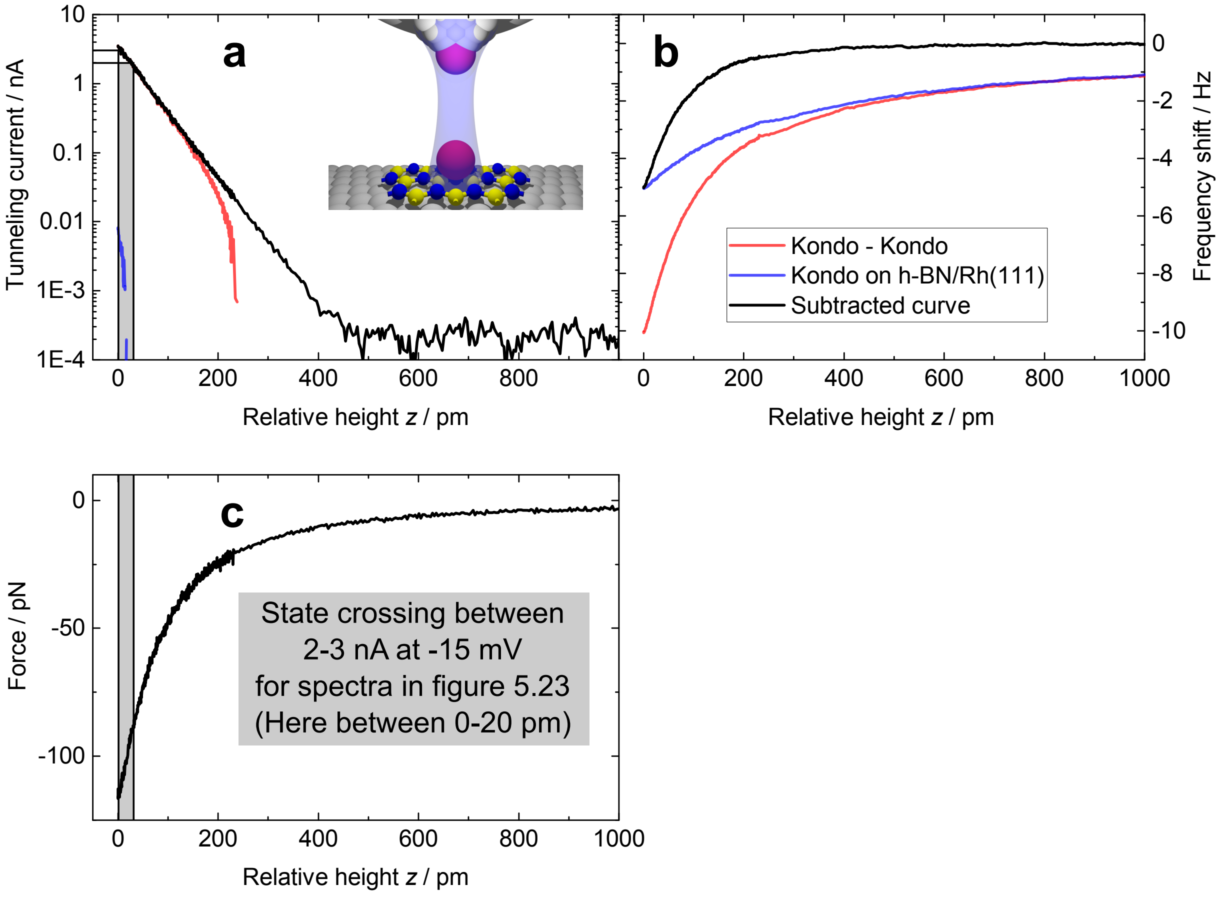

Figure 5.24: Approach curve over the same Kondo system in figure 5.23 at 4 T and 1.3 K with a Co-functionalized tip. The starting point at 230 pm is set by a setpoint conductance of V_B = -15 mV and I_T = 20 pA from which the approach and retract curves were taken. (a) and (b) show the subtracted curves for the tunneling current and frequency shift contributions. The deconvoluted force signal in (c) (A = 50 pm) shows no significant deviations from the common approach curves over CoH_x systems compared to chapter four. Comparing the conductance at -15 mV with the spectroscopic dataset in figure 5.23 defines the grey shaded distance region in which we expect the exchange force signal of the state crossing.

5.7 Discussion

This chapter has shown how spin-spin correlations can lead to an observable asymmetry in the differential conductance. We were able to control this asymmetry by tuning the exchange coupling strength between two spin systems in which the decoupled CoH spin system on the h-BN/Rh(111) surface served as a sensor in the sense that its polarized eigenstates made it susceptible to the Co/Pt tip correlations by angular momentum selection rules in electron transport. The magnetic anisotropy of the CoH system is crucial for this behavior as its transverse magnetic anisotropy term, E, is responsible for mixing the m_z^s = -1, +1 states so that the average magnetization remains zero. Coupling this CoH system to another spin system on the tip effectively polarizes the eigenstates to specific m_z^s = -1, +1 projections (compare figure 5.12a) which makes it highly sensitive to the correlation effects in the Co/Pt tip. The effect of the E term strength on the observed asymmetries is simulated in figure 5.26.

Even though STM experiments allow for a precise characterization of the sample, the tip structure is mostly unknown and needs to be indirectly determined by keeping track of the history during vertical atom manipulation events and taking into account topographic features as well as the tip spectroscopy on the bare h-BN/Rh(111) background. The mostly unknown structure of the Co/Pt tip system leads to speculations about the exact cause of the different afm and fm correlations between the Co system on the Pt tip and the conduction electrons in the Pt metal that have been observed for different Co/Pt tips. The sharp topography that was always present for a Co-functionalized Pt tip suggests that we are scanning with an atomic orbital of the Co atom and also perform IETS using these orbitals. So the next question would be: Where do the correlations actually originate from? Are they directly present in the involved orbitals or is it the correlation with the nearby Pt electron bath? These two cases are equivalent in our experimental setup and an additional measurement in between the two coupled spins would be necessary to determine the exact correlation at every point of the transition from bath-tip-sample-bath or back.

While we previously only distinguished between Heisenberg ($J_{12} = J_x = J_y = J_z$) and Ising-like ($J_{12} = J_z$) coupling to fit the energy evolution to the coupling strength, we could also allow other ratios between the xyz-components[3] as well as their sign as we fixed the coupling to be positive (afm) based on the measurements in magnetic field. A fit to the two datasets from figure 5.9 and 5.10 is shown in figure 5.25 where we also allow negative coupling strengths (fm). Although this would fit the data well, we discard this approach as the tunneling current is exponentially dependent on the distance, z, between the two spin systems and is proportional to the coupling strength which would exclude for example a dipolar-dipolar interaction that is

---

[3] To account for e.g. dipolar-dipolar coupling

proportional to z^{-3}. Furthermore, the measurements in magnetic field show that in this case, only afm coupling is able to describe the evolution of the asymmetry back to zero.

The most probable reason for the difference in afm and fm correlations is the Co atom configuration on the Pt tip apex. Not only the adsorption site (e.g. fcc, hcp for Pt(111)) changes the spin signature and coupling to the substrate but also the number of direct neighbors or the proximity to other Co atoms from previous vertical manipulation events could influence the effective correlation. As mentioned in the introduction chapter, Co atoms on Pt(111) are special as they are known to induce a strong substrate polarization [11] [98] while being spectroscopically dark, i.e. non-descriptive, and have been employed for a variety of theoretical approaches and experiments that focus on the substrate interactions (compare table 1.1). At this point we can only speculate about the exact origin of the two different tip behaviors but have clearly shown that this difference exists, can be modeled with a correlation strength, and does not depend on the CoH_x sample systems.

A similar asymmetry was observed for coupled quantum dots where its origin was attributed to potential scattering [104]. We simulate the possible outcome of such potential scattering, U, included in the Kondo exchange Hamiltonian: $\boldsymbol{\sigma} \cdot \boldsymbol{S} + U$, and its influence on the spectral evolution in [92] and conclude that it would primarily lead to an overall slope of the spectrum and only has a minor influence on the inner step asymmetry that could even explain the offset to our simulations in figures 5.16 and 5.17 for the inner step.

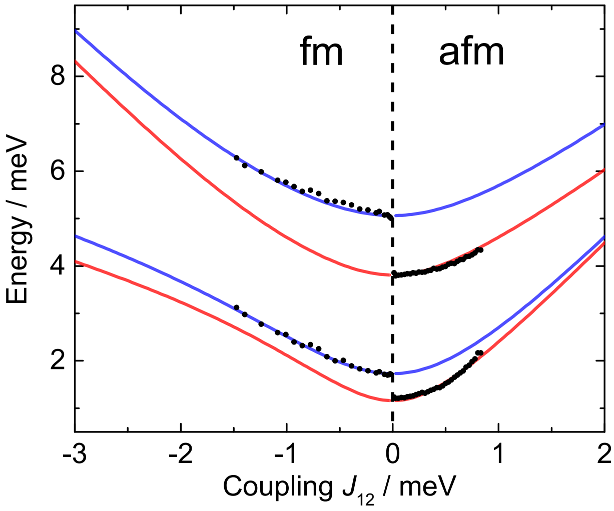

Figure 5.25: Fits to the energy evolutions shown in figure 5.16 (blue curves) and 5.17 (red curves) without restrictions. While we previously distinguished between Heisenberg ($J_{12} = J_x = J_y = J_z$) and Ising ($J_{12} = J_z$) for positive J_{12}, i.e. afm, we now also allow fm coupling. With this, both datasets are well fitted using the parameters $2J_x = 2J_y = J_z$.

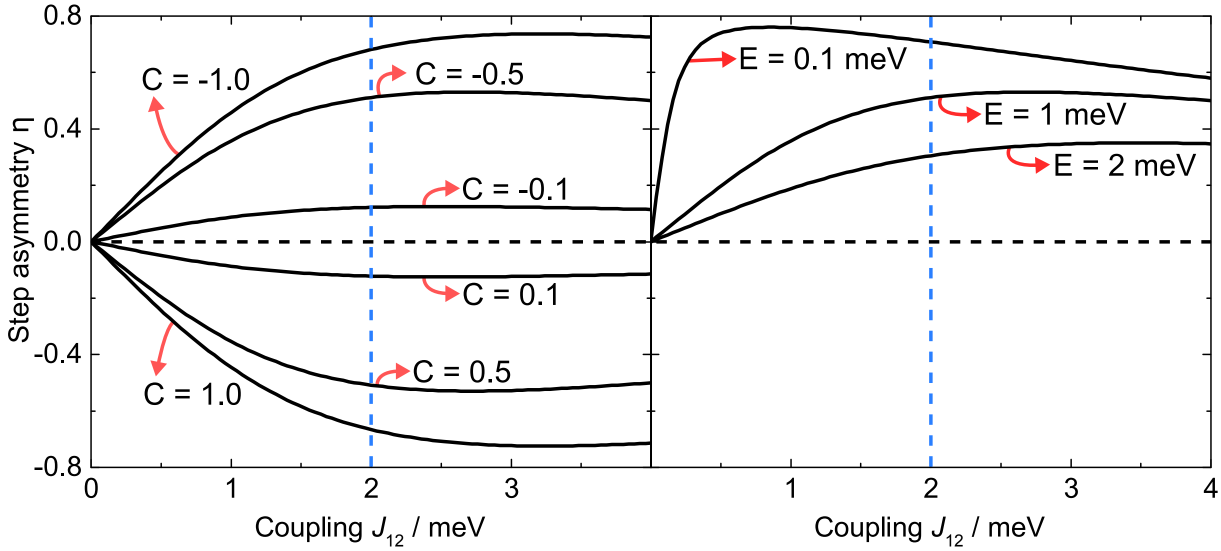

Figure 5.26: Evolution of η with J_{12} for different correlation strengths, C, in the Co/Pt tip and different transverse magnetic anisotropies, E, of the CoH $S = 1$ system on the sample. Left: With magnetic anisotropy parameters of D = -5 meV and E = 1 meV of the CoH system, the asymmetry saturates around 80 % even for the strongest correlations $|C| = 1$. Right: Changing the transverse anisotropy term, E, at a correlation strength of $C = -0.5$ shows the strong effect on the asymmetry due to different m_z^s polarizations in -1 and +1.

CHAPTER 6

SPIN MANIPULATION VIA A CONTROLLABLE HYDROGEN LIGAND

The main results of the following chapter were published in Science Advances, April 2017[1].

The difference between a $S = 1/2$ CoH_2 and a $S = 1$ CoH system only consists in one hydrogen atom as argued in chapter 3. Here we show how a hydrogen-functionalized tip that is brought in close proximity to a CoH system can reversibly change its topographic and spectroscopic signatures to that of a CoH_2 system. Simultaneous force and current measurements allow us to track the change between the two systems and complete the overall understanding with DFT calculations. Furthermore, outliers in which blunt but non-functionalized tips change the magnetic anisotropy and spin of CoH_x systems are correlated with force measurements.

---

[1] P. Jacobson, M. Muenks, G. Laskin, O. Brovko, V. Stepanyuk, Markus Ternes, Klaus Kern, "Potential energy driven spin manipulation via a controllable hydrogen ligand". (https://arxiv.org/abs/1609.00612); M.Muenks and P. Jacobson with equal contribution.

6.1 An STM tip functionalized as a hydrogen ligand

The vertical atom manipulations of CoH$_x$ systems with the Pt tip to create Co-functionalized tips as outlined in the beginning of the last chapter led to events in which the hydrogen instead of the cobalt atom moved to the tip apex. The typical features of such H-functionalized tips in the STM topography are shown in figure 6.1 and exhibit a similar sharp contrast change for similar functionalized tips [105] [106] [107] [108] [109] especially on metal hydride atoms [110]. The resulting sharp topographic contrast of around 20 pm on the h-BN/Rh(111) surface is localized at parts of the dipole ring near the rim regions around the h-BN valley regions, the same region where the CoH$_x$ systems preferentially bind to [111] [112]. Scanning with the H-functionalized tip over these trapping potentials that periodically repeat along the h-BN surface leads to a repeating pattern depending on the tip shape. The tip apex is most likely not symmetric and offers an abundance of different adsorption positions for the hydrogen which could explain the different periodic patterns that were observed on the h-BN surface for different H-functionalized tips.

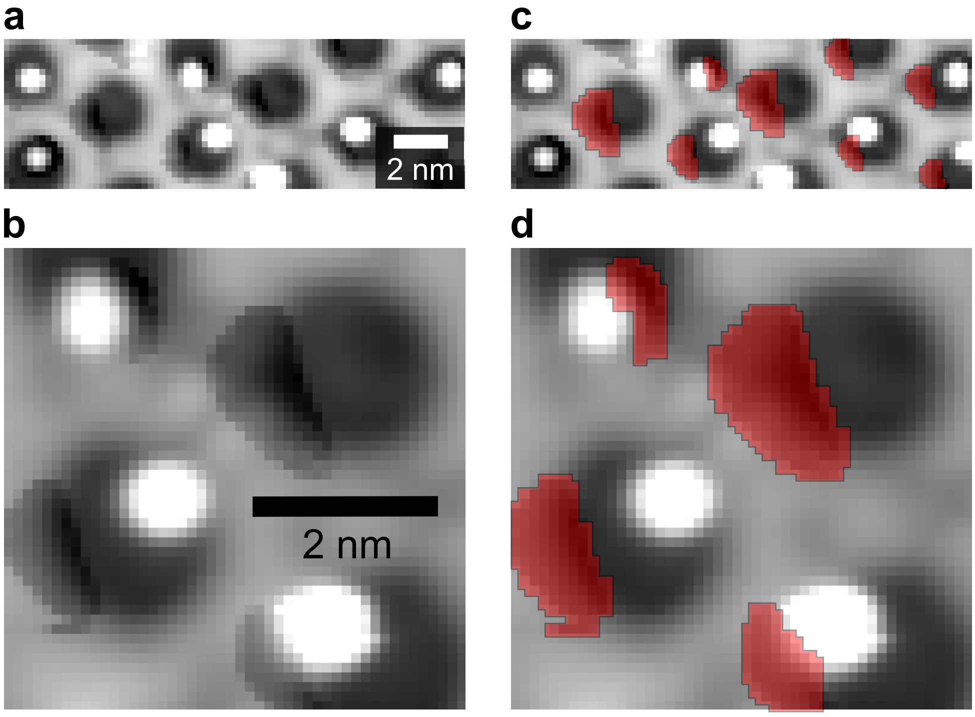

Figure 6.1: Signs of hydrogen in STM topography. (a) and (b) show constant current STM topography images taken at I_T = 20 pA and $V_B = -100$ mV (equivalent to a conductance of $G = I_T/V_B = 2.58 \cdot 10^{-6} G_0$). Besides the h-BN/Rh(111) sample and a few CoH$_x$ systems, a distinct height contrast ($\Delta_z = 20$ pm) is visible at similar rim regions of the h-BN surface. This contrast is visually enhanced with a red overlay in (c) and (d). The image size in (b) and (d) is kept to 4096 px.

6.2 Switching the magnetic state from CoH to CoH$_2$

When the H-functionalized tip images a CoH $S = 1$ system, the sharp topographic feature from figure 6.1 overlaps with the CoH system. At large separation distances at STM scanning conditions with a tunneling setpoint conductance of around $|G| = I_T/V_B = 20\text{pA}/100\text{mV} = 2.58 \cdot 10^{-6} G_0$, no switching processes or changes in topography are observed. The $S = 1$ spectrum is the same on the entire area occupied by the CoH system shown in figure 6.2a. When bringing the H-functionalized closer to the CoH system by decreasing the bias voltage, a sharp jump in conductance and therefore height, is observed below -1.7 meV as shown in figure 6.2b-f for different bias voltages.

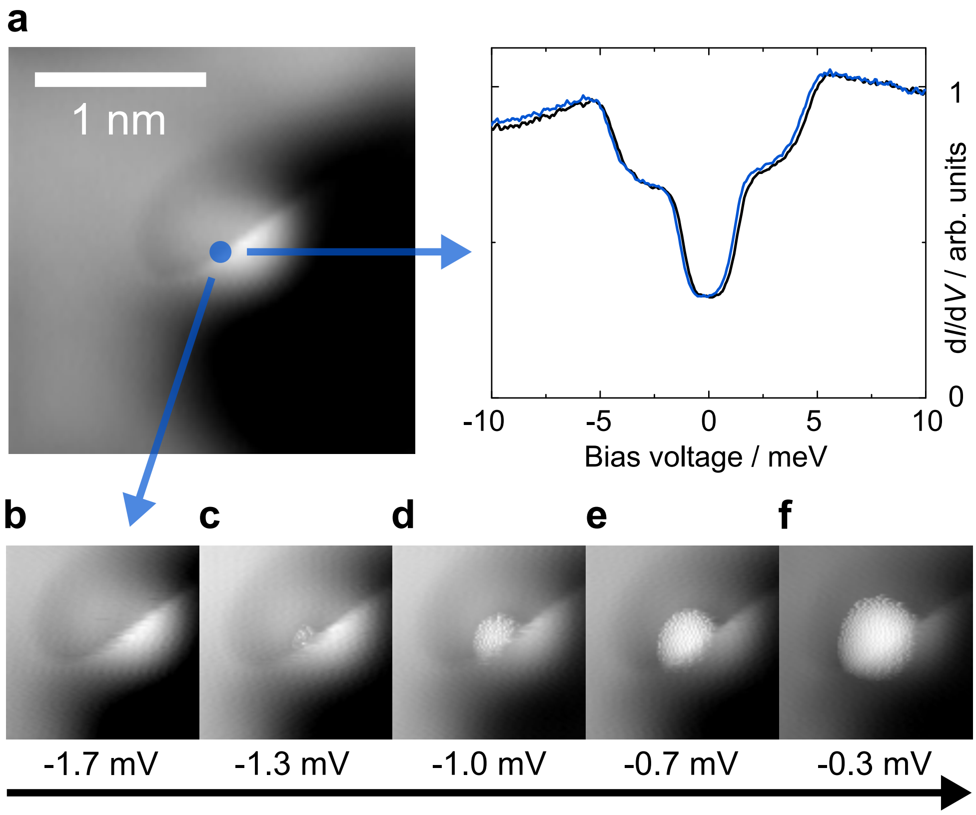

Figure 6.2: Topography of a CoH $S = 1$ system that is approached with a H-functionalized tip. (a) At typical scanning conditions of around 20 pA and -15 mV the sharp topographic hydrogen induced height difference of 20 pm simply overlaps with the underlying CoH system in constant current mode. STS yields the magnetic $S = 1$ state that was introduced in chapter 3 (black: forward sweep, blue: backward sweep). (b-f) Keeping I_T = 20 pA and lowering the bias voltage to -1.7 meV and below ($G = 1.51 \cdot 10^{-4} G_0$ to $8.60 \cdot 10^{-4}$) changes the topography drastically: At the edge where the hydrogen contrast overlaps with the CoH system, a bistable increase in the conductance is observed. This conductance change is confined to a noise speckled circle with the center still located at the edge of the overlap and its radius increasing for even shorter tunneling distances.

Together with the topographic change for shorter distances between the CoH system and the H-functionalized tip, also a change in the spectroscopic features is observed. Stabilizing the H-functionalized tip over the center of this CoH system (blue dot in figure 6.2a), the stable $S = 1$ signature at large separation distances changes to a stable Kondo resonance at short distances. In between, the spectra undergo a noisy transition region from which a Kondo resonance emerges. Comparing the topography with the spectroscopy we find that the Kondo resonance only occurs at short distances in the region in which the noise speckled circle emerges (compare figure 6.2f and figure 6.3 red circle in top right image). This dependency of the spectra on the topography for H-functionalized tips can be explained if we assume that the hydrogen at the tip apex prefers to bond to the CoH system when it is brought into close proximity. This process is mediated by the tip-sample distance set by the conductance setpoint and is completely reversible. Forward and backward $I(z)$ curves and spectra taken with a H-functionalized tip over CoH systems show that there is no sign of hysteresis and that the spectrum changes back from a Kondo resonance to a $S = 1$ spectrum once the tip is retracted (see figure 6.4).

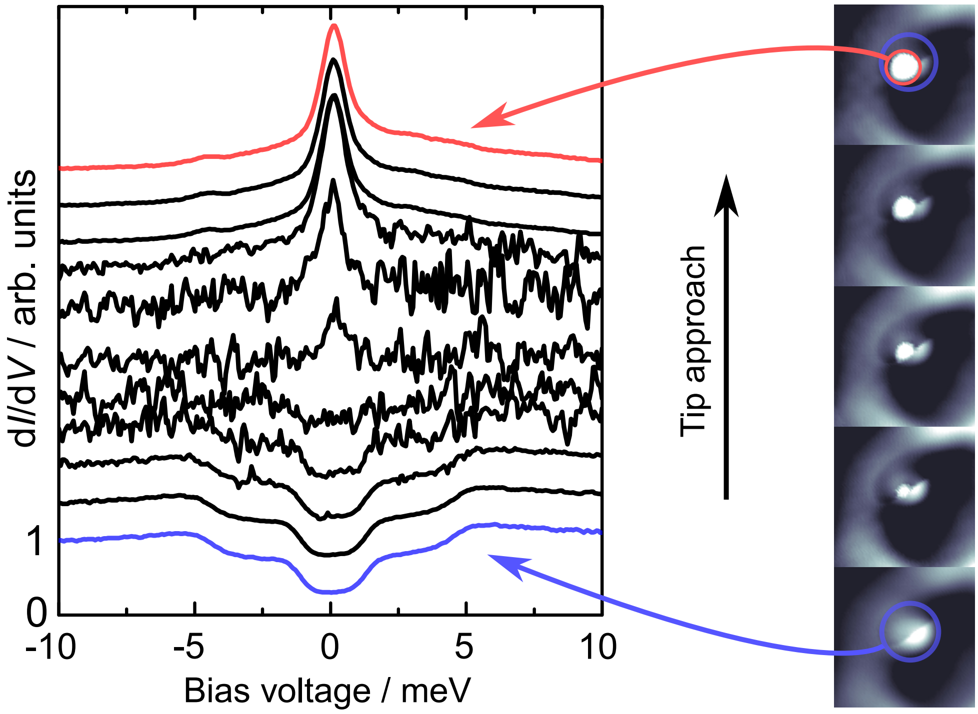

Figure 6.3: Spectroscopy taken over the center of the switching CoH system ranging from large tip-sample distances ($G_S = 6.45 \cdot 10^{-4} G_0$, blue $S = 1$ spectrum) to short distances ($G_S = 12.9 \cdot 10^{-4} G_0$, red Kondo resonance) in steps of $\Delta G_S = 0.16 \cdot 10^{-4} G_0$. The change in spectroscopy corresponds to the change in topography. All spectra are normalized and offset.

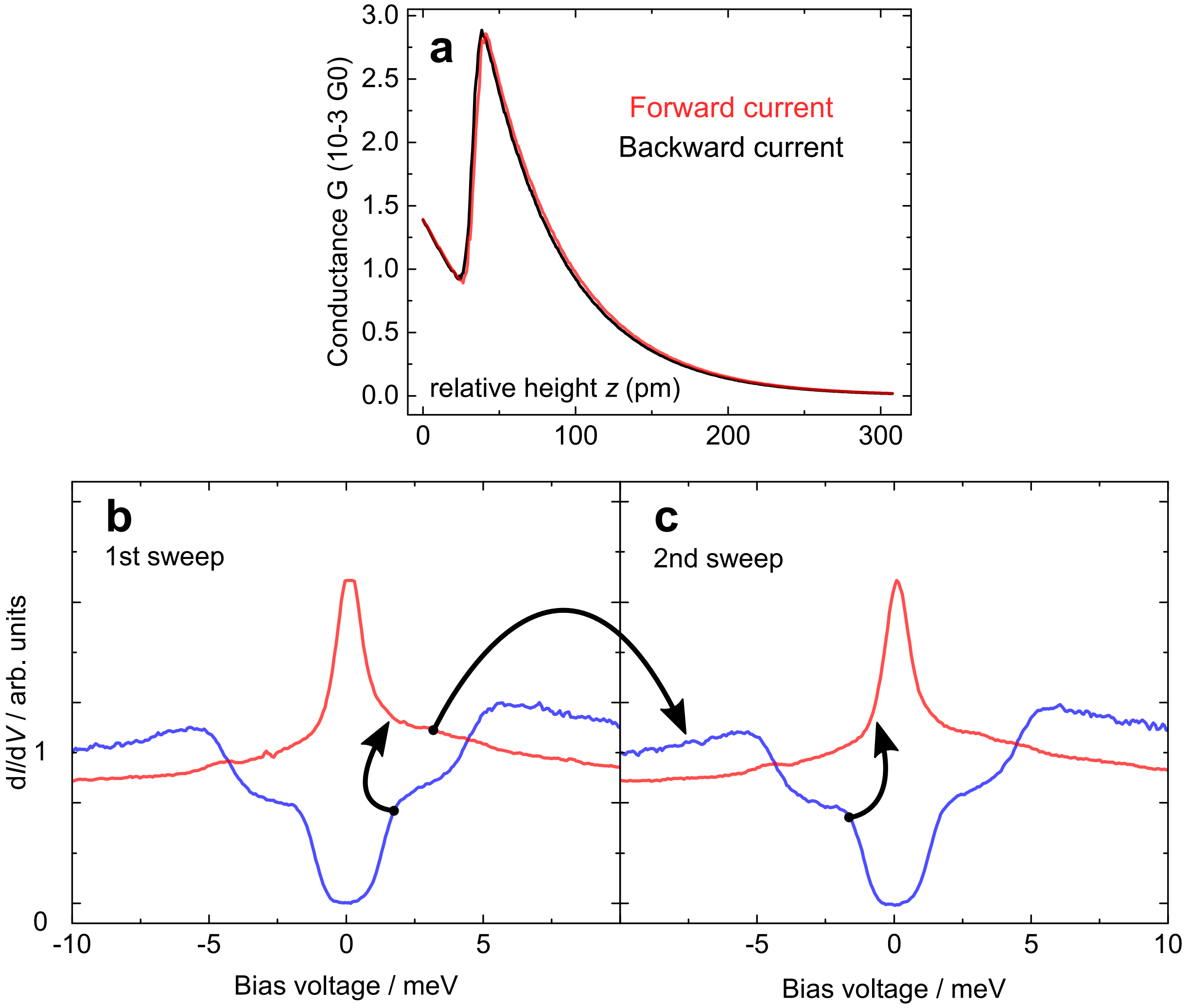

Figure 6.4: Reversibility of the switching process. $I(z)$ curves taken without tuning fork oscillation show the distinct jump to a lower conductance around 38 pm when a CoH system is approached with a H-functionalized tip. No signs of hysteresis are observed as the forward (red) and backward (black) curves match up and the conductance recovers back to its original value when the tip is retracted. (b) and (c): Two consecutive spectroscopy sweeps (black arrows) at low and high conductances taken over the same CoH system with a H-functionalized tip. After approaching the CoH system and observing the Kondo resonance the tip is withdrawn and reproduces the exact same CoH $S = 1$ spectrum as before.

6.3 Simultaneous force and current measurements complemented by theory

Now that the spectra and topographic changes have clearly shown that we can reversibly switch the spin state from a CoH spectrum to a CoH_2 Kondo resonance, we further employ the tuning fork for simultaneous current and force measurements on the switching complex. First, the tunneling current approach curves are shown in figure 6.5 to compare the exponential behavior without the influence of the tuning fork oscillation. From these curves we deduce that the H-functionalized tips follow a non-exponential $I(z)$ behavior in accordance with observations from other groups for similar functionalized tips [113]. Furthermore, DFT calculations carried out by Oleg Brovko show in figure 6.5c how the proximity of a H-functionalized tip can effectively change the magnetic d-orbitals of the CoH system. Details of the DFT calculations are accessible in [114].

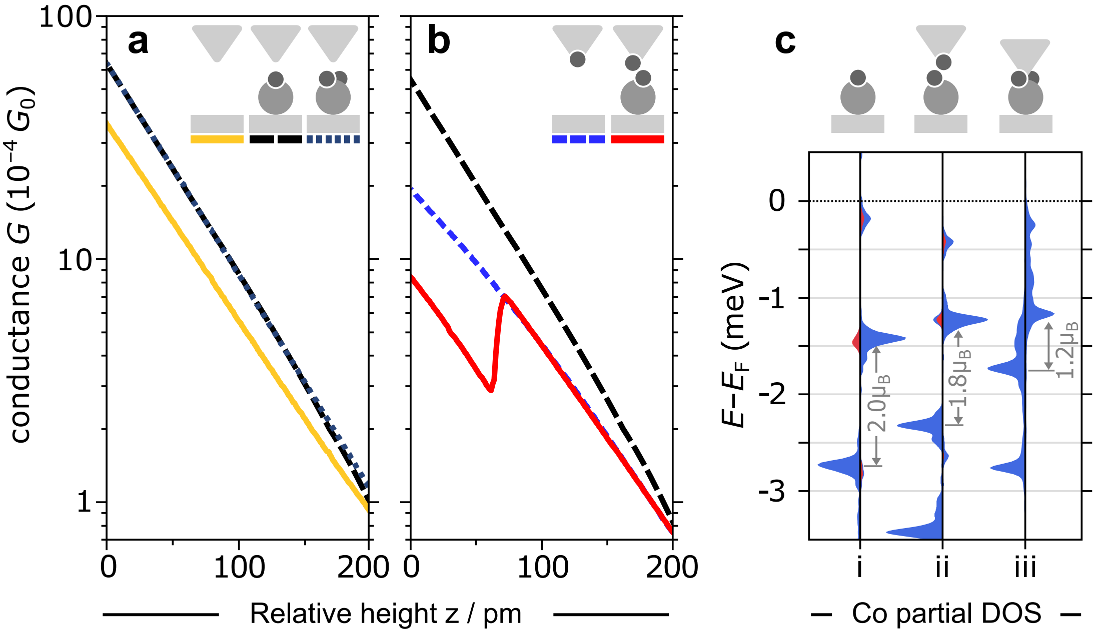

Figure 6.5: Conductance vs. distance spectroscopy. (a) $G(z)$ curves with a bare Pt tip on h-BN/Rh(111) (yellow), CoH (dashed black) and CoH_2 (dashed blue line) at V_B = -10 mV. (b) Repeating these curves with a H-functionalized tip yields non-exponential curves over the bare h-BN/Rh(111) surface (dashed blue curve) and a CoH system (red curve) with the distinct jump to lower conductance at around 70 pm. (c) Plots of the majority (left) and minority (right) spin projected density of states with the d-orbitals in blue and the sp orbitals in red of a CoH system. A simulated approach shows that the Stoner splitting (grey arrows) changes the magnetic moment from 2.0 μ_B for an unperturbed CoH system to 1.2 μ_B for close proximity of the H-functionalized tip, making it similar to a CoH_2 system.

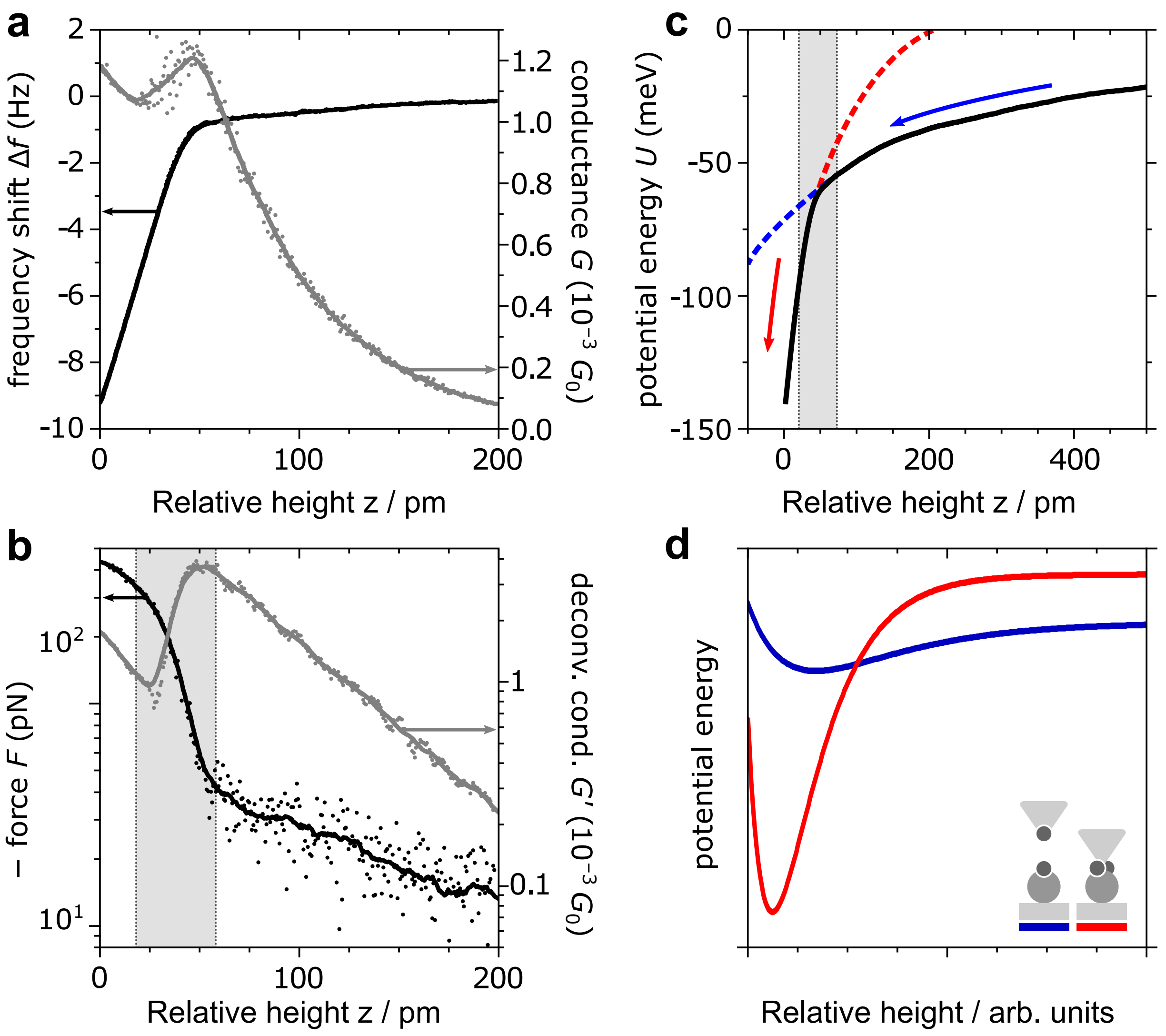

Figure 6.6: Simultaneous force and current measurements over the switching complex. (a) The raw datasets for the conductance and frequency shift with approach over a switching CoH system with a H-functionalized tip (Oscillation amplitude: 100 pm). The deconvoluted force and conductance in (b) show that the sharp drop to lower conductances, here at around 50 pm, coincides with a simultaneous force increase. (c) Integrating the force yields the potential energy (black curve) for the $S = 1$ to $S = 1/2$ transition. The point around 50 pm at which a lower potential landscape becomes accessible to the system is highlighted by the intersection of two fictitious lines (dashed blue and red curves) that are also shown in (d). The sudden dislocation of the hydrogen from the tip to the CoH system can be understood as a switch from the CoH potential curve (blue) to a CoH_2 potential curve (red). See the supplemental information of our publication [114] for the details of a DFT simulation that leads to a similar conclusion.

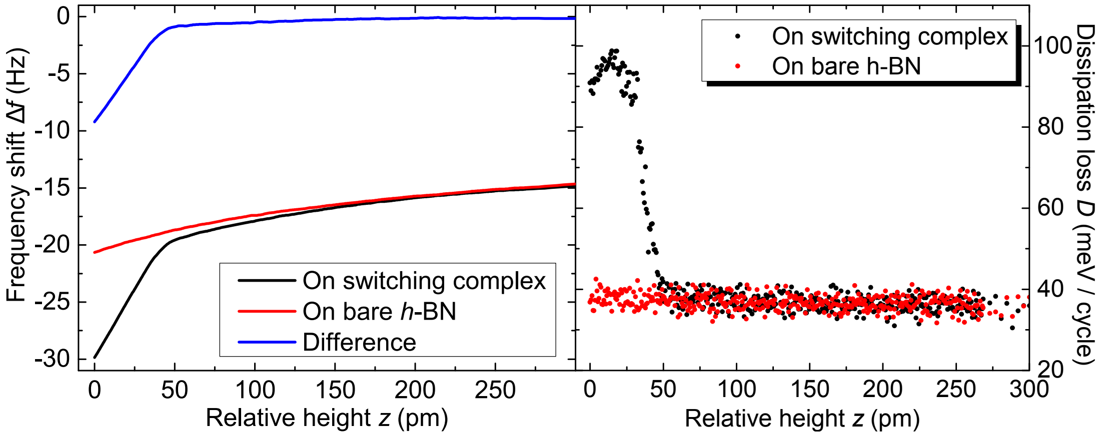

Figure 6.7: The original frequency shift curves over the switching CoH system and the h-BN layer from figure 6.6. The increase in power dissipation per cycle of around 55 meV corresponds to the same potential energy range covered by the tuning fork oscillation during the transition shown in figure 6.6c (grey area).

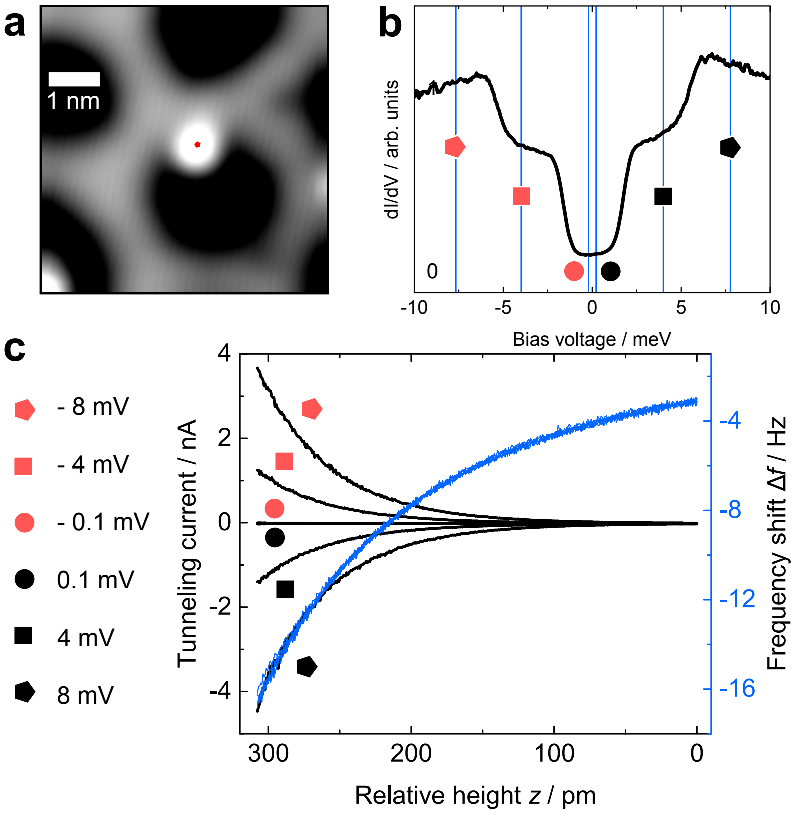

Figure 6.8: Bias and polarity dependent $\Delta f(z)$ curves over a CoH system. The negligible change in the frequency shift around 0.5 Hz (For V_B = -8 meV and 8 meV) is most likely due to the shift of the workfunction. Furthermore, we find that the transitions to excited states of the CoH system do not influence the frequency shift signal at this resolution.

6.4 Switching the magnetic state from CoH_2 to CoH

Non-functionalized Pt tips can lead to the removcal of the hydrogen atom for CoH_2 or CoH systems. Two of these cases are shown in this and the next subsection. Unlike the previous case in which a hydrogen atom is transferred from the tip to the Co system, no distinct change in the current is observed and only the change in the force signal coincides with the spectroscopic changes of the system.

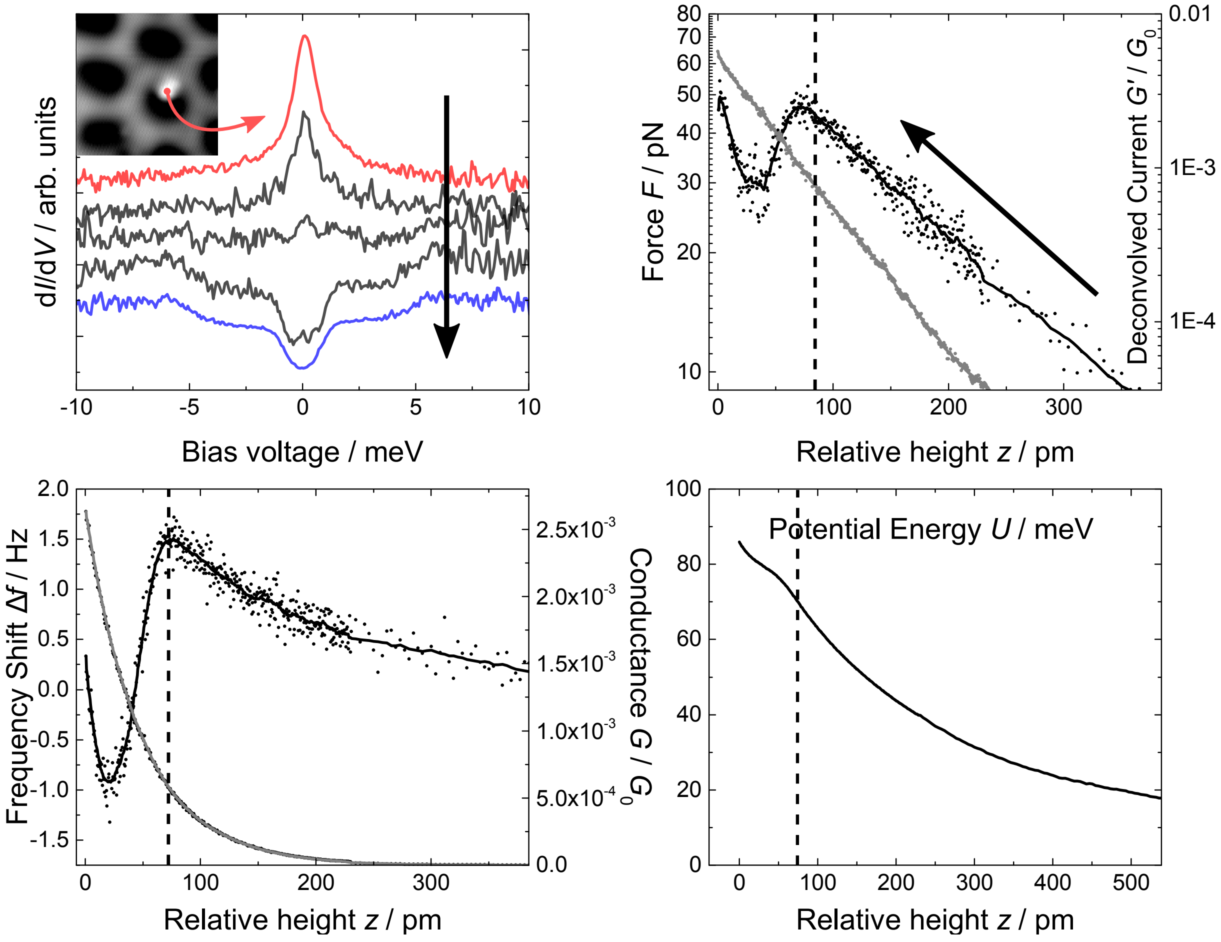

Figure 6.9: Rare observation of a switch from a CoH_2 $S = 1/2$ resonance to a CoH $S = 1$ with tip approach. The topography shows a non-functionalized Pt tip that is not atomically sharp as seen by the elliptic shape of the CoH system that also repeats for other nearby systems. Approach the CoH system in spectroscopy from low to high conductance setpoints follows a similar reversed transition as in figure 6.3. Simultaneous conductance and frequency shift measurements show that, unlike the previous case in the last three subsections, no distinct change in the current is observed and the exponential behavior is present for the entire approach and retract curves. However, a distinct signal in the frequency shift and also the deconvoluted force shows the change within the tunnel junction. The integrated force yields the potential energy potential that shows the transition point around 60 pm coinciding with the spectroscopic change.

6.5 Magnetic anisotropy changes with approach

Here we show simultaneous tunneling current and frequency shift measurements on a CoH system that was approached with a blunt tip. The spectroscopy in figure 6.11 shows that the transverse magnetic anisotropy, E, perishes when the tip is in close proximity. As argued in the introduction to the magnetic anisotropy of the CoH systems, the magnetic anisotropy, E, is likely to stem from the tilting of the hydrogen atom or the corrugation of the underlying h-BN/Rh(111) surface. The axial magnetic anisotropy, D, is due to the adsorption site on the N atom of the h-BN sheet resulting in a threefold symmetry. Thus, removing said hydrogen or pushing the h-BN sheet flat, could result in a negligible transverse term as it is observed here.

The manipulation shown in the previous subsection where the dislocation of a H atom from a CoH_2 system changed the magnetic signature from $S = 1/2$ to $S = 1$ was performed with a blunt tip apex that is visible in the STM topography showing similar distortions for all CoH_x systems. Contrary to the addition of a hydrogen atom from the H-functionalized tip and a distinct new favorable potential minimum as shown in subsection 6.3, the cases in this and the previous subsection both show a repulsive force that could stem from local distortions of the CoH_x complexes due to the tip proximity.

These cases however, were observed with non-functionalized Pt tips that show no deviating signatures in spectroscopy nor topography. Thus, all CoH and CoH_2 systems on h-BN/Rh(111) should be subject to manipulation when approached with a bare Pt tip. This was, however, rarely the case and the spectroscopy stayed remarkably stable until the tip gets to close leading to vertical manipulation of the CoH_x system. Hence, one could argue that the soft part of the h-BN layer is not as wide as it seems in STM topography as argued in chapter four, therefore leading to stable local h-BN layer for most of the CoH_x systems. Or it may be that a blunt tip is required to induce a larger tip impact upon approach of a CoH_x system as both manipulations of the magnetic anisotropy were performed with a blunt tip apex.

Changes and control of the magnetic anisotropy due to an induced change in the local crystal field have been observed before [115] where an STM tip mechanically changes the environment of a single iron(II) porphyrin molecule with approach.

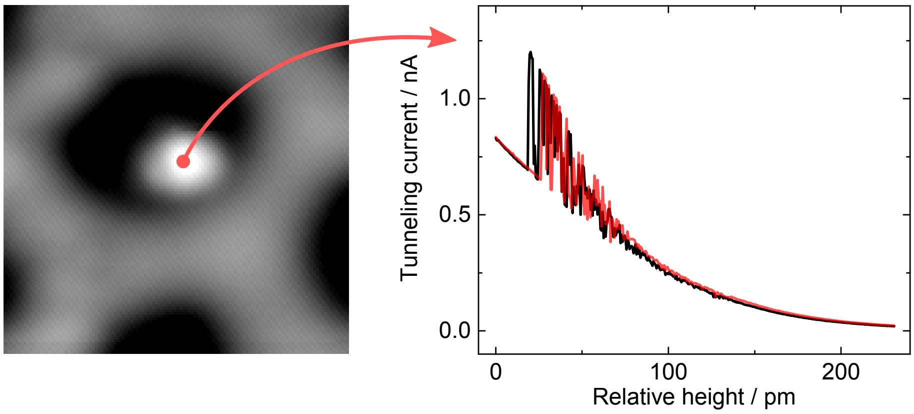

Figure 6.10: Topography and $I(z)$ curve over a switching CoH complex. The topography in constant current STM (-15 mV and 20 pA) shows a blunt tip apex that leads to similar distortions over other CoH$_x$ systems. The forward (black) and backward (red) $I(z)$ curves (Starting setpoint: -15 mV and 20 pA) taken over the center of the CoH system both show two stable exponential $I(z)$ curves with a bistable switching between 20 pm and 70 pm. The $I(z)$ curve was taken without an oscillating tuning fork and does not need to deconvoluted.

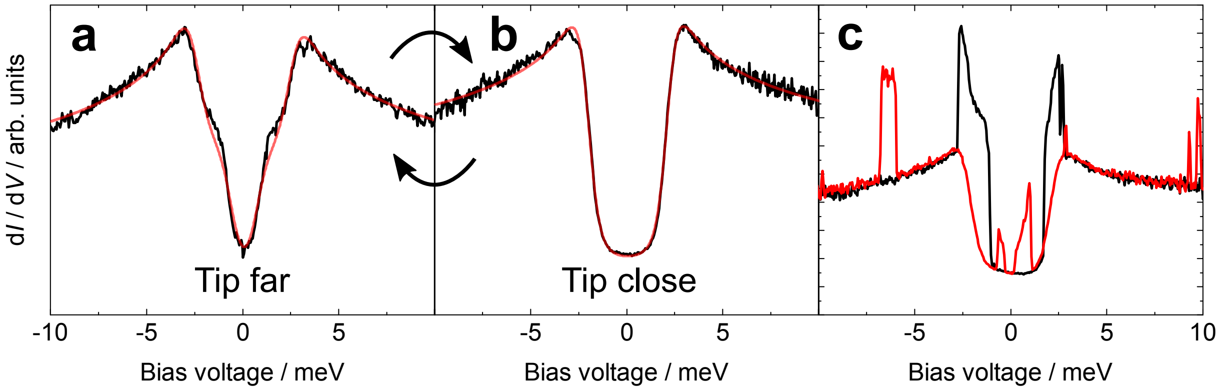

Figure 6.11: Spectroscopy over the same switching CoH system from figure 6.10 at 1.1 K and 0 T approached with a Pt tip. (a) When the tip is far from the CoH system at a setpoint conductance of $V_B = -15$ mV and $I_T = 100$ pA, a stable $S = 1$ spectrum (black curve) with fitted parameters (red curve): $D = -2.23$ meV, $E = 0.32$ meV and $J\rho_s = -0.64$, is observed. (b) When the tip is brought closer to the sample by at around $V_B = -15$ mV and $I_T = 1$ nA, again a stable spectrum (black curve) is observed that can still be fitted (red curve) with an $S = 1$ model if the transverse magnetic anisotropy is set to zero, i.e.: $D = -2.11$ meV, $E = 0$ meV and $J\rho_0 = -0.11$. The spectra in (a) and (b) are normalized for comparison. (c) The transition region around a setpoint conductance of $V_B = -15$ mV and $I_T = 700$ pA shows a bistable switching between the two spectra shown in (a) and (b) during spectroscopy in which the conductance of the spectrum with $E = 0$ meV is lower than the original one. The spectra are completely reversible and only depend on the setpoint conductance, i.e. the tip-sample distance.

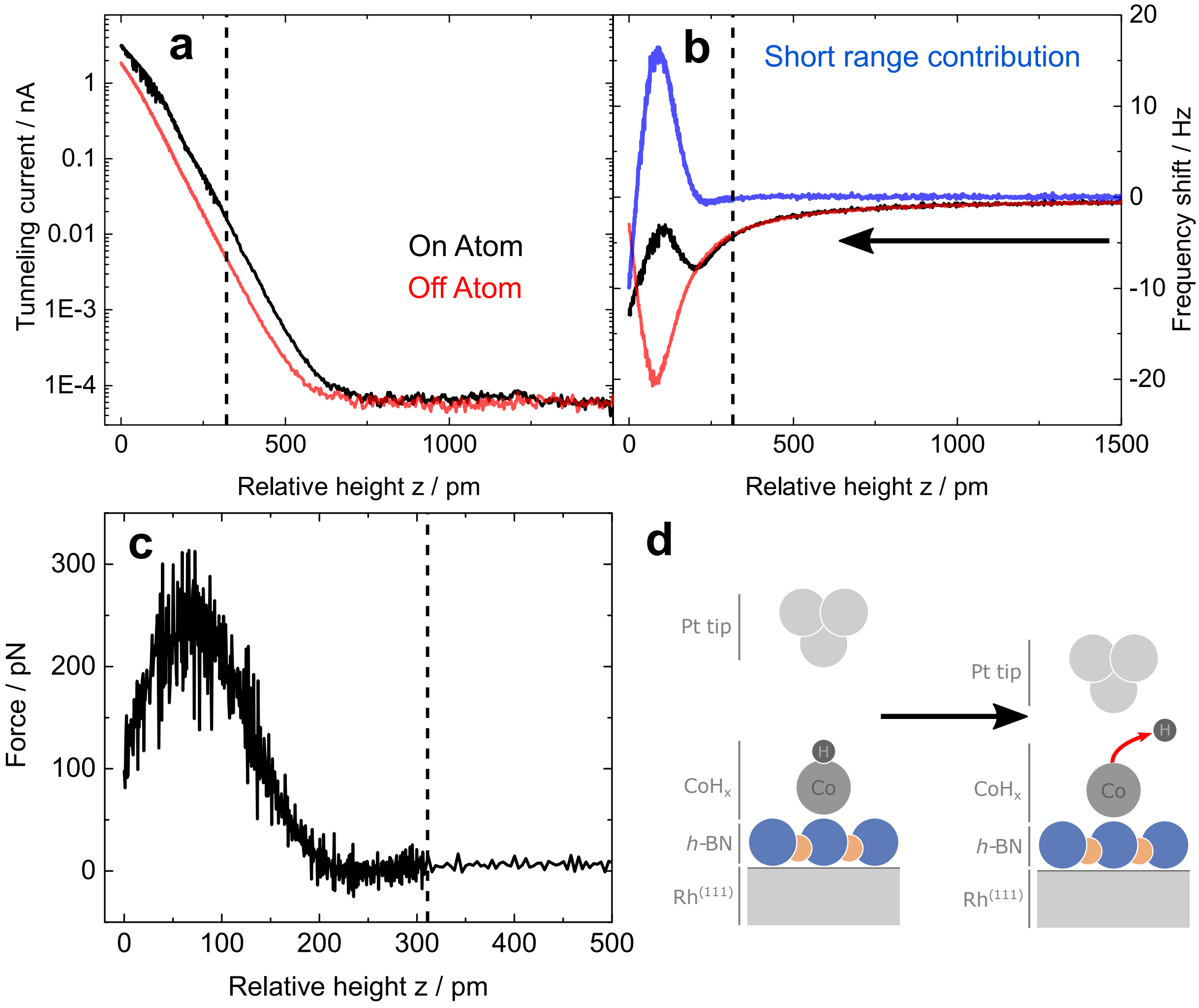

Figure 6.12: Simultaneous force and current measurements over the same switching complex shown in the previous two figures. For all approach and retract curves the tip was stabilized at -15 mV and 20 pA corresponding to a relative height of around 310 pm. (a) Tunneling current taken over the CoH atom (black curve) and the h-BN/Rh(111) background (red curve) with the noise visible occuring at the transition region of around 700 pA or 200 pm. (b) Simultaneous frequency shift curves are subtracted to obtain the short range contributions (blue curve) over the CoH switching complex. (c) The deconvoluted force shows a repulsive part up to several hundreds of pN until it gets lowered at around 50 pm. (d) Thought experiment: One possible explanation for the disappearance of the transverse anisotropy and the early onset of repulsive forces could be an interaction of the hydrogen atom on the CoH system with the Pt tip. At close proximity of the tip the hydrogen atom might be dislocated (red arrow). Another mechanism leading to a change in magnetic anisotropy could be the h-BN sheet being pushed towards the Rh(111) thus smoothening the spatial corrugation or the change of adsorption site of the CoH complex on the h-BN lattice.

6.6 Discussion

Perturbing single magnetic atoms with a combined STM and AFM in magnetic fields and low temperatures is a powerful technique to broaden our understanding of the physics and chemistry of such systems. Not only local topography and spectroscopy that identify the spin but also simultaneous tunneling current and force measurements give us a more complete picture when the system is subject to change such as the presented manipulation events with hydrogen atoms. Together with DFT calculations we have shown that we can reversibly switch the spin state of a single magnetic Co atom by attaching and removing hydrogen atoms with the Pt tip in a controlled way.

The question arises if the H-functionalized tip could harbor a H_2 molecule instead of a single H atom. While this is a possibility, we believe that several indications favor the single hydrogen atom interpretation. First of all, the DFT calculations distinguish the spin states according to CoH for a $S = 1$ system and CoH_2 for a $S = 1/2$ Kondo resonance based on the difference of one hydrogen atom. The spin states were confirmed in magnetic field where a switching event from a split Kondo resonance to a $S = 1$ signature is shown in figure 6.13, thus confirming the magnetic origin of the spectra and ruling out vibrations or other causes for a resonance around the Fermi energy. Second, the missing onset of vibrations or rotations typical for H_2 molecules trapped in tunnel junctions at low energies. Note that the spectroscopic noise shown in figure 6.3 does not depend on the applied bias voltage. Furthermore, by changing the bias voltage during approach curves, we have shown, that the applied bias voltage does not influence the frequency shift in any significant way (see figure 6.8). Third, based on the repeating patterns over the periodic h-BN/Rh(111) surface shown for H-functionalized tips, it is evident that it must the tip that is different and not the CoH system on the h-BN/Rh(111) surface. The constant cycling between the two states of the CoH and CoH_2 configuration leads to a dissipative behavior in the 50 pm oscillation range of the tuning as clearly shown in figure 6.7 where the dissipation loss per cycle increase is around 55 meV, which is similar to the potential energy difference in the grey shaded region of figure 6.6c.

Open questions remain regarding the origin of the repulsive forces. Consulting the results from chapter four we could argue that the CoH system in figure 6.10 sits in the flat valley region of the h-BN layer which should not lead to such strong repulsive forces, extending over 100 pm in figure 6.12c. Judging from this range it could due to Pauli repulsion that is distributed over the soft rim region and slowly moves this h-BN part closer to the Rh(111) surface. In both cases where a non-functionalized tip led to these drastic changes in spectroscopy the tip apex was not symmetric based on the STM topography and could be the reason for these changes.

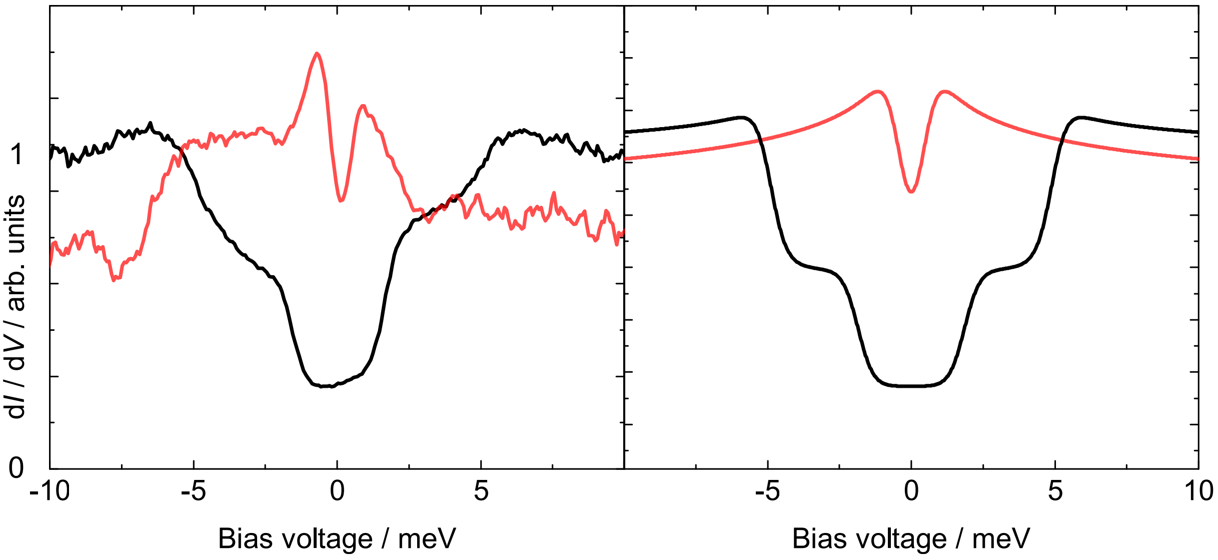

Figure 6.13: Switching event of a CoH $S = 1$ signature to a CoH_2 $S = 1/2$ split Kondo resonance with a H-functionalized tip approach in a magnetic field of 4 T and 1.3 K. The simulations on the right reproduce the spectral shape of the experimental data on the left except the overall asymmetry that in this case is probably due to potential scattering (see discussion in chapter five).

CHAPTER 7

OUTLOOK

The results presented in this thesis are just the first steps in exploring spin-spin correlations via coupled spin systems and observing the potential energy landscapes in single molecular ligand manipulations. The ultrasoft h-BN decoupling layer is key to these experiments as it mediates the interface between a single atom or a molecular unit and their metal electrode. It is reasonably flat and controllable which makes it suitable for scanning probe experiments on the atomic scale while its lateral and vertical stiffnesses provide interesting experimental configurations. The active control of the h-BN corrugation, i.e. "pushing it" toward the Rh(111) electrode, alters the local crystal field symmetries that could lead to a better understanding of how to tune and control the magnetic anisotropy of adsorbed magnetic impurities [116] [115]. The lifetime broadening that was observed for a Co-functionalized tip approach on a soft part of the h-BN rim site (see section 5.5) and the termination of the transverse anisotropy with tip approach (see section 6.5) are the first hints for these effects and should be investigated in more detail. As the tip-sample interaction is vital for these experiments, a precise control and characterization of the tip apex will be necessary.

Not only the exact control and modulation of magnetic anisotropy energies of magnetic atoms or molecules on metal electrodes due to the local crystal field leaves open questions but also the Kondo exchange coupling that is fine tuning these energies is crucial. While it has been shown that the Kondo exchange strength of a Co atom to its Rh(111) or Cu(100) electrode seems to depend on their relative adsorption site on the decoupling layer, the exact mechanism is still not yet pinned down and controllable. Instead of h-BN/Rh(111), a more suitable substrate would be h-BN/Cu(111) as it is flat and only exhibits an electronic corrugation. This substrate would allow us to distinguish the influence of the substrate's conduction electrons or other mechanisms from known factors such as local strain or defects. The determination and control of the coupling of spin systems to a metal electrode is a topic that is not only interesting for a general scientific understanding but also provides application guidelines for the design of atomic qubits that could mediate and control the qubits' decoherence with the environment.

In terms of spin-spin correlations, the results have proven the existence of either ferromagnetic or antiferromagnetic correlations between a magnetic impurity and its nearby electron bath that were previously spectroscopically non-descriptive. Not only were we able to visualize these correlations as an asymmetry in the differential conductance but also, to control the onset and strength of the asymmetry via the precise coupling of two atomic spins. The exact mechanism leading to the different sign and strength of the correlation is yet to be discovered and would lead to a new understanding of correlated materials in general. A next step could be an inverted tip-sample geometry in which the tip harbors a decoupled spin system with axial and transverse magnetic anisotropy that couples to a correlated electron sample.

A unique capability of the nanoscale department at the MPI Stuttgart is the combination of physics, chemistry and biology at the atomic scale. An electrospray ionization deposition technique [117] was already employed for larger molecules such as $Mn_{12}O_{12}(CH_3COO)_{16}$, also known as Mn_{12}, which showed signs of $S = 10$ signatures in tunneling spectroscopy [60] . As we begin to understand the intrinsic design rules to create stable molecular and atomic magnets the focus will shift to their coupling to free electrons in metal electrodes or photon interactions in microwave spin resonances or their ability to form self-assembled networks [118].

In order to *wire molecules into circuits* [119] [40] the ligand functionalities have to be designed while maintaining the magnetic properties of the molecular core. The first *magnetic-core memory* units in the 1950s employed a matrix of copper wires and ferromagnetic toroids that could be magnetized and read out by simply applying current pulses in two intersecting wires that added up in the center of one of the rings in the matrix and permanently magnetized it in one direction depending on the current direction. While this copper wire matrix was braided by hand, a self-assembled molecular crystal could provide similar pathways for photons or electrons that could write and read the magnetic state of each molecular core mediated by engineered molecular ligands [120] [121]. Pre-grown photonic crystals [122] or surface templates [123] such as the h-BN Moire pattern could serve as a template for such systems. Quantum coherence effects, as seen for ortho, meta and para configurations when transporting electrons through simple aromatic rings, lead to destructive or constructive interferences that could enhance or weaken certain conductance paths [40]. Combining these ideas with the here introduced spin-spin correlations could lead to a whole new approach to engineer quantum transport [124].

Bibliography

[1] Immanuel Bloch. Ultracold quantum gases in optical lattices. *Nature Physics*, 1(1):23–30, October 2005.

[2] S. Tarucha, D. G. Austing, T. Honda, R. J. van der Hage, and L. P. Kouwenhoven. Shell Filling and Spin Effects in a Few Electron Quantum Dot. *Physical Review Letters*, 77(17):3613–3616, October 1996.

[3] F. H. L. Koppens, C. Buizert, K. J. Tielrooij, I. T. Vink, K. C. Nowack, T. Meunier, L. P. Kouwenhoven, and L. M. K. Vandersypen. Driven coherent oscillations of a single electron spin in a quantum dot. *Nature*, 442(7104):766–771, August 2006.

[4] R. Hanson, L. P. Kouwenhoven, J. R. Petta, S. Tarucha, and L. M. K. Vandersypen. Spins in few-electron quantum dots. *Reviews of Modern Physics*, 79(4):1217–1265, October 2007.

[5] A. J. Heinrich, J. A. Gupta, C. P. Lutz, and D. M. Eigler. Single-Atom Spin-Flip Spectroscopy. *Science*, 306(5695):466–469, October 2004.

[6] Feng Wei. STM study of single cobalt atoms and clusters adsorbed on Rh (111) and Pd (111). *Acta Physica Sinica*, 61(17), 2012.

[7] V. Madhavan, W. Chen, T. Jamneala, M. F. Crommie, and N. S. Wingreen. Tunneling into a Single Magnetic Atom: Spectroscopic Evidence of the Kondo Resonance. *Science*, 280(5363):567–569, April 1998.

[8] P. Wahl, L. Diekhoener, M. A. Schneider, L. Vitali, G. Wittich, and K. Kern. Kondo Temperature of Magnetic Impurities at Surfaces. *Physical Review Letters*, 93(17):176603, October 2004.

[9] Nikolaus Knorr, M. Alexander Schneider, Lars Diekhoener, Peter Wahl, and Klaus Kern. Kondo Effect of Single Co Adatoms on Cu Surfaces. *Physical Review Letters*, 88(9):096804, February 2002.

[10] V. Schendel, C. Barreteau, M. Brandbyge, B. Borca, I. Pentegov, U. Schlickum, M. Ternes, P. Wahl, and K. Kern. Strong paramagnon scattering in single atom Pd contacts. *arXiv:1702.02407 [cond-mat]*, February 2017. arXiv: 1702.02407.

[11] A. A. Khajetoorians, T. Schlenk, B. Schweflinghaus, M. dos Santos Dias, M. Steinbrecher, M. Bouhassoune, S. Lounis, J. Wiebe, and R. Wiesendanger. Spin Excitations of Individual Fe Atoms on Pt(111): Impact of the Site-Dependent Giant Substrate Polarization. *Physical Review Letters*, 111(15):157204, October 2013.

[12] A. A. Khajetoorians, M. Valentyuk, M. Steinbrecher, T. Schlenk, A. Shick, J. Kolorenc, A. I. Lichtenstein, T. O. Wehling, R. Wiesendanger, and J. Wiebe. Tuning emergent magnetism in a Hund's impurity. *Nature Nanotechnology*, 10(11):958–964, November 2015.

[13] P. Gambardella, S. Rusponi, M. Veronese, S. S. Dhesi, C. Grazioli, A. Dallmeyer, I. Cabria, R. Zeller, P. H. Dederichs, K. Kern, C. Carbone, and H. Brune. Giant Magnetic Anisotropy of Single Cobalt Atoms and Nanoparticles. *Science*, 300(5622):1130–1133, May 2003.

[14] M. Steinbrecher, A. Sonntag, M. dos Santos Dias, M. Bouhassoune, S. Lounis, J. Wiebe, R. Wiesendanger, and A. A. Khajetoorians. Absence of a spin-signature from a single Ho adatom as probed by spin-sensitive tunneling. *Nature Communications*, 7:10454, February 2016.

[15] F. Donati, A. Singha, S. Stepanow, C. Waeckerlin, J. Dreiser, P. Gambardella, S. Rusponi, and H. Brune. Magnetism of Ho and Er Atoms on Close-Packed Metal Surfaces. *Physical Review Letters*, 113(23):237201, December 2014.

[16] Alexander A. Khajetoorians, Bruno Chilian, Jens Wiebe, Sergej Schuwalow, Frank Lechermann, and Roland Wiesendanger. Detecting excitation and magnetization of individual dopants in a semiconductor. *Nature*, 467(7319):1084–1087, October 2010.

[17] Romana Baltic, Marina Pivetta, Fabio Donati, Christian Waeckerlin, Aparajita Singha, Jan Dreiser, Stefano Rusponi, and Harald Brune. Superlattice of Single Atom Magnets on Graphene. *Nano Letters*, 16(12):7610–7615, December 2016.

[18] Hector Gonzalez-Herrero, Jose M. Gomez-Rodriguez, Pierre Mallet, Mohamed Moaied, Juan Jose Palacios, Carlos Salgado, Miguel M. Ugeda, Jean-Yves Veuillen, Felix Yndurain, and Ivan Brihuega. Atomic-scale control of graphene magnetism by using hydrogen atoms. *Science*, 352(6284):437–441, April 2016.

[19] Peter Jacobson, Tobias Herden, Matthias Muenks, Gennadii Laskin, Oleg Brovko, Valeri Stepanyuk, Markus Ternes, and Klaus Kern. Quantum engineering of spin and anisotropy in magnetic molecular junctions. *Nature Communications*, 6:8536, October 2015.

[20] Cyrus F. Hirjibehedin, Chiung-Yuan Lin, Alexander F. Otte, Markus Ternes, Christopher P. Lutz, Barbara A. Jones, and Andreas J. Heinrich. Large Magnetic Anisotropy

of a Single Atomic Spin Embedded in a Surface Molecular Network. *Science*, 317(5842):1199–1203, August 2007.

[21] Alexander F. Otte, Markus Ternes, Kirsten von Bergmann, Sebastian Loth, Harald Brune, Christopher P. Lutz, Cyrus F. Hirjibehedin, and Andreas J. Heinrich. The role of magnetic anisotropy in the Kondo effect. *Nature Physics*, 4(11):847–850, November 2008.

[22] Taeyoung Choi and Jay A. Gupta. Building blocks for studies of nanoscale magnetism: adsorbates on ultrathin insulating Cu_2N. *Journal of Physics: Condensed Matter*, 26(39):394009, 2014.

[23] S. Baumann, F. Donati, S. Stepanow, S. Rusponi, W. Paul, S. Gangopadhyay, I.G. Rau, G.E. Pacchioni, L. Gragnaniello, M. Pivetta, J. Dreiser, C. Piamonteze, C.P. Lutz, R.M. Macfarlane, B.A. Jones, P. Gambardella, A.J. Heinrich, and H. Brune. Origin of Perpendicular Magnetic Anisotropy and Large Orbital Moment in Fe Atoms on MgO. *Physical Review Letters*, 115(23):237202, December 2015.

[24] Fabian D. Natterer, Kai Yang, William Paul, Philip Willke, Taeyoung Choi, Thomas Greber, Andreas J. Heinrich, and Christopher P. Lutz. Reading and writing single-atom magnets. *Nature*, 543(7644):226–228, March 2017.

[25] Ileana G. Rau, Susanne Baumann, Stefano Rusponi, Fabio Donati, Sebastian Stepanow, Luca Gragnaniello, Jan Dreiser, Cinthia Piamonteze, Frithjof Nolting, Shruba Gangopadhyay, Oliver R. Albertini, Roger M. Macfarlane, Christopher P. Lutz, Barbara A. Jones, Pietro Gambardella, Andreas J. Heinrich, and Harald Brune. Reaching the magnetic anisotropy limit of a 3d metal atom. *Science*, 344(6187):988–992, May 2014.

[26] Jascha Repp, Gerhard Meyer, Fredrik E. Olsson, and Mats Persson. Controlling the Charge State of Individual Gold Adatoms. *Science*, 305(5683):493–495, July 2004.

[27] F. E. Olsson, S. Paavilainen, M. Persson, J. Repp, and G. Meyer. Multiple Charge States of Ag Atoms on Ultrathin NaCl Films. *Physical Review Letters*, 98(17):176803, April 2007.

[28] Ali Yazdani, B. A. Jones, C. P. Lutz, M. F. Crommie, and D. M. Eigler. Probing the Local Effects of Magnetic Impurities on Superconductivity. *Science*, 275(5307):1767–1770, March 1997.

[29] Gerbold C. Menard, Sebastien Guissart, Christophe Brun, Stephane Pons, Vasily S. Stolyarov, Francois Debontridder, Matthieu V. Leclerc, Etienne Janod, Laurent Cario, Dimitri Roditchev, Pascal Simon, and Tristan Cren. Coherent long-range magnetic bound states in a superconductor. *Nature Physics*, 11(12):1013–1016, December 2015.

[30] Shuai-Hua Ji and Jin-Feng Jia. Application of magnetic atom induced bound states in superconducting gap for chemical identification of single magnetic atoms. *Applied Physics Letters*, 96(7):073113, February 2010.

[31] J. Honolka, A. A. Khajetoorians, V. Sessi, T. O. Wehling, S. Stepanow, J.-L. Mi, B. B. Iversen, T. Schlenk, J. Wiebe, N. B. Brookes, A. I. Lichtenstein, Ph. Hofmann, K. Kern, and R. Wiesendanger. In-Plane Magnetic Anisotropy of Fe Atoms on $Bi_2Se_3(111)$. *Physical Review Letters*, 108(25):256811, June 2012.

[32] M. Wasniowska, M. Sikora, M. Dobrzanski, T. Eelbo, M. M. Soares, M. Rams, I. Miotkowski, R. Wiesendanger, R. Berndt, Z. Kakol, and A. Kozcowski. Investigating the differences between Co adatoms states on surfaces of selected bismuth chalcogenides. *Physical Review B*, 92(11):115412, September 2015.

[33] T. Eelbo, M. Wasniowska, M. Sikora, M. Dobrzanski, A. Kozcowski, A. Pulkin, G. Autes, I. Miotkowski, O. V. Yazyev, and R. Wiesendanger. Strong out-of-plane magnetic anisotropy of Fe adatoms on Bi_2Te_3. *Physical Review B*, 89(10):104424, March 2014.

[34] M. Vondracek, L. Cornils, J. Minar, J. Warmuth, M. Michiardi, C. Piamonteze, L. Barreto, J. A. Miwa, M. Bianchi, Ph. Hofmann, L. Zhou, A. Kamlapure, A. A. Khajetoorians, R. Wiesendanger, J.-L. Mi, B.-B. Iversen, S. Mankovsky, St. Borek, H. Ebert, M. Schueler, T. Wehling, J. Wiebe, and J. Honolka. Nickel: The time-reversal symmetry conserving partner of iron on a chalcogenide topological insulator. *Physical Review B*, 94(16):161114, October 2016.

[35] O. Sipr, S. Bornemann, J. Minar, and H. Ebert. Magnetic anisotropy of Fe and Co adatoms and monolayers: Need for a proper treatment of the substrate. *Physical Review B*, 82(17):174414, November 2010.

[36] Focko Meier, Samir Lounis, Jens Wiebe, Lihui Zhou, Swantje Heers, Phivos Mavropoulos, Peter H. Dederichs, Stefan Bluegel, and Roland Wiesendanger. Spin polarization of platinum (111) induced by the proximity to cobalt nanostripes. *Physical Review B*, 83(7):075407, February 2011.

[37] Lihui Zhou, Jens Wiebe, Samir Lounis, Elena Vedmedenko, Focko Meier, Stefan Bluegel, Peter H. Dederichs, and Roland Wiesendanger. Strength and directionality of surface Ruderman Kittel Kasuya Yosida interaction mapped on the atomic scale. *Nature Physics*, 6(3):187–191, March 2010.

[38] Susanne Baumann, William Paul, Taeyoung Choi, Christopher P. Lutz, Arzhang Ardavan, and Andreas J. Heinrich. Electron paramagnetic resonance of individual atoms on a surface. *Science*, 350(6259):417–420, October 2015.

[39] Paul Stoll, Matthias Bernien, Daniela Rolf, Fabian Nickel, Qingyu Xu, Claudia Hartmann, Tobias R. Umbach, Jens Kopprasch, Janina N. Ladenthin, Enrico Schierle, Eugen Weschke, Constantin Czekelius, Wolfgang Kuch, and Katharina J. Franke. Magnetic anisotropy in surface-supported single-ion lanthanide complexes. *Physical Review B*, 94(22):224426, December 2016.

[40] Mark Ratner. A brief history of molecular electronics. *Nature Nanotechnology*, 8(6):378–381, June 2013.

[41] Tobias Herden. *Combined Scanning Tunneling and Atomic Force Microscopy and Spectroscopy on Molecular Nanostructures*. Universitaet Konstanz, Konstanz, 2014.

[42] G. Binnig, H. Rohrer, Ch. Gerber, and E. Weibel. Surface Studies by Scanning Tunneling Microscopy. *Physical Review Letters*, 49(1):57–61, July 1982.

[43] J. Tersoff and D. R. Hamann. Theory and Application for the Scanning Tunneling Microscope. *Physical Review Letters*, 50(25):1998–2001, June 1983.

[44] Gerd Binnig and Heinrich Rohrer. Scanning tunneling microscopy from birth to adolescence. *Reviews of Modern Physics*, 59(3):615–625, July 1987.

[45] G. Binnig, C. F. Quate, and Ch. Gerber. Atomic Force Microscope. *Physical Review Letters*, 56(9):930–933, March 1986.

[46] Franz J. Giessibl. Advances in atomic force microscopy. *Reviews of Modern Physics*, 75(3):949–983, July 2003.

[47] Farid F. Abraham, Inder P. Batra, and S. Ciraci. Effect of tip profile on atomic-force microscope images: A model study. *Physical Review Letters*, 60(13):1314–1317, March 1988.

[48] Noriaki Oyabu, Oscar Custance, Insook Yi, Yasuhiro Sugawara, and Seizo Morita. Mechanical Vertical Manipulation of Selected Single Atoms by Soft Nanoindentation Using Near Contact Atomic Force Microscopy. *Physical Review Letters*, 90(17):176102, May 2003.

[49] Franz Giessibl. A direct method to calculate tip sample forces from frequency shifts in frequency-modulation atomic force microscopy. *Applied Physics Letters*, 78(1):123–125, December 2000.

[50] Markus Ternes. *Atomic Manipulation on Metal Surfaces*. Noncontact Atomic Force Microscopy, Springer, 2009.

[51] Franz J. Giessibl. Atomic Resolution of the Silicon (111)-(7x7) Surface by Atomic Force Microscopy. *Science*, 267(5194):68–71, January 1995.

[52] Franz Giessibl. Atomic resolution on Si(111)(7x7) by noncontact atomic force microscopy with a force sensor based on a quartz tuning fork. *Applied Physics Letters*, 76(11):1470–1472, March 2000.

[53] Yoshiaki Sugimoto, Pablo Pou, Masayuki Abe, Pavel Jelinek, Ruben Perez, Seizo Morita, and Oscar Custance. Chemical identification of individual surface atoms by atomic force microscopy. *Nature*, 446(7131):64–67, March 2007.

[54] Leo Gross, Fabian Mohn, Nikolaj Moll, Peter Liljeroth, and Gerhard Meyer. The Chemical Structure of a Molecule Resolved by Atomic Force Microscopy. *Science*, 325(5944):1110–1114, August 2009.

[55] Hatem Labidi, Martin Kupsta, Taleana Huff, Mark Salomons, Douglas Vick, Marco Taucer, Jason Pitters, and Robert A. Wolkow. New fabrication technique for highly sensitive qPlus sensor with well-defined spring constant. *Ultramicroscopy*, 158:33–37, November 2015.

[56] A. Nagashima, N. Tejima, Y. Gamou, T. Kawai, and C. Oshima. Electronic Structure of Monolayer Hexagonal Boron Nitride Physisorbed on Metal Surfaces. *Physical Review Letters*, 75(21):3918–3921, November 1995.

[57] Robert Laskowski, Peter Blaha, and Karlheinz Schwarz. Bonding of hexagonal BN to transition metal surfaces: An ab initio density-functional theory study. *Physical Review B*, 78(4):045409, July 2008.

[58] R. Laskowski and P. Blaha. Unraveling the structure of the h-BN/Rh(111) nanomesh with ab initio calculations. *Journal of Physics: Condensed Matter*, 20(6):064207, 2008.

[59] Martina Corso, Willi Auwaerter, Matthias Muntwiler, Anna Tamai, Thomas Greber, and Juerg Osterwalder. Boron Nitride Nanomesh. *Science*, 303(5655):217–220, January 2004.

[60] Steffen Kahle, Zhitao Deng, Nikola Malinowski, Charlene Tonnoir, Alicia Forment-Aliaga, Nicha Thontasen, Gordon Rinke, Duy Le, Volodymyr Turkowski, Talat S. Rahman, Stephan Rauschenbach, Markus Ternes, and Klaus Kern. The Quantum Magnetism of Individual Manganese-12-Acetate Molecular Magnets Anchored at Surfaces. *Nano Letters*, 12(1):518–521, January 2012.

[61] Sangita Bose, Antonio M. Garcia-Garcia, Miguel M. Ugeda, Juan D. Urbina, Christian H. Michaelis, Ivan Brihuega, and Klaus Kern. Observation of shell effects in superconducting nanoparticles of Sn. *Nature Materials*, 9(7):550–554, July 2010.

[62] Fabian Donat Natterer, Francois Patthey, and Harald Brune. Ring State for Single Transition Metal Atoms on Boron Nitride on Rh(111). *Physical Review Letters*, 109(6):066101, August 2012.

[63] Daniel Rosenblatt. *Construction of a low temperature STM and studies of large molecular systems*. EPFL, Lausanne, 2015.

[64] G. Cassabois, P. Valvin, and B. Gil. Hexagonal boron nitride is an indirect bandgap semiconductor. *Nature Photonics*, 10(4):262–266, April 2016.

[65] M. Etzkorn, C. F. Hirjibehedin, A. Lehnert, S. Ouazi, S. Rusponi, S. Stepanow, P. Gambardella, C. Tieg, P. Thakur, A. I. Lichtenstein, A. B. Shick, S. Loth, A. J. Heinrich, and H. Brune. Comparing XMCD and DFT with STM spin excitation spectroscopy for Fe and Co adatoms on Cu_2N. *Physical Review B*, 92(18):184406, November 2015.

[66] Dante Gatteschi and Cristiano Benelli. *Introduction to Molecular Magnetism: From Transition Metals to Lanthanides*. Wiley-VCH Verlag GmbH & Co. KGaA, 11th ed. edition, 2015.

[67] Leo Gross, Nikolaj Moll, Fabian Mohn, Alessandro Curioni, Gerhard Meyer, Felix Hanke, and Mats Persson. High-Resolution Molecular Orbital Imaging Using a p-Wave STM Tip. *Physical Review Letters*, 107(8):086101, August 2011.

[68] C. Julian Chen. Tunneling matrix elements in three-dimensional space: The derivative rule and the sum rule. *Physical Review B*, 42(14):8841–8857, November 1990.

[69] K. McElroy, G.-H. Gweon, S. Y. Zhou, J. Graf, S. Uchida, H. Eisaki, H. Takagi, T. Sasagawa, D.-H. Lee, and A. Lanzara. Elastic Scattering Susceptibility of the High Temperature Superconductor Bi2Sr2CaCu2O8. *Physical Review Letters*, 96(6):067005, February 2006.

[70] Markus Ternes. Scanning tunneling spectroscopy at the single atom scale. *Ph.D. Thesis, EPFL*, 2006.

[71] J. Fernandez-Rossier. Theory of Single-Spin Inelastic Tunneling Spectroscopy. *Physical Review Letters*, 102(25):256802, June 2009.

[72] Nicolas Lorente and Jean-Pierre Gauyacq. Efficient Spin Transitions in Inelastic Electron Tunneling Spectroscopy. *Physical Review Letters*, 103(17):176601, October 2009.

[73] Mark A. Reed. Inelastic electron tunneling spectroscopy. *Materials Today*, 11(11):46–50, November 2008.

[74] A. A. Khajetoorians, S. Lounis, B. Chilian, A. T. Costa, L. Zhou, D. L. Mills, J. Wiebe, and R. Wiesendanger. Itinerant Nature of Atom-Magnetization Excitation by Tunneling Electrons. *Physical Review Letters*, 106(3):037205, January 2011.

[75] Leo Kouwenhoven and Leonid Glazman. Revival of the Kondo effect. *Physics World*, 14(1):33, 2001.

[76] Joel A. Appelbaum. Exchange Model of Zero-Bias Tunneling Anomalies. *Physical Review*, 154(3):633–643, February 1967.

[77] Markus Ternes, Andreas J. Heinrich, and Wolf-Dieter Schneider. Spectroscopic manifestations of the Kondo effect on single adatoms. *Journal of Physics: Condensed Matter*, 21(5):053001, 2009.

[78] H. O. Frota. Shape of the Kondo resonance. *Physical Review B*, 45(3):1096–1099, January 1992.

[79] Wulf Wulfhekel. Magnetic properties: The exchange changes everything. *Nature Nanotechnology*, 9(1):13–14, January 2014.

[80] Jenny C. Oberg, M. Reyes Calvo, Fernando Delgado, Maria Moro-Lagares, David Serrate, David Jacob, Joaquin Fernandez-Rossier, and Cyrus F. Hirjibehedin. Control of single-spin magnetic anisotropy by exchange coupling. *Nature Nanotechnology*, 9(1):64–68, January 2014.

[81] F. Donati, L. Gragnaniello, A. Cavallin, F.D. Natterer, Q. Dubout, M. Pivetta, F. Patthey, J. Dreiser, C. Piamonteze, S. Rusponi, and H. Brune. Tailoring the Magnetism of Co Atoms on Graphene through Substrate Hybridization. *Physical Review Letters*, 113(17):177201, October 2014.

[82] Seizo Morita, Franz J. Giessibl, Ernst Meyer, and Roland Wiesendanger. *Noncontact Atomic Force Microscopy*. Springer, May 2015.

[83] S. Hudlet, M. Saint Jean, C. Guthmann, and J. Berger. Evaluation of the capacitive force between an atomic force microscopy tip and a metallic surface. *The European Physical Journal B*, 2(1):5–10, March 1998.

[84] Ulrich Zerweck, Christian Loppacher, Tobias Otto, Stefan Grafstroem, and Lukas M. Eng. Accuracy and resolution limits of Kelvin probe force microscopy. *Physical Review B*, 71(12):125424, March 2005.

[85] S. A. Burke, J. M. LeDue, Y. Miyahara, J. M. Topple, S. Fostner, and P. Gruetter. Determination of the local contact potential difference of PTCDA on NaCl: a comparison of techniques. *Nanotechnology*, 20(26):264012, 2009.

[86] Dawn Bonnell, editor. *Scanning Probe Microscopy and Spectroscopy: Theory, Techniques, and Applications*. Wiley-VCH, New York, 2 edition edition, December 2000.

[87] Intermolecular and Surface Forces. In Jacob N. Israelachvili, editor, *Intermolecular and Surface Forces (Third Edition)*, page iii. Academic Press, San Diego, 2011. DOI: 10.1016/B978-0-12-375182-9.10025-9.

[88] Hans P. Latscha and Helmut Klein. *Anorganische Chemie: Chemie-Basiswissen I*. Springer, 8 edition, 2002.

[89] John Sader. Accurate formulas for interaction force and energy in frequency modulation force spectroscopy. *Applied Physics Letters*, 84(10):1801–1803, March 2004.

[90] Joachim Welker, Esther Illek, and Franz J Giessibl. Analysis of force-deconvolution methods in frequency-modulation atomic force microscopy. *Beilstein Journal of Nanotechnology*, 3:238–248, March 2012.

[91] Tobias Herden, Markus Ternes, and Klaus Kern. Lateral and Vertical Stiffness of the Epitaxial h-BN Monolayer on Rh(111). *Nano Letters*, 14(6):3623–3627, June 2014.

[92] Matthias Muenks, Peter Jacobson, Markus Ternes, and Klaus Kern. Correlation-driven transport asymmetries through coupled spins in a tunnel junction. *Nature Communications*, 8:14119, January 2017.

[93] A. Spinelli, M. Gerrits, R. Toskovic, B. Bryant, M. Ternes, and A. F. Otte. Exploring the phase diagram of the two-impurity Kondo problem. *Nature Communications*, 6:10046, November 2015.

[94] A. A. Khajetoorians, M. Steinbrecher, M. Ternes, M. Bouhassoune, M. dos Santos Dias, S. Lounis, J. Wiebe, and R. Wiesendanger. Tailoring the chiral magnetic interaction between two individual atoms. *Nature Communications*, 7:10620, February 2016.

[95] Philip Ball. Quantum objects on show. *Nature*, 462(7272):416–416, November 2009.

[96] M. F. Crommie, C. P. Lutz, and D. M. Eigler. Confinement of Electrons to Quantum Corrals on a Metal Surface. *Science*, 262(5131):218–220, October 1993.

[97] V. V. Mazurenko, S. N. Iskakov, M. V. Valentyuk, A. N. Rudenko, and A. I. Lichtenstein. Orbital-selective conductance of Co adatom on the Pt(111) surface. *Physical Review B*, 84(19):193407, November 2011.

[98] A. Hamzic, S. Senoussi, I. A. Campbell, and A. Fert. Orbital magnetism of transition metal impurities in platinum. *Journal of Magnetism and Magnetic Materials*, 15:921–922, January 1980.

[99] Sebastian Loth, Christopher P. Lutz, and Andreas J. Heinrich. Spin-polarized spin excitation spectroscopy. *New Journal of Physics*, 12(12):125021, 2010.

[100] Q. Dubout, F. Donati, C. Waeckerlin, F. Calleja, M. Etzkorn, A. Lehnert, L. Claude, P. Gambardella, and H. Brune. Controlling the Spin of Co Atoms on Pt(111) by Hydrogen Adsorption. *Physical Review Letters*, 114(10):106807, March 2015.

[101] Benedikt Schweflinghaus, Manuel dos Santos Dias, and Samir Lounis. Observing spin excitations in $3d$ transition-metal adatoms on Pt(111) with inelastic scanning tunneling spectroscopy: A first-principles perspective. *Physical Review B*, 93(3):035451, January 2016.

[102] Markus Ternes. Probing magnetic excitations and correlations in single and coupled spin systems with scanning tunneling spectroscopy. *Progress in Surface Science*, 92(1):83–115, February 2017.

[103] Jasper van Veen. *Internship report*. Delft University of Technology and Max-Planck Institute for Solid State Research, Stuttgart, 2014.

[104] J. Paaske, A. Rosch, P. Woelfle, N. Mason, C. M. Marcus, and J. Nygard. Non-equilibrium singlet triplet Kondo effect in carbon nanotubes. *Nature Physics*, 2(7):460–464, July 2006.

[105] Christian Wagner and Ruslan Temirov. Tunnelling junctions with additional degrees of freedom: An extended toolbox of scanning probe microscopy. *Progress in Surface Science*, 90(2):194–222, May 2015.

[106] Hatem Labidi, Mohammad Koleini, Taleana Huff, Mark Salomons, Martin Cloutier, Jason Pitters, and Robert A. Wolkow. Indications of chemical bond contrast in AFM images of a hydrogen-terminated silicon surface. *Nature Communications*, 8:14222, February 2017.

[107] Lars Bartels. Controlled vertical manipulation of single CO molecules with the scanning tunneling microscope: A route to chemical contrast. *Applied Physics Letters*, 71(2):213–215, July 1997.

[108] Alfred John Weymouth, Thomas Hofmann, and Franz J. Giessibl. Quantifying Molecular Stiffness and Interaction with Lateral Force Microscopy. *Science*, 343(6175):1120–1122, March 2014.

[109] Georgy Kichin, Christian Weiss, Christian Wagner, F. Stefan Tautz, and Ruslan Temirov. Single Molecule and Single Atom Sensors for Atomic Resolution Imaging of Chemically

Complex Surfaces. *Journal of the American Chemical Society*, 133(42):16847–16851, October 2011.

[110] Marina Pivetta, Markus Ternes, FranÃğois Patthey, and Wolf-Dieter Schneider. Diatomic Molecular Switches to Enable the Observation of Very-Low-Energy Vibrations. *Physical Review Letters*, 99(12):126104, September 2007.

[111] Marcella Iannuzzi, Fabien Tran, Roland Widmer, Thomas Dienel, Kevin Radican, Yun Ding, Juerg Hutter, and Oliver Groening. Site-selective adsorption of phthalocyanine on h-BN/Rh(111) nanomesh. 16(24):12374–12384, May 2014.

[112] Hugo Dil, Jorge Lobo-Checa, Robert Laskowski, Peter Blaha, Simon Berner, Juerg Osterwalder, and Thomas Greber. Surface Trapping of Atoms and Molecules with Dipole Rings. *Science*, 319(5871):1824–1826, March 2008.

[113] C. Weiss, C. Wagner, C. Kleimann, M. Rohlfing, F. S. Tautz, and R. Temirov. Imaging Pauli Repulsion in Scanning Tunneling Microscopy. *Physical Review Letters*, 105(8):086103, August 2010.

[114] Peter Jacobson, Matthias Muenks, Gennadii Laskin, Oleg O. Brovko, Valeri S. Stepanyuk, Markus Ternes, and Klaus Kern. Potential Energy Driven Spin Manipulation via a Controllable Hydrogen Ligand. *arXiv:1609.00612 [cond-mat]*, September 2016. arXiv: 1609.00612.

[115] Benjamin W. Heinrich, Lukas Braun, Jose I. Pascual, and Katharina J. Franke. Tuning the Magnetic Anisotropy of Single Molecules. *Nano Letters*, 15(6):4024–4028, June 2015.

[116] Noriyuki Tsukahara, Ken-ichi Noto, Michiaki Ohara, Susumu Shiraki, Noriaki Takagi, Yasutaka Takata, Jun Miyawaki, Munetaka Taguchi, Ashish Chainani, Shik Shin, and Maki Kawai. Adsorption-Induced Switching of Magnetic Anisotropy in a Single Iron(II) Phthalocyanine Molecule on an Oxidized Cu(110) Surface. *Physical Review Letters*, 102(16):167203, April 2009.

[117] Sabine Abb, Ludger Harnau, Rico Gutzler, Stephan Rauschenbach, and Klaus Kern. Two-dimensional honeycomb network through sequence-controlled self-assembly of oligopeptides. *Nature Communications*, 7:10335, January 2016.

[118] N. Henningsen, R. Rurali, C. Limbach, R. Drost, J. I. Pascual, and K. J. Franke. Site-Dependent Coordination Bonding in Self Assembled Metal Organic Networks. *The Journal of Physical Chemistry Letters*, 2(2):55–61, January 2011.

[119] Emanuel Loertscher. Wiring molecules into circuits. *Nature Nanotechnology*, 8(6):381–384, June 2013.

[120] Mario Ruben, Javier Rojo, Francisco J. Romero-Salguero, Lindsay H. Uppadine, and Jean-Marie Lehn. Grid-Type Metal Ion Architectures: Functional Metallosupramolecular Arrays. *Angewandte Chemie International Edition*, 43(28):3644–3662, July 2004.

[121] Mario Ruben, Jean-Marie Lehn, and Paul Mueller. Addressing metal centres in supramolecular assemblies. *Chemical Society Reviews*, 35(11):1056–1067, 2006.

[122] David J. Norris. Photonic Crystals: A view of the future. *Nature Materials*, 6(3):177–178, March 2007.

[123] Johannes V. Barth, Giovanni Costantini, and Klaus Kern. Engineering atomic and molecular nanostructures at surfaces. *Nature*, 437(7059):671–679, 2005.

[124] M. Urdampilleta, S. Klyatskaya, J.-P. Cleuziou, M. Ruben, and W. Wernsdorfer. Supramolecular spin valves. *Nature Materials*, 10(7):502–506, July 2011.

APPENDIX A

SCILAB CODE FOR SIMULATING A COUPLED SPIN SYSTEM

```
//////////////////////////////////////////////////////////////
//////////////////////////////////////////////////////////////
//         - Transport calculations through a coupled       //
//           spin 1 and spin 1/2 system -                   //
//           2015/10/1 - Matthias Muenks                    //
//////////////////////////////////////////////////////////////
//////////////////////////////////////////////////////////////

// Define spin operators for spin 1/2 system
sx_half=(1/2)*[0 1; 1 0];
sy_half=(1/2)*[0 -%i; %i 0];
sz_half=(1/2)*[1 0; 0 -1];

// Define spin operators for spin 1 system
sx_one=(1/sqrt(2))*[0 1 0; 1 0 1; 0 1 0];
sy_one=(1/(sqrt(2)*%i))*[0 1 0; -1 0 1; 0 -1 0];
sz_one=[1 0 0; 0 0 0; 0 0 -1];

// Taking the tensor product
sx_both=kron(sx_one, sx_half);
sy_both=kron(sy_one, sy_half);
sz_both=kron(sz_one, sz_half);

// Calculate spin operators that act on eigenstates:
sx_op=kron(sx_one,eye(2,2))+kron(eye(3,3),sx_half);
sy_op=kron(sy_one,eye(2,2))+kron(eye(3,3),sy_half);
// S_z will give m_z if it acts on an eigenstate
sz_op=kron(sz_one,eye(2,2))+kron(eye(3,3),sz_half);
// And the final S^2 operator
s_sq=(sx_op^2)+(sy_op^2)+(sz_op^2);

sx_op1=kron(sx_one,eye(2,2));
sx_op2=kron(eye(3,3),sx_half);
sy_op1=kron(sy_one,eye(2,2));
sy_op2=kron(eye(3,3),sy_half);
// S_z will give m_z if it acts on an eigenstate
sz_op1=kron(sz_one,eye(2,2));
sz_op2=kron(eye(3,3),sz_half);

////////////////////////////////////////////////////////////////////////
// Calculate Spin-Spin Hamiltonian for a spin-1 and a spin-1/2 system //
////////////////////////////////////////////////////////////////////////

// If fm_coupling = 0 == AFM coupling True
fm_coupling = 1;
// Correlation strength between magnetic moment on tip and local conduction electrons in Pt
CS = 0.5;
// Set direct exchange coupling strength J
// It is a scalar since we only assume an isotropic contribution
J=1;

// Set dummy matrix for asymmetry values
asymmetry=zeros(2,1);

// If needed, output evolution of spectra with this for loop
for images=1:1

//Heisenberg (xyz) or Ising (z) coupling
Jx = J;
Jy = J;
Jz = J;

J=J+0 // for the image loop

// Calculate isotropic part of Spin-Spin Hamiltonian

H_SS=Jx*(sx_both)+Jy*(sy_both)+Jz*(sz_both);

//////////////////////////////////////////////////////////////////////////////////////
// Include magnetic anisotropy with Crystal Field Hamiltonian for the spin 1 system //
//////////////////////////////////////////////////////////////////////////////////////

// For the magnetic anisotropy, calculate the same dimensional space just
// without the spin 1/2 contribution since it is still isolated in its subspace
sx_fakespin_one=kron(sx_one, eye(2,2));
sy_fakespin_one=kron(sy_one, eye(2,2));
sz_fakespin_one=kron(sz_one, eye(2,2));

// And for the spin 1/2 Sz operator to find its m_z values:
sz_fakespin_half=kron(eye(3,3), sz_half)
```

```

// Define Magnetic Anisotropy Energies
// Generic sample atom used in most of the examples
D = -5;
E = 1;

// Zeeman Hamiltonian - alligned with axial direction of MAE i.e. z act on both spins
B_z = 0;
g = 2;
// Bohr magneton in mev / T
bohrmagneton = 0.0578838;
zeeman_one = g * bohrmagneton * B_z * sz_fakespin_one;
zeeman_half = g * bohrmagneton * B_z * sz_fakespin_half;

axial = D*(sz_fakespin_one*sz_fakespin_one);
transverse = E*((sx_fakespin_one*sx_fakespin_one)-(sy_fakespin_one*sy_fakespin_one));

// The total crystal field Hamiltonian
H_CF = axial + transverse;

///////////////////////////////////////////////////////////////////////
// Now define complete Hamiltonian that defines the coupled system   //
///////////////////////////////////////////////////////////////////////

H_coupled = H_CF + H_SS + zeeman_one + zeeman_half;

// Diagonalize Hamiltonian
[eigenstates, eigenvalues]=spec(H_coupled);

//Force energies to be positive by adding an offset equal to the smallest eigenvalue
smallest_eigenvalue=min(eigenvalues);
for r=1:6
    eigenvalues(r,r)=eigenvalues(r,r)-smallest_eigenvalue;
end

// Now calculate transition matrix probabilities for the tunneling electron that
// provides the necessary angular momentum

// First, create simple spin up and spin down eigenstates
// statistical probabilities of the tip electrons as density matrices:
tipprob1=eye(2,2);
tipprob2=eye(2,2);
tipprob3=eye(2,2);
tipprob4=eye(2,2);
tipprob5=eye(2,2);
tipprob6=eye(2,2);

// use the coupled spin eigenstates to determine the polarization probabilities
// of the spin 1/2 coupled to the AFM or FM coupled tip conduction electrons
// do this later in the actual matrix elements calculation
// statistical probabilities of the sample electrons
sampleprob=eye(2,2);
sampleprob(1,2)=0; // equal ensemble in sample spin up
sampleprob(2,1)=0; // equal ensemble in sample spin down
sampleprob(1,1)=0.5; // equal ensemble in sample spin up
sampleprob(2,2)=0.5; // equal ensemble in sample spin down

/////////////////////////////////////////////////////////////////////////////////////
// Calculate transition probabilities for the spin-1 system multiplied with the spin //
// 1/2 conduction electrons /////////////////////////////////////////////////////////
/////////////////////////////////////////////////////////////////////////////////////

// For each of the six total states, calculate the correlation with the conduction
// electrons as a statistical ensemble
correlations = list(tipprob1,tipprob2,tipprob3,tipprob4,tipprob5,tipprob6);

if (fm_coupling == 1) then
    for i=1:6
        alpha=abs(eigenstates(1,i))^2+abs(eigenstates(3,i))^2+abs(eigenstates(5,i))^2;
        correlations(i)(1,1)=(CS*alpha)+(0.5*(1-CS));
        bravo=abs(eigenstates(2,i))^2+abs(eigenstates(4,i))^2+abs(eigenstates(6,i))^2;
        correlations(i)(2,2)=(CS*bravo)+(0.5*(1-CS));
    end
else
    for i=1:6
        alpha=abs(eigenstates(1,i))^2+abs(eigenstates(3,i))^2+abs(eigenstates(5,i))^2;
        correlations(i)(2,2)=(CS*alpha)+(0.5*(1-CS));
        bravo=abs(eigenstates(2,i))^2+abs(eigenstates(4,i))^2+abs(eigenstates(6,i))^2;
        correlations(i)(1,1)=(CS*bravo)+(0.5*(1-CS));
    end
```

```
end

// Calculate the single spin 1 transition matrix elements in x y z
Monex = zeros(6,6);
Money = zeros(6,6);
Monez = zeros(6,6);
            for f=1:6
                for i=1:6
                        Monex(f,i)=(eigenstates(:,f)'*(sx_op1)*eigenstates(:,i));
                        Money(f,i)=(eigenstates(:,f)'*(sy_op1)*eigenstates(:,i));
                        Monez(f,i)=(eigenstates(:,f)'*(sz_op1)*eigenstates(:,i));
                end
            end

// Calculate the single spin 1/2 transition matrix elements in x y z
// Electron traversing from TIP to SAMPLE
Mts=zeros(6,6);

for f=1:6
    for i=1:6
                for r=1:2
                    for c=1:2
                        xterm=(sqrt((sampleprob(:,r))))'*(sx_half)*(sqrt(correlations(i)(:,c)));
                        yterm=(sqrt((sampleprob(:,r))))'*(sy_half)*(sqrt(correlations(i)(:,c)));
                        zterm=(sqrt((sampleprob(:,r))))'*(sz_half)*(sqrt(correlations(i)(:,c)));
                        Mts(f,i)=Mts(f,i)+(abs(Monex(f,i)*xterm+Money(f,i)*yterm+Monez(f,i)*zterm)^2);
                    end
                end
    end
end

// Electron traversing from SAMPLE to TIP
Mst=zeros(6,6);

for f=1:6
    for i=1:6
                for r=1:2
                    for c=1:2
                        xterm=(sqrt((correlations(f)(:,r)))'*(sx_half)*(sqrt(sampleprob(:,c))));
                        yterm=(sqrt((correlations(f)(:,r)))'*(sy_half)*(sqrt(sampleprob(:,c))));
                        zterm=(sqrt((correlations(f)(:,r)))'*(sz_half)*(sqrt(sampleprob(:,c))));
                        Mst(f,i)=Mst(f,i)+(abs(Monex(f,i)*xterm+Money(f,i)*yterm+Monez(f,i)*zterm)^2);
                    end
                end
    end
end

// Define different conductance values for each energy regime based on matrix elements
// Here for T -> 0, otherwise the higher states could also be populated
conductancets=zeros(3,1);
conductancets(1,1)= Mts(1,1)+Mts(1,2)+Mts(2,2)+Mts(2,1);
conductancets(2,1)= (Mts(1,4)+Mts(1,3))+(Mts(2,3)+Mts(2,4));//+Mts(3,3)+Mts(4,4)+Mts(3,4)+...;
conductancets(3,1)= (Mts(1,6)+Mts(1,5))+(Mts(2,5)+Mts(2,6));//+Mts(5,5)+Mts(6,6)+...;

conductancest=zeros(3,1);

conductancest(1,1)= Mst(1,1)+Mst(1,2)+Mst(2,2)+Mst(2,1);
conductancest(2,1)= (Mst(1,4)+Mst(1,3))+(Mst(2,3)+Mst(2,4));//+Mst(3,3)+Mst(4,4);
conductancest(3,1)= (Mst(1,6)+Mst(1,5))+(Mst(2,5)+Mst(2,6));//+Mst(5,5)+Mst(6,6);

//for the loop the asymmetry calculation
asymmetry(images,1)=(conductancets(3,1)/conductancest(3,1));

// Boltzmann distribution for population of eigenstates
// Zustandssumme
zustandssumme=0;
// Boltzmann constant in meV/T
k_b=0.08617;
T=1.5;
for i=1:6
    zustandssumme=zustandssumme+exp(-eigenvalues(i,i)/(k_b*T));
end
// Now the actual probability per state
population=zeros(6,1);
for i=1:6
    population(i,1)=(exp(-eigenvalues(i,i)/(k_b*T)))/zustandssumme;
end

////////////////////////////////////////////////////////////////////
// Plot the actual conduction using a Boltzmann step function //////
```

```
//////////////////////////////////////////////////////////////////////
// just the voltage range, defining the number of points
x = -15:.1:15;
x=x';
// the actual energy used
x2=x;
// and the conductance final results
y=x;

// adding up matrix elements and probabilities (possible at T -> 0 instead of step function)

for r=1:(length(x)),
    if (r < (length(x)/2)) then
          if (abs(x(r))<eigenvalues(3,3))  then
            y(r)=conductancets(1,1);
          elseif (abs(x(r))==eigenvalues(3,3) | (abs(x(r))>eigenvalues(3,3) & abs(x(r))<eigenvalues(5,5))) then
            y(r)=conductancets(1,1)+conductancets(2,1);
          else y(r)=conductancets(1,1)+conductancets(2,1)+conductancets(3,1);
          end,
    else
          if (abs(x(r))<eigenvalues(3,3))  then
            y(r)=conductancest(1,1);
          elseif (abs(x(r))==eigenvalues(3,3) | (abs(x(r))>eigenvalues(3,3) & abs(x(r))<eigenvalues(5,5))) then
            y(r)=conductancest(1,1)+conductancest(2,1);
          else y(r)=conductancest(1,1)+conductancest(2,1)+conductancest(3,1);
          end,
    end
end

//abort

clf() //clear the content of the old image
f=get("current_figure");
f.figure_position;
f.figure_size=[900,850];
a=get("current_axes");//get the handle of the newly created axes
a.font_size = 5; //font size of the ticks
xlabel("Bias Voltage / meV", "fontsize",6);
ylabel("Differential Conductance / arb. units", "fontsize",6);
title("Field = "+string(B_z)+" T | Coupling = "+string(Jz)+" meV | Correlation = "+string(CS*100)+" %","fontsize",6,"color","red");
a.data_bounds=[-15,-0.02;15,(max(y)+0.1*max(y))]; //(max(y)+0.2*max(y)) if based on height
plot(x,y)
p = get("hdl");
p.children.thickness = 4;
//Print image in PNG file in the same directory
xs2png(gcf(),sprintf("example_%03d.png",images));

// Print desired results in file
results=[x,y];
fprintfMat(pwd()+"\results.dat", results, "%e");

sleep(100);

end
```

APPENDIX B

SCILAB CODE FOR FORCE CALCULATION

```
//////////////////////////////////////////////////////////////////////
//////////////////////////////////////////////////////////////////////
// Automatic Force Calculation in Scilab /////////////////////////////
// MPI Stuttgart - Matthias Muenks 3/2016 Nanonis file format ////////
// Based on the paper: ///////////////////////////////////////////////
// Analysis of force-deconvolution methods in ////////////////////////
// frequency-modulation atomic force microscopy (Giessibl et al.) ////
//////////////////////////////////////////////////////////////////////
//////////////////////////////////////////////////////////////////////

// Provide the raw data filepaths
// For ON atom approach 400pm and retract 2000pm
filepathOn400 = pwd()+"\ON_400_Spectroscopy172.dat"
filepathOn2000 = pwd()+"\ON_2000_Spectroscopy173.dat"
// For OFF atom approach 400pm and retract 2000pm
filepathOff400 = pwd()+"\OFF_400_Spectroscopy174.dat"
filepathOff2000 = pwd()+"\OFF_2000_Spectroscopy175.dat"

// Read the numerical values of files in Matrix
[MOff400]=fscanfMat(filepathOff400);
[MOff2000]=fscanfMat(filepathOff2000);
[MOn400]=fscanfMat(filepathOn400);
[MOn2000]=fscanfMat(filepathOn2000);

// Standard for z-position is cloumn 1
// therefore read column 1 of the two matrices
zOff1=MOff400(:,1);
zOff2=MOff2000(:,1);
// Shift z values so that the following is true:
// z is a vector of length n and has values in the unit m
// z(i) is closer to surface than z(i+1)
// z(i) < z(i+1)
zOff1=-zOff1;
// delete last datapoint since it is redundant
zOff1(400)=[];
// Continue with Off z data and shift it
zOff2=zOff2+(4.000D-10);
// Add the two vectors
z=cat(1,zOff1,zOff2);
// For best drift match take bwd curve of 400pm approach curve
// and fwd curve of 2000pm retract curve
// Get tunneling current as I(z) (400pm bwd + 2000pm fwd)
offCurrent=cat(1,flipdim(MOff400(:,11),1),MOff2000(:,2));
offCurrent(400)=[];
onCurrent=cat(1,flipdim(MOn400(:,11),1),MOn2000(:,2));
onCurrent(400)=[];
// Get frequency shift as F(z) (400pm bwd + 2000pm fwd)
offFreq=cat(1,flipdim(MOff400(:,18),1),MOff2000(:,9));
offFreq(400)=[];
onFreq=cat(1,flipdim(MOn400(:,18),1),MOn2000(:,9));
onFreq(400)=[];

// Substract OnAtom Data with OffAtom Data
deltaF=onFreq-offFreq;
current=onCurrent-offCurrent;

////////////////////////////////////////////////////////////////////
// Employ the Sader-Jarvis Algorithm ///////////////////////////////
////////////////////////////////////////////////////////////////////
// Set Tuning Fork Values
f_0=29077; // Center Frequency
k=1800; // Stiffness
A=50E-12; // Oscillation Amplitude
pi=3.14159265358;

// Reduced Frequency Shift Omega
omega=deltaF/f_0;

// Derivative of the reduced frequency shift dOmega_dz
domega_dz=diff(omega)./diff(z);

// Adjust length to length of the derviation dOmega_dz
// by deleting the last element
z(length(z))=[];
deltaF(length(deltaF))=[];
omega(length(omega))=[];

// Integrate stepwise in a for loop
for j=1:(length(z)-2)
    // start at j+1 due to pole at t=z
```

```
        t=z(j+1:length(z));
        // adjust length of Omega und dOmega_dz to length of t
        omega_tmp=omega(j+1:length(omega));
        domega_dz_tmp=domega_dz(j+1:length(domega_dz));
        // calculate integral using Scilab inttrap instead of Matlab trapz

integral= inttrap(t, (1+sqrt(A)./(8*sqrt(pi*(t-z(j))))).*omega_tmp-A^(3/2)./sqrt(2*(t-z(j))).*domega_dz_tmp);
        // correction terms for t=z from
        corr1 = omega(j)*(z(j+1)-z(j));
        corr2 = 2*(sqrt(A)/(8*sqrt(pi))) * omega(j) * sqrt(z(j+1)-z(j));
        corr3 = (-2)*(sqrt(A)^3/sqrt(2)) * domega_dz(j) * sqrt(z(j+1)-z(j));
        F(j)=2*k*(corr1+corr2+corr3+integral);
    end

    // adjust length to length of the force F
    z=z(1:length(F));
    // add an offset to F so that all values are positive
    Foffset=F-(min(F));
    // add an offset to current so that all values are positive
    currentoffset=current-(min(current));

    // Write results in matrix that is later printed into a txt file
    results(:,1)=z;
    results(:,2)=onCurrent(1:length(z));
    results(:,3)=offCurrent(1:length(z));
    results(:,4)=current(1:length(z));
    results(:,5)=currentoffset(1:length(z));
    results(:,6)=onFreq(1:length(z));
    results(:,7)=offFreq(1:length(z));
    results(:,8)=deltaF(1:length(z));
    results(:,9)=F;
    results(:,10)=Foffset;

    fprintfMat(pwd()+"\results.dat", results, "%e");

    //plot(results(:,1),results(:,2))
```